Constraining ore genesis and palaeoclimate change using (U-Th)/He/Ne dating and stable isotope geochemistry.

David Currie

BSc Hons, University of Glasgow

Submitted in fulfilment of the requirements for the degree of

Doctor of Philosophy

Scottish Universities Environmental Research Centre (SUERC)

College of Science and Engineering

University of Glasgow

March 2023

Abstract

Providing absolute geochronological constraints on events in Earth history is of fundamental importance to modern geology. In ore geology, understanding the absolute timing of ore-forming processes provides insight into the tectonic and/or climatic events that drove their formation and can inform ore exploration models. Ore deposits are typically dated by U-Pb geochronology of various U and Th – bearing accessory minerals related to the ore system, like zircon, apatite, and monazite. However, many ore deposits do not contain these accessory minerals thus, it is necessary to continue with the development of new analytical techniques to date ore mineralisation.

In this PhD I have developed the (U-Th)/He and Ne geochronology techniques for Fe-oxide/oxyhydroxides, and applied them to two distinct ore systems:

The Attepe iron deposits of Central Anatolian Plateau, Turkey, provided the opportunity to develop (U-Th)/He dating to deeply weathered supergene ore mineralisation. This has been used to unravel the timing of palaeoclimate change on the Anatolian plateau.

In the second study I have revisited the paragenesis of the Leadhills-Wanlockhead Pb-Zn deposit in the Southern Uplands of Scotland, identifying previously unrecorded hematite mineralisation. Careful sample selection was followed by hematite (U-Th)/Ne dating, while He and S stable isotope analysis of sulfides were used to determine the source of ore fluids and metals.

Established Fe-oxide-oxyhydroxide (U-Th)/He techniques determine U, Th and He on the same mineral fragment. However, volatilisation of U and Th during the heating required for He extraction is common and leads to erroneously old He ages and over-dispersed age populations. The method developed in this thesis completely avoids the volatilisation issue by determining the He content of minerals separately from U and Th in multiple aliquots of several mg of each sample. A repeatable and time efficient sample preparation, petrography, chemistry, laser heating, and gas analysis schedule was established. New He age determinations of the Attepe iron deposits, central Turkey, have been used to determine climatic history of the Anatolian plateau. The data reveal pervasive supergene mineralisation and He loss-corrected (U-Th)/He ages of between 5.18 and 0.95 Ma. The presence of supergene iron oxy-hydroxides throughout the ore deposits suggests that the Plio-Pleistocene climate was hotter and more humid than today. The latest goethite precipitation (0.95 Ma) constrains the onset of aridification across the region to sometime in the last million years.

Hematite (U-Th)/Ne dating relies on the production of nucleogenic ^{21}Ne from the reaction $^{18}O(\alpha,n)^{21}Ne$. To resolve the concentration of radiogenic ^{21}Ne from the atmosphere-derived Ne trapped in minerals, a Thermo Fisher ARGUS VI mass spectrometer and an automated ultra-high vacuum gas purification and separation system was developed specifically for Ne isotope analysis. Sample preparation, petrography and chemistry work was similar to the (U-Th)/He analysis. In addition, I developed a repeatable and time efficient laser heating and gas analysis schedule for multi-aliquot (U-Th)/Ne analysis. Developments mean less sample material is required compared to previous studies and it negates the use of flux-melting based extraction of Ne which can result in damage to hardware.

Hematite is widespread in the Leadhills-Wanlockhead Orefield (LWO) and post-dates early (Caledonian) quartz veining and pre-dates the main phase base metal mineralisation that has previously been shown to be Carboniferous in age. New hematite (U-Th)/Ne ages reveal three hematite precipitation phases at around 230 Ma, 200 Ma, and 155 Ma. Sulfur isotope composition of ore sulfides revealed a homogenous signal and an equilibrium precipitation temperature of 170 to 210°C. Sulfur and metals are suggested to be sourced from the underlying basement. Helium isotope composition of ore sulfides reveals a crustal source of helium was the source of heat in the ore-forming process at LWO. The highest $^{3}He/^{4}He$ recorded is < 1% of typical mantle signature, implying that mantle-derived heat from deep magmatic bodies was not the driver of the ore fluids. The timing of Pb-Zn mineralisation across the LWO is suggested to be linked to a wider western European series of tectonic events associated with the breakup of Pangaea.

Contents

List of Tables

List of Figures

Acknowledgements

I started my journey in higher education studying music performance at Reid Kerr College. To Chris, John, and Grant and all my band-mates and friends, thank you for giving me the confidence boost I needed to go on to my undergraduate years at University of Glasgow.

The Scottish university system allows 1st year students to study three subjects, and for that I thank them. Studying music at University of Glasgow only lasted around a fortnight before I switched to Geography, Earth Science, and Archaeology and it wasn't until the end of my second year of undergraduate that I solidified my main subject as Earth Science. The residential fieldtrip to Arran was the clincher. Shoutout to The Silver Hammers for sharing not-entirely-legal accommodation with me that year. I moved to Nova Scotia in the autumn of 2015 to undertake my 3rd year of Earth Science as an international exchange student at Dalhousie University. I would like to give a huge shoutout to all my Canadian buds who helped me move seamlessly by enjoying beers and games of pool at the Oasis dive and also to Mike and John for leading such a great trip out to Death Valley to end my time abroad. On returning to Glasgow, I headed north to Eriboll with my now wife, Marli, for summer mapping and on return we moved in to our first flat together in the idyllic surrounds of Maryhill. We would go on to complete our degrees together and move to the more culturally diverse Govanhill the following summer. Thank you to all staff and students I have interacted with over the undergraduate years at University of Glasgow.

This PhD started in October of 2017, and it feels like it has taken even longer than 7 years to complete. The whole process was far from smooth sailing, and we battled through some rough waters to land this thesis. In all honesty, I don't think my heart was ever in it. The flip-side was going into geoengineering, and I didn't much fancy that either. Doing a PhD is great if you enjoy being stressed and skint. Being stressed, skint, and in East Kilbride is the holy grail of bad times. There were moments of clarity between 2017 and 2020, most of which were experienced on my cycle commute to and from East Kilbride or in well-oiled good company (shoutout to Glasgow friends, PhD Society Wednesdays, and to getting married). Laboratory analysis ground to a halt as COVID-19 swept across the world and my time at SUERC ended around then, too. Thank you to all staff and students at SUERC who have given me their time over those years, most notably Fin, Luigia, Dom, Marta, Biying (Celia), Adrian, Alison, Ross, Kathy, and Andrew Tait. Special mention to John Faithfull for assistance with fieldwork and sampling and for his musings over the weird and wonderful aspects of mineralogy and all

things Scottish geology. Special mention to Peter Chung and Claire Wilson for assistance with SEM and XRD, respectively.

When the funding stopped, I had to find work and try to complete the thesis simultaneously. Those two things didn't work out for me, and I took an extended break from the PhD. Thanks to the College of Science and Engineering at University of Glasgow for being so understanding. I eventually found work at Share Scotland in Govan as a support worker. Gary, Edward, Mark, and Adelle were a pleasure to support, and I still appreciate every second of my time spent there. It was around this time, in the summer of 2020, that Marli and I welcomed our wee boy, Alasdair, into the world. I became an expert in supporting people over the next few years and very rarely thought about mass spectrometers, isotopes, or ore-forming processes. A peaceful period, upon reflection.

In the spring of 2022, Marli and I noticed a job opportunity with the British Geological Survey. We both applied for the single position, the first geology job I had applied for in over 2 years, and we both made it to final interviews. Marli got the job, and I was left hanging. A few days later, I was called by my now manager and offered a similar role to that advertised. We moved to Keyworth in early September of 2022 and have both worked with BGS since. We have been fortunate to have entered such a welcoming environment with likeminded people around us. Getting back into geology was not easy to begin with, but I feel like I have found some steadier footing now. Thanks to the minerals team and Kathryn Goodenough in particular for looking out for me.

Finally, thank you to my friends and family who have always supported, and questioned, my endeavours. Special mention to my mum, dad, and grandparents for believing in me in whichever direction I go through life. And to my wife, Marli, thank you for your constant and unwavering support in every possible way. You have saved me from the void.

I will take this opportunity to remember Rod Brown who passed during the completion of this work. I first met Rod in my undergraduate degree at Glasgow and got to know him better as I progressed with my PhD. I will always remember him as such a joyful character with so much time to give. Thermo2018 in Quedelinburg was that extra bit special by getting to hear his stories with several pints flowing. Cheers, Rod.

"What's the bravest thing you ever did? He spat in the road a bloody phlegm. Getting up in the morning, he said" – from The Road by Cormac McCarthy.

Author's Declaration

I, David Currie, declare that, except where explicit reference is made to the contribution of others, this dissertation is the result of my own work and has not been submitted for any other degree at the University of Glasgow or any other institution. Any published or unpublished work by other authors has been given full acknowledgement in the text.

Signature:

Date: 27/03/2023_____

1.0 Introduction

1.1 Dating ore deposits

Understanding how and when ore deposits form allows us to gain insight into tectonic, magmatic, hydrological, and biological processes at crustal scale in three dimensions across billions of years of Earth history (Jenkin et al., 2015). Thus, ore deposits provide an ideal opportunity to better understand the evolution of the planet, but only if we have the tools to unravel the processes that form them.

Over the 20th century the geological timescale has gradually become better quantified due to the development of radiometric methods for dating mineral formation. Many minerals contain measurable amounts of radioactive isotopes (parents) that decay to produce daughter isotopes. If the amount of parent and daughter isotopes can be measured precisely and the decay constant is known the technique has the potential to be used as an absolute chronometer. The development of geochronology over the past 100 years has changed the way we think about our planet; allowing radical improvement in our understanding of age (Patterson et al., 1955), and evolution (Zachos et al., 2001 and references therein), as well as the development plate tectonics (Dietz and Holder, 1970 and references therein).

Ore deposits are conventionally dated by U-Pb geochronology of U- and Th–bearing accessory minerals (zircon: Valley et al., 2009; apatite and monazite: Neymark et al., 2016; monazite: Rasmussen et al., 2006 for example). Although the U-Pb system provides us with a wealth of geochronological data, but it is not without its challenges. Valley et al. (2009) recognised that mineral phases like apatite and titanite can incorporate common Pb (^{204}Pb) in their structure which can affect age determination. From apatite provenance studies, Chew et al. (2011) discussed how low U-Th and radiogenic Pb, common Pb, and the lack of U-Th-Pb apatite standard material are distinct challenges for application of apatite LA-ICPMS geochronology. The presence of multiple mineral generations, dissolution-reprecipitation, intergrowths and mineral inclusions can affect apatite dating of ore mineralisation (Neymark et al., 2016). Cherniak et al. (2004) recognised that distinct age and/or compositional domains in monazite can be present in samples with fluid recrystallisation histories. Furthermore, few ore deposits contain these accessory minerals in their paragenesis and are not amenable to dating.

Recognition of these difficulties and the need for direct dating of ore mineralisation to better inform models of ore forming processes has resulted in the development of new geochronology systems. For example, the dating of Cornish cassiterite by high-precision ID-TIMS U-Pb systematics (Tapster and Bright, 2020; Moscati and Neymark, 2020) and ID-TIMS, SHRIMP and LA-ICP-MS hematite U-Pb geochronology of the Olympic Dam Cu-U-Au-Ag deposit (Courtney-Davies et al., 2019). Again, these studies are not without challenges and require detailed petrography, data screening, and interpretation of what the data may mean in the wider context of ore forming processes. The relative success of these developmental methods highlights the necessity to continue developing methods to directly date ore mineralisation and to select the most applicable method for the mineralisation in question.

1.2 The trouble with dating Fe-oxide-oxyhydroxides

Over the past decade or so, the hematite and goethite (U-Th)/He and (U-Th)/Ne chronometers have become established methods for quantifying the timing of near surface processes like hydrothermal mineralisation (Lippolt et al., 1995; Farley and Flowers, 2012; Farley and McKeon, 2015; Wu et al., 2019); supergene mineralisation and weathering events (Cooper et al., 2016; Deng et al., 2017; Shuster et al., 2005; Heim et al., 2006; Vasconcelos et al., 2013; Monteiro et al., 2014; Danišík et al., 2013; Wells et al., 2019); and fault activity (Ault, 2020 for review). However, these chronometers are not widely utilised due to challenging analytical procedures, issues surrounding U-loss, and the difficulty in quantifying diffusive loss of the daughter product (see Hofmann et al., 2020 for example).

In standard protocols helium and neon are extracted from minerals by heating in ultra-high vacuum conditions. This gas is purified by a series of getters and cryogenically cooled charcoal traps to remove the active gases and unwanted heavy noble gas species before analysis by magnetic sector mass spectrometer (Wu et al., 2019 for example). Most commonly, the mineral used for He or Ne measurement is used for the determination of the concentration of the parent isotopes (Vasconcelos et al., 2013 for example). In this procedure problems can arise due to U-loss during sample heating resulting in spuriously old ages (Vasconcelos et al., 2013, for example). This can be avoided if the parent isotopes and daughter products are measured in separate mineral aliquots (Wu et al., 2019). This requires more sample (several 100 mg) and can result in the loss of sample-specific age data as it determines an average age for a sample

rather than a succession of ages spanning the entire history of mineral precipitation, a key aspect of some studies (Wells et al., 2019).

Goethite forms primarily at Earth surface and precise ages record the timing of particular climatic conditions. Even at surface temperatures He can diffuse out of goethite thus care has to be taken when selecting samples on the basis of grain size and crystallinity (Shuster et al., 2005; Heim et al., 2006; Wells et al., 2019). Although typically more retentive of He than goethite (Farley, 2018), hematite in epithermal systems can be held at or near He closure temperature (T_c) for sustained periods or be subject to multiple passes through T_c. This can result in a complex thermal history where the (U-Th)/Ne age may represent the precipitation age and (U-Th)/He age reflects the cooling history (Farley and Flowers, 2012). Quantifying diffusive loss of He (and to a lesser extent Ne) requires good understanding of sample mineralogy and grain size, a pre-requisite for ensuring that ages are geologically meaningful.

1.3 Thesis outline

In this thesis I show how the development and application of iron oxide-oxyhydroxides (U-Th)/He and (U-Th)/Ne chronometry can be used to date otherwise undatable processes. In doing so I constrain the timing of supergene iron oxide-oxyhydroxides mineralisation at the Attepe iron deposits in Central Anatolian Plateau by (U-Th)/He dating. This data provides insight into how and when the region switched from a hot-humid climate to the modern semi-arid climate. In a second study, I use He and S isotopes a large suite of hydrothermal sulfides from the Leadhills-Wanlockhead Pb-Zn deposit in southern Scotland to constrain the source of heat and fluid-rock interaction history. Further work uses the newly developed (U-Th)/Ne dating technique applied to hematite from the Leadhills-Wanlockhead Pb-Zn deposit. I show that the hematite predates the main phase Pb-Zn mineralisation such that dating constrains the timing of Pb-Zn mineralisation. The combination of these data allows a new ore genesis model for this enigmatic orefield to be suggested.

Chapter 2 provides an overview of the principles and key developments in the field of iron oxide-oxyhydroxides (U-Th)/He and (U-Th)/Ne chronometry, the primary focus of this PhD. By relating the dating technique to several other more prominent thermochronometers, its usefulness in the wider field of study is established. The differences between multi- and single-aliquot methods are explained prior to showing how ages for both He and Ne ages are

calculated in this study. This chapter concludes by providing context for how the field of low temperature thermochronology have quantified He and Ne retention and extraneous He (and Ne) in hematite and goethite and how these factors can affect age data.

Chapter 3 reports the analytical conditions and protocols developed during this PhD. The techniques for both (U-Th)/He and (U-Th)/Ne dating are detailed and compared with procedures developed elsewhere with recommendations made for future work in this area of analysis.

In chapter 4 the multi-aliquot (U-Th)/He method (adapted from Wu et al. 2019) is applied to a suite of iron oxide-oxyhydroxides from the supergene zone of the Attepe iron deposits in southern Turkey. Supergene Fe-oxide-oxyhydroxides reveal (U-Th)/He ages between 1 and 5 Ma. Implied rock uplift rates (6 and 12 m/Ma) are low suggesting that the region was at or near the current elevation by 5 Ma. Data presented suggests that aridification across the region occurred in the last million years and was likely driven by regional climate cooling rather than tectonic uplift. This contrasts starkly with the prevailing view which considers the onset of aridification across the southern margin of the Central Anatolian Plateau (CAP) by the middle Pliocene a result of uplift and reorganisation of drainage rather than climate change (Meijers et al., 2020). Ultimately, this chapter shows that by adapting the methods of Wu et al. (2019), iron oxide-oxyhydroxide (U-Th)/He dating can be applied to challenging sample sets and produce reproducible and geologically meaningful data.

Chapters 5 through 6 are focussed on the genesis of the Leadhills-Wanlockhead Pb-Zn deposit of southern Scotland. Chapter 5 shares the findings of a revised paragenesis in which hematite was recognised to post-date early quartz veining and pre-date sulfide mineralisation. Dating of hematite by (U-Th)/Ne geochronology is then applied with ages ranging from 230 to 150 Ma, consistent with multiple precipitation events related to distal effects of rifting. This is around 100 Ma younger than the prevailing hypothesis and provides the earliest timing possible for main ore-phase mineralisation at Leadhills-Wanlockhead Orefield (LWO).

Chapter 6 documents the sulfur isotope analysis of over sixty samples representing at least seventeen ore veins to assess the sulfur source for the orefield. It was found that $\delta^{34}S$ values of galena, sphalerite, and chalcopyrite are remarkably homogeneous and consistent with the derivation of S from fluids that have equilibrated with the Lower Palaeozoic basement with ore fluid temperature of 190±20°C. Barite, though determined to be cogenetic with base metal mineralisation, was not in equilibrium and may be indicative of fluid derivation for another

source like intracontinental brines. Chapter 6 also addresses the source of heat driving ore fluids across the LWO using the helium isotope composition of gases released from the crushing of sulfides. Most sample have $^{3}He/^{4}He \leq 0.05\ R_a$, implying that the ore fluids were not driven by heat advected from the mantle, but rather from crustal convection. Chapter 6 ends by providing a discussion on the results of chapters 5 and 6 and puts them in relation to a wider, more European facing perspective. The timing of ore-phase mineralisation may coincide with a distinct phase of crustal extension across Western Europe synchronous with the break-up of Pangaea/opening of the Atlantic in Jurassic times.

Chapter 7 discusses the techniques developed in this thesis and how the use of iron oxide-oxyhydroxide (U-Th)/He/Ne dating is being developed and applied to a wider set of problem in Earth science in collaboration with other methods.

2.0 Principles of Fe-mineral (U-Th)/He and Ne thermochronology

2.1 Introduction

Many minerals contain trace amounts of radioactive isotopes, such as ^{238}U, ^{235}U, and ^{232}Th. These parent isotopes decay at known rates to produce daughter products. If the present-day amount of parent and daughter isotopes in a target mineral can be measured. and the decay constants are known, the system can be used as an absolute chronometer.

The retention of daughter products in minerals is typically temperature dependent. Their loss by diffusion from the crystal lattice or lattice defects provides the ability to use the system as thermochronometers (Farley, 2000 for example). Below the mineral closure temperature (T_c), the temperature at which diffusive loss of the daughter product is insignificant, daughter products accumulate within the crystal lattice of mineral phases (Dodson, 1973). Rutherford (1905) reported the first radiogenic age of the Earth based on U/He system. Strutt (1905) was quick to spot the error in Rutherford's age and reported that the diffusive loss of the daughter product from the crystal lattice of minerals may be a limiting factor for determining absolute ages and that it resulted in an age that was younger than expected. Work by Zeitler et al. (1987) provided a quantitative explanation for spuriously young ages, and in doing so kicked off the field of thermochronology where "cooling ages" can be used to determine low-temperature thermal history of rocks. Continued work has refined our understanding of thermochronometers and in doing so has allowed a multitude of questions regarding Earth history to be answered (see Farley, 2002; Reiners et al., 2005 for example)

In many mineral systems used as chronometers, the temperature range over which partial diffusive loss of daughter products occurs has been quantified (Fig. 2.1). For example, zircon is a widely used target mineral for multiple chronometers. At the high T_c end of the spectrum, U-Pb and U-series disequilibrium dating of zircon has revealed that zircon crystallisation can predate volcanic eruption (Simon and Reid, 2005). The T_c for diffusion of radiogenic Pb in zircon is higher than that of a volcanic eruption which is typically >1000°C (Crowley et al., 2007). Gautheron et al., (2006) used zircon (U-Th)/Ne ages of well constrained slowly cooled plutonic rocks to interpolate a T_c of ~400°C based on cooling rates from time of formation ages. This was the first time the zircon (U-Th)/Ne system had been tested as a chronometer following

earlier work on ^{21}Ne production rates (Yatsevich and Honda, 1997; Leya and Weiler, 1999). Below 400 °C, the switch from geochronology to thermochronology is more pronounced and questions being answered tend to focus on surficial processes like mountain uplift and erosion (Tremblay et al., 2015) and the resetting of daughter products by thermal events (Young et al,. 2013).

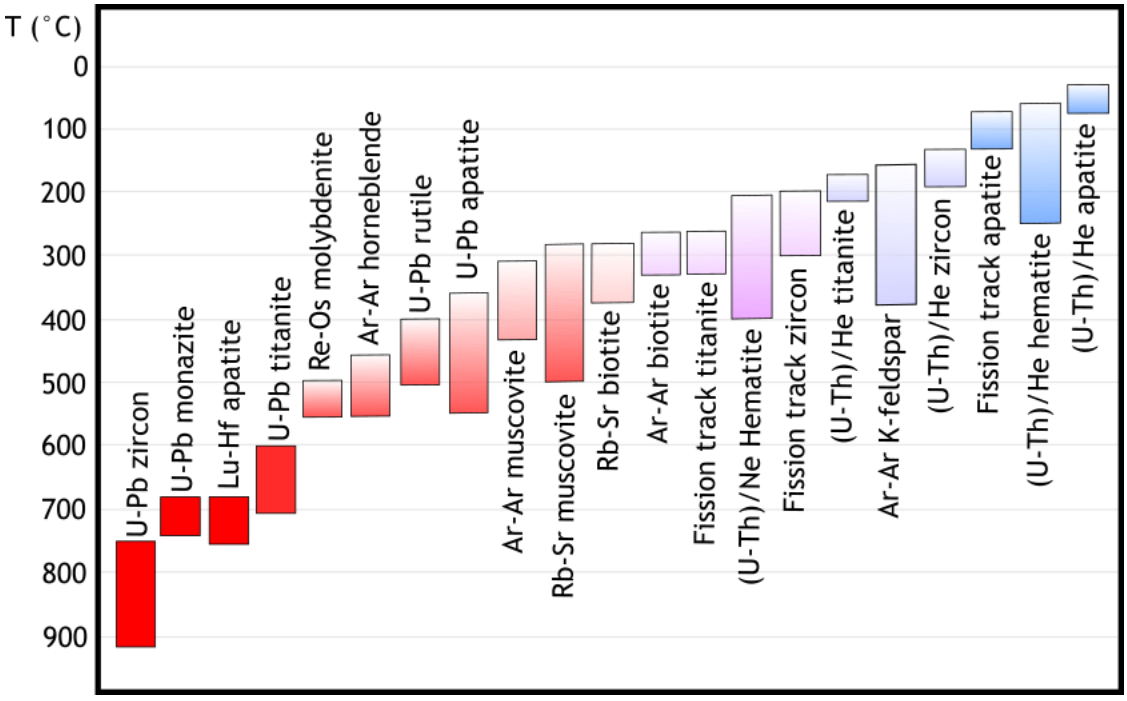

Figure 2.1: Effective closure temperatures for commonly used thermochronometers including hematite (U-Th)/He/Ne. Based on Chew and Spikings (2015).

As a target mineral in low temperature thermochronology, zircon is increasingly well understood (Reiners et al., 2005 for discussion). It is relatively stable at Earth's surface so the effect of diffusive loss of the daughter product due to surface conditions is negligible. However, for minerals like goethite (FeOOH) which forms primarily at Earth surface, surface temperature, climatic conditions, and the duration the mineral has spent in that climate range affects retentivity of the daughter product (Shuster et al., 2005; Heim et al., 2006; Wells et al., 2019). The amount of He retained in the mineral lattice is governed by crystallite size and polycrystalline morphology of the mineral (Farley, 2018; Allard et al., 2018; Monteiro et al., 2014; Shuster et al., 2005 for example), the potential for contamination from other daughter-rich phases proximal to the analysed material (Vasconcelos et al., 2013), and the loss of the daughter product through α-ejection (Ketcham et al., 2011; Vasconcelos et al., 2013).

Therefore, prior to applying a mineral chronometer to a problem, it is crucial that factors affecting its ability to supply insightful data must be rationally considered.

This chapter provides an overview of the theoretical basis of (U-Th)/He thermochronometry applied to hematite (Fe_2O_3) and (U-Th)/Ne dating of hematite.

2.2 Applications

2.2.1 (U-Th)/He technique

Over the past decade (U-Th)/He dating of Fe-oxide-oxyhydroxide has become an established methods for quantifying the timing of hydrothermal mineralisation (Lippolt et al., 1995; Wu et al., 2019); supergene mineralisation and weathering events (Cooper et al., 2016; Deng et al., 2017; Shuster et al., 2005; Heim et al., 2006; Vasconcelos et al., 2013; Monteiro et al., 2014; Danišík et al., 2013; Wells et al., 2019); and fault activity (Ault, 2020 for review). The following section highlights several prominent methods currently used to arrive at a meaningful age or age range for the studied sample-set.

All studies begin with the selection of material most likely to provide meaningful age data. In studies concerned with the dating of ore hematite and hematitic fault surfaces, hematite can be routinely removed from hand specimens using rotary tools and/or fine point tweezers in the field (Ault, 2020). To avoid the collection of poor quality samples, Shuster et al. (2005) set out a guide for the selection of appropriate goethite for weathering (U-Th)/He geochronology in which material should be directly precipitation from a weathering solution into cavities, have botryoidal growth habits, be pure and devoid of primary contaminants, be composed of an aggregate of goethite crystallites <1 μm, and be associated with other dateable supergene phases with known paragenetic relationship to each other. A knowledge of depth from surface or elevation may also be key when selecting sample material, especially in weathering chronometry (Deng et al., 2017; Cooper et al., 2016 for example).

Depending on the hypothesis being tested, multiple methods have been employed to characterise sample material. Most studies use a combination of binocular, reflected and transmitted light, and scanning electron microscopy coupled with energy dispersive X-ray analysis, Raman spectroscopy, and X-ray diffractometry to determine paragenetic relationships, textures, mineralogy, and the crystal morphology and crystallite size of the sample set

(Vasconcelos et al., 2013; Danišík et al., 2013; Shuster et al., 2005; Allard et al., 2018; Ault, 2020 for example).

The original method of Fe mineral (U-Th)/He dating was by splitting a large sample into multiple aliquots for separate analysis of He from U and Th (Strutt, 1908). This multi-aliquot method (Wernicke and Lippolt, 1994; Wu et al., 2019), or two-aliquot method (Farley and Flowers, 2012; Farley and McKeon, 2015) requires large amounts of sample (100's of mg to grams) and can lead to inaccurate ages as a consequence of parent element heterogeneity. It leads to the generation of average ages for samples rather than individual ages for sub-domains that may exist in hand specimens, a caveat necessary for unravelling the history of pisolites for example (Wells et al., 2019). However, the multi-aliquot method avoids the issue of U-loss during He extraction (Vasconcelos et al. 2013) and can provide reproducible and informative data (Wernicke and Lippolt, 1994; Wu et al., 2019; Farley and Flowers, 2012; Farley and McKeon, 2015). Samples are typically wrapped in Pt, Nb or Sn foil packets to ensure homogeneous heating (Wu et al., 2019).

Similar to apatite and zircon (U-Th)/He dating (Reiners et al., 2005 and references therein), the single-aliquot method is commonly applied to Fe-mineral dating (Shuster et al., 2005; Vasconcelos et al., 2013). Both He and U-Th are measured on the same single aliquot. The age calculation is based on absolute amounts of U-Th and He rendering sample mass and aliquot homogenization inconsequential (Vasconcelos et al., 2013). Far greater spatial resolution can be achieved than in multi-aliquot dating and allowing multi-generations within the larger sample to be dated (Wells et al., 2019 for example). As alluded to earlier, the single-aliquot method can lead to the issue of U-loss during He extraction if temperatures needed to extract He exceed 1000°C (Vasconcelos et al. 2013). However, recent work by Hofmann et al., (2020) identified that U loss is associated with a phase change from goethite and hematite to magnetite at 800-900°C in vacuum conditions typical of gas extraction systems. Increasing the temperature of this phase transition to ~1250°C by increasing the partial pressure of oxygen in the degassing chamber, they show that samples can be fully degassed at ~1150°C without experiencing U-loss.

By dissecting a polycrystalline aggregate of hematite, Jensen et al. (2018) were able to identify and isolate hematite plates of between 8 to 80 µm and separate them prior to He degassing and U-Th determination to reveal geologically sensible dates of >650 Ma. The results of

experimental single-crystal study by Farley (2018) are discussed in Section 2.4 as it has implications for He retention in hematite.

2.2.2 (U-Th)/Ne technique

The hematite (U-Th)/Ne chronometer is a more recent development and is less widely applied. Theoretical work by Wetherill (1954) and Yatsevich and Honda (1997) provided production rates of nucleogenic Ne which have since been tested by Gautheron et al., (2006) using predictive models and by direct measurement by Cox et al., (2015). Farley et al., (2020) then developed improved analytical techniques for extraction and analysis of neon from a range of mineral phases including hematite. Further discussion on their work in provided later in this thesis.

The first application of the chronometer to answering a geological question was carried out by Flowers and Farley (2012). They aimed to determine the age of hydrothermal hematite from the Grand Canyon. In their study, hematite was crushed to 100-400 µm diameter chips. Following sample purification, chips were loaded into Cu-foil and heated in double-walled vacuum for up to 14 hours during step heating analysis at temperatures up to 1375°C. However, analysis for dating of hematite by (U-Th)/Ne method occurred by double-walled vacuum furnace at 1250 °C with reheats at 1375 °C to ensure complete degassing. Uranium and Th were measured on separate material by isotope dilution analysis.

Farley and McKeon (2015) are the only other study to apply hematite (U-Th)/Ne geochronology to a geological problem, determining regional burial and exhumation histories of hydrothermal hematite from the Gogebic iron range, Michigan, USA. In doing so they refined the methods developed by Flowers and Farley (2012) and are backed by then newly confirmed production rates of nucleogenic Ne from Cox et al., (2015).

2.3 Helium age calculations

Hematite and goethite incorporate parts per million levels of U, Th, and Sm which decay to produce daughter products. In the He chronometer, α-particles which come to rest as ^{4}He are produced from the decay of ^{238}U, ^{235}U, ^{232}Th, and ^{147}Sm with ingrowth equation:

(Equation 1)

$$He = 8\,^{238}U\left(e^{\lambda_{238}t} - 1\right) + 7\left(^{238}U/137.88\right)\left(e^{\lambda_{235}t} - 1\right) + 6\,^{232}Th\left(e^{\lambda_{232}t} - 1\right)$$

Where ^{4}He, U, and Th refer to present day amounts, t is the accumulation time (He age), and λ is the decay constant ($^{\lambda}238$ = 1.551 x10^{-10}/yr; $^{\lambda}235$ = 9.849 x $10^{-10/}$yr; $^{\lambda}232$ = 4.948 x10^{-11}/yr) (From equation 1 in Farley, 2002). The coefficients preceding U and Th abundances are the multiple α-particles emitted within each of the decay series, with the factor 1/137.88 being the present day ^{235}U/^{238}U ratio (Farley, 2002). The concentration of ^{147}Sm is often relatively low and since its α-production rate is considerably lower than that of the other parent isotopes, it is commonly omitted from iterative ^{4}He accumulation time calculations (Farley, 2002). This approach assumes no initial concentration of ^{4}He is present since ^{4}He is uncommon in the atmosphere, and that no other mineral or fluid phase with the potential of carrying ^{4}He is present in the sample being analyses. Here, the following non-iterative approach for hematite and goethite (U-Th)/He age calculation is applied:

(Equation 2)

$$t_{app} = \frac{1}{\lambda_{wm}} \ln\left(\frac{\lambda_{wm}}{P}[He] + 1\right)$$

Where t_{app} is the apparent age, λ_{wm} is the weighted-mean decay rate of α-production from ^{238}U, ^{235}U, and ^{232}Th, and P is the total production rate of ^{4}He (From Meesters and Dunai, 2005). Therefore, if the amount of ^{4}He, U, and Th can be measured, potentially meaningful ages for target minerals may be determined.

2.4 Neon age calculations

^{21}Ne is produced from reactions induced by the same α-emitting parent isotopes as above. Most α-particles emitted come to rest as ^{4}He, however if the α-particle emitted has enough energy to enter the nucleus of an adjacent atom (~1 in 10 million) it leads to an overexcited compound nucleus which then loses a neutron (n) in order to stabilise. In the case of ^{18}O this leads to the production of nucleogenic ^{21}Ne (Cox et al., 2015). This reaction is commonly notated as ^{18}O(α,n)^{21}Ne (first noted by Wetherill, 1954).

Nucleogenic ^{21}Ne can be produced from reactions along the entire α-particle trajectory as it loses energy prior to reaching rest (Gautheron et al., 2006). Therefore, ^{21}Ne production will be higher early in the trajectory history, where α particle decays with high characteristic energy, and will also depend on how fast α-particles lose energy within the host mineral (Gautheron et al., 2006; Cox et al., 2015). The production rate of ^{21}Ne from this reaction depends on three criteria: chemical composition of the host mineral (hematite); the reaction cross section of the target nuclide (in this case ^{18}O), where the larger the cross section the higher the likelihood of the reaction taking place; and the stopping power, the rate of energy loss of a particle (in this case ^{4}He) as it travels through the mineral lattice (Gautheron et al., 2006; Cox et al., 2015). Since ^{21}Ne production rates increase toward the higher end of α-energies produced by U and Th decay, these decays dominate production of ^{21}Ne. ^{147}Sm is not considered in age determinations as it produces relatively insignificant amounts of ^{21}Ne (Cox et al., 2015). Production rate ratios in hematite for each decay chain from ^{18}O were derived by Cox et al. (2015) and are as follows: ^{238}U (^{21}Ne/^{4}He) = 2.80 x 10^{-8}; ^{235}U (^{21}Ne/^{4}He) = 3.89 x 10^{-8}; and ^{232}Th (^{21}Ne/^{4}He) = 4.21 x 10^{-8}.

By adapting equation 1, Gautheron et al. (2006) derived the following equation to calculate Ne ages:

(Equation 3)

$$Neage = \left(\frac{(^{21}Ne)_m}{F_{T,Ne}\, x \left(\frac{^{21}Ne}{^{4}He}\right) p \; x \; 10^{-15} x \left(121.7+28.7\,\frac{Th}{U}\right) x \; U}\right)$$

Where Ne_{age} is in years, U and Th are present day amounts in ppm, $F_{T,NE}$ is the factor of ^{21}Ne loss due to ejected α-particles and the recoil loss of ^{21}Ne (from Fig. 6A in Gautheron et al., 2006), $\left(\frac{^{21}Ne}{^{4}He}\right) p$ is the production ratio averaged over the three decaying isotopes, and ^{21} Ne_m is the Ne production value (Gautheron et al., 2006). The constants in the equation (121.7 and 28.7) are derived from production ratios of Ne and He from the three producers (^{238}U, ^{235}U and ^{232}Th) (Gautheron et al., 2006) If the present-day amounts of ^{21}Ne, U, and Th can be measured, potentially meaningful ages for target minerals may be determined. In this study we use MATLAB code provided by Cox et al. (2015) to compute (U-Th)/Ne ages for hematite. In this code, the user may change reaction cross section, stopping power, mineral stoichiometries, and oxygen content if necessary (Cox et al., 2015).

2.5 He and Ne retention in Fe-minerals

Knowledge of the closure temperature (T_c) and to what degree the daughter product is retained at surface conditions within a mineral, alongside the mineral's geological context, are essential when applying chronometers to problems. For example, in a slowly cooling or poorly understood epithermal system, hematite can be held at or near daughter product T_c for sustained periods or be subject to multiple passes through T_c, resulting in a complex thermal history such that the Ne age may represent a precipitation age and He age a cooling age (Farley and Flowers, 2012). If hematite cools quickly through T_c, the He age records the time of mineral precipitation, like in traditional geochronology (Wu et al., 2019).

For Fe-minerals precipitated at or near to planetary surfaces, like in supergene weathering zones, isothermal diffusive loss must be considered (Shuster et al., 2005). This is better understood as the effect a constant temperature has on a minerals ability to retain a daughter product within its crystal lattice over geological time. For example, a goethite sample held at 25°C for 10 Myr may lose 10% of its He (Shuster et al., 2005). Therefore, an age correction, making precipitation age older to account for He lost, should be carried out as well as the consideration of an increase to total errors on age determinations to account for uncertainties on the amount of He lost (Shuster et al., 2005).

In the following section, He and Ne retention in hematite and He retention in goethite will be discussed alongside steps taken to account for the loss, or gain, of He and Ne in samples.

2.5.1 He retention in hematite

In many other systems, like in apatite or zircon thermochronology, the dimension of the individual crystal governs He diffusion rate (Reiners and Farley, 1999; Farley, 2000). Early studies show that hematite is particularly retentive of He at roughly similar temperatures to more widely studied minerals like apatite and zircon (Bahr et al., 1994). For specular hematite (specularite) with crystallites (individual crystals that make up a grain) up to 5 mm, T_c was determined to be >200°C whereas in botryoidal hematite of crystallite size > 10 µm T_c is likely 90°C to 160°C (Bahr et al., 1994). More recently, and by determining He diffusion coefficient in hematite using a computational multi-scale approach, Balout et al. (2017a) were able to

determine T_c for crystallite sizes of 0.1 µm and 10 µm to be 83°C and 154°C respectively. Their study is based on hematite being held at Earth surface conditions typically <30 °C.

In hematite, He diffusivity was thought to be strongly related to the size distribution of constituent crystallites that make up a grain and that by varying the size of the grain no effect on He diffusion was observed (Farley and Flowers, 2012). The idea was contested by Farley (2018) who, following analysis of a single-diffusion-domain crystal of hematite (rare in nature as hematitic samples typically consists of polycrystalline aggregates), suggest that diffusivity varies with the dimension of the analysed fragment. Therefore, the diffusion domain (the distance the diffusant must travel to escape the specimen) is directly linked to the dimension of the physical grain. This means that if the dimensions of the grain, which is potentially made of a polycrystalline aggregate, is known, then so too is the range of T_c for that material being analysed.

Using fragments of a coarse, euhedral single crystal of hematite from Minas Gerais, Brazil, Farley (2018) was able to report new parameters for He diffusion in hematite for application to chronometry. By conducting bulk step-heating diffusion experiments after proton irradiation, Farley (2018) were able predict He diffusion behaviour of any sized hematite crystal or aggregate in which the crystallite size distribution had been estimated. In doing so, they found that for crystallite size of 1 mm a T_c of ~250 °C is likely, whereas at 20 nm it may have a T_c of ~70 °C assuming a spheroidal crystal morphology and cooling rate of 10 °C/Myr (Fig. 2.2). Therefore, Farley (2018) supports the idea that individual crystallites act as diffusion domains, with the smallest radii diffusing He early in the heating process followed by larger radii crystallites diffusing He at higher temperatures. Further, their study confirms hematite has higher T_c than same-sized crystals of apatite but is similar to higher temperature estimates for zircon and titanite. It is thought that T_c for He in hematite may be as low as <20 °C in some cases (Farley and McKeon, 2015).

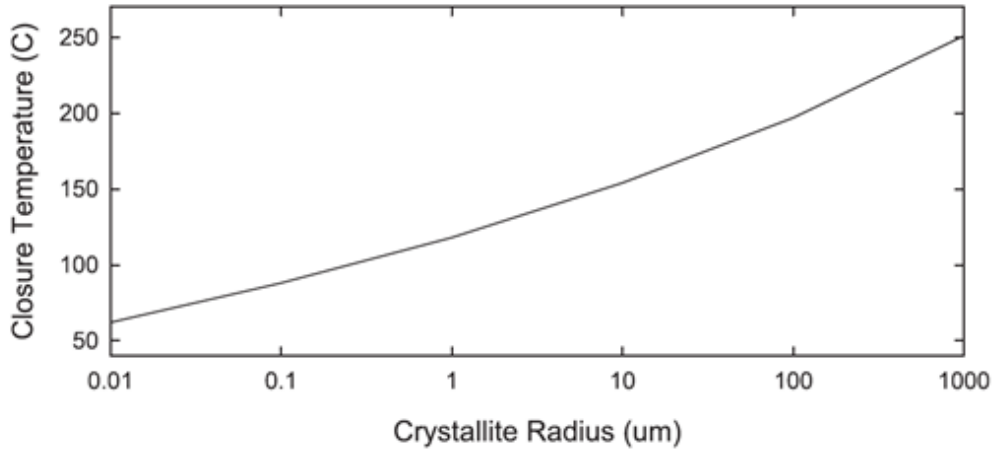

Figure 2.2: closure temperatures for natural hematite crystallites of varying radii. Graph shows that as hematite crystallite size increases so to does closure temperature; a crystallite of 1 mm radius will have a closure temperature of around 250 °C whereas with a crystallite size of 20 nm closure temperature may be around 70 °C (From Farley, 2018).

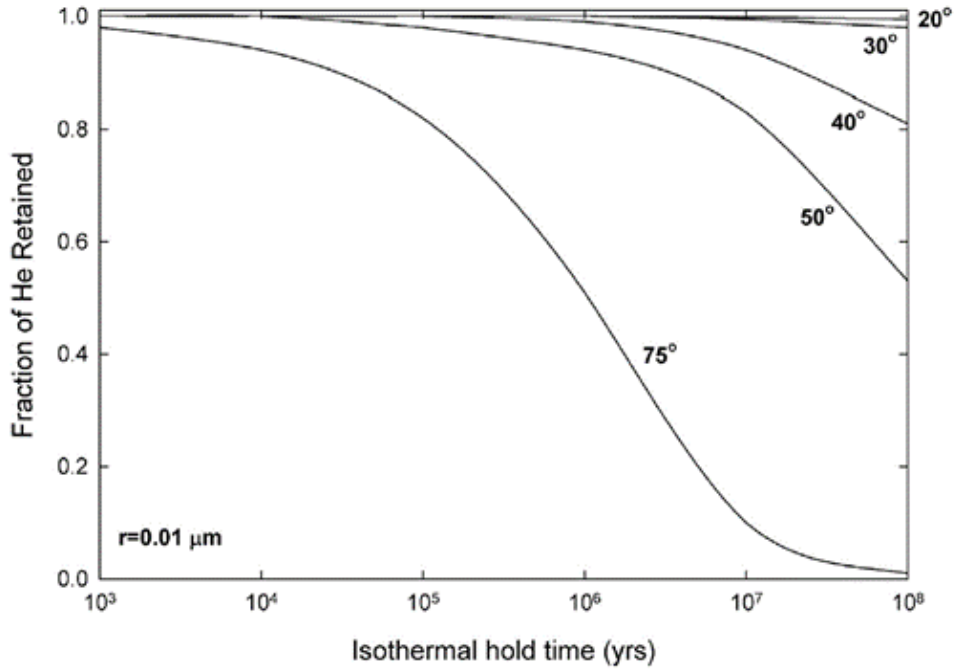

Figure 2.3: Fractional retention of radiogenic or cosmogenic He produced in natural hematite of r = 0.01 μm over geological timescale at multiple temperatures. This graph shows He is strongly retained for tens to hundreds of millions of years at Earth surface temperatures even in grain sizes of 0.01 μm (From Farley, 2018).

Hematite can be precipitated at or near to planetary surfaces and remain there for millions of years (Shuster et al., 2012 for example). For this reason, isothermal diffusive loss in hematite has been assessed (Farley, 2018). They demonstrate that for crystallite size of 1 mm radius held

at temperatures up to 50 °C for >100 Myr, less than 1% of He would be lost from the sample (Fig. 2.3). Moreover, in more extreme cases where hematite with crystallite size of 20 nm held at 30 °C for >100 Myr, the sample will still retain 92% of ingrown He (Farley, 2018). Therefore, at most of Earth's surface conditions, isothermal diffusive loss of He from hematite is negligible. Hematite appears to be more He retentive than commonly used dating minerals like apatite, zircon, and titanite (Farley, 2018).

2.5.2 Ne retention in hematite

As in the He system, Ne diffusion in hematite is linked to crystallite size distribution (Farley and Flowers, 2012). Farley and Flowers (2012) note that Ne was strongly retained at temperatures >150 °C and that the age recorded for hydrothermally precipitated hematite corresponded to a hydrothermal event with temperatures proposed to reach >350 °C. Cox et al. (2015) were able to further constrain the closure temperature of Ne in the most retentive hematite crystallites to approximately 500°C with 94 % of Ne being retained at temperatures over 290 °C. At a cooling rate of 10°C/Myr, the theoretical T_c for Ne in hematite has been calculated to be 297°C, 250°C, and 210°C for spherical domains (crystallites) of 1 µm, 0.1 µm, and 0.01 µm (or 10 nm) respectively (Balout et al., 2017). Thus, Ne is retained in hematite at higher temperatures than He. Further, Balout et al. (2017b) suggest that Ne is almost completely retained in crystallites of 10 µm at temperatures <40 °C which is significantly higher than most of Earth's average surface temperature.

2.5.3 He retention in goethite

Metal concentrations residing at or near Earth's surface can be subject to grade enrichment by climatically influenced chemical weathering over geological time. This process of dissolution, remobilisation, and reprecipitation of metals is known as supergene enrichment and is key in forming economically viable concentrations of elements (Vasconcelos et al., 2015). Modern analogues show that climate conditions necessary to form these deposits reflect annual mean cold and warm temperature ranges and annual mean precipitation amounts (Thorne et al., 2012). Surface mining of supergene ore deposits can provide direct access to geological material to depths of <1 km and widths >5 km, making them the ideal natural laboratory for bettering our

understanding of ore-forming processes and terrestrial climates through geological time if an absolute chronometer can be applied accurately (Reich and Vasconcelos, 2015; Heim et al, 2006). However, prior to applying (U-Th)/He dating to supergene goethite, and occasionally hematite, several complications surrounding He retentivity must be considered.

Goethite is commonly found as a polycrystalline weathering product at Earth's surface where temperatures are typically below 50°C. In such conditions, diffusive loss of He is likely to be slow and insignificant compared to that in deeper crustal or hydrothermal settings. Therefore, T_c is not an applicable method for quantifying He retentivity rather the degree of He retention is modelled based on isothermal diffusive loss at an expected surface temperature (Shuster et al., 2005). In their study, Shuster et al. (2005) found that two goethite samples with different crystallite shape, size, and packing density had different He retention capabilities when held at a constant temperature for a set period (Fig. 2.4). Within each sample, low retentivity domains (LRD) and high retentivity domains (HRD) were recognised with LRD thought to account for the majority of diffusive loss of ^{4}He. Based on ^{4}He/^{3}He analysis, if samples were held at 25°C for 10 Myr, one sample lost 2.5% of its He while the other lost 10%; referred to as the deficit gas fraction (Shuster et al., 2005). By applying a deficit gas fraction of 10% (maximum diffusive loss of He in the HRD), Shuster et al. (2005) were able to calculate a corrected age which assumes no diffusive loss of He in the sample. Recognising non-quantitative ^{4}He retention in goethite and applying an age correction based on it is suggested to improve the accuracy of precipitation age determination over determining a basic (U-Th)/He age (Shuster et al., 2005).

Like in Shuster et al. (2005), Heim et al. (2006) noted LRD and HRD within ferruginised channel iron deposit, goethite samples from Hamersley province, Australia. Here, the HRD were suggested to contains all ^{4}He present in the samples. In two samples studied, one lost ~10% of all ^{4}He while the other lost ~20% thus allowing for maximum possible diffusive loss to be considered in corrected age and uncertainty calculations. By applying a 20% error to age calculations, results in Heim et al. (2006) became statistically reproducible.

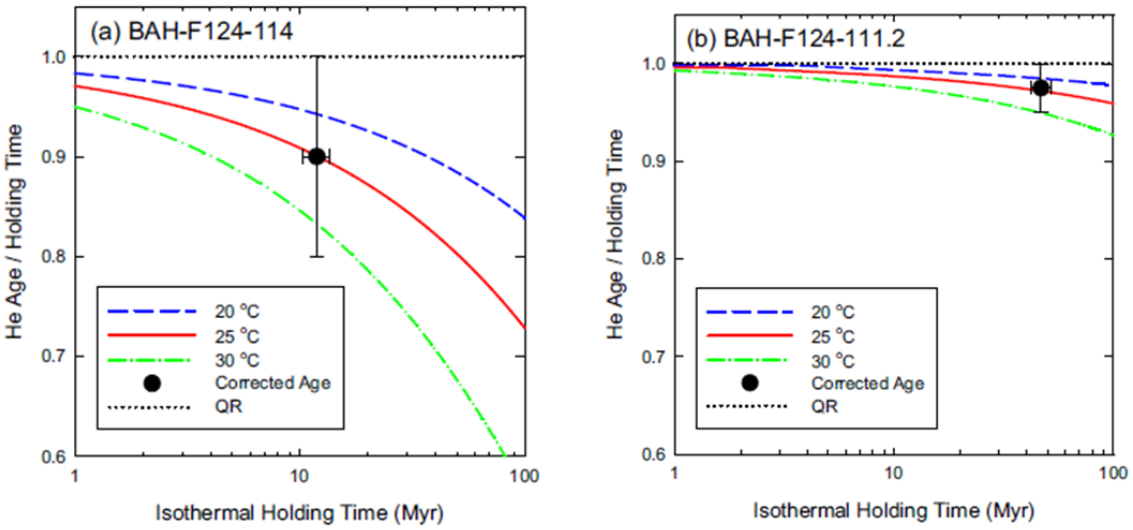

Figure 2.4: ^{4}He retention curves in goethite from Bahia, Brazil (hence BAH sample name in top box of diagrams), where ^{4}He retentivity factor is He age over isothermal holding time. This example from Shuster et al. (2005) shows how retentivity changes over time as a factor of temperature for samples with differing ratios of low and high retentivity domains (LRD and HRD, respectively). QR denotes quantitative 4He retention in the HRD.

Using goethite in colluvium and channel iron deposits of Western Australia, Vasconcelos et al. (2013) found that, like in Shuster et al. (2005) and Heim (2006), each sample can be split into LRDs and HRDs. Vasconcelos et al. (2013) show that excess ^{4}He, up to 4% but commonly <1% and insignificant, can reside in LRD reservoirs either as interstitial space between goethite crystallites; poorly crystallized goethite; goethite crystals damaged during sample preparation or proton irradiation; or a combination of two or more of these environments. However, ^{4}He is almost entirely retained in the HRDs but is rapidly lost in LRDs (Vasconcelos et al., 2013). In some samples, even under extreme surface condition of Western Australia, almost complete ^{4}He retentivity for up to 64 Myr was recorded. However, it was more common for goethite to contain 60% to 90% of radiogenic ^{4}He, thus an appropriate age correction for diffusive loss of He was necessary as in Shuster et al. (2005) and Heim et al. (2006).

By inserting crystallographic characterisations of goethite from pesoliths in ferruginous duricrusts in central Amazonia into He production/diffusion HeFTy code (Ketcham, 2005), Allard et al. (2018) were able to simulate the percentage of He retention in spherical domains of different radii (Fig. 2.5). They also varied diffusion coefficient based on those used in Shuster et al. (2005) and Vasconcelos et al. (2013) to better understand the effect this has on He retention. Results show that between 10% and 25% of He is lost in a grain with crystallite sizes of between 20 nm and 13 nm respectively assuming samples were held at surface conditions of 25°C since crystallisation. As a result of these findings, Allard et al. (2018)

applied a ~20 % age correction and a 15% error to the corrected age to represent analytical error plus the potential error on diffusive loss of He estimations.

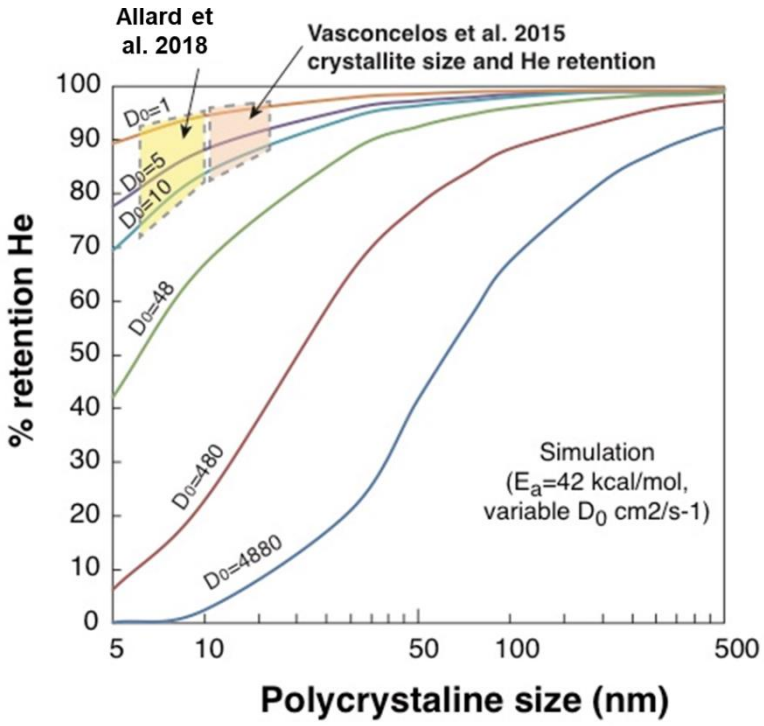

Figure 2.5: He retention as a function of crystallite size with multiple diffusion coefficients (D_o) and single activation energy (E_a) from Allard et al. (2018; supplementary information).

To avoid serious issues regarding retention of He in goethite and make age determinations of goethite more robust, Monteiro et al. (2014) provide a set of recommended procedures. First, sample selection should focus on large masses of visually pure goethite, typically black to dark brown in colour due to larger crystal size and more dense packing of crystallites. This reduces the chance of He loss as orange to yellow goethite have smaller crystallite size and are less densely packed thus allowing for He loss. This was confirmed by $^{4}He/^{3}He$ step-heating studies (Monteiro et al., 2014). Second, thorough sample characterisation is required, primarily by optical and scanning electron microscopy, electron microprobe, thermogravimetric analysis, and x-ray diffraction. However, this level of scrutiny is not strictly necessary for well crystallized goethite. Further, Monteiro et al. (2014) suggest that at least six grains from each sample should be dated to provide knowledge of age range variability and that each sample should be analysed by the $^{4}He/^{3}He$ method (outlined below). If this method is not employed, they suggest that >50 samples must be analysed to understand the weathering history of a land

surface or weathering profile. Based on previous work noted above, Monteiro et al. (2014) applied a ±10% age uncertainty to account for analytical error combined with uncertainty regarding diffusive loss of He and added ~10% onto their measured He age to account for the deficit gas fraction, thus allowing determination of a corrected He age. This approach was also applied by Riffel et al. (2016) who allowed up to 20% uncertainty to be applied to corrected ages in some cases.

2.5.4 Proton-irradiation $^4He/^3He$ method for quantifying ^4He loss

To quantify diffusive loss of ^4He in Fe-minerals, several studies noted above applied the proton-irradiation $^4He/^3He$ method developed by Shuster and Farley (2004). By bombarding minerals with a <150 MeV proton beam, they were able to produce a uniform concentration of spallation ^3He and negligible excess spallogenic ^4He in samples that generally contained no ^3He prior to bombardment. Therefore, the uniformly distributed spallation ^3He generated acts as a proxy for radiogenic ^4He when the sample is subject to step-heat diffusion experiments thus allowing for accurate He diffusivities and concentration profiles across the sample to be obtained (Shuster and Farley, 2004). In comparison to independently known He diffusivities in well studied Durango apatite, Fish Canyon tuff titanite, and Guadalupe olivine, the diffusion experiments conducted by Shuster and Farley (2004) are in agreeance with those previously determined for ^4He. This then allowed E_a and $\ln(Do/a^2)$ (frequency factor) to be calculated for each mineral which in turn allows for T_c to be determined. Further, samples that have experienced diffusive loss of ^4He in their history will show curvature at the edges of their time-temperature paths and an almost unchanging $^4He/^3He$ ratio after initial ~10% ^3He has been released by step heating (Fig. 2.6). Therefore, data generated can be used to correct (U-Th)/He ages by determining how much He has been lost.

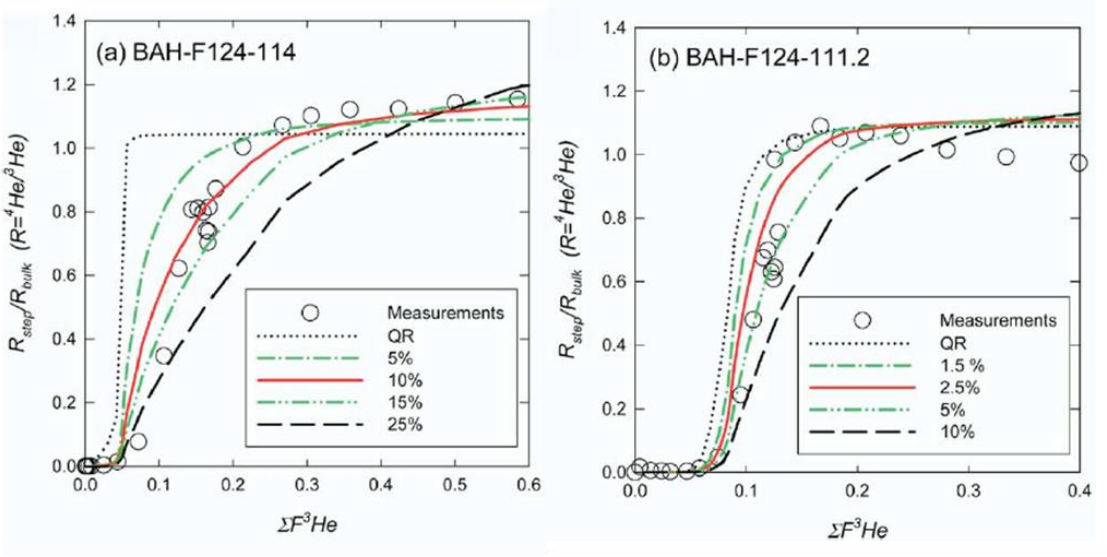

Figure 2.6: Measured and modelled goethite $^4He/^3He$ vs. Σ^3He ratio evolution diagrams for two samples. R_{step} ($R = ^4He/^3He$), normalized to the bulk ratio R_{bulk} plotted vs. the cumulative ^3He release fraction, Σ^3He. In the legend within the diagram, QR = quantitative ^4He retention in the HRD and different lines represent % deficit gas fractions of the HRDs. The measurements for each sample have 5% error (twice diameter of circles) but measurements can be seen to lie on or close to a specific % deficit gas fraction of the HRD. For BAH-F124-114, 10% was selected. For BAH-F124-111.2, 2.5% was selected. Therefore, each of these samples had that % added on to their measured age resulting in a 'corrected age'. From Shuster et al., (2005) and using same samples as in Fig. 2.4.

2.5.5 Alpha-ejection correction in Fe-minerals

Alpha particles produced by radioactive decay are emitted with MeV of kinetic energy and travel many μm from their origin. This is known as α-stopping distance (Ziegler, 1977; Farley et al., 1996; Ketcham et al., 2011). In the (U-Th-Sm)/He system, mean α-stopping distance associated with a specific parent isotope differs for each mineral phase the α-particle is travelling through with ^{147}Sm having the shortest α-stopping distance, followed by ^{238}U, ^{235}U, and ^{232}Th with the longest α-stopping distance (Ketcham, 2011). Further, α-stopping distance varies depending on the density of the mineral it is moving through (Farley et al., 1996). For example, an α-particle released from ^{238}U decay travelling through hematite (density = 5.18 g/cm^3) has a mean α-stopping distance of 13.59 μm but the same α-particle would travel 18.81 μm in apatite (density = 3.20 g/cm^3). Thus, when attempting to date individual crystals only a few 10s to a few 100s of μm in diameter, correcting ages for ejection of α-particles from the crystal lattice is necessary to avoid spuriously young ages (Farley et al., 1996 for example).

In Fe-mineral chronometry, unless the Fe-mineral grain is isolated in a non-Fe-mineral matrix, there is not real need to consider the α-ejection correction. When using single-crystal hematite

(U-Th)/He thermochronology, the closest comparison to the single-crystal apatite and zircon (U-Th)/He thermochronometers in which α-ejection correction is common, Jensen et al. (2018) deemed it unnecessary since the single-crystal hematite analysed was sourced from a dense polycrystalline mass of hematite and that α-particle implantation from adjacent hematite crystals in the bulk sample are assumed to balance α-particle loss by ejection.

In the hematite (U-Th)/Ne system, since α-particles are more energetic closer to the emitter and Ne is produced in the higher energy range, the α-ejection correction is smaller than that for He in hematite (Gautheron et al., 2006). The same rule stated by Jensen et al. (2018) applies for hematite (U-Th)/Ne dating Again, this renders the α-ejection correction unnecessary.

2.6 Extraneous ^{4}He

Extraneous ^{4}He from adjacent and inclusion zircon, rutile, and ilmenite was found to account for up to 11% of the bulk ^{4}He concentration in some goethite samples (Vasconcelos et al., 2013). The occurrence of these contaminants adjacent to the sample is not common, but if they are recognised to be present another sampling site is recommended. Extraneous ^{4}He will result excessively old ages and poorly reproducing ages (Vasconcelos et al., 2013). This has been noted in apatite (U-Th)/He thermochronology and includes the presence of extraneous ^{4}He in fluid inclusions (Farley. 2002; Persano et al, 2002), thus an age correction in the younger direction may occasionally be necessary. It is best practice to carry out petrographic investigation of samples prior to analysis to be aware of potential extraneous ^{4}He from contaminants.

3.0 Analytical procedures for Fe-oxide-oxyhydroxide (U-Th)/He and (U-Th)/Ne geochronology.

3.1 Overview

In Chapter 4 I report new (U-Th)/He ages of Fe-oxide-oxyhydroxides from the Attepe Fe deposits of southern Turkey. In Chapter 5 I report new (U-Th)/Ne ages of hematite from the Leadhills-Wanlockhead Pb-Zn deposit in southern Scotland. Both studies required the development of a repeatable sample preparation and weighing methods, as well as new analytical techniques, both for the measurement of noble gases (He and Ne) and the wet chemistry and ICP-MS analysis of U and Th.

This chapter reports the protocols developed during the PhD and the analytical conditions used for the measurements reported in Chapters 4 and 5. The techniques for both (U-Th)/He and (U-Th)/Ne dating are compared with those developed elsewhere for Fe-oxide-oxyhydroxide analysis and recommendations are made for future work.

The procedures and techniques developed in this chapter, to go from experimentation to structured analysis, were the most time-consuming aspect of this thesis. I will now expand on this regarding sample preparation, He and Ne analysis, and U and Th chemistry.

Developing a sample preparation procedure on these at time friable samples (especially goethite) demanded laborious amounts of hand picking under binocular microscope to avoid mixing gangue and Fe-oxide-oxyhydroxide phases during crush steps. The preparation of all samples for chapters 4 and 5 is estimated to have taken at least 6 weeks to 2 months in total. Many of the sample aliquots prepared did not make it into the thesis as they were purely for trial-and-error analysis or were sacrificed to the ‘mass spec Gods’ as the instrument, or laser, or furnace, started their day.

Trial-and-error laser heating experiments to perfect the He analysis procedure may have taken around 6 weeks to fully understand. Analysis of all samples for He work recoded in chapter 4 may have taken around 6 weeks to complete. Establishing procedures for Ne gas analysis using the ARGUS VI may have taken around 6 to 8 weeks. Attaching the laser system and fully understanding the amount of material needed to create detectable levels of Ne isotopes in samples and standards using the ARGUS VI may have taken around 3 weeks.

Beaker and column cleaning procedures for column chemistry may have taken around 3 months to refine and complete for the entire sample sets recorded in chapters 4 and 5.

For those interested in all raw data and all trial-and-error work, this may be recorded in the SUERC Thermochronology laboratory and ICP-MS desktop computers attached to respective instrument. I was advised not to include this data in this thesis as it was deemed unnecessary for the reader of this thesis. Please contact Prof. Fin Stuart if you have any questions.

3.2 (U-Th)/He dating: Helium analysis

3.2.1 Introduction

Most of the recent published Fe-oxide-oxyhydroxide (U-Th)/He studies have determine U, Th and He on the same mineral fragment (Shuster et al., 2005; Vasconcelos et al., 2013; Hofmann et al., 2020). However, it is widely appreciated that the volatilisation of U (and Th) during the heating (800-1000°C) required for He extraction is common and leads to erroneously old He ages and over-dispersed age populations (e.g. Cooper et al. 2016; Danišík et al., 2013; dos Santos Albuquerque et al., 2020). Although techniques have been developed to minimise these effects, they require major modifications to existing instrumentation that are challenging (Hofmann et al. 2020). I have developed procedures that completely avoid the volatilisation issue by determining the He content of Fe-oxide-oxyhydroxide minerals separately from U and Th in multiple aliquots of several mg of each sample. An earlier version of this procedure has been used successfully to date hematite mineralisation from Elba yielding ages that are indistinguishable from Ar/Ar ages of cogenetic adularia (Wu et al. 2019). In this thesis, multiple aliquot data is used to calculate an average U, Th and He concentrations for each sample, which were then used to determine the sample (U-Th)/He age using the formulation of Meesters and Dunai (2005).

3.2.2 Sample preparation procedure

Samples were dried and gently crushed to 1-2 mm chips with gangue minerals the picked out under binocular microscope prior to further crushing, separation, and sieving. Gangue minerals, predominantly calcite and quartz, were removed from the 0.25-1 mm fraction using a Frantz

LB-1 magnetic separator and hand-picking under binocular microscope. This fraction was re-crushed and gangue minerals removed from the 150-250 µm fraction. A final crush step using a quartz-agate pestle and mortar was used to produce a <38 µm fraction for powder X-ray diffraction (XRD), and He, Ne, and U and Th determinations. XRD was carried out using a Panalytical X'Pert PRO MPD (A3-26) at School of Chemistry, University of Glasgow. The diffractometer is equipped with a Cu target tube operated at 40 kV and 40 mA and was set to scan between 10 and 60° 2θ scan range with a step size of 0.017° with each step taking between 60-150 seconds. Small rock chips were imaged using a FEI Quanta 200F environmental scanning electron microscopy (SEM) operated at 20 kV at the ISAAC facility at University of Glasgow (Lee et al., 2014).

3.2.3 He concentration determinations

Aliquots of Fe-oxide-oxyhydroxide minerals are placed in >99% pure 5 x 1 mm Pt packets made from 0.1 mm thick tube. Sample and tube weights were determined using a Mettler Toledo MX5 microbalance. The Pt packets were weighed three times empty and three times packed to established sample aliquot mass and the uncertainty in sample weight. This latter point is important as the (U-Th)/He and (U-Th)/Ne dating techniques rely on concentration measurements, not isotope ratio determinations.

Typically, four sample aliquots and one empty Pt packet were placed 10 mm apart in recesses in a degassed Cu pan and covered with a sapphire window prior to overnight pumping at 80°C to minimise background levels of H and CH_4. Sapphire windows have significantly lower He backgrounds than quartz glass, although they required at least 48 hours of independent heating at 80°C whilst being pumped to a turbo molecular pump prior to attachment to the Cu pan to ensure that it makes negligible contribution to the He blank.

Initially the Cu pan was packed to capacity (9 recesses) allowing for the degassing of 8 aliquots and 1 hot blank per load. This was done to reduce the amount of opening and closing of the vacuum system thus reduce the risk of equipment malfunction and potential leaks. Helium was extracted by heating Pt packets to 1000 ± 20°C for between 1200 and 1500 seconds using a 960 nm diode laser heating system (Fusions 960, Photon Machines) with laser power regulated using the inbuilt pyrometer which maintained sample temperature as outlined in Wu et al. (2019). The gas extraction line is outlined in detail by Dobson (2006).

An extended period of experimentation led to the recognition that the heating of adjacent sample aliquots during He extraction step as a consequence of heat conduction through the Cu pan. This was recognised by, for example, an inability to achieve consistent mean ^{4}He concentration and the need for several heating steps in order to release all He from a sample. This was resolved by shortening the heating time to 300 seconds from 1500 seconds and reducing to 4 sample aliquots and 1 blank per pan, allowing for larger spacing between each aliquot. Once this method for sample spacing and heating duration was established, no further degassing issues were encountered.

Following heating the evolved gases were purified for 600 seconds using two liquid nitrogen-cooled charcoal traps. Gases were introduced to a Hiden HAL3F quadrupole mass spectrometer operated in static mode for He abundance determinations following established procedures (Foeken et al. 2006). All aliquots were re-heated to 1000°C for 300 seconds to ensure complete He extraction. Re-heats released on average 0.2% of the initial He from each aliquot and were not used in He concentration determinations.

The ^{4}He content of each aliquot was calculated by peak height comparison against repeated measurements of a calibrated He standard. Typically, two calibrations were carried out before and after every two sample aliquots with two carried out prior to sample analysis and two at the end of the day. Analytical periods for He concentration determination on Fe-oxide-oxyhydroxide typically lasted between 1 and 3 weeks with He sensitivity typically varying by ±2-4% across these analytical periods. Per day, He sensitivity typically varied by ±1%.

Helium blanks were determined by heating empty Pt tubes, typically one tube per pan load. Blank levels averaged over the analytical period were 3.6×10^{-11} ccSTP He ± 73 % (n = 62). Helium in samples was always more than 100 times that of the blank level, thus no correction for blank levels of He was considered. There was no systematic variation throughout the course of the analytical period. Within a typically day of analysis, one cold blank and two calibrations were run prior to laser heating. If no abnormalities were noted, a hot blank and two sample aliquots were run. If system pressure increased by > 2 orders of magnitude the charcoal traps were heated and pumped to reduce contamination from other gas species. Two calibrations were then carried out prior to the last two sample aliquots remaining in the pan. A further hot blank and two more calibrations were run at the end of each day. This allowed for 4 aliquots from a single sample to be analysed per day and a new set of aliquots to be loaded into the Cu

pan, covered with the sapphire window, sealed under ultrahigh vacuum, and pumped overnight at 80°C to minimise background levels of H and CH_4 ready for analysis in the morning.

3.2.4 Data Quality

The total uncertainty in He concentration of a single aliquot is controlled by the weighing uncertainty, mass spectrometer sensitivity and blank correction. The uncertainty in mass spectrometer sensitivity is the largest contribution and is typically around 1 % for each individual aliquot. This could be improved by increasing the number of calibrations which may result in a smaller standard deviation, though this would become time consuming. Attention must be paid to weighing uncertainty as this can contribute significantly to total analytical uncertainty if using an unsuitable balance. In this study the weighing error was commonly <0.05%. Blank correction error, like with calibrations, could be improved by carrying out more blanks and reducing standard deviation.

The uncertainty in the He concentration of a sample is the standard deviation of the mean of all aliquot He concentrations for that sample. This is typically 4 to 7 %, which is greater than the uncertainty of individual aliquot He content, typically <2 %. The uncertainty of the sample may reflect the homogeneity of the aliquots measured. For example, when separating the Fe-oxide-oxyhydroxide phases care must be taken to remove a single generation where multiple generations may be present. This is done by following the paragenetic petrography already established prior to sample preparation. Mixing of multiple generations could lead to aliquot heterogeneity and the occurrence of large sample uncertainties.

3.3 (U-Th)/Ne dating

3.3.1 Introduction

Hematite (U-Th)/Ne dating relies on the production of nucleogenic ^{21}Ne from the reaction $^{18}O(\alpha,n)^{21}Ne$ as outlined in chapter 2. Resolving the concentration of radiogenic ^{21}Ne from the atmosphere-derived Ne trapped in minerals requires precise Ne isotope ratio determinations (Farley et al., 2020). For this I used a Thermo Fisher ARGUS VI mass spectrometer and an

automated ultra-high vacuum gas purification and separation system developed specifically for Ne isotope analysis.

The ARGUS VI mass spectrometer was originally developed for multi-collector Ar isotope analysis (Kim and Jeon, 2015; Bai et al., 2018). However, by tuning magnetic position and individual deflection voltages on the detectors, neon isotope peak coincidence has been achieved (Györe et al., 2019). This has allowed the simultaneous accurate and precise measurement of the three stable isotopes of neon (^{20}Ne, ^{21}Ne, and ^{22}Ne) in natural gases on Faraday detectors (Gilfillan et al. 2019). The low Ne abundance in terrestrial mineral samples required further modification of the ARGUS VI. Individual Ne isotope abundances are measured independently using the compact discrete dynode (CDD) electron multiplier in peak jumping (or pulse counting) mode (Györe et al., 2019).

3.3.2 Gas extraction and purification

For each set of analyses, seven sample aliquots, two CREU-1 quartz standards, and one empty Pt packet were placed 10 mm apart in recesses in a degassed Cu pan and covered with a sapphire window and attached to the gas purification line by flexible stainless-steel piping. This system was heated overnight at 80°C to minimise background levels of H and CH_4. Neon was extracted by heating the Pt packets to 1000 ± 20°C for 600 seconds using a 960 nm diode laser heating system (Fusions 960, Photon Machines). Laser power is regulated using the inbuilt pyrometer which maintained sample temperature.

Gases released from the minerals are expanded to an all-metal gas purification system under ultra-high vacuum achieved by a combination of turbo molecular (Pfeiffer ^{HI}CUBE) and ion pumps (Agilent StarCell). The gas purification-separation line is modified from that developed by Györe et al. (2019) for redetermination of ^{21}Ne/^{20}Ne of air (Fig. 3.1). Active gases are removed by 600 seconds exposure to a GP50 ZrAl alloy getter (SAES) held at 250°C. Residual gases (noble gases and H) are then exposed to liquid nitrogen-cooled charcoal for 600 seconds at -196°C (77 K) to adsorb Ar, Kr, and Xe. The remaining gas is then exposed to charcoal at -248°C (25 K) for 600 s using a Sumitomo coldhead (cryopump) (ICEoxford – DRY ICE ACTIVE SORB) to adsorb Ne. The residual He is pumped from the extraction line and cryopump volume by opening to a triode ion pump for 10 seconds prior to the release of the Ne into the gas phase at -195°C (78 K). The cryopump temperature is controlled using

LakeShore Cryotronics cryogenic temperature controller with temperature of Ne adsorption and desorption based on recommendations in Farley et al. (2020). To allow Ne to completely desorb to the gas phase, a further 600 second waiting time is used prior to introduction of the gas to the ThermoFisher ARGUS VI mass spectrometer. A GP50 ZrAl alloy getter held at room temperature and a liquid nitrogen-cooled charcoal finger installed on the source block reduced the levels of H, CO_2 and Ar during Ne isotope analysis. Following gas inlet into the mass spectrometer for analysis, cryopump temperature was set to -148 °C (125 K) and pumped to fully desorb all attached gases prior to new sample introduction. The same procedure applies to the analysis of the standard material.

Once Ne has been fully degassed from the sample, the gas purification and analysis is fully automated using Qtegra software. This can be done remotely, as can instrument blanks and calibrations, which allows for these procedures to be done from home for example or set to run automatically overnight. The delivery of liquid nitrogen to cold fingers is also automated using 25 L tanks connected to a sensor system attached to the coldfinger and encasing dewar. This removes the risk of human error, release of unwanted gas from the charcoal, and reduces liquid nitrogen consumption.

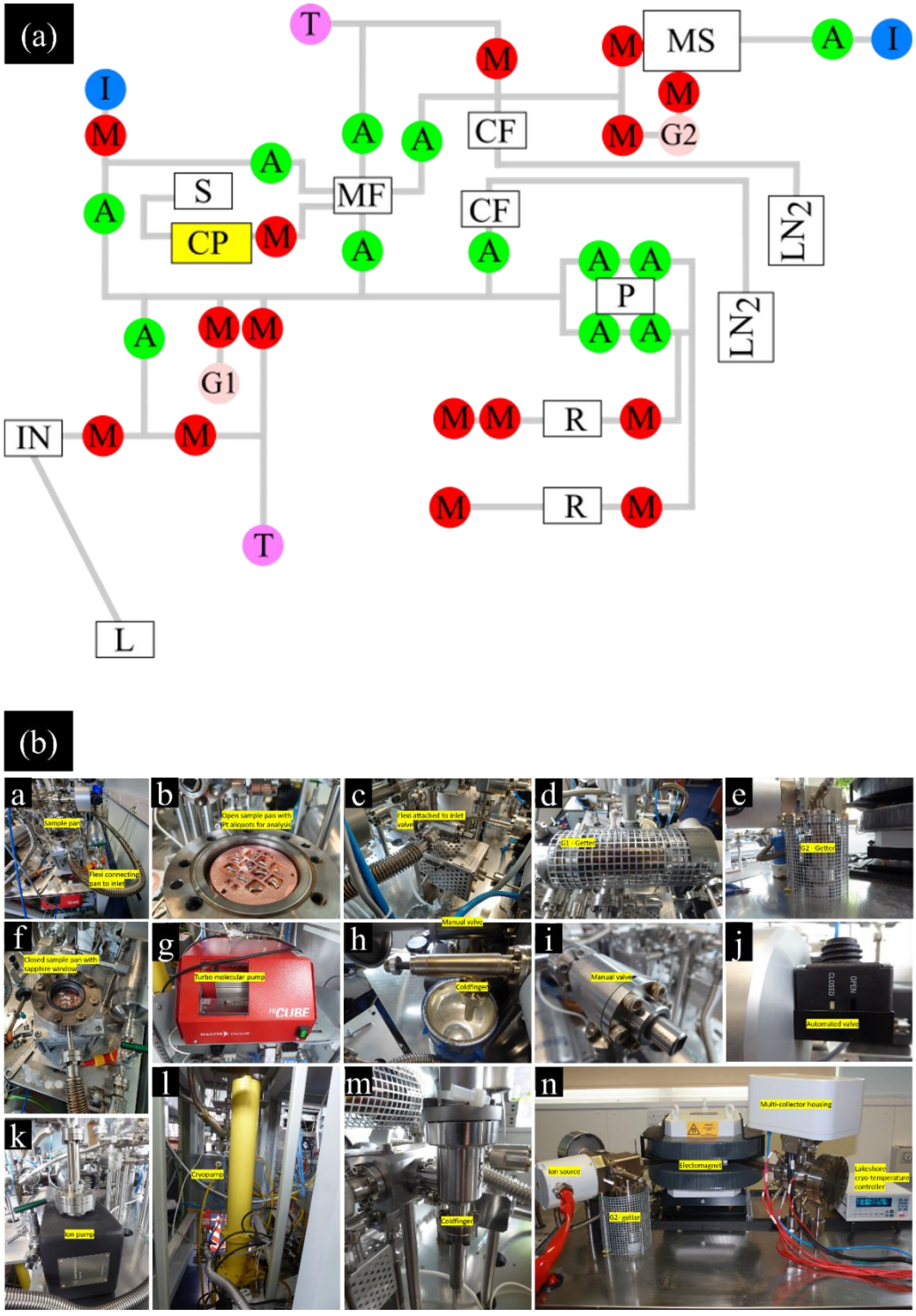

Figure 3.1: Panel (a) Schematic diagram of ARGUS VI and gas preparation line showing how each piece of the system is connected: L= laser system; T = turbo pump; IN = inlet valve; M = manual valve; A= automated valve; G1 = GP50 ZrAl alloy getter (SAES) held at 250 °C; G2 = GP50 ZrAl alloy getter held at room temperature; CP = cryopump; S = power and water source; I = ion pump; MF = manifold; CF= coldfinger; R = reservoir; P = pipette; LN_2 = liquid nitrogen tanks; MS = mass spectrometer. Panel (b) shows components of the gas preparation line (a to m) and view of mass spectrometer (n).

3.3.3 Ne isotope analysis

The analytical system, as well as operating schedule, source parameters, and isobaric interference corrections used to determine Ne isotope abundances for samples analyses using the ARGUS VI at SUERC is outlined in Györe et al (2021).

Isobaric interference identified at each mass of neon are reported in detail by Györe et al. (2019). In this study all measurements of ^{20}Ne are corrected for $^{40}Ar^{+2}$ and ^{22}Ne corrected for $^{12}C^{16}O_2^{+2}$. On average $^{40}Ar^{2+}$ accounted for 1.5% of ^{20}Ne abundance in samples and standards whilst $^{12}C^{16}O_2^{2+}$ accounted for 8.1 % of ^{22}Ne on average (n=21). Correction for ^{20}NeH at ^{21}Ne mass as reported in Györe et al. (2019) is unnecessary as this correction only applies to simultaneous collection on Faraday detectors at high pressure.

3.3.4 Blanks and calibrations

The ^{20}Ne content accumulated in sample pan (cold blank) for same duration and sample extraction is $4.1 \times 10^{-11} \pm 2.1 \times 10^{-11}$ ccSTP, with approximately atmospheric isotope composition. Heating empty Pt tube (hot blank) yields on average $^{20}Ne = 3.5 \times 10^{-11} \pm 3.2 \times 10^{-11}$ ccSTP. Average sample ^{20}Ne is $9.2 \times 10^{-11} \pm 3.2 \times 10^{-11}$ ccSTP thus are approximately 4 times the cold blank and 3 times hot blank levels.

A pipette system delivers 2.2×10^{-8} ccSTP of air-derived Ne per aliquot from a 5-litre tank for instrument calibration. Over the analytical period, $^{21}Ne/^{20}Ne$ was 0.002998 ± 0.000014 (0.4 %) and $^{22}Ne/^{20}Ne$ was 0.099429 ± 0.002167 (2.1%). Over the course of a single day of analysis, ^{20}Ne abundance of the calibration gas varied by < 1 %.

3.3.5 CREU-1 quartz standard

Eight CREU-1 quartz standards (19.36 – 20.88 mg) were measured as a check on isotope ratio determinations and reproducibility of Ne concentration determinations. They yielded mean ^{21}Ne concentration of 345 ± 21 million atoms/g (Mat/g) and range from 322 to 386 Mat/g. Following the same analytical procedure but with an additional 1000°C laser heat, each standard aliquot reheat ^{21}Ne counts per second was <5 % of first heat value, thus each aliquot was degassed effectively by first heat. A large inter-laboratory comparison of CREU-1 quartz

provided average ^{21}Ne concentration of 348 ± 10 Mat/g (Vermeesch et al., 2015). Our data overlap the accepted value. In the same study and using the MAP 215-50, SUERC laboratory reported ^{21}Ne concentration of 355 ± 12 Mat/g and 348 ± 12 Mat/g for the 125-250 µm and 250-500 µm fractions of CREU-1, respectively. Sample mass of this study was typically 200 mg. Thus, results for CREU-1 here are in line with those recommended from Vermeesch et al. (2015) but used ~10 times less sample material to achieve the results.

The isotope ratio data lie on or close to the air-cosmogenic ^{21}Ne line given by Niedermann et al. (1994) and Schaffer et al. (1999) (Fig. 3.2). Mean ARGUS VI data here fall within error of interlaboratory and SUERC data presented in Vermeesch et al. (2015) and Cronus-A quartz standard data, tied to CREU-1 quartz, produced by Farley et al. (2020) (Table 3.1; Fig. 3.3). Farley et al. (2020) use between 120 and 246 mg of sample material to produce similar results by furnace heating and analysis on a Helix-MC-Plus^{10K} mass spectrometer which has been modified to allow for isobar-free measurements of Ne. The ARGUS VI + laser system sample mass needed to produce similar data is around 10 times less.

Using the ARGUS VI + laser system, uncertainty on each individual aliquot of CREU-1 ^{21}Ne abundance ranges between 2.3 % and 4.6 % with standard deviation of the mean of 6.1 %, whereas on SUERC MAP 215-50 each individual aliquot of CREU-1 ^{21}Ne abundance ranges between 3.2 % and 6.7 % with standard deviation of the mean of 4.9 %. Therefore, ARGUS VI is as accurate and precise as MAP 215-50 when consistently using around 10 times less sample material.

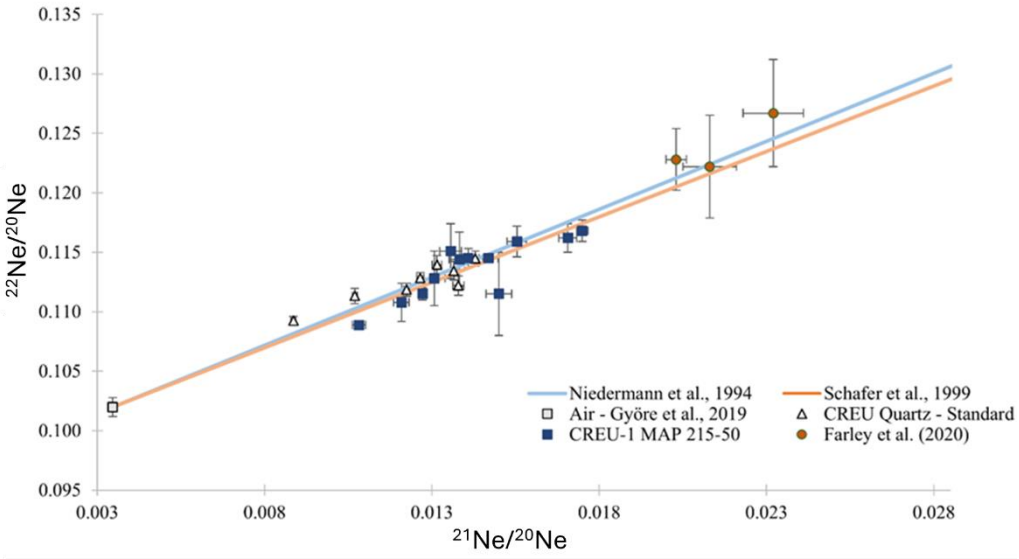

Figure 3.2: Ne isotope ratios in CREU-1 using ARGUS VI and MAP 215-50 with complimentary data from SUERC results in Vermeesch et al. (2015) and Cronus-A quartz standard from Farley et al. (2020). Air-cosmogenic Ne mixing lines of Niedermann et al. (1994) and Schäfer et al. (1999) with Ne isotope ratio of air from Györe et al. (2019) are used as reference data.

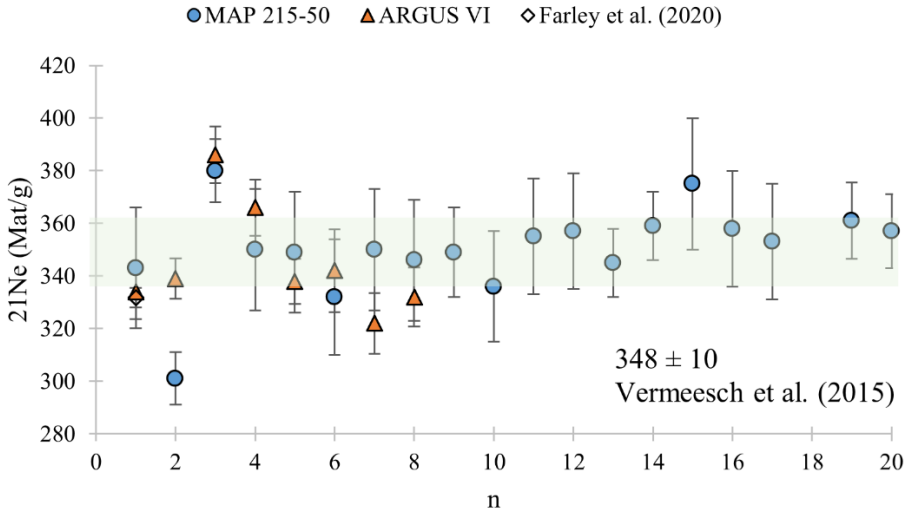

Figure 3.3: ^{21}Ne isotope abundance in CREU-1 quartz standard using ARGUS VI and MAP 215-50 with complimentary data from SUERC results in Vermeesch et al. (2015) and Cronus-A quartz standard from Farley et al. (2015). Mean ^{21}Ne abundance in CREU-1 (348 ± 10 Mat/g), highlighted by the green bar, is from Vermeesch et al. (2015). The ARGUS VI data was achieved using around 10 times less sample material than the other studies.

Table 3.1: CREU-1 and Cronus-A data used for comparison to ARGUS VI data form this study.

CREU-1	SUERC-1	165.1	0.0145	0.00038	0.1115	0.0035	343	23
	SUERC-2	239.6	*				301	10
	SUERC-3	258.4	*				380	12
	SUERC-4	203.0	0.01257	0.00032	0.1128	0.0023	350	23
	SUERC-5	204.6	0.01332	0.0003	0.1144	0.0023	349	23
Vermeesch et al. (2015)	SUERC-6	261.3	0.01306	0.00033	0.1151	0.0023	332	22
	SUERC-7	160.2	0.01159	0.00023	0.1108	0.0016	350	23
	SUERC-10	174.5	*				346	23
	SUERC-11	209.2	*				349	17
	SUERC-12	187.8	*				336	21
	SUERC-13	202.3	0.01359	0.00022	0.1145	0.0008	355	22
	SUERC-14	92.8	0.01222	0.00012	0.1115	0.0005	357	22
	SUERC-15	378.6	*				345	13
	SUERC-16	237.1	*				359	13
	SUERC-17	33.0	0.01504	0.00029	0.1159	0.0013	375	25
	SUERC-18	156.2	0.01656	0.00027	0.1162	0.0012	358	22
	SUERC-19	166.0	0.01699	0.00017	0.1168	0.0009	353	22
	CREU-1-1	36.8	0.01032	0.00020	0.10889	0.00008	361	14.5
MAP 215-50	CREU-1-2	68.8	0.01419	0.00029	0.11450	0.00008	357	14.1
	A	19.67	0.00836	0.00007	0.10924	0.00036	334	10.3
	B	19.45	0.01019	0.00007	0.11133	0.00064	339	7.7
ARGUS VI	C	19.36	0.01316	0.00011	0.11345	0.00078	386	10.8
	D	20.08	0.01215	0.00011	0.11286	0.00043	366	10.6
	E	20.88	0.01174	0.00010	0.11185	0.00054	338	8.6
	F	20.29	0.01380	0.00022	0.11446	0.00063	342	15.7
	H	19.44	0.01329	0.00017	0.11220	0.00082	322	11.6
	J	19.98	0.01265	0.00014	0.11395	0.00078	332	11.2
					mean		345	
					±		21	
Cronus-A		126.85	0.0208	0.0008	0.1222	0.0043	331.7	3.7
Farley et al. (2020)		120.13	0.0227	0.0009	0.1267	0.0045		
		246.22	0.0198	0.0003	0.1228	0.0026		

* Step heating carried out, no ratio available.

Table 3.2: CREU-1 and Cronus-A data used for comparison to ARGUS VI data form this study.

3.4 Summary of neon development

The original method of dating minerals was by splitting a large sample into multiple aliquots for separate analysis of He from U and Th (Strutt, 1908). This multi-aliquot method (Wernicke and Lippolt, 1994; Wu et al., 2019), or two-aliquot method (Farley and Flowers, 2012; Farley and McKeon, 2015; Farley et al., 2020) requires large amounts of sample (commonly 100s mg to several grams) and can lead to a loss of data regarding finer details of parent and daughter inhomogeneity. It also leads to an average age for a sample rather than a succession of ages spanning the entire sample, a caveat necessary for unravelling the history of multi-layered pisolites for example (Wells et al., 2019). However, it avoids the issue of U-loss during gas extraction (Vasconcelos et al. 2013; Hofmann et al., 2020) and can provide reproducible and informative data (Wernicke and Lippolt, 1994; Wu et al., 2019; Farley and Flowers, 2012; Farley and McKeon, 2015; Farley et al., 2020). The multi-aliquot method is applied here to avoid U-loss during gas extraction and provides an average age for each sample.

Here, the use of less sample material has been made possible by using the ARGUS VI + laser system. To release gases for Ne measurement from hematite, a flux-melting-based extraction technique was used by Farley et al. (2020) and Farley and McKeon (2015). By using a resistance furnace for heating samples, Pt or other metal packaging used for encapsulating samples can fail or become problematic as they build up within the furnace resulting in high blank values or failed analyses (Farley et al., 2020; Vermeesch et al., 2015). Farley et al. (2020) note that furnace heating can cause damage to the heater element, liner, and crucible. They use a lithium borate flux to lower the melting point of minerals being extracted, but this can still result in damage to the equipment and cause a plug to form as the flux climbs up the liner. Therefore, using a laser system and low sample mass will reduce the chance of damage to the extraction system and occurrence of failed analyses making the technique more economically sustainable.

Thus far single-aliquot (Shuster et al., 2005; Vasconcelos et al., 2013) or single-crystal (Jensen et al., 2018) Ne dating is yet to be attempted for hematite (U-Th)/Ne dating due to the low concentrations of Ne in samples relative to the more traditional He method, but a combination

of the ARGUS VI + laser presented here and depressurised oxygenated degassing of samples piloted by Hofmann et al. (2020) with standard ICP-MS measurements of U and Th could open that possibility. This would allow for the measurement of Ne isotopes and U and Th on the same aliquot of a sample without the need for excessive amounts of sample material or possibility of U-loss during Ne extraction.

3.5 Uranium and thorium analysis procedure

U and Th concentrations were measured in multiple aliquots of bulk homogenized powdered Fe-oxide-oxyhydroxide used for He and Ne isotope determinations. The procedures were modified from those reported in Wu et al. (2019) to reduce blank levels and reduce sample U and Th standard deviation. This was done by adding beaker, column, and resin cleaning steps to eliminate contamination prior to sample analysis. Unfortunately, this analysis was carried out on only a few beakers to test these procedures and no systematic assessment or data recording was undertaken.

3.5.1 Cleaning

Sealable Savillex PFA beakers were used for sample dissolution and column chemistry solution collection steps. To minimise the U and Th carried over from previous samples a new cleaning procedure was developed. This involved three steps of soaking beakers in 50 % dilute Analar HNO_3 (6 M) at 90°C for 24 hours. The final step involved adding 2 ml of 3 M Analar HCl to each jar and sealing jar at 90°C for 24 hours.

The TR-B50-S resin used for separation of U and Th from matrix was cleaned in MilliQ H_2O overnight, then soaked in equal parts 6 M Ultrapure HCl, 6 M Aristar HNO_3, and MilliQ H_2O overnight. This procedure was repeated, and the clean resin stored in MilliQ H_2O. Columns were cleaned in 6 M Analar HCl for 24 hours prior to use.

3.5.2 Spiking, dissolution, and evaporation of samples

Each sample aliquot was weighed and placed in a Savillex beaker prior to addition of spike solution of ^{235}U - ^{230}Th whilst the sample-bearing beaker is still on the balance. 2 ml of 12 M Ultrapure HCl was then added to each beaker prior to sealing and placing on a hotplate for 48 hours at 130 °C to dissolve sample. Solution was left to evaporate until only the slightest solution remains with 2 ml of 1.5 M HNO_3 then added. Beakers were sealed and placed on hotplate at 130 °C for 24 hours to reflux sample solution ready for column chemistry.

Column chemistry was carried out as soon as dissolution and evaporation procedures were completed to negate cross-contamination. Waste beakers were placed beneath each column and each column is rinsed with 0.1 M Ultrapure HCl + 0.3 M Aristar HF (referred to as cleaning solution). Each column was rinsed with MilliQ H_2O prior to addition of 0.4 ml of resin to each column followed by 9 ml of 0.2 M Ultrapure HCl to columns in 1 ml + 4 ml + 4 ml steps. The resin was cleaned by adding 9 ml of cleaning solution in 1 ml + 4 ml + 4 ml steps prior to re-conditioning resin by adding 9 ml of 1.5 M Aristar HNO_3 in 1 ml + 4 ml + 4 ml steps. Samples were loaded into columns and cleaned using 12 ml of 1.5 M Aristar HNO_3 in 4 ml + 4 ml + 4 ml steps. Waste beakers were then replaced with pre-cleaned Savillex beakers prior to eluting U and Th from the sample by adding 13 ml of cleaning solution in 1 ml + 4 ml + 4 ml + 4 ml steps. This solution was then evaporated on hotplate at 80°C until near dryness, 5 % Aristar HNO_3 + trace HF was added to each beaker with beakers sealed and samples left to reflux on hotplate at 130 °C for 48 hours.

3.5.3 U and Th analysis procedure

Uranium and thorium concentrations were determined using an Agilent 7500ce Q-ICP-MS. 2 ml aliquots of HNO_3 and U500 standard were measured prior to sample introduction with U500 then measured every three samples. A challenge faced when measuring U and Th from supergene mineralisation was that a veneer could form on the skimmer cones making it unsociable process in shared laboratory spaces. Separate skimmer cones were kept for all iron oxide work to avoid cross contamination. Skimmer cones should be cleaned regularly to avoid veneer build-up.

3.5.4 Blanks and standards

Blank levels of U and Th were determined by following exact same spiking, column chemistry, and ICP-MS procedure used for samples, except samples were not introduced. This resulted in mean blanks of 0.19 ± 0.05 ppm ^{238}U and 0.11 ± 0.10 ppm ^{232}Th. All samples yielded U and Th significantly above blank levels and no blank corrections were undertaken. U and Th concentrations were measured in four aliquots of Elba hematite previously reported in Wu et al. (2019). They yielded 0.30 to 0.32 ± 0.01 ppm ^{238}U and 0.40 to 0.43 ± 0.01 ppm ^{232}Th, thus comparable to that study.

Nore: All raw data should be stored in instrument software and associated spreadsheets in the Thermochronology Laboratory, SUERC, East Kilbride. If anyone would like this data, please contact Prof. Fin Stuart.

4.0 Pleistocene aridification of the Eastern Taurides, Turkey revealed by (U-Th)/He ages of supergene mineralisation in Attepe iron deposits.

Note: this chapter is presented in the format of a journal article and is intended for submission to Tectonics.

4.1 Introduction

The uplift of high elevation regions such as the Tibetan Plateau and Altiplano-Puna has driven changes in regional and global climate (Molnar et al., 1993; Molnar, 2005; Allmendinger et al. 1997, Ehlers and Poulsen 2009). The Central Anatolian plateau (CAP) is a western expression of the Himalayan-Tibetan orogen to the east (Hatzfeld and Molnar 2010) and covers approximately 120,000 km^2 at an average elevation of around 1 km above sea level (Çiner et al. 2015). It is fringed to the north by the Pontid mountains and to the south by the Taurus mountains (Fig. 4.1). The Taurides have an average elevation of 2.4 km and act as an orographic barrier to precipitation separating the semi-arid CAP (Schemmel et al. 2013) from the mild Mediterranean climate to the south (Sensoy, 2004). The paucity of terrestrial climate records makes it difficult to determine accurately when the current semi-arid climate became established across the southern margin of the Central Anatolian Plateau (smCAP), and how it relates to the uplift of the Tauride mountains. Consequently, the timing of uplift of the Taurides and its influence on regional climate, especially in the aridification of the CAP, is contentious.

Stable isotope records of lacustrine carbonates record a relatively humid climate in the Mut Basin/Ecemis Corridor regions of the CAP from the late Oligocene to early Miocene (Lüdecke et al., 2013). While, by the early Miocene, the CAP was yet to be fringed by orographic barriers to the north and south, the depositional environment had shifted from large, open freshwater to smaller closed saline lakes despite high humidity climate (Lüdecke et al., 2013). The lack of significant pre-Miocene orographic rain-out has been recognised in the $\delta^{18}O$ composition of carbonates from large continental basins, although the data point to the onset of uplift and establishment of an orographic barrier by 5 Ma (Lüdecke et al., 2013; Meijers et al., 2016; 2018). Throughout the late Miocene the smCAP drained internally, however by the early Pliocene it was connected to the Mediterranean Sea (Meijers et al., 2020). In the eastern

Mediterranean, underplating of material derived from the African plate during progressive collision with the Anatolian plate led to Late Messinian uplift of marine sediments in the Adana basins, south of the Taurides, establishing drainage to the Mediterranean Sea and resulting in the deep incision of the Taurides (Jaffey and Robertson 2005). The initiation of uplift across the smCAP from late Miocene times may reflect lithospheric slab break-off and upwelling of mantle asthenosphere, and perhaps the arrival of the Eratosthenes Seamount at the collision zone south of Cyprus (Cosentino et al. 2012, Schildgen et al., 2012, Schildgen et al., 2014, Radeff, 2014).

Meijers et al. (2020) proposed that a sub-humid Anatolian climate persisted during late Miocene surface uplift. They suggest that the smCAP had a relatively low relief during CAP uplift, with stable (>1 Ma) palaeoenvironmental and hydrological conditions based on the stable isotope composition of lacustrine carbonates. Delayed aridification of the CAP and its southern margin was potentially caused by an increase in mean annual precipitation into the Pliocene (Kayseri-Özer 2017). The Quaternary marine terraces along the smCAP allowed Racano et al. (2020) to develop a landscape evolution model that suggested the mountain belt was essentially formed during a pulse of rapid uplift (1.9 to 3.5 m/kyr) between 500 and 200 kyr that resulted in 1.5-2 km of surface uplift (Racano et al., 2020). This is supported by the occurrence of middle Pleistocene benthic fauna, indicative of an epibathyal marine environment, now identified along the smCAP on a palaeocoastline at ~1500 m above sea level to suggest a short-lived pulse of rapid uplift (3.2-3.4 m/kyr) since the middle Pleistocene (~450 kyr) (Öğretmen et al., 2018). This requires that the modern topography and the orographic barrier along the smCAP was established in the last 500 kyr.

Fe-oxides-oxyhydroxides (Fe-O) are ubiquitous near surface weathering products formed in relatively wet humid climates (Tardy and Nahon, 1985; Vasconcelos et al., 2015). Such supergene ore deposits form when the dissolution, remobilisation, and reprecipitation of elements of economic interest is promoted by chemical weathering processes at or near Earth's surface (Vasconcelos et al., 2015). Continued dissolution, transport, and redeposition of metals over extended period can create chemically stratified weathering profiles, thus recording chemical reactions occurring at or near Earth's surface that may have lasted for as long as 70 Ma and giving researchers the opportunity to study valuable climate histories at many locations globally (Reich and Vasconcelos, 2015). Supergene ore deposits, if worked as open pits, give excellent access to complete sections of weathered crust. At times, an open pit may be up to 6 km wide and more than 1 km deep (Heim et al., 2006, Vasconcelos et al., 2015). In a recent

study of climate conditions conducive to current Ni laterite formation, Thorne et al (2012) suggest that laterite formation requires >1000 mm/yr precipitation, have cold month mean (CMM) temperatures between 15 and 27 °C, and warm month mean (WMM) temperatures between 22 and 31 °C. This combination of conditions does not currently exist anywhere in Turkey.

Age determinations of supergene minerals within weathering profiles are now widely used to provide constraints on the timing of climate and tectonic processes that control chemical weathering rates (Vasconcelos, 1999; Beauvais et al., 2016; Deng et al., 2017). The modest U and Th content of Fe-O minerals results in the generation of significant and measurable amounts of ^{4}He by radioactive decay. At surface temperatures the diffusion rate of He within Fe-O minerals is low enough that it is quantitatively retained and the (U-Th)/He ages can be used to determine the timing of mineral precipitation (Shuster et al., 2005; Danišík et al., 2013). Consequently Fe-O He ages are now widely used to determine when climate conditions were conducive to supergene mineralisation (Vasconcelos et al., 2015), and they have proved useful for constraining how and when tectonic uplift initiate a change in climate, for example, the onset of aridity in the Central Andes (Cooper et al. 2016) and changes to Asian monsoon dynamics (Deng et al. 2017).

The Attepe iron deposits are located at 1.5-2 km above sea-level on the northernmost fringe of western extremity of the Eastern Taurus mountains and are ideally located to track the climate and uplift history of the smCAP (Fig. 4.1). Over 90% of the iron production and exploration is concentrated in 20-50 m thick oxidised zones in the upper part of all deposits (Küpeli, 2010; Keskin and Ünlü, 2016). The current cold, semi-arid climate of the region is not conducive to supergene oxidation (Sarıkaya et al., 2015). Consequently, dating the supergene alteration of the deposits has the potential to constrain the timing of climate change in the Taurides and how this relates to mountain belt evolution. Here we characterise supergene mineralisation and present (U-Th)/He ages from four mines within the Attepe district to determine when climate conditions on the smCAP were conducive to supergene enrichment and when the current cold semi-arid climate was established.

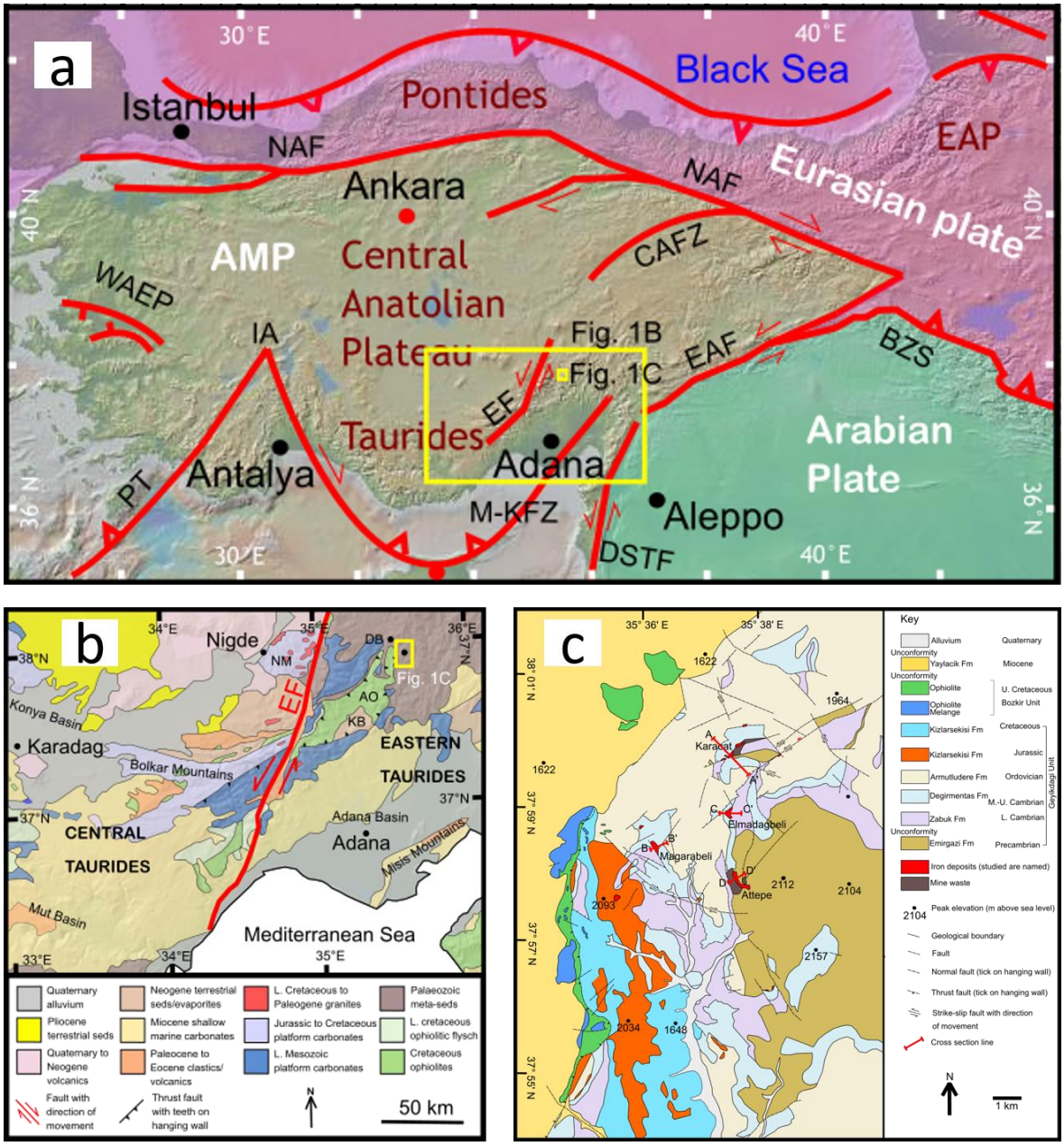

Figure 4.1: a) Large-scale map of Greater Anatolia showing major faults and tectonic plate arrangement adapted from Dilek and Sandvol (2009) and Walsh-Kennedy et al. (2014). b) Regional geology of the central southern margin of the Central Anatolian Plateau (smCAP) adapted from Dilek and Sandvol (2009). c) Geological map of the Attepe iron deposits adapted from Keskin (2016). Formation descriptions in stratigraphic column (Fig. 4.2). AO – Aladag ophiolite, KB – Karsanti Basin, DB– Dikme Basin, NM – Nigde Massif, EAP – East Anatolian Plateau, AMP – Anatolian microplate, NAF- North Anatolian fault, CAFZ – Central Anatolian fault zone, WAEP – Western Anatolian extensional province, IA – Isparta Angle, PT – Pliny trench, M-KFZ – Misis-Kyrenia Fault Zone, EF – Ecemis fault zone, EAF – East Anatolian fault, DSTF – Dead Sea transform fault, BZS – Bitlis-Zagros suture. Panel a and b background from GeoMapApp (Ryan et al., 2009).

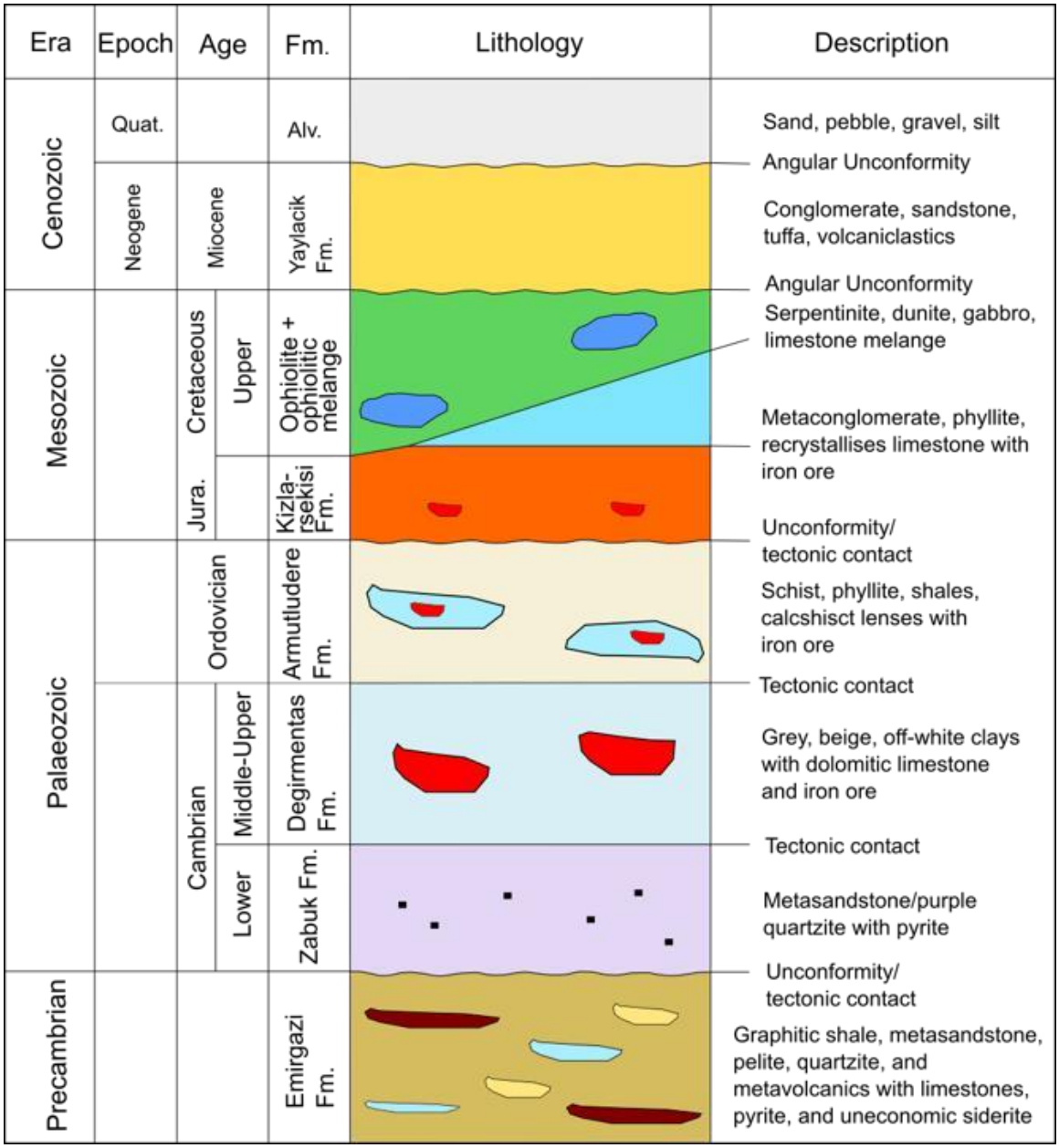

Figure 4.2: Stratigraphic column showing the main geological units across the Attepe ore deposit region. Adapted from Keskin (2016)

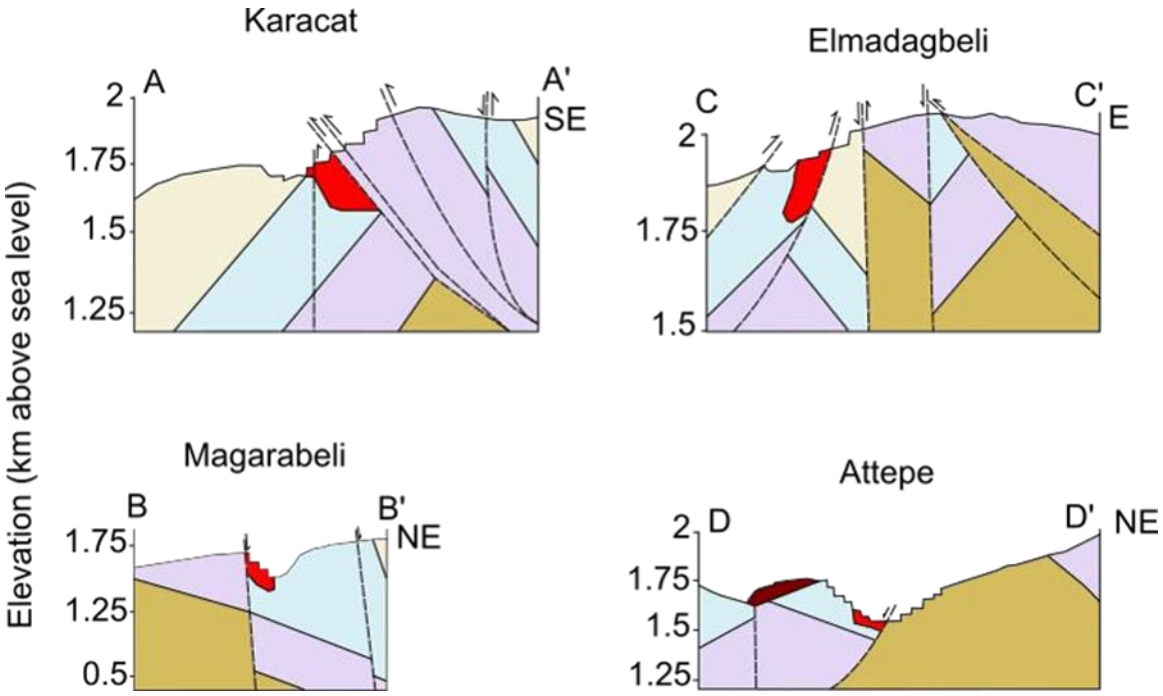

Figure 4.3: Cross sections of each mine showing relationship to main lithologies and faults. Cross section lines are taken from Fig. 1. C. Adapted from Keskin (2016)

4.2 Geological setting

The Taurus Mountain chain runs for over 1,500 km across southern Turkey to Iran. They record a complete plate-tectonic cycle beginning with Palaeoozoic rifting, followed by seafloor spreading, and final collision of African and Eurasian plates during the late Mesozoic to early Cenozoic (Robertson et al., 2007). They are widely interpreted to be composed of continental fragments rifted from North Africa during the Mesozoic opening of the Southern Neotethys Ocean (Şengör and Yilmaz 1981; Dixon and Robertson, 1984). The progressive closure of the Southern Neotethys Ocean is associated with ophiolite emplacement during the late Cretaceous and ultimately closure by the Miocene (Robertson et al., 2007). Further convergence resulted in the westward escape of the Anatolian microplate along the Northern and Eastern Anatolian fault zones from the mid-Miocene (Şengör et al., 1985; Bozkurt, 2001). This movement continues today as Anatolia undergoes counter-clockwise rotation and westward escape from Eastern Anatolia at a rate of ~30 mm/yr (Bozkurt, 2000). The Tauride Mountains are typically divided into Western, Central, and Eastern Taurides, with the latter found east of the Ecemis Fault and of primary interest to this study.

Middle to late Miocene marine fossil assemblages in the Dikme basin, ~10 km northwest of the Attepe district, records the final marine incursion into the smCAP (Ocakoğlu, 2002). To

the south-west, 6.7 Ma marine sediments of the Mut-Ermenek Basin are now at 1.5-2 km implying that surface uplift rates of 200-300 m/Myr (Cosentino et al., 2012; Schildgen et al., 2012). This may have been initiated by the switch from crustal shortening to extension along the smCAP, linked to oceanic slab break off and tearing in middle to late Miocene (Schildgen et al., 2014). Cosmogenic nuclide surface exposure ages of strath terraces in the Mut basin reveal average uplift rates of 250 to 370 m/Myr since 8 Ma with periods of higher uplift rate of between 600 to 700 m/Myr after 1.66 Ma (Schildgen et al., 2012). From early to middle Pleistocene, this increase in uplift across southern Turkey may be the result of collision between the Eratosthenes Seamount and the subduction trench where African and Eurasian plates converge to the south of Cyprus (Schildgen et al., 2012).

The Attepe mining district is between 1.5 and 2 km above sea level on the western side of the Eastern Taurus Mountains in the Kayseri-Adana region of southern Turkey (Fig. 4.1) (Küpeli 2010). It is one of Turkey's most important Fe-ore producers, with proven reserves of up to 70 Mt and an estimated 1 Mt of ore currently extracted annually from the Attepe and Elmadagbeli mines at average grade of 45-58 % Fe_2O_3 (Küpeli, 2010; Keskin, 2016). The main ore hosting formations are present within the metasedimentary rocks of the 4 km thick Palaeozoic Geyikdagi Unit containing the Degirmentas formation and Armuludere formation (Figs. 4.2-4 and 7). Basement lithologies have been subject to low grade metamorphism with multiphase deformation superimposed during Caledonian, Hercynian and Alpine orogenic events (Küpeli 2010; Keskin, 2016).

The oldest mineralisation phase is an uneconomic syn-sedimentary pyrite and hematite hosted in Precambrian Emirgazi formation metasedimentary and metavolcanic units (Küpeli 2010). A later phase of Paleocene to Lower Eocene hydrothermal-metasomatic vein-type iron carbonate mineralisation is hosted in middle to upper Cambrian Degirmentas formation dolomitic limestones. The ore bodies occur as veins, lenses or stocks composed ankerite and siderite with associated hematite, chalcopyrite, tetrahedrite, pyrite and marcasite veins hosted in the Emirgazi, Cambrian Degirmentas and Armutludere, and Jurassic Kizlarsekisi formations (Küpeli, 2010; Keskin, 2016). The mineralisation is controlled by NE-SW and ENE-WSW trending fault systems which provided pathways for hydrothermal fluid flow. The most economic deposits occur where the fault systems intersect (Küpeli, 2010; Keskin and Ünlü, 2016).

The hydrothermal-metasomatic mineralisation has been subjected to extensive supergene alteration, termed karstic Fe-oxi-hydroxide (KIO) mineralisation by Küpeli et al. (2007). Weathering profiles are present at all mines, evident from the 20-80 m thick zones of dominantly limonite, goethite, and hematite, with less abundant malachite, azurite, lepidocrocite, manganite and calcite. The uppermost part of the supergene zones have been removed in many cases. The oxidation zones in each mine are not laterally consistent within the deposits, they tend to replace the vein-type ores along faults and fracture systems (Figs 4.3-7). In the field the oxidation zones are recognised as intensely weathered friable rock, boxwork textures, and occurrences of botryoidal/reniform goethite (Figs. 4.8-9). The oxidation phase is the dominant source of iron ore in the district, accounting for more than 90% of the extracted iron (Küpeli 2010). The Attepe mine is the largest and most economically important of the deposits, approximately 500 x 500 m and in places up to 200 m deep (Fig. 4.3) (Küpeli 2010; Keskin, 2016).

The climate of the region is classed as semi-arid; mean summer temperatures are 23°C, mean winter are typically -2°C and annual precipitation rarely if ever exceeds 500 mm (Schemmel et al., 2013). The town of Niğde ~80 km west of the Attepe district at ~1300 m above sea level has a cold semi-arid climate, with hot dry summers (mean temperature 20°C) cold and often snowy winters (mean 4.3°C) and 90% of the precipitation (<350 mm) falling between autumn and spring (Sarıkaya et al., 2015). To the south of the smCAP a mild Mediterranean climate prevails where mean annual rainfall exceeds 1000 mm (Sensoy, 2004). Topography immediately to the north of the Attepe iron deposits becomes less mountainous and merges with the CAP, whereas to the south it becomes mountainous with steep river valleys and defined peaks > 2 km. The Zamanti River drains the region and runs from the north near Kayseri, south past Dikme ~10 km to the NW of Attepe iron deposits and through the Taurides before joining the Göksu River and forming the Seyhan River, the largest river draining to the Mediterranean, ~ 80 km to the north of Adana.

4.3 Samples

We have analysed seven Fe-O samples from four mines: Attepe, Magarabeli, Karacat, and Emladagbeli (Figs. 4.4-10; Tables 4.1 and 2). In-situ samples were taken from the weathering sections near the diffuse base of the supergene zone of the active mine workings (Figs. 4.4-7).

All samples were taken from veins or cavity and fracture infills. Areas of high purity were selected to minimise contamination by hypogene phases. The purity, composition, and crystal morphology of all samples were investigated by X-ray diffraction analyses and scanning electron microscopy. From the XRD spectra samples S1, S3, and S11 are pure goethite, S4 and S8 are hematite-goethite mixtures, S9 is a mixture of hematite with minor magnetite (Fe_3O_4) and S10 is hematite only (Table 4.1; Fig. 4.10). No minor phases were present above detection limit (<1%). All samples are poly-crystalline, showing boxwork texture indicative of supergene weathering with many crystal forms (e.g. botryoidal, reniform, prismatic, needle-like, fibrous or platy) (Fig. 4.8). Colloform banding provides evidence of mineral precipitation from a fluid phase into open spaces (Fig. 4.9). Crystal dimensions range from 0.1 µm to 300 µm and typically make up larger aggregates of crystals or form ribs in the pervasive boxwork texture (Fig. 4.9).

The average crystallite size (or mean coherent domain size) for each sample was obtained by applying the Scherrer equation to each sample x-ray diffractogram result (Table 4.1). Average crystallite sizes range from 28 ± 10 nm to 84 ± 2 nm. The pure goethite samples tend to record greater average crystallite size, though not entirely (Table. 1). Crystallite size is generally taken as the cube root of the volume of a crystallite and, using the Scherrer equation to calculate it, provides a lower estimate of crystallite size since the effects of strain and crystal lattice imperfections on peak width are not considered (Speakman, 2014). Further, if sample material has average crystallite size <100 nm it is taken as the thickness of the crystallite analysed (Monshi et al., 2012). Crystallite size is not necessarily grain size, since grains can be composed of many crystallites (Monshi et al., 2012). This method for crystallite size estimation allows for the correction of diffusive loss of He from Fe-O, like in Allard et al. (2018). However, Allard et al. (2018) use Rietveld refinement prior to calculation of crystallite size which accounts for strain and crystal lattice imperfection.

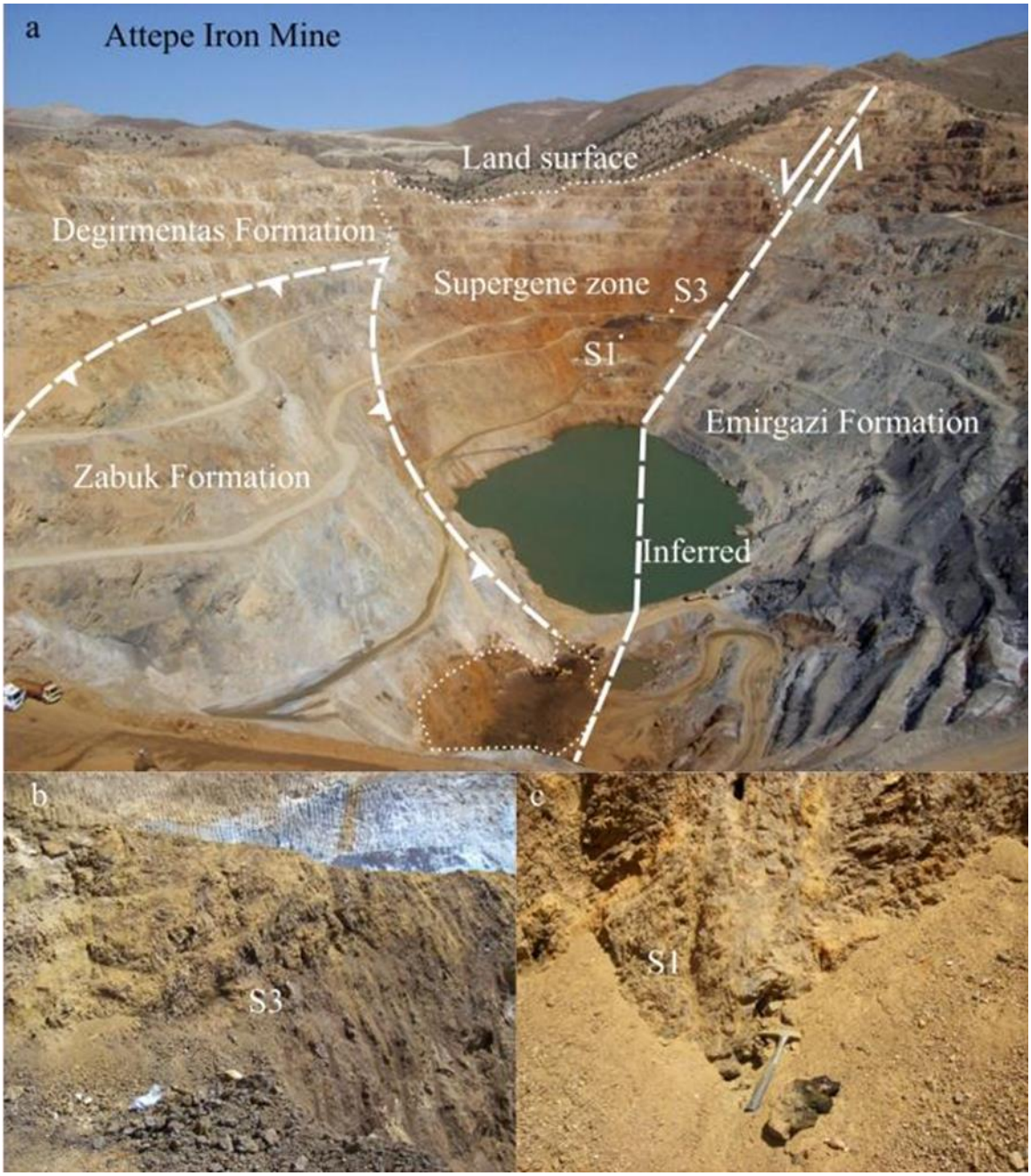

Figure 4.4: Field images of Attepe iron mine. A) view of the open pit mine. B) location of sample S1. C) location of sample S3

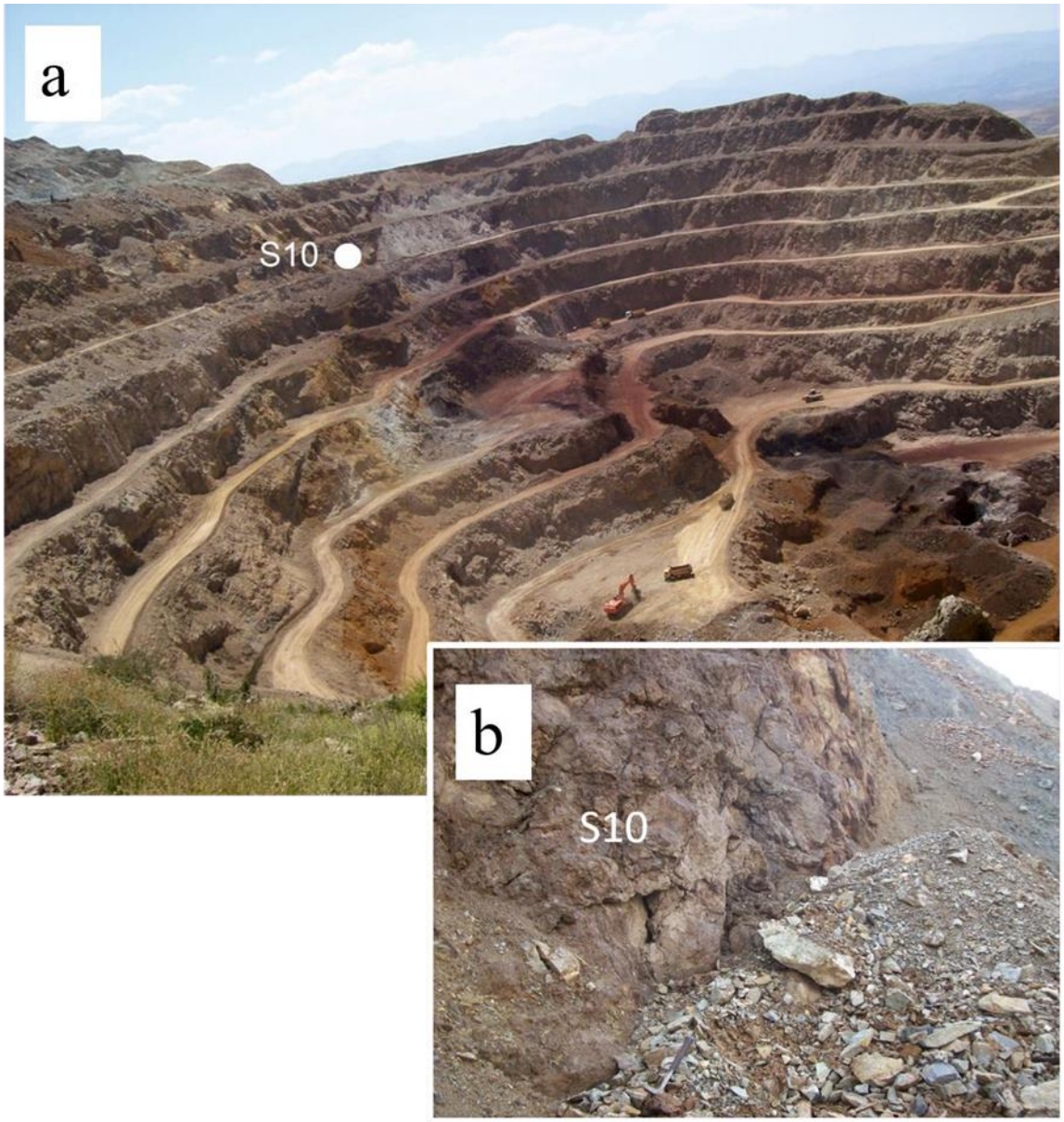

Figure 4.5: Field images of Karacat iron mine A) and B) the location of sample S10.

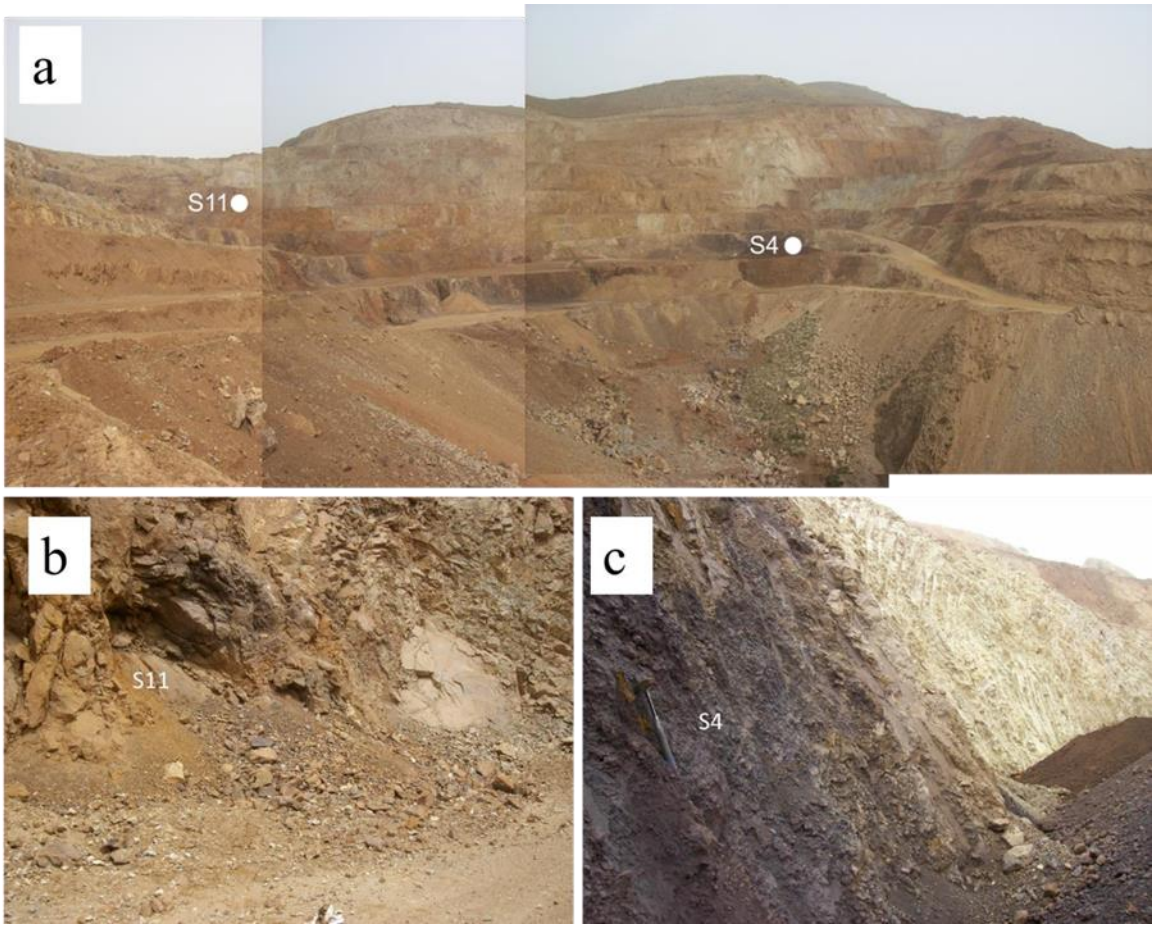

Figure 4.6: Field images of Elmadagbeli iron mine showing the open pit mine A) and the location of samples S11 (B) and S4 (C).

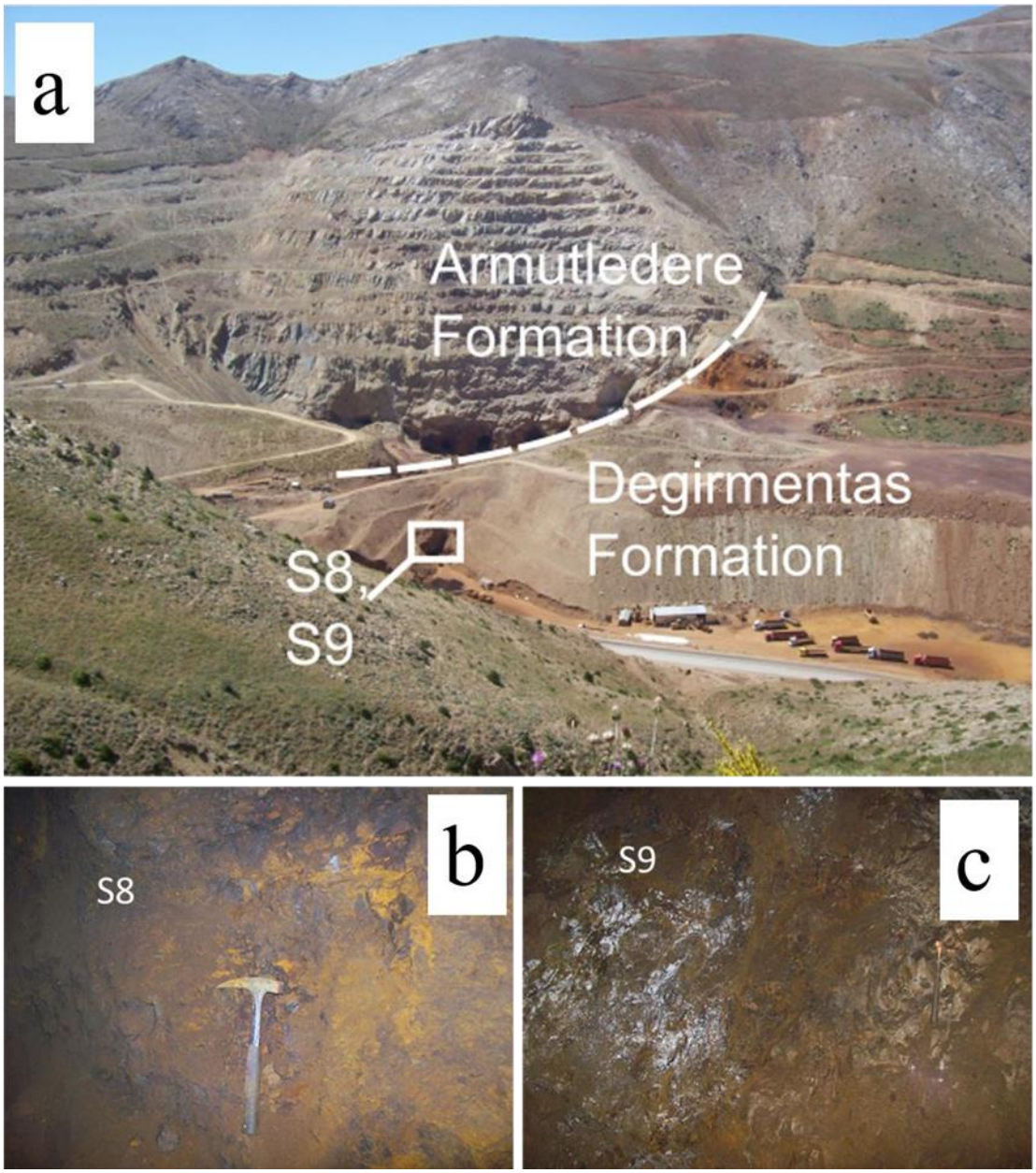

Figure 4.7: Photograph of the Magarabeli iron mine (A). Samples were taken from section of the mine highlighted within the white box in image A. B) context of sample S8. C) context of sample S9.

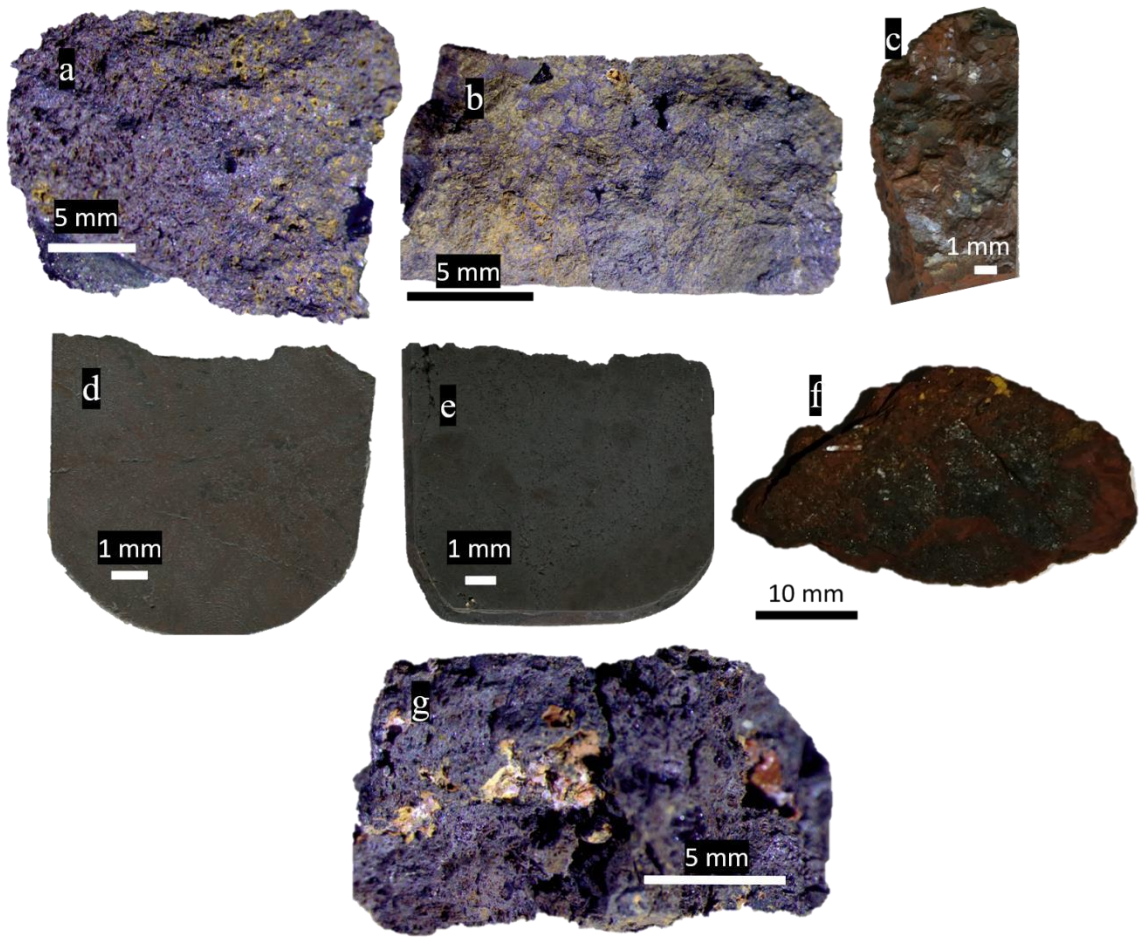

Figure 4.8: Images of hand samples used in this study. A) Sample S1: fresh surface of a chip liberated from larger sample. Metallic grey of goethite with friable yellow weathering evident. B) Sample S3: fresh surface of a chip liberated from larger sample. Metallic grey of goethite with friable yellow weathering evident. C) Sample S4: Representative broken chip, similar to that used for SEM analysis, showing fresher metallic grey of hematite and deeper red weathering. D) Sample S8: Broken polished block showing metallic lustre of hematite and weathered hematite/goethite red/brown patchy surface. E) Sample S9: Broken polished block showing metallic lustre of hematite/magnetitie and weathered red patchy surface. F) Sample S10: Broken chip showing darker metallic lustre of hematite alongside friable weathered red and yellow patches. G) Sample S11: fresh surface of a chip liberated from larger sample. Metallic grey of goethite with friable yellow weathering evident.

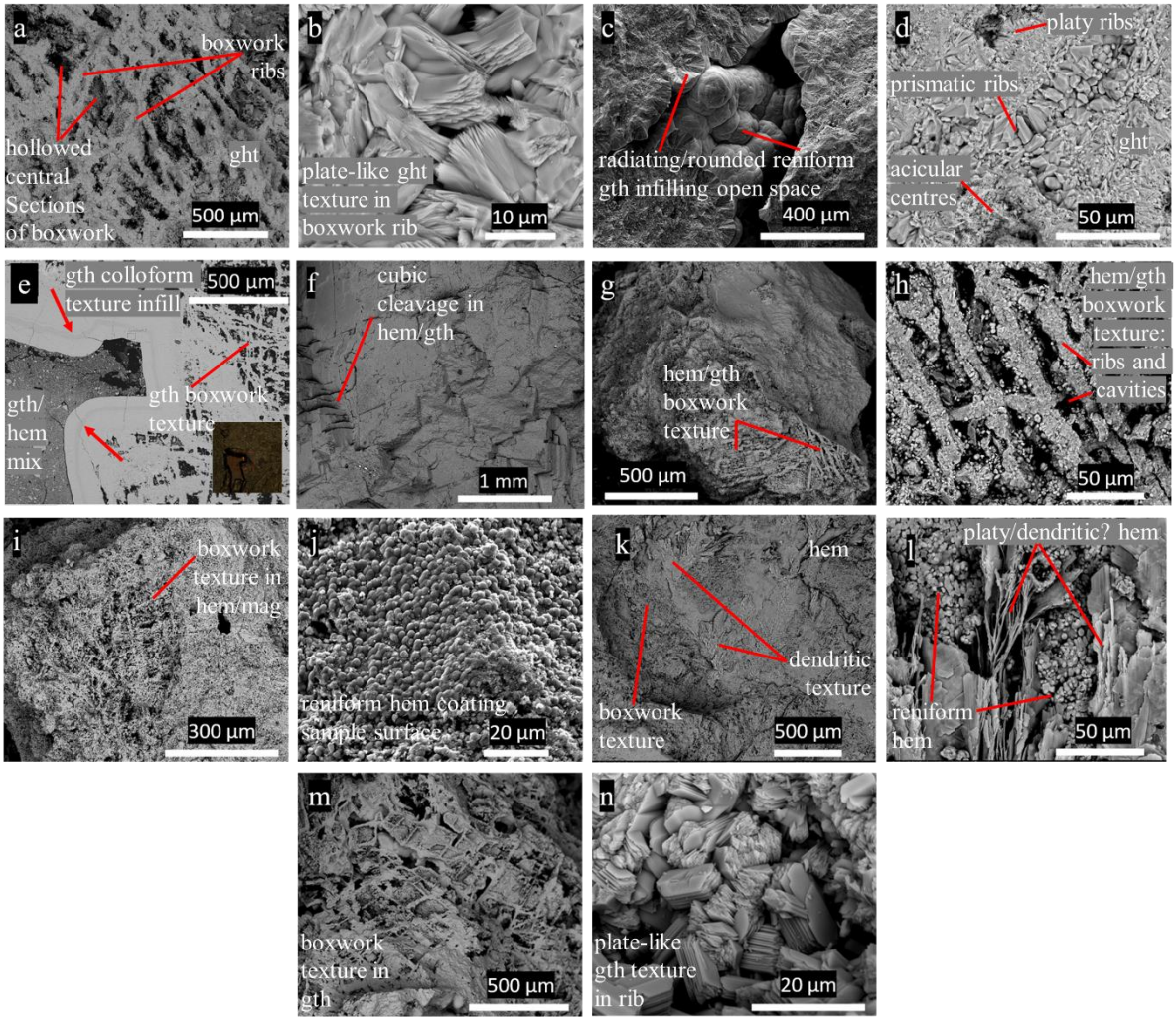

Figure 4.9: Back-scattered electron SEM images of supergene iron oxide-oxyhydroxide textures from the Attepe iron ore deposits. a) sample S1 B) sample S1. c) sample S3. d) S3: Poly-crystalline goethite from sample S3. Boxwork ribbing is typically composed of plate-like and prismatic morphology whereas hollowed central sections are primarily filled with needle-like goethite. e) Sample S3: colloform texture of goethite filling open/partially filled space with boxwork texture on the inner surface of colloform banding (top, right, and bottom right of image) This implies that final boxwork development is synchronous with colloform banding. f) sample S4. g) Sample S8: Fractured chip highlighting pervasive boxwork texture. h) Sample S8. i-j) Sample 9. k-l) Sample S10. m-n) Sample S11

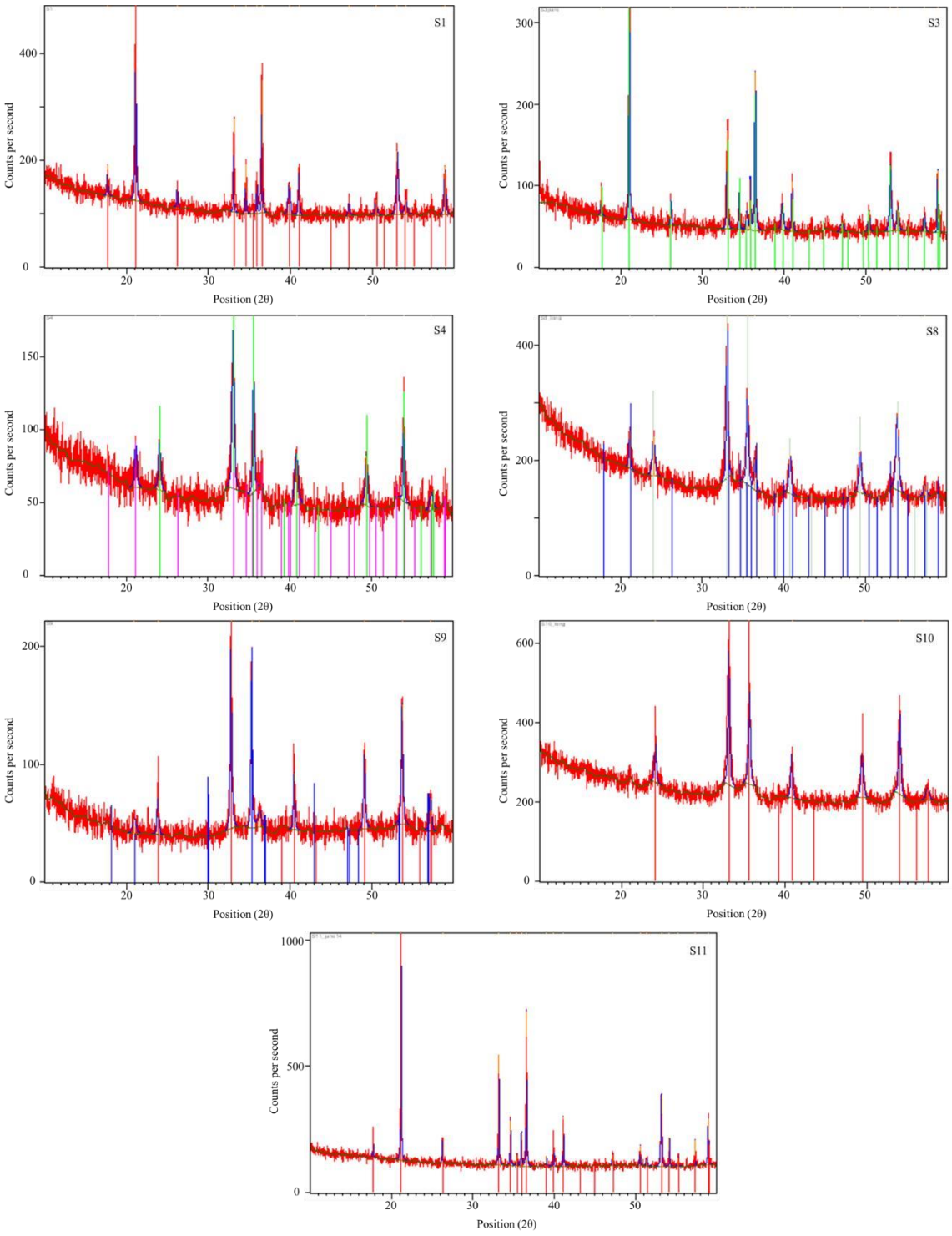

Figure 4.10: Diffractograms of each sample. S1: Highest intensity peak recorded at 21.1θ indicative of goethite. S3: Highest intensity peak recorded at 21θ indicative of goethite. S4: Highest intensity peak recorded at 31.1θ indicative of hematite. S8: Highest intensity peak recorded at 31.1θ indicative of hematite, with goethite a minor component. S9: Highest intensity peak recorded at 32.8θ indicative of hematite, with magnetite recording a at 35.3θ (blue lines under diffractogram). S10: Highest intensity peak recorded at 31.1θ indicative of hematite. S11: Highest intensity peak recorded at 21.1θ indicative of goethite.

Table 4.1: XRD diffractogram data from iron oxide/oxyhydroxide samples from the Attepe iron deposits, Turkey.

Sample	Mineralogy	Relative Intensity (%)	FWHM (degrees)	FWHM (radians)	Peak Position (degrees)	Peak Position (radians)	D	D average	stdev	error
S1	FeOOH	100	0.1428	0.0025	21.1	0.2	59.1	72.2	29.9	41.4%
	FeOOH	48	0.0816	0.0014	33.1	0.3	106.1			
	FeOOH	69	0.1020	0.0018	36.6	0.3	85.7			
	FeOOH	33	0.2448	0.0043	53.1	0.5	37.9			
S3	FeOOH	100	0.1428	0.0025	21.1	0.2	59.1	65.6	30.0	45.7%
	FeOOH	78	0.1632	0.0028	36.5	0.3	53.5			
	FeOOH	49	0.1428	0.0025	33.1	0.3	60.6			
	FeOOH	33	0.2448	0.0043	53.0	0.5	37.9			
	FeOOH	31	0.0816	0.0014	58.8	0.5	116.7			
S4	Fe_2O_3	100	0.2856	0.0050	33.1	0.3	30.3	27.6	10.0	36.2%
	Fe_2O_3	88	0.2040	0.0036	35.6	0.3	42.7			
	FeOOH	63	0.4896	0.0085	54.0	0.5	19.0			
	FeOOH	32	0.4896	0.0085	40.8	0.4	18.1			
	Fe_2O_3	31	0.3264	0.0057	49.4	0.4	28.0			
S8	Fe_2O_3	100	0.2856	0.0050	33.1	0.3	30.3	27.9	4.4	15.7%
	Fe_2O_3	57	0.2856	0.0050	35.6	0.3	30.5			
	FeOOH	52	0.4080	0.0071	53.9	0.5	22.8			
S9	Fe_2O_3	100	0.2040	0.0036	32.8	0.3	42.4	40.1	2.9	7.1%
	Fe_3O_4	78	0.2040	0.0036	35.3	0.3	42.7			
	Fe_2O_3	61	0.2448	0.0043	53.7	0.5	38.0			
	Fe_2O_3	38	0.2448	0.0043	49.1	0.4	37.3			
S10	Fe_2O_3	100	0.2244	0.0039	33.1	0.3	38.6	34.5	5.7	16.5%
	Fe_2O_3	61	0.2856	0.0050	35.6	0.3	30.5			
	Fe_2O_3	57	0.2448	0.0043	54.0	0.5	38.0			
S11	FeOOH	100	0.1020	0.0018	21.2	0.2	82.8	84.4	1.5	1.8%
	FeOOH	48	0.1020	0.0018	33.2	0.3	84.9			
	FeOOH	68	0.1020	0.0018	36.6	0.3	85.7			
							Average D (nm)	50.3	23.3	46.2%

Scherrer equation $D = k \times \lambda / \beta (\cos\theta)$

D = crystallite size (nm)

k = Scherrer's Constant (for spherical crystallites with cubic symmetry) 0.94

λ = x-ray wavelength Cu K-alpha 1.5406; or 0.15406 Angstrom.

β = FWHM (Full Width Half Maximum in radians - peak width)

θ = peak position (radians) 0.5

4.4 Analytical procedures

Samples were dried, gently crushed and 1-2 mm chips free of gangue minerals were picked, crushed, and sieved. Gangue minerals, predominantly calcite and quartz, were removed from the 0.25-1 mm fraction using a Frantz LB-1 magnetic separator and hand-picking under binocular microscope. This fraction was re-crushed and gangue minerals removed from the 150-250 µm fraction. A final crush step using a quartz-agate pestle and mortar was used to produce a <38 µm fraction for powder X-ray diffraction (XRD), and He, U and Th determinations. XRD was carried out using a Panalytical X'Pert PRO MPD (A3-26) at School of Chemistry, University of Glasgow. The diffractometer is equipped with a Cu target tube operated at 40 kV and 40 mA and was set to scan between 10 and 60° 2θ scan range with a step size of 0.017° with each step taking between 60-150 seconds. Small rock chips were imaged using a FEI Quanta 200F environmental scanning electron microscopy (SEM) operated at 20 kV at the ISAAC facility at University of Glasgow (Lee et al., 2014).

Analytical procedures for He dating were similar to those of Wu et al. (2019). In order to avoid problems associated with the volatilisation of U and Th during the heating (800-1000°C) required for He extraction (e.g. Vasconcelos et al. 2013; Danišík et al., 2013; Hofmann et al. 2020) we have determined He separately from U and Th in multiple aliquots of several mg of each sample. This data was used to calculate an average He concentration and average U and Th concentration for each sample, which were used to determine the sample (U-Th)/He age using the formulation of Meesters and Dunai (2005). This procedure has been used successfully to date hematite mineralisation from Elba yielding ages that are indistinguishable from Ar/Ar ages of cogenetic adularia (Wu et al. 2019). The technique differs from the standard technique where multiple single aliquots are dated, which often yields over-dispersed age populations (e.g. Cooper et al. 2016; Danišík et al., 2013; dos Santos Albuquerque et al., 2020).

Helium concentrations were determined in 6-9 aliquots of each sample. Between 3 and 9 mg of <38 µm fraction were weighed into Pt-foil packets. Typically, four sample aliquots and one empty packet were placed 10 mm apart in recesses in a degassed Cu pan and covered with a sapphire window prior to overnight pumping at 80°C to minimise background levels of H and CH4. Helium was extracted by heating the Pt packets to 1000 ± 20°C for 300 seconds using a 960 nm diode laser heating system (Fusions 960, Photon Machines). Laser power was regulated using the inbuilt pyrometer which maintained sample temperature. All sample tubes were re-heated to ensure complete He extraction. Sample re-heats released on average 0.2% of the

initial He and were not used in He concentration determinations. The evolved gases were purified for 600 seconds using a combination of hot and cold SAES TiZr getters and two liquid nitrogen-cooled charcoal traps. Helium abundances were determined using a Hiden HAL3F quadrupole mass spectrometer operated in static mode (Foeken et al. 2006). Absolute ^{4}He concentrations in samples were calculated by peak height comparison against repeated measurements of a calibrated He standard. Blocks of standard determinations were carried out before and after every two sample aliquots. Within these distinct analytical periods He sensitivity varied by ±1%. Helium blanks (3.6 x 10-11 ccSTP ± 73 %, n = 62) were determined by heating empty Pt tubes. Sample He contents were always more than 100 times the blank values.

Uranium and thorium concentrations were determined on 3-5 aliquots of 2-5 mg Fe-O. The sample dissolution procedures were essentially identical to those developed by Wu et al. (2019). U and Th were measured in Agilent 7500ce Q-ICP-MS. Blank levels were between 0.06 ± 0.05 ppm for U and 0.11 ± 0.10 ppm for Th. U and Th analysed in four aliquots of hematite (Italy-4) from the Rio Marina mine Elba yielded ^{238}U and ^{232}Th concentrations that overlapped values determined by in Wu et al. (2019) (Table 4.2).

4.5 Results

^{4}He concentrations range from 0.49 to 8.3 x 10-10 ccSTP/mg (Table 4.2). Weighing error, blank corrections and mass spectrometer sensitivity variation means that individual He concentration determinations have an uncertainty of ±2 %. This is less than the range of He concentrations measured of multiple aliquots of each sample (±4-7 %). ^{238}U concentrations range from 0.07 to 1.55 ppm. Th was only measurable in four of the seven samples, ranging from 0.01 to 0.19 ppm. Th/U ratios in the four Th-bearing samples vary from 0.16-2.43 but tend to be consistent within sample. Single U and Th concentration determinations typically have an uncertainty of ±2 %. The within-sample effective uranium content (eU = [U] + 0.235 x [Th]) is ± 5 % in all but one sample.

Average (U-Th)/He ages for each sample calculated using the mean He and eU concentrations range from 0.90 to 5.08 Ma (Table 4.2). No alpha ejection correction was applied, consistent with other studies of Fe-O (e.g. Shuster et al., 2005; Vasconcelos et al., 2013; Allard et al.,

2018; dos Santos Albuquerque et al., 2020). The total uncertainty of the average He ages is ±5-18 % (1σ).

Table 4.2: Sample information and (U-Th)/He data for Fe-O samples from the Attepe iron deposits, Turkey.

Sample	Mineralogy	Deposit	Elevation(m)	Mean Crystallite Size (nm)	Aliquot	Mass (mg)	^{4}He (ccSTP/mg) (10^{-10})	Mean ^{4}He (ccSTP/mg) (10^{-10})	Error	Aliquot	Mass (mg)	232U (ppm)	Error	232Th (ppm)	Error	Th/U	eU	He age (Ma)	Error	Corrected Age	error
S1	Gth	Attepe	1796	72	1.1	4.3	1.09	1.15	0.04	1.7	2.2	0.38	0.01	0.12	0.01	0.32	0.41	2.27	0.12	2.32	0.13
					1.2	4.4	1.10			1.8	2.4	0.48	0.02	0.11	0.11	0.23	0.51				
					1.4	4.9	1.18			1.9	1.8	0.39	o.01	0.11	0.11	0.28	0.42				
					1.6	5.0	1.17			1.10	2.2	0.36	0.01	0.10	0.11	0.28	0.38				
					1.7	4.9	1.22			1.11	5.1	0.42	0.01	0.14	0.11	0.33	0.45				
					1.8	5.0	1.15														
					1.9	4.5	1.15														
S3	Gth	Attepe	1811	66	3.10	5.4	7.33	7.48	0.50	3.1	5.1	1.28	0.14	*	*	*	1.28	4.54	0.59	4.68	0.61
					3.11	4.5	7.20			3.2	5.3	1.46	0.14				1.48				
					3.12	6.0	6.47			3.3	4.8	1.30	0.15				1.31				
					3.16	4.0	7.40			3.4	4.9	1.29	0.15				1.30				
					3,17	3.6	7.31			3.5	4.7	1.39	0.16				1.40				
					3.18	5.6	8.26														
					3.19	5.9	7.61														
					3.20	5.4	7.84														
					3.21	5.4	7.84														
S9	Hem/Mag	Magarabeli	1542	40	9.7	4.5	3.37	3.30	0.23	9A	4.3	1.01	0.01	*	*	*	1.02	2.86	0.32	2.97	0.34
					9.8	3.3	3.33			9B	3.9	0.90	0.01				0.90				
					9.9	6.2	3.32			9C	4.1	0.91	0.01				0.91				
					9.10	5.3	2.91			9D	4.1	0.97	0.01				0.97				
					9.11	5.3	3.01														
					9.12	5.5	3.38														
					9.13	4.8	3.51														
					9.14	5.6	3.57														
S8	Hem/Gth	Magarabeli	1550	28	8.10	9.1	5.98	5.79	0.32	8.1	5.3	1.46	0.14	*	*	*	1.46	3.21	0.36	3.4	0.38
					8.11	5.4	5.85			8.2	5.0	1.55	0.15				1.56				
					8.12	5.5	5.56			8.3	5.1	1.49	0.14				1.50				
					8.14	4.0	5.27			8.4	4.8	1.43	0.15				1.44				
					8.15	4.4	5.49			8.5	5.1	1.43	0.14				1.44				
					8.16	5.1	5.89														
					8.17	5.4	6.10														
					8.18	6.5	6.21														
S4	Hem/Gth	ELmadagbeli	1954	28	4.1	5.0	0.59	0.52	0.04	4.7	2.0	0.43	0.01	0.07	0.01	0.16	0.45	0.90	0.14	0.95	0.15

					4.2	6.4	0.50			4.8	1.9	0.46	0.02	0.07	0.01	0.16	0.48				
					4.3	4.7	0.50			4.9	1.9	0.47	0.02	0.11	0.01	0.23	0.50				
					4.4	4.2	0.52														
					4.6	5.2	0.49														
					4.8	5.7	0.52														
S11	Gth	Elmadagbeli	2002	84	11.1	5.4	0.86	0.92	0.06	11A	4.1	0.11	0.02	0.19	0.01	1.73	0.15	5.08	0.93	5.18	0.95
					11.2	5.9	0.90			11B	4.3	0.10	0.02	0.19	0.01	1.90	0.14				
					11.3	5.6	0.91			11C	4.1	0.07	0.02	0.17	0.01	2.43	0.11				
					11.4	5.4	0.89			11D	4.2	0.09	0.02	0.18	0.01	2.00	0.13				
					11.5	5.4	0.95														
					11.6	5.0	1.02														
S10	Hem	Karacat	1757	35	10.1	5.1	0.73	0.67	0.03	10A	4.2	0.42	0.02	0.12	0.003	0.29	0.45	1.19	0.10	1.25	0.10
					10.2	4.5	0.67			10B	4.1	0.45	0.02	0.12	0.002	0.26	0.48				
					10.3	4.7	0.68			10C	3.8	0.46	0.02	0.13	0.01	0.27	0.49				
					10.4	4.8	0.63			10D	4.0	0.42	0.02	0.11	0.01	0.26	0.45				
					10.5	5.4	0.66														
					10.6	5.3	0.67														
Italy 4C	Hem	Elba						2.76^	0.02^	A	7.90	0.30	0.01	0.43	0.01	1.44	0.40	5.60	0.23		
										B	8.10	0.31	0.01	0.42	0.01	1.35	0.41	5.58	0.20		
										C	8.47	0.32	*	0.40	0.01	1.23	0.42	5.43	0.10		
										D	9.13	0.32	*	0.41	0.01	1.27	0.41	5.48	0.10		

***Value at or below detection limit**

^From Wu et al (2018)

4.6 Discussion

4.6.1 Post-formation He loss

Diffusive loss of He from Fe-O can be significant at low temperatures and should be accounted for when determining mineral crystallisation ages from (U-Th)/He data (Shuster et al., 2005; Vasconcelos et al., 2013; Allard et al. 2018). Helium diffusion rates are governed by mineral chemical composition and temperature, while the proportion of radiogenic He lost from any sample is strongly dependent on mineral grain size (Farley, 2018). Where the deficit gas fraction has been determined on specific samples using the $^{4}He/^{3}He$ technique (e.g. Shuster et al., 2005; Heim et al., 2005; Deng et al., 2017), the percentage of He lost by diffusion can be constrained and corrected He age calculated. However, the parameters of He diffusion in the goethite and hematite are well established (Shuster et al., 2005; Farley 2018) and the extent of He loss can be determined, and (U-Th)/He ages reconstructed, if mineral composition and grain size is known (e.g. Allard et al. 2018).

Helium diffusion in crystalline hematite is slow at low temperature (Bahr et al. 1994; Farley et al. 2018). For example, over 90 % of He is retained in 20 nm crystallites held at 30°C for 100 Ma, comparable to the He loss rate from 100 µm diameter apatite grains (Farley 2018). Goethite is typically composed of poly-crystalline aggregates of varying properties and the more open crystal structure results in faster He diffusion. Shuster et al. (2005) showed that goethite contains regions with distinct He retention properties termed low resistivity domains (LRD) which likely account for most of the diffusive loss of ^{4}He. Extrapolating the data derived from $^{4}He/^{3}He$ analysis they showed that 3 to 10% of the He is lost at 25°C (Shuster et al. 2005). These distinct retention domains have been recognised in subsequent studies (Heim et al. 2006, Vasconcelos et al., 2013; Deng et al. 2017). By incorporating the crystallographic characterisations of goethite from ferruginous duricrust into the He production-diffusion code HeFTy (Ketcham 2005), Allard et al. (2018) were able to simulate He retention in spherical domains of different radii. Using the diffusion coefficients of Shuster et al. (2005) and Vasconcelos et al. (2013) they determined that 10 to 25% of He is lost from 20 nm and 13 nm diameter goethite crystallites respectively at 25°C.

The crystallite-size of the samples in this study leaves them susceptible to He loss and requires that a correction be made to the (U-Th)/He ages (Table 4.2). By assuming the maximum diffusion coefficient (Do) value of 10 (Shuster et al., 2005; Vasconcelos et al., 2013), adopting the relationship between Do and crystallite size defined by Allard et al. (2018) and using the mean crystallite size of samples determined by XRD, we can determine an upper limit on the proportion of He lost. Using this technique, we calculate that the goethite samples (S1, S3, and S11) have lost up to 6% of their He. The age correction to the mixed hematite-goethite samples (S8 and S4) has been determined based on the proportion of goethite as measured by XRD and does not exceed 6%. Sample S10 from the Magarabeli mine is essentially pure hematite and requires an age correction of up to 4%. The diffusion-corrected ages suggest that the upper limit on the supergene mineralisation ages (0.95 ± 0.15 to 5.18 ± 0.95 Ma) are not significantly different to the uncorrected ages, and the age difference is within the analytical uncertainty (Table 4.2). We conservatively use the diffusion-corrected ages in the following discussion. There is no relationship between age and crystallite size, mineralogy or eU (Figs. 4.11-12).

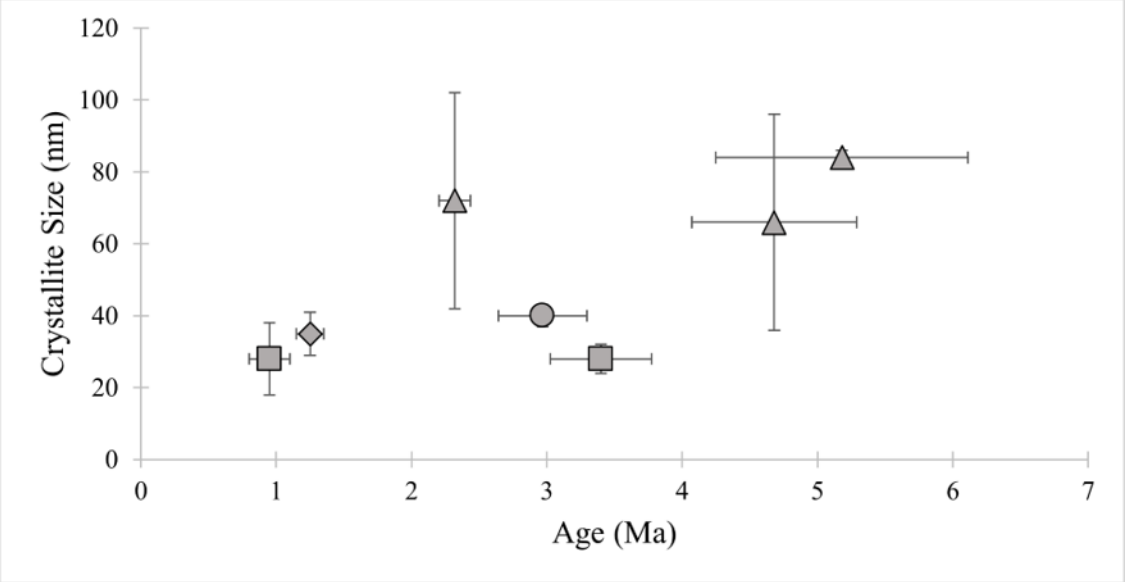

Figure 4.11: Age versus crystallite size and mineralogy plot. Triangle = goethite; circle = hematite/magnetite mix; square = hematite/goethite mix; rhombus = hematite

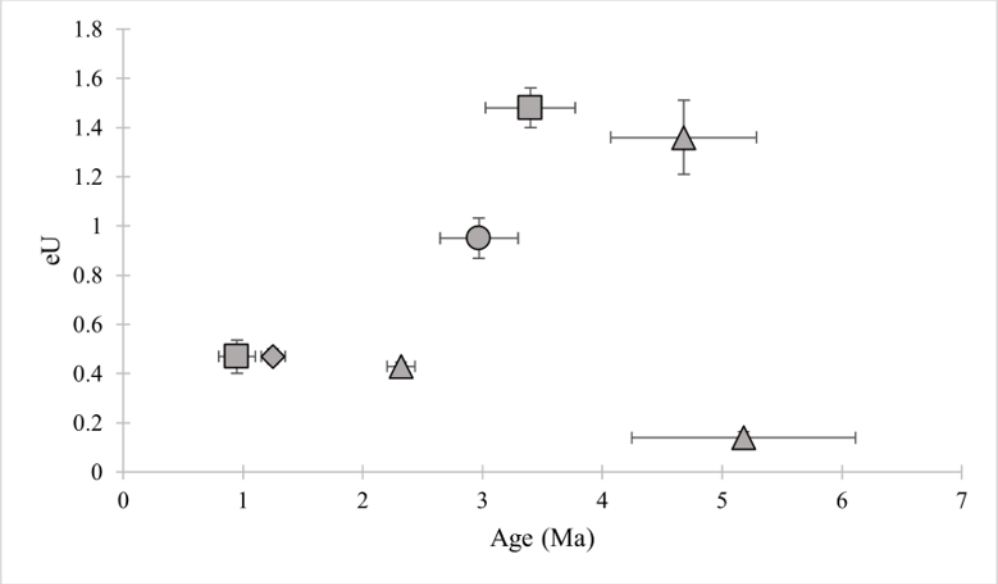

Figure 4.12: Age versus eU and mineralogy plot. Triangle = goethite; circle = hematite/magnetite mix; square = hematite/goethite mix; rhombus = hematite.

4.6.2 Implications for the climate and uplift history of the smCAP

4.6.2.1 Uplift history

The earliest supergene mineralization is recorded by goethite from the Elmadegbeli deposit, the highest altitude sample (2002 m), which formed at 5.18 Ma. The latest supergene phase is S4 (0.95 Ma), the lower sample from the Elmadegbeli mine (1994 m). The lowest altitude sample from the Attepe mine (S1; 1796 m) is younger than S8 from the Magarabeli mine despite it being from more than 200 m higher elevation. It is likely that the water table was locally variable, and that faulting post-formation of the supergene profiles has changed the elevation of the weathering profiles relative to each other. For instance, the Ecemis Fault Zone that runs NE-SW through the smCAP has experienced ~60 km of sinistral displacement (Jaffey and Robertson, 2001). The Ecemis Fault Zone is a present-day seismic hazard and is one of Turkey's most prominent fault zones (Yıldırım et al., 2016). Movement on the Civizlik Fault, ~60 km WSW of the Attepe iron deposits, has caused 13 m of vertical offset in moraine and talus fan surfaces in the last 22 ka, while the adjacent Kartal Fault records 120 m of vertical offset in the past 104 ka (Yıldırım et al., 2016).

The earliest He age recorded in this study (5.18 ± 0.95 Ma) are consistent with Late Miocene pollen records for the Kersihir-Kizilok region, 200 km northwest of the study area, that reveal climate conditions were conducive for supergene Fe-O enrichment; mean annual temperature

of 17°C and precipitation of 1045 mm (Kayseri-Özer, 2017). The persistence of similar climate regime into the early Pliocene has been documented across Central and Eastern Anatolia (Kayseri-Özer 2017). Evidence of earlier supergene Fe-O mineralisation in the region awaits a more detailed investigation.

The Attepe iron deposits lie on the northern edge of the smCAP. It is likely that they were already at significant elevation by the late Miocene (Schildgen et al., 2012; Cosentino et al., 2012; Schildgen et al., 2014; Radeff, 2014) with an emergent orographic barrier in proximity (Lüdecke et al., 2013; Meijers et al., 2016; Meijers et al., 2018). For instance, the early Miocene Dikme basin, approximately 15 km to the northwest of the Attepe district, has been above sea level since 14 Ma (Ocakoğlu, 2002) and was likely at ~1.8 km elevation by 5 Ma (Meijers et al., 2018). Uplift relative to base level would have caused drainage reorganisation (Jaffey and Robertson 2005; Meijers et al., 2020) and driven the generation of weathering profiles if local water table reduced relative to land surface so long as the climate was conducive to supergene enrichment.

The Fe-O age data are difficult to reconcile with the model of rapid rock uplift resulting in the Attepe region reaching its current elevation in the past 500 ka (Öğretmen et al. 2018; Racano et al. 2020). This would have generated significantly younger He ages as the absence of an orographic barrier until 500 ka would have allowed hot-humid climate to have persisted across the region, resulting in continued precipitation of supergene minerals into the middle Pleistocene. The youngest ages of 1.25 ± 0.10 Ma and 0.95 ± 0.15 Ma do not reflect this.

In the three mines where two samples were analysed (Elmadegbeli, Attepe, and Magarabeli) there is a systematic age increase with elevation (Table 4.2). Such age-depth relationships are typical of supergene profiles and are widely held to reflect the downward migration of a weathering front related to lowering of the local water table (e.g. Vasconcelos 1999; Cooper et al. 2016; Deng et al. 2017). In a climate conducive to supergene enrichment, rock uplift and consequent river channel incision lower the water table, resulting in mineral precipitation ages that decrease with depth in a weathering profile (e.g. Deng et al. 2017). The elevation-age relationships at Attepe and Elmadagbeli mines record average incision rates of induced lowering of the water table relative to the land surface of 12.3 and 6.4 m/Myr between 5 and 1 Ma and 2.2 and 4.8 Ma respectively. Such low incision/rock uplift rates are broadly consistent with the low rate determined for the CAP on the basis of river incision over the last few Myrs (Doğan, 2011) and supports the prevailing view that the Eastern Taurides must have been at or

close to current elevation prior to 5 Ma. The preservation of the thin carapace of weathered rock on the Attepe deposits is difficult to reconcile with the majority of the 1-2 km of uplift required for the current elevation to have occurred in the last million years.

4.6.2.2 Climate history

The youngest supergene He ages (1.25 ± 0.10 Ma and 0.95 ± 0.15 Ma) from samples from near the base of the Karacat and Elmadagbeli mines record the latest supergene enrichment. They require that hot-humid climatic conditions across the region persisted into the Middle Pleistocene and imply that the current cooler and drier climate regime was established sometime in the last million years or so. This contrasts starkly with the prevailing view which considers that the onset of aridification across the CAP began by the middle Pliocene due to uplift and reorganisation of drainage (Meijers et al., 2020). It is, however, consistent with $\delta^{13}C$ and fauna data from pedogenic carbonates and calcretes in the Cal Basin which record a shift from Pliocene sub-humid to Pleistocene arid climate (Alçiçek and Alçiçek, 2014). Soil stratigraphy and the occurrence of palygorskite and kaolinite in the Adana basin, ~150 km south of Attepe, indicate that the wet to dry climate transition occurred during the Pleistocene (Kapur et al., 1993). Further study revealed mean annual temperatures in the northern portion of the Adana basin to be 21-23°C with the presence of palygorskite and tree, shrub, and grass vegetation suggesting a semi-arid climate between 782 and 250 ka (Kaplan et al., 2013). Using calcrete formations, Eren et al. (2008) propose that semi-arid climate was established in the northern Adana Basin between 782 ka and 250 ka. They suggest a mean annual temperature of ~18°C and mean annual precipitation of <300 mm/yr; similar in temperature yet more arid than that of today in that region (>600 mm/yr) (Eren et al., 2008). Alluvial fan deposits in the high elevation (>2 km) Ecemis River drainage area, ~60 km to the west of the Attepe region, record major climate shifts between cooler glacial periods and warmer interglacial/interstadial conditions from ~136 ka until the Pleistocene-Holocene transition (Sarıkaya et al., 2015).

Continuous long-term terrestrial climate records of Eastern Mediterranean and Western Asia are sparse. By interpreting European Cenozoic cool-temperature tree flora, Svenning (2003) showed that the vegetation widespread today are those most tolerant of a cold growing season whilst those in the Mediterranean region are cold-sensitive but relatively drought resistant. The 1.35 Ma Tenaghi Phillippon pollen record in northeast Greece records a major shift towards

greater aridity during interglacial periods at ~650 ka (Tzedakis et al., 2006). They suggest that continental vegetation change was independent of high-latitude glacial-interglacial marine and ice sheet records and that changes may have been a direct result of a climate change (Tzedakis et al., 2006).

Lake Van sits to the north of the orographic barrier created by the Bitlis Massif at >1600 m asl in the Eastern Anatolian high plateau region (Litt et al., 2014). The pollen record of the interglacial periods over the last 600 ka record an increase in abundance of pine (more cold-resistant) over oak (thermophilous) species. Like the Tenaghi Phillippon pollen record, the Lake Van record does not coincide perfectly with global marine and ice sheet climate records, particularly around the mid-Brunhes event (~430 ka) and marine isotope excursion 7 (250 ka), thus suggesting that obliquity/eccentricity/processional climate mechanisms may cause different responses within continental interiors (Litt et al., 2014). However, a general cooling and aridification trend is recognised, broadly consistent with global climate data in the past million year (Zachos et al., 2001; Lisiecki and Raymo, 2005).

4.7 Conclusions

Fe-oxide/oxy-hydroxides from the weathering profile of the Attepe iron deposits in the Eastern Taurides in southern Turkey yield He loss-corrected (U-Th)/He ages of between 5.18 and 0.95 Ma. In the three mines where two samples were analysed, He ages decrease with elevation, typical of a lowering water table. This is consistent with river incision and rock uplift rates of between 12.3 to 6.4 m/Myr between 5 and 1 Ma across the region. This suggests that the region was already at or close to its current elevation by the late Miocene and not a product of rapid uplift in the last 500 Ka. Uplift/incision rates are closer to climate-induced uplift/incision recorded within the CAP over the past 2 Ma. The presence of supergene iron oxide/oxy-hydroxides throughout the ore deposits of the Attepe region suggest that the Plio-Pleistocene climate at the time was hotter and more humid than today. The latest goethite precipitation age (0.95 Ma) constrains the onset of aridification across the region to sometime in the last million years. The clear evidence for regional and global cooling implies that changing climate rather than surface uplift was the main driver of aridification across the Attepe region.

4.8 Background of work undertaken to achieve results in this chapter

Field work and sample selection. Fieldwork for this chapter was carried out by Serdar Keskin at an unknown point in time prior to the beginning of this PhD. I was not involved in any kind of fieldwork. Samples were sent by post with images and geographic data by email shortly after I started the PhD in October of 2017. The sample set was sent as a test of the methods to be developed in the SUERC Thermochronology laboratory as part of my PhD. Serdar Keskin and Prof. Fin Stuart had an established relationship prior to me starting the PhD and had spoken of the potential of this project.

Sample preparation. Initially, multiple weeks (perhaps months) spent separating hematite and goethite from quartz, carbonate phases, and other gangue and sulfide phases to create as pure a separate as possible. This included many days of hand picking and magnetic separation. Many more days were then spent creating hematite powders used for X-ray diffraction and geochronological purposes. Sample weighing procedures were refined from those in Wu et al. (2019) by using a more accurate balance and weighing each sample aliquot multiple times to give an idea of weighing error per aliquot which then fed into error calculations for ages. This was a laborious task and took many days/weeks to complete for all samples (He and Ne).

Gas extraction and purification (Chapter 3: Section 3.3). This method had previously been established for hydrothermal hematite by Wu et al. (2019). Very minor changes to gas holding time in the purification process were experimented with, but the most important aspect of this was in realising when the pressure build-up in the turbo pumps and coldfingers were taking place (likely due to how pervasive the iron oxide-oxyhydroxide powder was throughout the gas line following combustion. Many hours were spent simply pumping the gas line and coldfingers to reduce pressure build-up which then allowed for sensible and reproducible calibrations and acceptable gas levels in cold and hot blanks. The final process for gas extraction and purification is documented in Chapter 3 Section 3.3, though, unfortunately, all the failures are not documented as they were so many and frequent.

Laser combustion procedure (Chapter 3: Section 3.3): Initially, Prof. Stuart believed that the laser combustion process for weathered material (hematite and goethite in this case) would be similar if not the same as that recorded in Wu et al. (2019). However, we quickly realised this would not be the case as we found that we were not able to fully degas or replicate He concentrations in sample aliquots. This is documented briefly in Chapter 3 Section 3.2.3. Experimentation to resolve these issues and achieve repeatable results may have taken around 3 months to fully realise and it is this data that is presented in Chapter 4. Robust recording of these trial-and-error experiments were not taken in any kind of documentable format due to their frequency and at times very short notice nature (having to perform emergency stops on gas analysis and pump all gas to turbo pumps to avoid spending several days baking the gas extraction and purification line hindered meticulous data recording, for example). Further, I was advised that recording this sort of data was not appealing to the reader.

Chemistry procedure (Chapter 3: Section 3.5): Minor changes to the chemistry procedure were developed from those in Wu et al. (2019) such as adding cleaning steps. Realising that the higher than expected blanks were the product of remnant residues in beakers and columns took a while to realise, but once realised was not too difficult to rectify (perhaps a week to run through an entire column chemistry process for a trial sample set to check if the adjustments worked, for example). One unforeseen time sapping event was that when carrying out heating of beakers, both containing samples and for cleaning purposed, an electrical failure or overheating of the hot plate, or overly close spacing of beakers, resulted in the complete melting of beakers which in turn lead to the loss of sample material and having to repeat weeks' worth of work from sample preparation right through the entire chemistry procedure. Fortunately, chemistry for all samples, including Ne material in Chapter 5 was completed in the final week of the pre-Covid era just as UK Government was announcing the first lockdown in March 2020.

All raw data should be stored in instrument software and associated spreadsheets in the Thermochronology Laboratory, SUERC, East Kilbride. If anyone would like this data, please contact Prof. Fin Stuart.

5.0 Constraining the paragenesis and timing of ore mineralisation at Leadhills-Wanlockhead Orefield

5.1 Introduction

The reassessment of historic ore deposits using modern methods has led to renewed interest in their worth, either as potential commodities in a changing industrial landscape (Stensgaard et al., 2016) or as data sources in holistic larger scale ore exploration models (Hagemann et al., 2016; Groves et al., 2022). For example, it has led to the assessment of indium potential in southwest England (Andersen et al., 2016), U-Pb dating of cassiterite associated with the Cornubian orefield (Moscati and Neymark, 2020), and the development of environmentally friendly methods of precious metal recovery (Jenkin et al., 2016).

The Leadhills-Wanlockhead orefield (LWO) is an enigmatic hydrothermal epigenetic vein-type Pb-Zn mineralisation in southern Scotland. First records of mining date to the 13th century, though it was most productive during a period of continuous mining from 16th until the mid-19th centuries prior its closure in the late 1950's (Brown, 1925; Gillanders, 1981). At its peak it was Scotland's primary Pb-Zn mine with up to 500,000 tons of Pb and approximately 1 million oz of Ag from galena, 10,000 tons of Zn from sphalerite, and minor Cu from chalcopyrite extracted from over 70 veins (Wilson and Flett, 1921; Brown, 1919; Mackay, 1959; Gillanders, 1981). The LWO is an importance source of alluvial gold (Leake et al., 1998) and is globally recognised for the secondary mineral assemblage being the type locality of ten minerals, including leadhillite, scotlandite and caledonite (Temple, 1954; Gillanders, 1981). However, the absence of datable mineral phases has previously prevented the absolute age determination of base metal mineralisation across the LWO. Consequently, genetic models for base metal mineralisation rarely have clear tectonic context. The development of the (U-Th)/He and (U-Th)/Ne techniques for directly dating base metal mineralisation offers the potential to provide quantitative geochronological constraints on tectonic context where it was once speculative or unknown (Wu et al. 2019; Farley and Flowers, 2012; Yakubovich et al., 2020).

Hercynian (Variscan) magmatism has long been considered the primary driver of hydrothermal ore fluids for the LWO (Temple, 1956). Stable isotopes and fluid compositions suggest that mineralising fluids were driven by heat supplied from deep hydrothermal convection, sulfur and metals sourced from the Lower Palaeozoic basement, and mineralising fluids of a mixed

meteoric source (Anderson et al., 1989; Pattrick and Russell, 1989; Samson and Banks, 1988). However, the tectonic context for the mineralisation is speculative as age constraints are poor. K-Ar dating of fault gouge clays yield an age range of 320 – 265 Ma (Ineson and Mitchell, 1974). Based on comparison of ore fluids to meteoric fluid sources in the geological past Samson and Banks (1988) propose a Dinantian (359.2 to 326.4 Ma) age for ore mineralisation.

In this study I use the identification of a phase of Fe-mineralisation, including hematite, that post-dates (Caledonian) quartz mineralisation and slightly pre-dates the main Pb-Zn mineralisation to re-assess the ore mineral paragenesis. This provides the opportunity to constrain the timing of main base metal mineralisation using newly developed hematite (U-Th)/Ne dating technique.

5.2 Geological setting

5.2.1 Geological background

The Southern Upland Terrane (SUT) covers 10,000 km^2 of southern Scotland and about 6,000 km^2 in the Down–Longford region of Ireland. It is a classic accretionary complex (Stone, 2014). The SUT formed on the Laurentian margin synchronously with the subduction of Iapetus oceanic crust beneath Laurentia during the Caledonian Orogeny, it is characterised by Ordovician and Silurian turbidite successions of greywacke sandstone, siltstone, and mudstone (Stone, 2014). The SUT consists of NE-SW striking, steeply dipping, folded and low-grade diagenetically metamorphosed tracts with distinct detrital mineralogy defining individual formations (Leggett et al. 1979; Kemp and Merriman 2001). The main formations are separated by high angle strike parallel thrust faults with or without associated imbricate zones comprising interbedded black shales, siliceous mudstones, extrusive igneous assemblages, and cherts (Leggett et al. 1979; Stone et al., 2012). The LWO is hosted by Ordovician Portpatrick Formation greywacke and sandstone and Silurian Moffat Shale siltstone, shales and cherts in the northern zone of the SUT (Fig. 5.1)

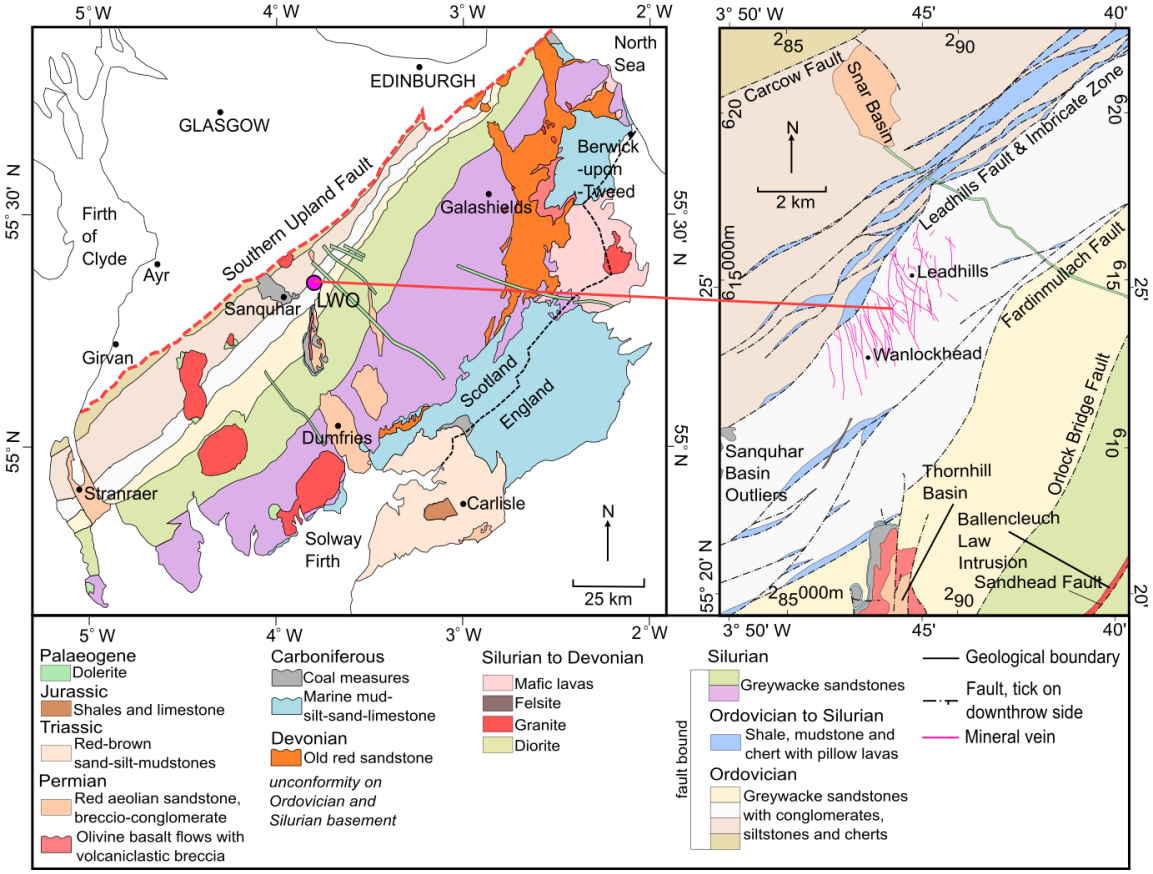

Figure 5.1: Geological map of the Southern Upland Terrane and LWO with ore veins in magenta. Map based on Stone (2014).

Igneous bodies across the SUT range from late Cambrian to Ordovician Ballantrae Complex to Devonian andesitic lavas and Palaeogene dykes (Stone and Rushton, 2018; Stone et al., 2012). Post-tectonic Siluro-Devonian granites, most notably the Loch Doon, Cairnsmore of Carsphairn, Cairnsmore of Fleet, Criffel-Dalbeattie and Tweeddale granites are the most substantial igneous bodies within the SUT, however the latter is based solely on gravity anomaly data (Lowry et al., 2005; Lagios and Hipkin, 1979).

Two late Silurian-Devonian intrusive bodies fringe the LWO area; the Ballencleuch Law granite and the Spango pluton granodiorite ~12 km to the ENE. The Ballencleuch Law granite is a 300 m wide by 2.5 km long body that does not crop out but appears as a boulder field straddling the Sandhead Fault 1 km to the east of Durisdeer (Stone et al., 2012). Several late Silurian-Devonian occasionally pyrite-bearing felsic intrusive bodies (microgranodiorite to granite) crop out adjacent to vein mineralisation and cut the greywacke sandstone, shales, and cherts across the orefield (BGS, 2015). These bodies, locally named ‘felsites’ are mapped to ~2 km in length as narrow dyke-like structures (BGS, 2005). The Spango pluton, a hornblende-biotite-granodiorite ~12 km to the north-west of LWO, is a more extensive body that covers

~10 km^2 (Stone et al., 2012). Tholeiitic quartz-bearing Palaeogene dolerite dykes run NW-SE and cut several Ordo-Silurian greywacke tracts to the north of the orefield with the closest cutting ~1 km to the north of the most north-easterly of the Pb-bearing veins (BGS, 2005).

As Scotland drifted across the equator from south to north, transtensional reactivation of NE-SW Caledonian structures resulted in broadly NW-SE trending Lower Devonian to Triassic basins across the SUT (Leeder, 1988; Anderson et al., 1995; Stone, 2014). To the east of the terrane, Lower Devonian sandstones and conglomerates of the Lanark and Reston Groups unconformably overlie eroded Lower Palaeozoic turbiditic sequences (Stone et al., 2012). Following a brief period of denudation during the Devonian period, Upper Palaeozoic fluviatile and aeolian sediments of the Stratheden Group were deposited unconformably over Silurian strata, with Hutton's unconformity at Siccar Point on the east coast being the world-changing example (Browne et al., 2002). A gradual conformable transition from continental to marine sedimentation is recorded across several basins of the SUT, with limestone and Yoredale cyclothem deposition unconformably overlying Lower Palaeozoic strata (Dean et al., 2011). In Upper Nithsdale and Canonbie the limestone and cyclothem sequences are overlain by productive Carboniferous Coal Measures with terrestrial and shallow marine bands. Upper portions of the Coal Measures record a return to arid terrestrial environments and deep weathering of Coal Measures is noted at Sanquhar and Thornhill basins (Simpson et al., 1936).

The N-S trending normal fault bound Thornhill Basin (~0.5 km by 4 km by 17 km) unconformably overlies vein-hosting Lower Palaeozoic basement ~4 km to the south of the LWO. Lower Carboniferous limestones in the south of the basin are overlain by shallow marine sediments and Westphalian coal measures, although the Thornhill coal measures were not productive due to intense weathering of coal seams (McMillan and Brand, 1995). A switch to compressional tectonics due to fringe effects from the Variscan orogeny then inverted and gently folded the Carboniferous strata forming erosional surfaces (Coward, 1993).

Further transtensional reactivation of Caledonian structures is suggested to have resulted in the NW to N-trending normal fault bound Permian successions in the Thornhill, Moffat, Dumfries, Lochmaben, and Carlisle Basins, the latter extending into the Solway Basin (Anderson et al., 1995). Permian alkali basalts overlain by stream flood breccias and aeolian sandstones unconformably overlie Carboniferous strata in the Thornhill Basin (McMillan and Brand, 1995). The Carlisle Basin records a similar stratigraphy albeit more complete stratigraphy

persisting into the Jurassic (Holliday et al., 2004). The total amount of eroded post-Devonian sediments is difficult to quantify, but the removal of ~1.2 km of material from the Southern Uplands due to thermal uplift during the Cenozoic is suggested (Łuszczak et al. 2018).

5.2.2 Ore mineralisation

The SUT has an abundance of small-scale ore bodies, the majority of which are primarily related to Silurian-Devonian plutonic bodies to the south west of the region as follows: As-Cu-Au at Fore Burn igneous complex on the northern fringe of the Southern Upland Fault (Allen et al., 1982); epigenetic Pb-Zn-Cu veins at Blackcraig, Wood of Cree, Cairnsmore mines and Pibble, and the Ni-As mineralisation at Talnotry are all associated with Cairnsmore of Fleet granite (Wilson and Flett, 1921); Woodhead mine epigenetic Pb (Zn-Cu) and Fe-breccia in Ordovician sandstone associated with Loch Doon pluton thermal aureole (Dawson et al., 1977); up to 8.8 ppm Au in hydrothermally altered breccia of Portpatrick Fm greywacke at Glenhead Burn associated with the southern margin of the Loch Doon granite (Leake et al., 1981); Black Stockarton Moor sub-volcanic complex porphyry Cu-(Mo), chalcopyrite-bornite hydrothermal alteration, with minor Sb-arsenopyrite-Au on the fringes of the Criffel-Dalbeattie granite (Leake et al., 1983; Brown et al., 1979); Auchinleck hematite vein cutting the western margin of the Criffel-Dalbeattie granite and Silurian sandstone of Hawick Group (Stone et al., 2012); Moorbrock Hill epigenetic Pb-Zn-(Cu-Au) east of the Cairnsmore of Carsphairn granite in Kirkcolm Fm sandstones and mudstones (Dawson et al., 1977); Hare Hill Sb-Au associated with a minor granodioritic intrusion near New Cumnock (Shaw et al., 1995); and minor epigenetic vein-type deposits including the Barlocco and Auchencairn Ba veins and Needles Eye U-polymetallic veins within Carboniferous Solway Basin sandstone directly to the south of the Criffel-Dalbeattie granite thermal aureole and North Solway Fault (Parnell et al., 1997). Farther east, ~12 km to the NW of Langholm, stratiform pyrite-arsenopyrite in Silurian greywacke sandstone is overprinted by multiple generations of fracture-controlled sulphide (As-Sb-Pb-Zn-Cu-Fe) veining with gangue calcite, quartz, and barite (Gallagher et al., 1983). Mining at Glendinning was small scale from mid-19th century and is thought to have ceased by 1920 (Gallagher et al., 1983).

Ore mineralisation at LWO occurs as fault-controlled fracture-related veins and breccia fracture-fill, bands, and infilled open spaces in Portpatrick Formation and Moffat Shale (Wilson and Flett, 1921; Temple 1954). Main phase ore mineralisation comprises galena (PbS),

sphalerite (ZnS), and chalcopyrite ($CuFeS_2$) with common gangue minerals as quartz (SiO_2), calcite ($CaCo_3$), barite ($BaSO_4$), pyrite (FeS_2), and (Fe-bearing) dolomite (Ca-Mg-Fe $(CO_3)_2$) which is referred to as ankerite by Temple (1954). Veins have maximum lateral extent of less than 3 km, predominantly trend NW-SE, commonly dip at >60°, range from a few mm to more than 1 m wide, and are constrained to the NW of the district by the NE-SW trending Leadhills Fault and associated imbricate zone of cherts, mudstone, and pillow basalts of Crawford Group and Moffat Shales (Wilson and Flett, 1921, Temple, 1954; Mackay, 1959). Most mine workings were shallow but with the deepest reaching 530 m below the surface (Brown, 1919; Wilson and Flett, 1921). Brown (1919) notes that zoning of the ore mineralisation may have occurred with barite often found near the surface in the New Glencrieff Mine but seldom seen at depth. Wilson and Flett (1921) go on to suggest that galena is most common in the upper levels of the New Glencrieff Mine (120 fathoms (220 m) to 200 fathoms (365 m) below surface) but only sphalerite was found below the 200-fathom level; similar sequences of ore mineralisation described at Brow Vein. Alluvial gold, still panned from nearby streams, is suggested to have four potential sources as follows: Lower Palaeozoic sedimentary rock; igneous origin, potentially Palaeogene basaltic dykes; glacial drift; Permian red-bed and basaltic volcanics along Lower Palaeozoic structures (Leake et al., 1998). A world class suite of secondary minerals, including leadhillite, caledonite, and lanarkite can be found across the LWO (Brown, 1919; Temple, 1954; Gillanders, 1981).

5.3 Previous paragenesis and geochronology

An early massive white quartz veining greywacke is described as the earliest mineralisation (Table 5.1; Temple, 1954). It is most easily recognised in the Pb-Zn veins in breccias and or slickensided on the walls of veins. Shattered remnants of early quartz are veined by ankerite or calcite. Within the massive early veins, Temple (1954) identified pyrite, white mica, albite, gold, and galena although evidence for gold association was not conclusive. However, alluvial gold with associated quartz has been found. The likelihood of quartz + galena veining being an early mineralisation event is debated and thought more likely to be associated with the main sulphide mineralisation event. The inclusion of white mica and albite with early quartz suggests an association with Caledonian-age dykes, and they link this phase to end stages of the Caledonian Orogeny (Temple, 1954).

Temple (1954) describes the main mineralisation as comprising two phases of sulfide mineralisation. The paragenesis of the main mineralisation, according to Temple (1954), occurs as follows: ankerite; galena-sphalerite-chalcopyrite-pyrite; calcite; and barite. This is followed by a replacement of all minerals by quartz and second phase of the earlier main mineralisation. Temple (1954) attributes this second phase main mineralisation to an upward movement of quartz which, as it moved upwards through the deposit and remobilised elements, subsequently reprecipitated a second generation of the original minerals. They state that although the quartz phase may be later, it is likely that the minerals originated simultaneously from a common source.

The encrustation/veining of sulfides on/through ankerite represents the main phase mineralisation for Temple (1954). Pyrite is often disseminated though ankerite. Chalcopyrite replaces ankerite along cleavage planes or forms in open spaces beside euhedral faces of ankerite, with minor occurrences of ankerite inclusions in chalcopyrite. Galena and sphalerite occur either encrusting or veining the ankerite with minor inclusions of ankerite in both sulphides. Gangue minerals generally encrust on ankerite or replace it. Galena and sphalerite are suggested to form in two generations, one earlier and one later than calcite and barite with the second generation devoid of pyrite and chalcopyrite, although two generations of chalcopyrite and pyrite are recorded by Temple (1954).

Table 5.1: Paragenesis from Temple (1954).

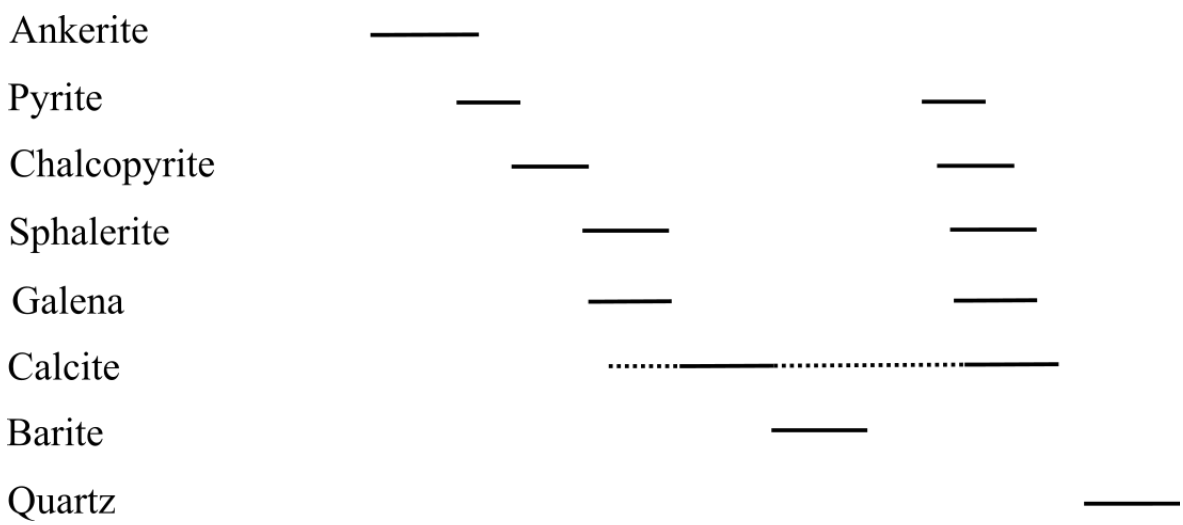

The only absolute age determination relevant to the LWO mineralisation is that from Ineson and Mitchell (1974). They suggest ore phase mineralisation occurred between 320 and 265 Ma based on K-Ar dating of fault gouge clays. This fit with Samson and Banks' (1988) interpretation of brines as Dinantian in age based on their similarity to meteoric fluids typical of that period. Anderson et al (1989) do not contest the Lower Carboniferous age previously reported, though Pattrick and Russell (1989) infer that LWO may have formed as a result of the extensional tectonic regime during that Carboniferous epoch.

5.4 Revised Paragenesis

5.4.1 samples and results

Temple (1954) notes the hematite-stained landscape of Whyte's Cleuch and East Stayvoyage as distinct features of the area. They acknowledged the presence of hematite at multiple sites as follows: scars of Glenkip Head (uncertain links to Susanna Vein); hematite staining on West Stayvoyage Vein surface dump, Cove Vein, and East Stayvoyage Vein; hematite staining of quartz and calcite and outcrop of hematite-stained brecciated greywacke at March Vein; vein rich in barite and hematite associated with Shieling Burn Vein; and common hematite at Lees Vein. Temple (1954) considers hematite as a secondary mineral and does not include it in any paragenesis in relation to main mineralisation.

With the development of hematite (U-Th)/Ne dating, an opportunity to suggest a relative timing for main base metal mineralisation at LWO was realised by my supervisors and I. Several visits to the mine dumps of the LWO were undertaken between 2016 and 2020 to collect samples with both hematite and sulfides present. Samples were cut, polished, and scanned at University of Glasgow's School of Geographical and Earth Sciences. Vein cross-cutting relationships and textures were assessed at hand-sample scale under binocular and scanning electron microscope (SEM) to provide a re-evaluated mineral paragenesis relative to Temple (1954). It is worth noting that this re-evaluation was not intended to overhaul the work of Temple (1954) but rather to place hematite relative to base metals. I am aware that the paragenesis study is lacking in detailed petrographic investigation and that looking only at hand samples and sample fragments is not the ideal method for assessing such detail. Unfortunately, thin sections were not made for these samples.

Access to underground workings across the LWO is limited to the Lochnell Vein for tourism use only, but material is widely available from mine dumps strewn across land surface with correlation to worked veins possible using maps of worked veins (Wilson and Flett, 1921; Gillanders, 1981). For revised paragenesis, the occurrence of Fe-mineralisation and sulphides in the same sample was necessary which has led to an apparent bias as Fe-mineralisation was discovered to be geographically restricted to the west of the orefield at New Glencrieff, Whyte's Cleuch, and Glengonnar Veins (Fig 5.2). Mineralisation has been split in to early, main, and late phase (Table 5.2).

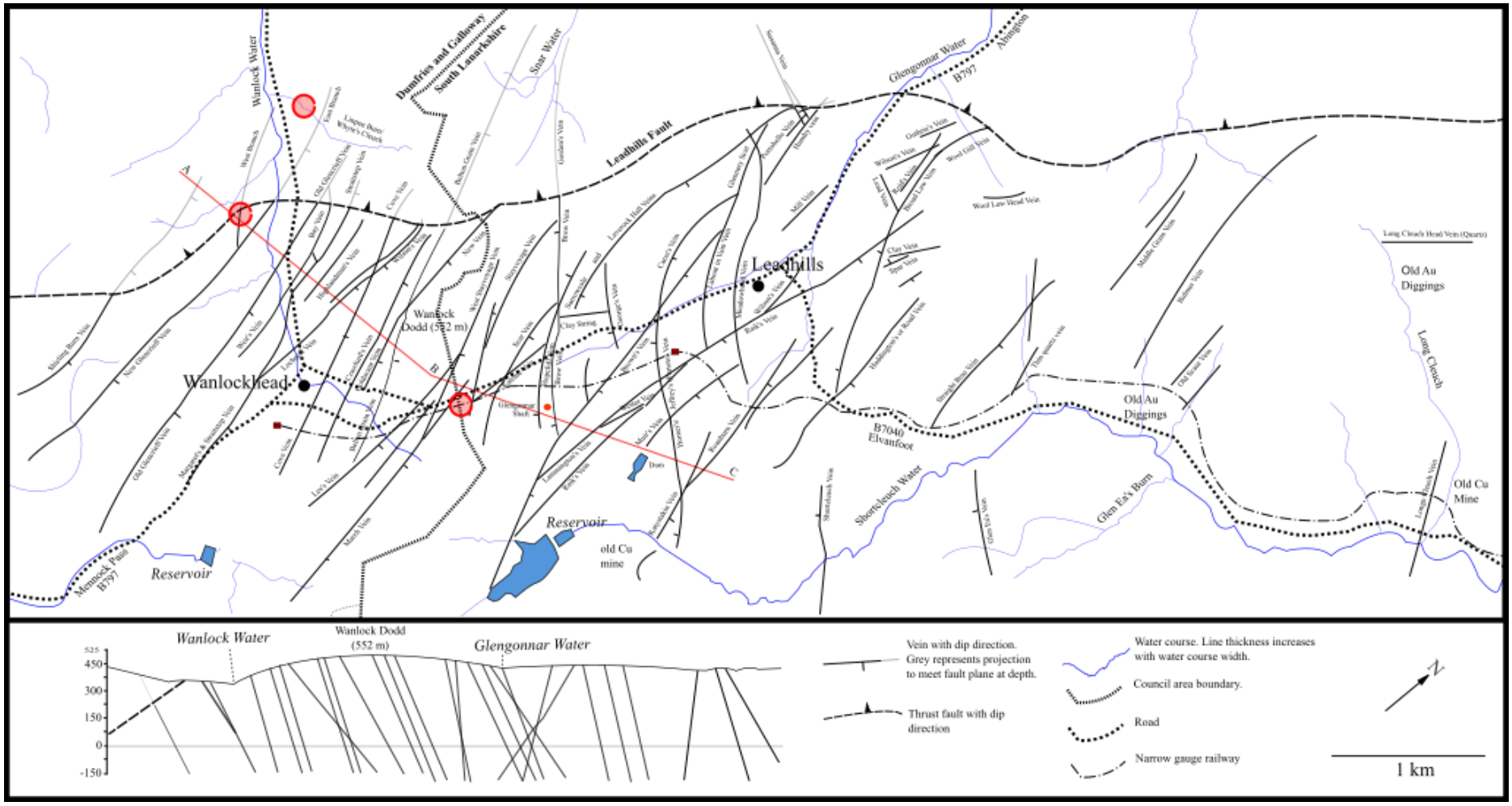

Figure 5.2: Veins recorded at the Leadhills-Wanlockhead orefield. Red circles indicate where hematite-bearing samples were collected. Map derived from combination of that in Wilson and Flett (1921) and Gillanders (1981) with cross-section from Wilson and Flett (1921).

Of the early phase, quartz veining throughout the greywacke basement is the earliest. This was described by Temple (1954) to be of Caledonian age and associated with pyrite, white mica, albite, gold, and galena. Here, quartz is barren and clear with no associated minerals at hand specimen level (Figs. 5.3, 5.11, 5.14). No absolute geochronology has been attempted on this phase of ore mineralisation at LWO.

Crosscutting early quartz, and Fe-carbonate, calcite, quartz, and hematite mineralisation is recognised either with pyrite or with a pyrite overprint. This mineralisation, especially hematite, is geographically restricted to the west of the LWO and is concentrated in the New Glencrieff, Whytes Cleuch, Hopeful, and Glengonnar mine dump areas (Figs. 5.4-5, 5.10-11, 5.15). This geographical restriction on a larger scale and was realised when searching for hematite mineralisation in spoil heaps across the entire orefield on foot on multiple occasions during the summer of 2020 and from discussions with staff at the Lead Mining Museum in Wanlockhead. Fe-carbonate typically takes colloform banded texture and can grades into pure hematite in veins no more than 20 mm width (Figs. 5.4-5, 5.8-15). Temple (1954) describes Fe-carbonate as ankerite, but caution is used here as ankerite is a specific carbonate, whereas the Fe-carbonate here seems variable and more of an encompassing term for iron-dolomitic mineralisation. Botryoidal hematite coated basement and early quartz clasts in brecciated material is common with younging direction of hematite growth outward from clasts (Figs. 5.8-11, 5.14). Calcite alongside colloform banded Fe-carbonate is evident (Fig. 5.9). Cubic pyrite within Fe-carbonate, as overprint, or as open space infill with rafted Fe-carbonate is common (Figs. 5.4-5, 5.8, 5.13).

Main phase mineralisation in this sample set is primarily calcite, dolomite, and galena in veins a few mm to 10s of mm in width. They are geographically widespread across the LWO. This mineralisation is seen to cut earlier quartz and Fe-mineralisations (Figs. 5.4-5, 5.7-12, 5.14). Massive cubic to spongy galena with calcite as open space filling is common and tends to form on the younger side of colloform banded Fe-carbonate and hematite when found in the same samples (Fig. 5.12). Sphalerite and chalcopyrite were the other ore minerals mined at LWO but are less common than galena on mine dumps. At New Glencrieff for example, sphalerite is found in bands sandwiched between dolomitic mineralisation (Fig. 5.6) but can be seen alongside chalcopyrite within calcite in open spaces (Fig. 5.8). Chalcopyrite mineralisation alongside galena is common, especially in calcite veining (Figs. 5.4-5, 5.7). This calcite veining is widespread and can contain rafted Fe-mineralisation or fractured basement clasts (Figs. 5.4, 5.8-11, 14). Galena, sphalerite, and chalcopyrite are therefore likely cogenetic.

Massive, bladed barite is common across the LWO, but the most abundant barite mineralisation is seen near Hopeful Vein mine dumps to the north of the B797 between the town of Wanlockhead and Leadhills. Barite infill with rafted hematite was identified at New Glencrieff mine (Fig. 5.15). Galena growing on top of and within barite was recognised at Big Wool Gill mine, near Leadhills, thus placing barite in the main mineralisation phase (Fig. 5.16).

To reiterate, hematite is recognised to occur prior to main mineralisation and not as a replacement mineralisation as described by Temple (1954).

Table 5.2: Paragenesis from new suite of samples from the Leadhills-Wanlockhead ore field. Hematite prior to base metal mineralisation. This is based on the 20 samples described in this chapter.

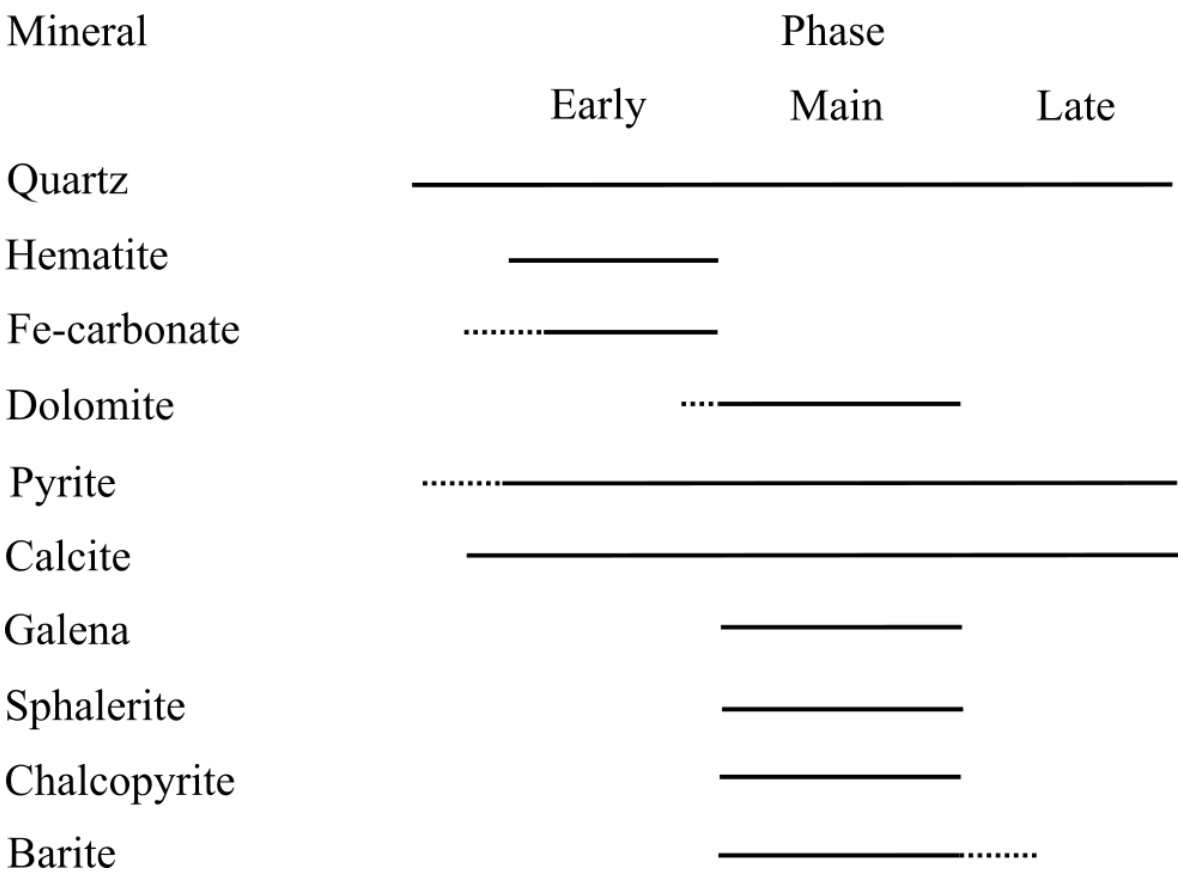

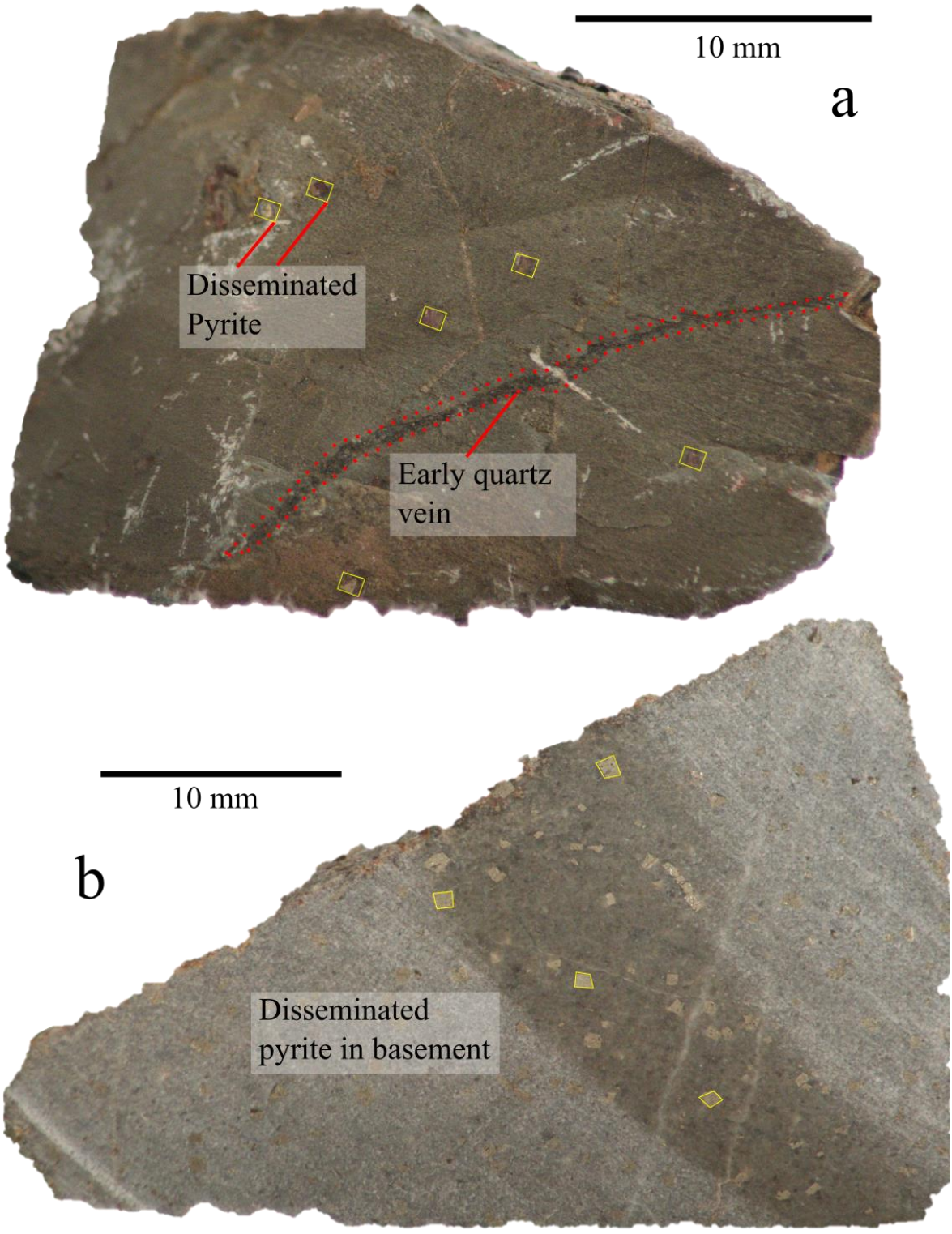

Figure 5.3: a) Sample NGP1A from New Glencrieff mine showing mudstone basement lithology with disseminated pyrite cut by early barren quartz vein. b) Greywacke with disseminated pyrite throughout from New Glencrieff mine.

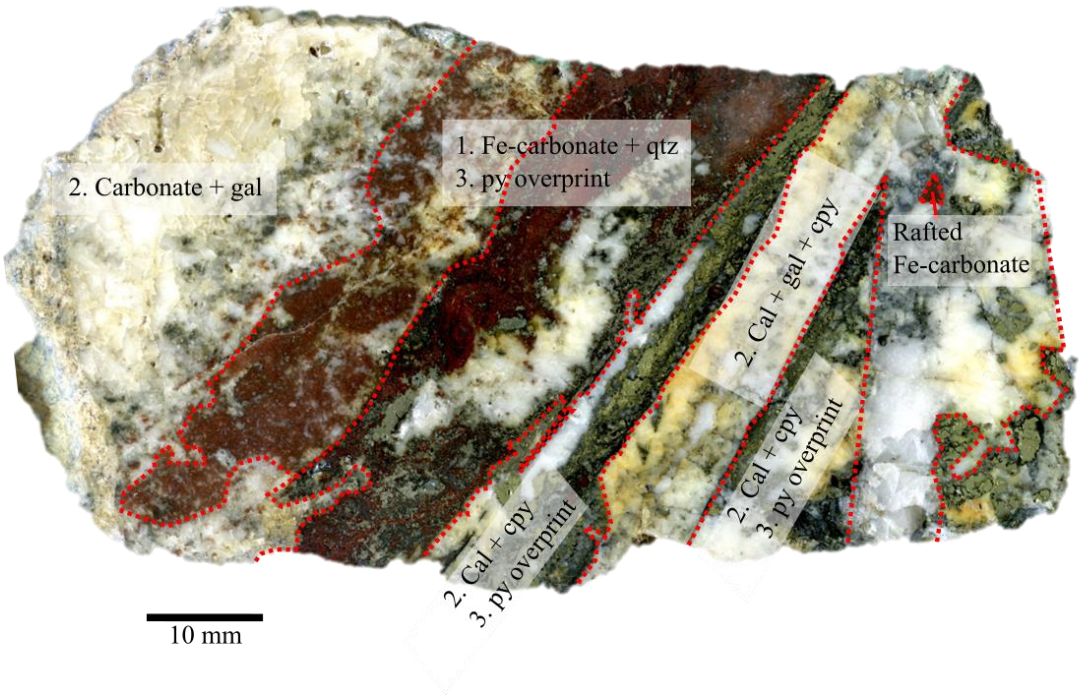

Figure 5.4: Scan of NG2, New Glencrieff mine. Earlier Fe-carbonate with quartz cut by carbonate and galena to the left of the image. On the right-centre of the image, calcite and chalcopyrite cut Fe-carbonate and quartz. To the right, rafted Fe-carbonate within calcite, galena, and chalcopyrite veining. Pyrite overprints Fe-carbonate and the calcite and chalcopyrite mineralisation.

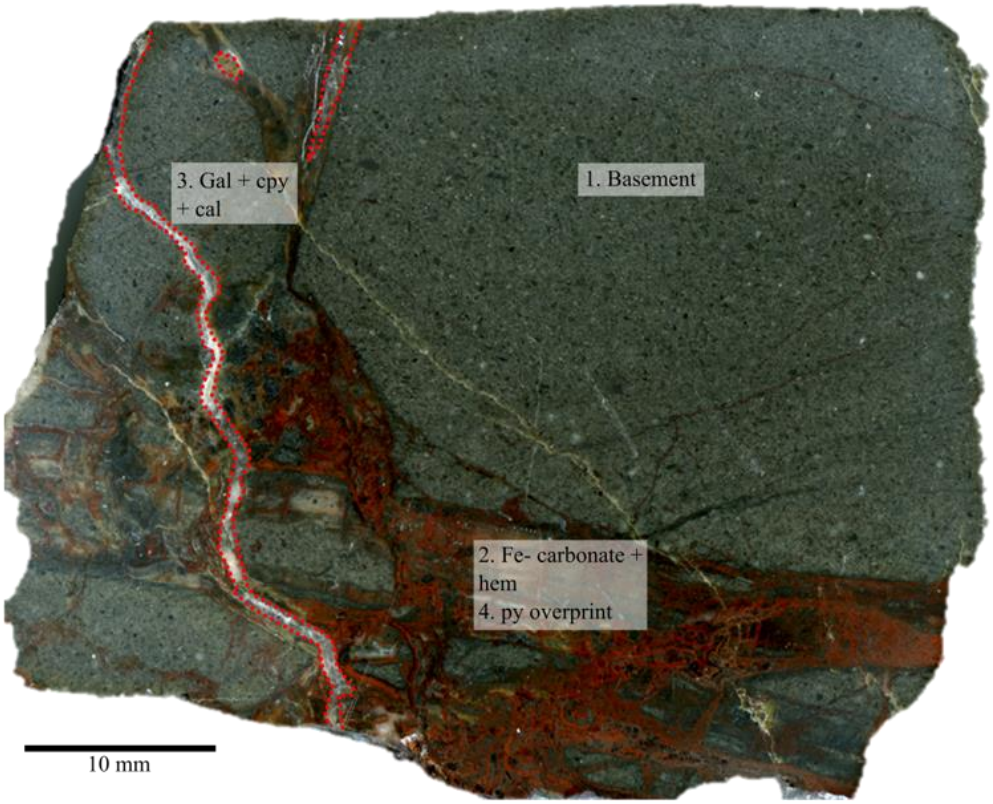

Figure 5.5: Scan of NG5, New Glencrieff mine. Basement cut by Fe-carbonate and hematite subsequently cut by galena, chalcopyrite, and calcite veining. A late pyrite overprint is superimposed on Fe-carbonate and hematite mineralisation.

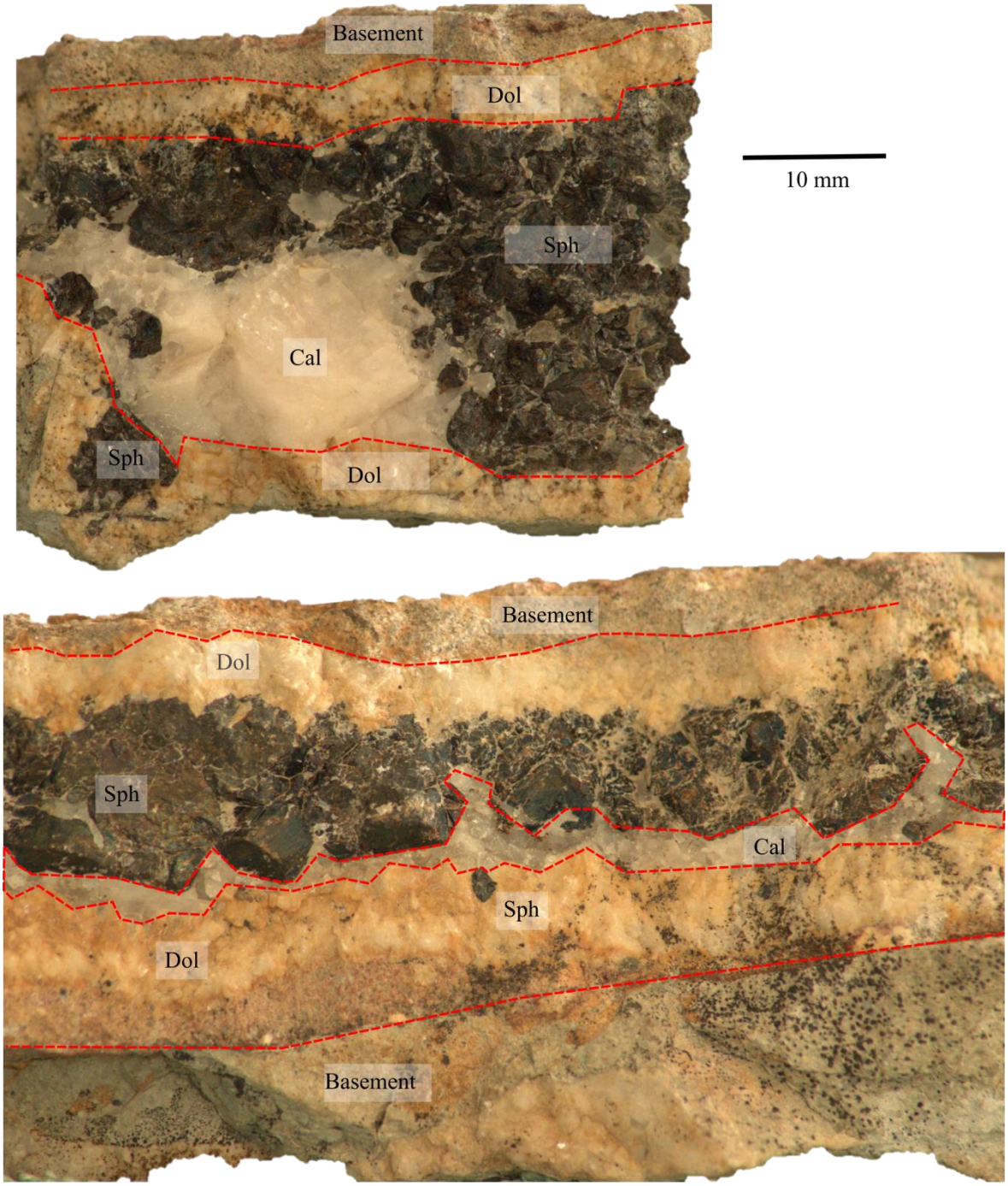

Figure 5.6: Sample NGS1 from New Glencrieff mine. Basement appears leached to a blue-green-grey. Sphalerite is associated with calcite and dolomite either as a band infill or in blebs within dolomite or calcite. Yellow tinge due to artificial lighting. Dolomite is close to white.

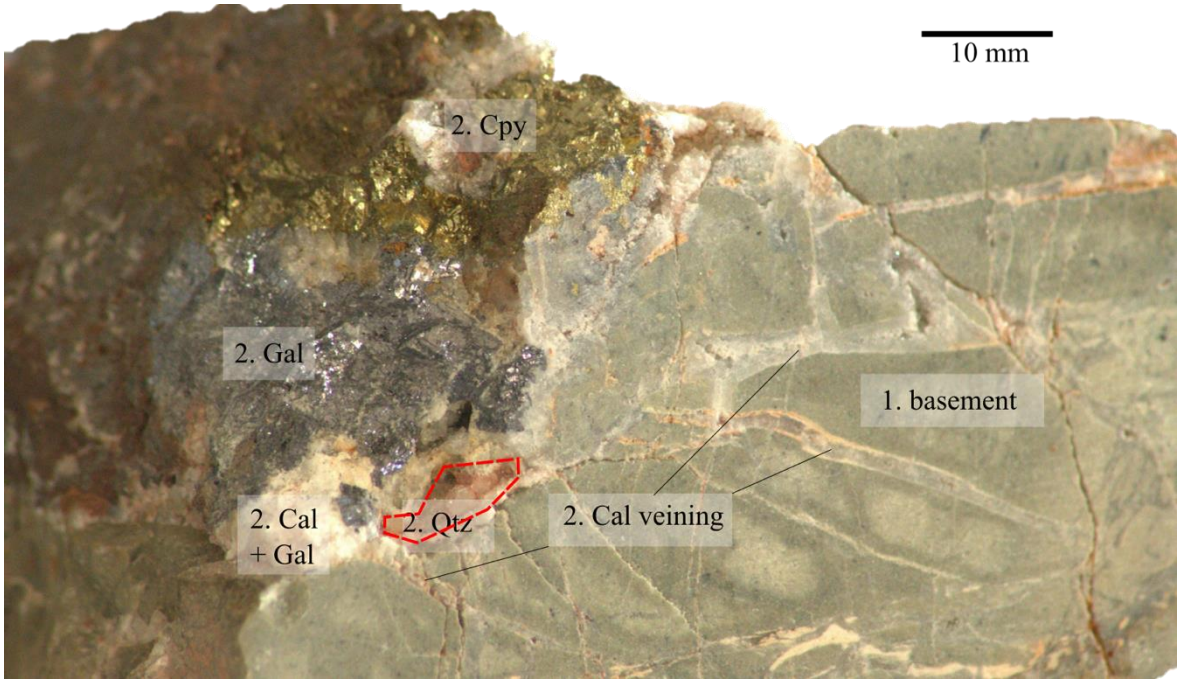

Figure 5.7: Sample NG12 from New Glencrieff mine. Basement graywacke appears leached to blue-green-grey and is cut by calcite veins which merge to form a cavity fill containing galena and chalcopyrite with minor quartz.

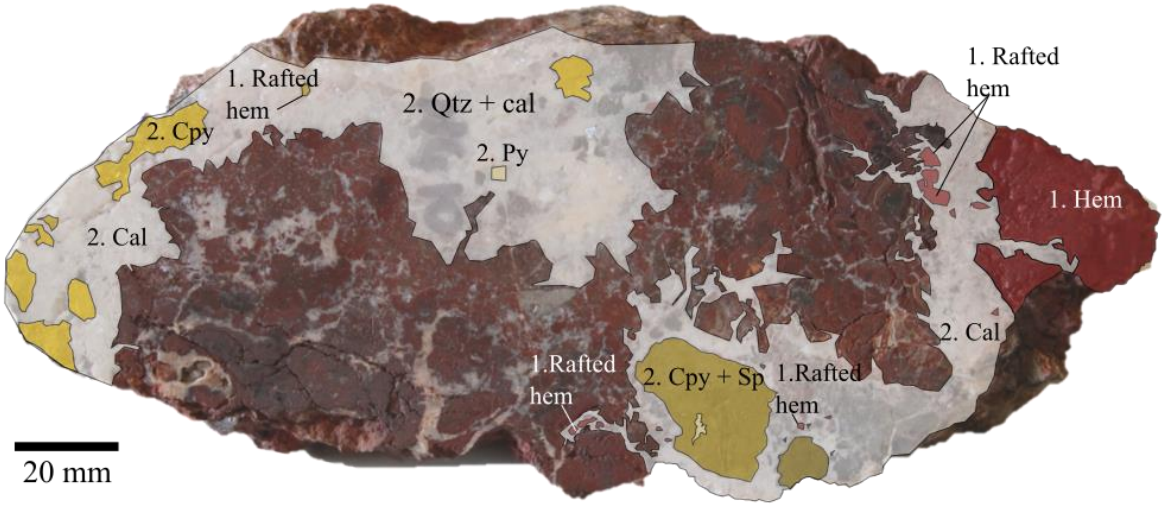

Fig 5.8: Scan of NG10, New Glencrieff mine. Botryoidal hematite cut by calcite with or without chalcopyrite, sphalerite, and pyrite mineralisation. Hematite also rafted in calcite veining in several locations.

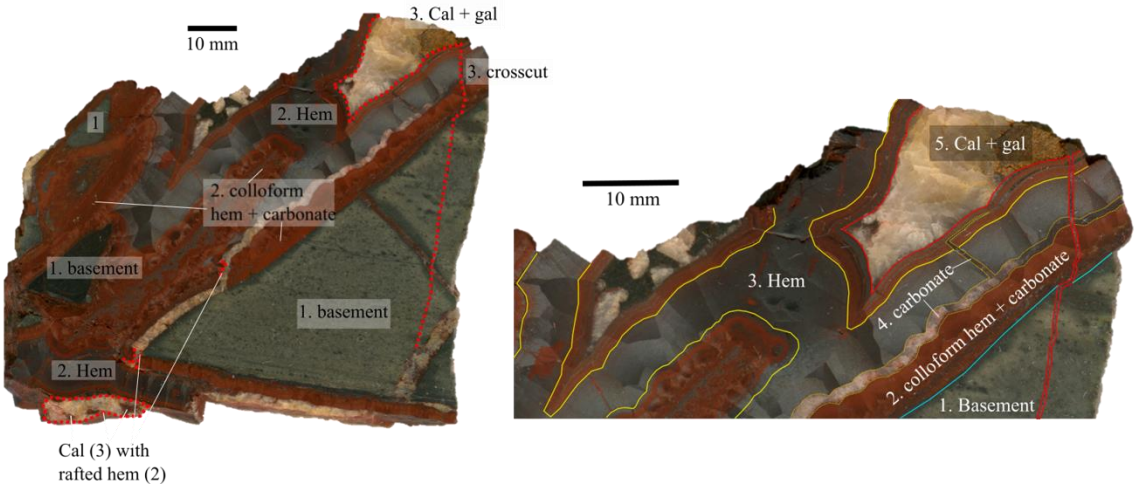

Figure 5.9: Scan of NGEM, New Glencrieff mine. Left image of whole sample of basement cut by hematite and carbonate mineralisation with both cut by later calcite and galena mineralisation. Rafted hematite in later calcite also evident on bottom left of image. Right image is zoom of top right corner of left image. Here, colloform hematite and carbonate are cut by a later carbonate. All, including earliest basement, are cut by a later calcite and galena vein. Fe-carbonate associated with hematite looks to have grown from edge of the basement into open space as fracture fill with Fe-carbonate transitioning to pure hematite in the centre of the mineralisation.

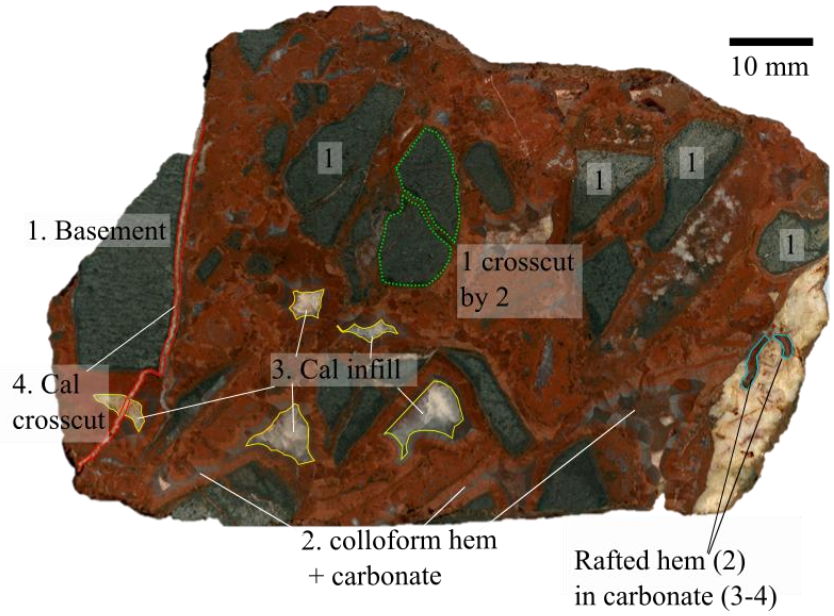

Figure 5.10: Scan of NGLC, New Glencrieff mine. Brecciated basement clasts cut by colloform hematite and carbonate or surrounded by later colloform hematite and carbonate mineralisation which fills open space. Open space filling has created bands with carbonate of the older edges transitioning to pure hematite in the centre of mineralisation. Open spaces have also been filled by calcite, determined to be younger than the hematite and carbonate mineralisation since it occurs exclusively on the younger side of colloform texture associated with hematite and carbonate mineralisation. Rafted hematite sits within later carbonate mineralisation. Latest calcite cuts hematite and carbonate and calcite infill mineralisation.

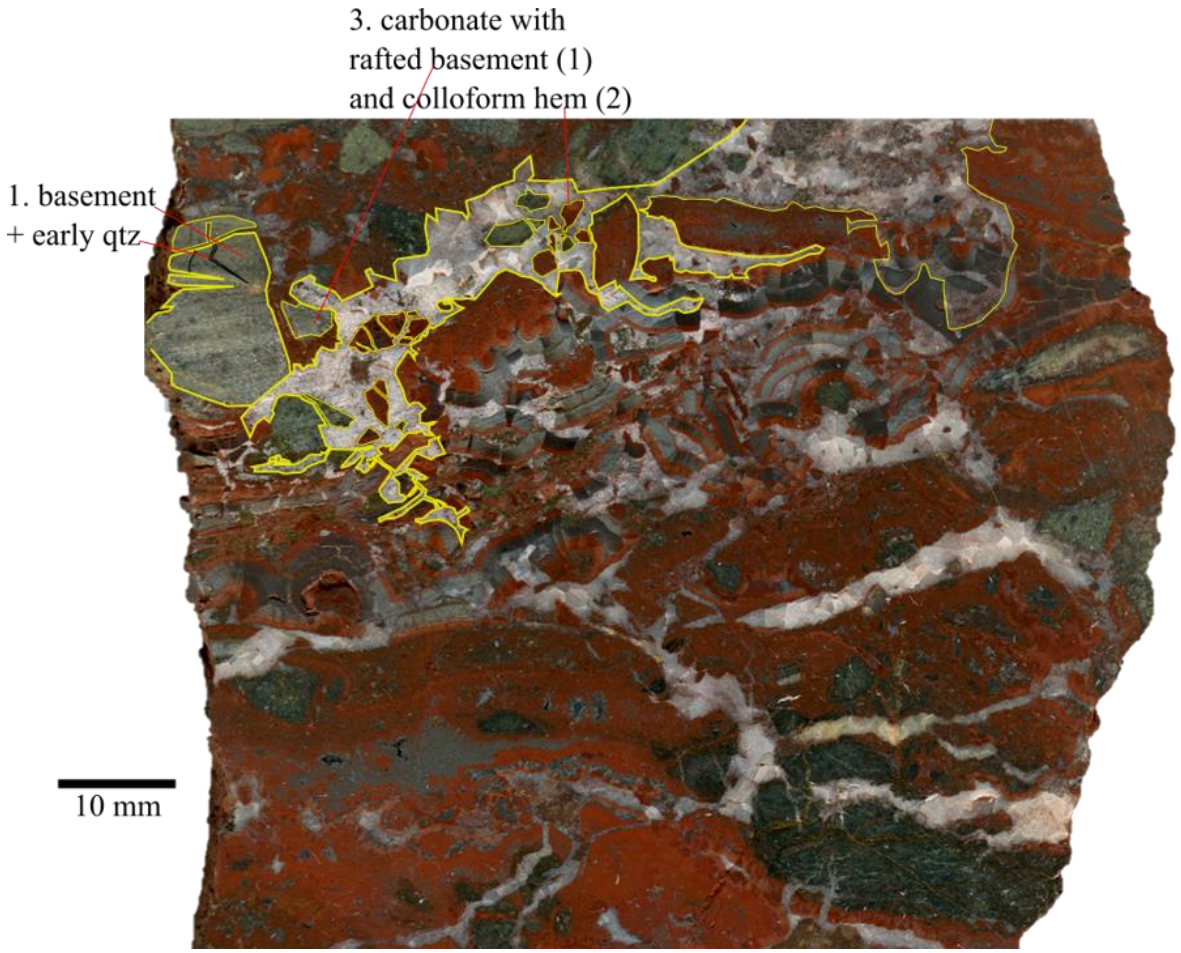

Figure 5.11: Scan of NGLF, New Glencrieff mine. Basement with early quartz cut by carbonate and hematite mineralisation. The later carbonate mineralisation contains fractured remnants of both basement and colloform hematite mineralisation.

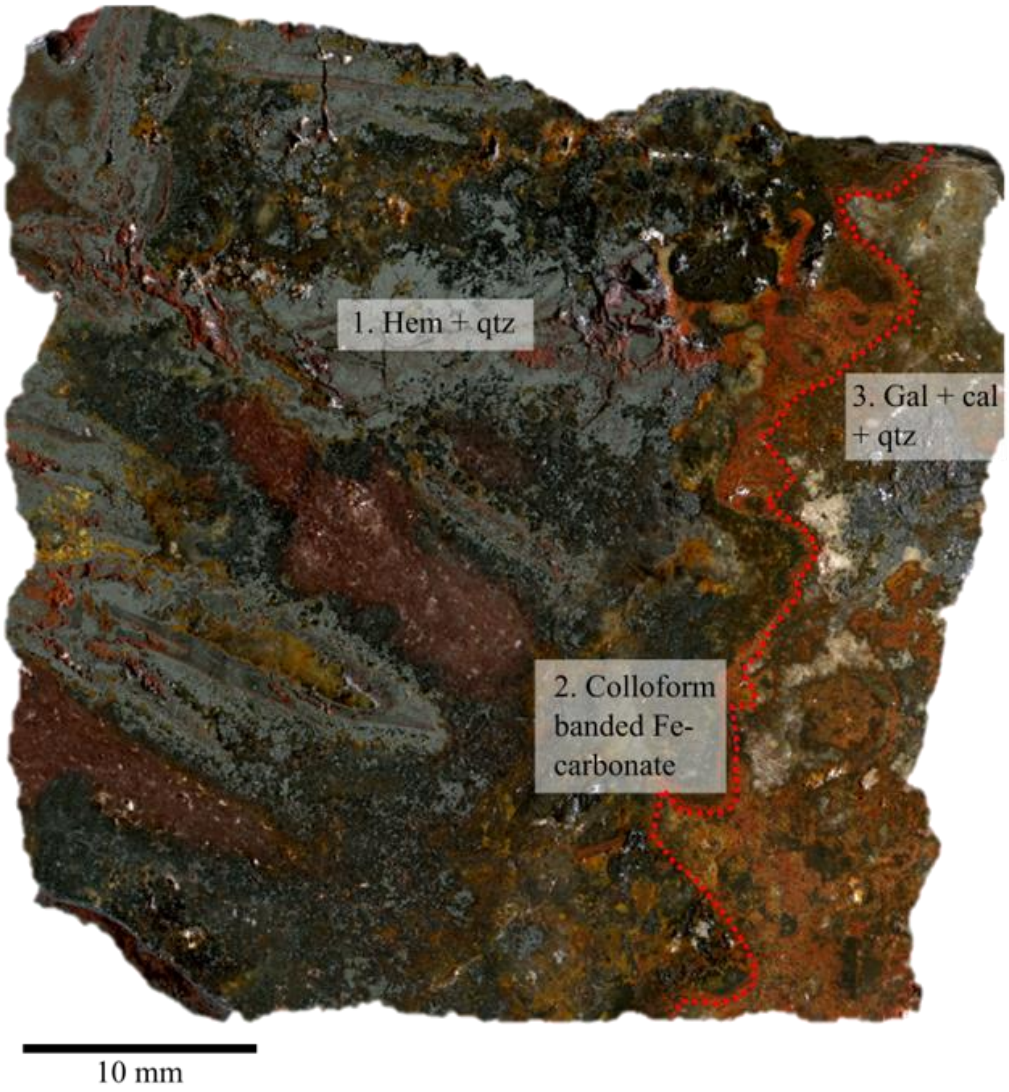

Figure 5.12: Scan of WC1, Whytes Cleuch. Colloform banded Fe-carbonate running down right side of image with hematite and quartz mineralisation on younger side and galena, calcite, quartz mineralisation on younger side.

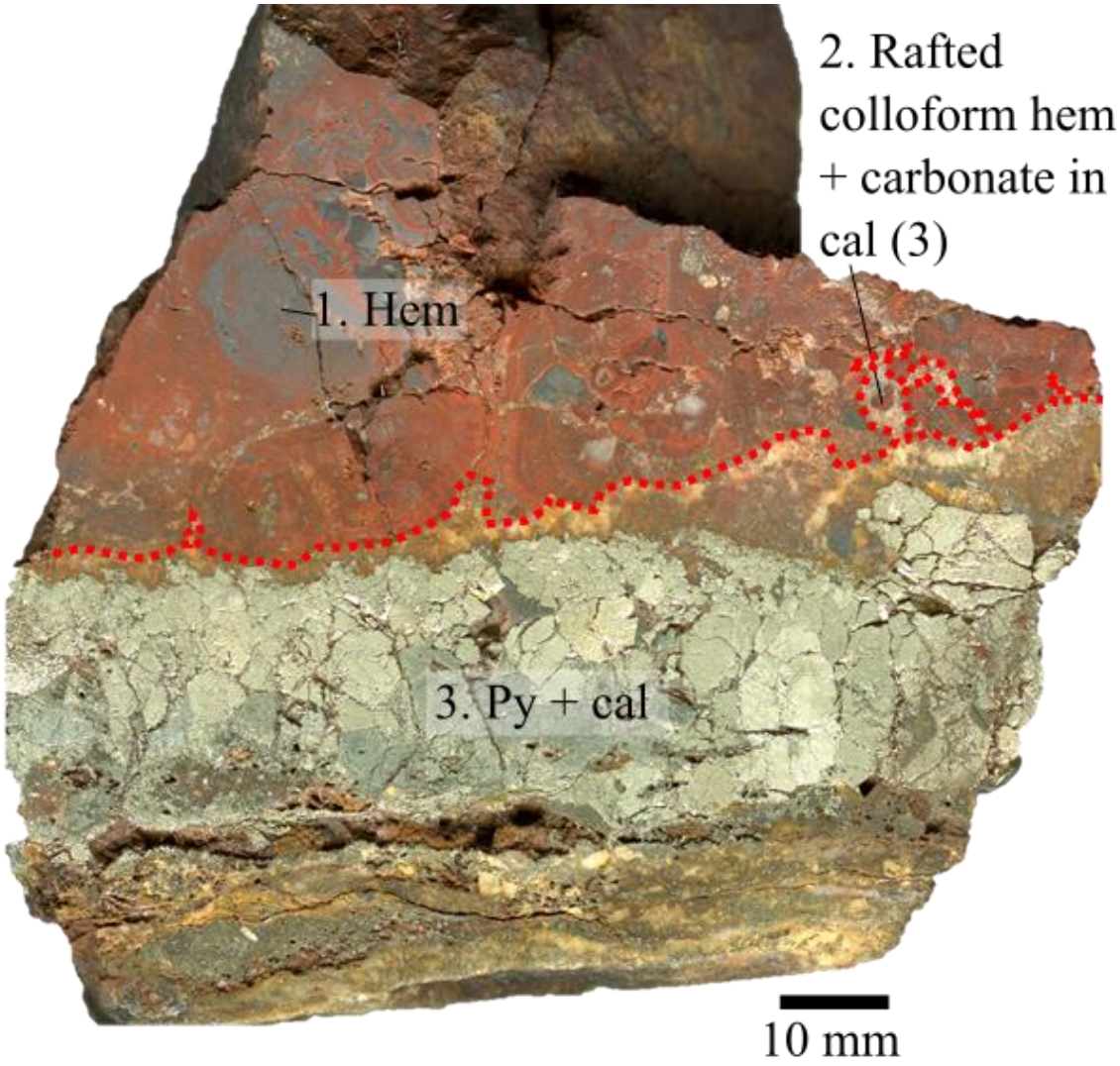

Figure 5.13: Scan of WCL1, Whytes Cleuch. Massive pyrite mineralisation with associated calcite veining. Calcite veining intrudes hematite mineralisation and also hosts rafted colloform hematite and carbonate mineralisation.

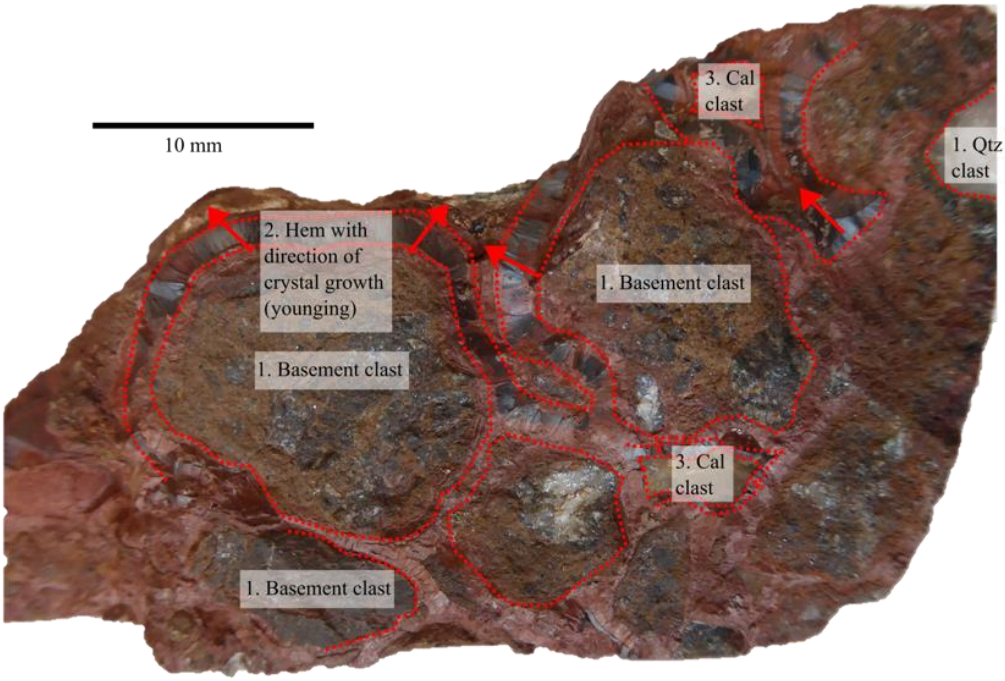

Figure 5.14: Scan of WH1, Glengonnar mine dump area. Basement and early quartz clasts cemented by hematite. Calcite infill on younger side of hematite banding.

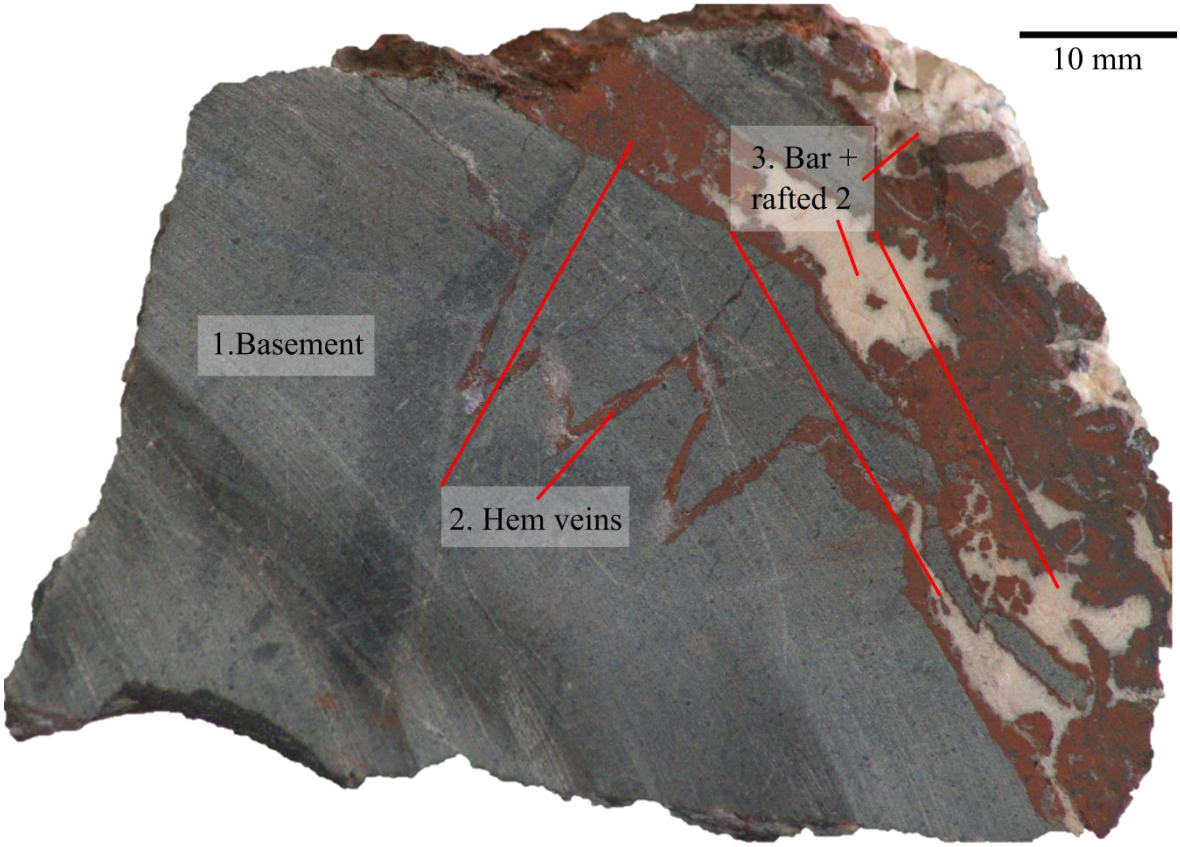

Figure 5.15: Sample NG13 from New Glencrieff mine showing basement cut by hematite veins which are subsequently found rafted in barite infill.

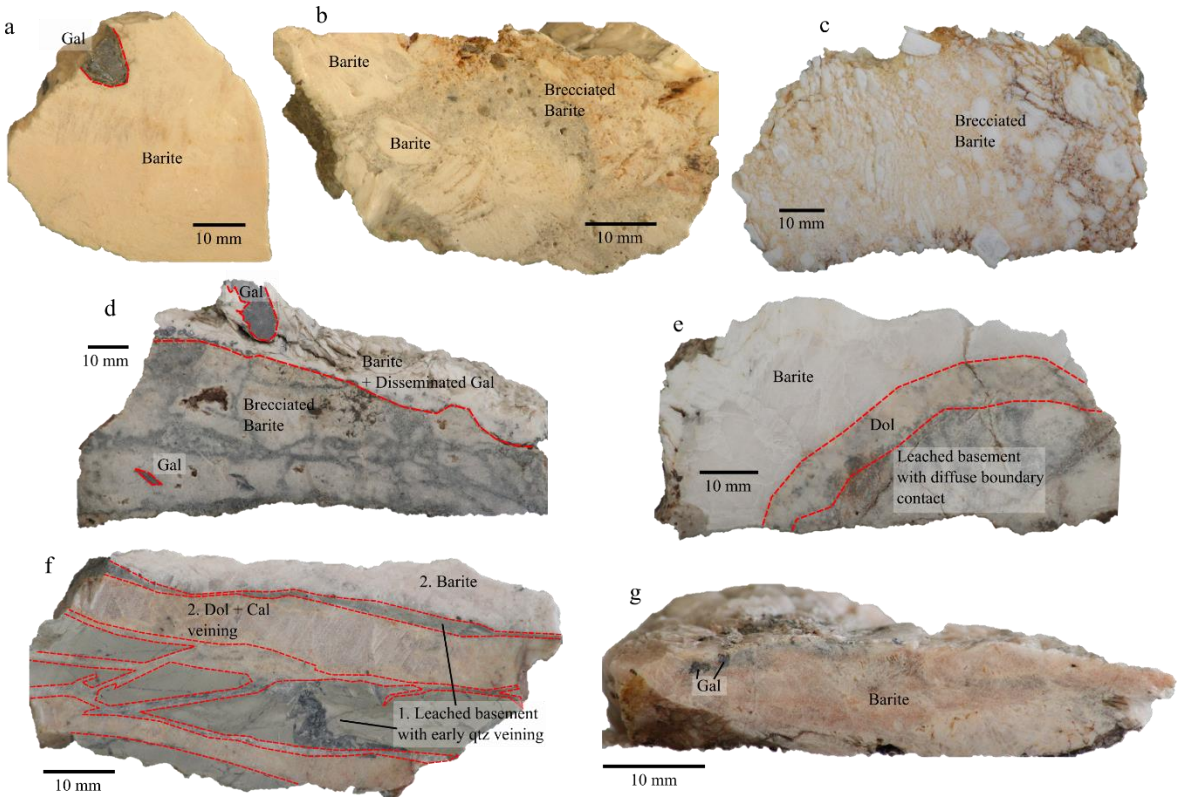

Figure 5.16: Barite samples used for $\delta^{34}S$ study and paragenesis. a) galena (BWGG1A) within barite (BWGB1A) from Big Wool Gill mine. b) BLB1A: brecciated barite from Broad Law mine. c) LMS4B1A: brecciated barite from Lady Manner's Scar mine. d) galena (GGG1A) within barite and brecciated barite (GGB1A) from Glengonnar mine. e) LAHB1A: barite on dolomite on leached basement. f) NGB1A: barite on leached basement with early quartz veining. Basement is cut multiple times by calcite and dolomite veining. g) WCB1A: barite with disseminated galena from Whyte's Cleuch mine dumps.

5.5 Hematite (U-Th)/Ne geochronology

5.5.1 Introduction

Ore deposits are conventionally dated by U-Pb geochronology of various U and Th–bearing accessory minerals related to the ore system (zircon: Valley et al., 2009; apatite and monazite: Neymark et al., 2016; monazite: Rasmussen et al., 2006 for example). Although the U-Pb system is generally accepted and provides otherwise unobtainable data, it is not without its challenges. Valley et al (2009) recognise mineral phases like apatite and titanite can incorporate common Pb (^{204}Pb) in their structure which can affect age determination. From apatite provenance studies, Chew et al. (2011) recognise low U-Th and radiogenic Pb, common Pb, and the lack of U-Th-Pb apatite standard material are distinct challenges for application of

apatite LA-ICPMS geochronology. The presence of multiple generations of datable minerals, dissolution-reprecipitation mechanisms, intergrowths and inclusions can affect apatite dating of ore mineralisation (Neymark et al., 2016). Cherniak et al. (2004) recognised distinct age and/or compositional domains in monazite can be present in samples with fluid recrystallisation histories. Further, not all ore deposits contain these accessory minerals in their paragenesis or wider geological surroundings.

Over the past three decades, Fe-oxide-oxyhydroxide (U-Th)/He/Ne chronometers have become established methods for quantifying the timing of hydrothermal mineralisation (Lippolt et al., 1995; Farley and Flowers, 2012; Farley and McKeon, 2015; Wu et al., 2019); supergene mineralisation and weathering events (Cooper et al., 2016; Deng et al., 2017; Shuster et al., 2005; Heim et al., 2006; Vasconcelos et al., 2013; Monteiro et al., 2014; Danisik et al., 2013; Wells et al., 2019); and fault activity (Ault, 2020 for review). Globally, many ore deposits have potentially dateable hematite mineralisation that is paragenetically associated with at least one phase of economic ore mineralisation. By further advancing geochronological capabilities, better understanding the timing of ore precipitation will place increased certainty into ore exploration models on a global scale, therefore reducing environmental impact.

Six samples of hematite have been dated using (U-Th)/Ne geochronology. They were selected based on their paragenetic relationship which has placed them later than early Caledonian quartz and earlier than the former economic base metal mineralisation. Dating hematite provides the earliest timing of main ore mineralisation at the LWO allowing for tectonic context to be placed on the deposit and a revised ore genesis model to be proposed. Prior to this study, ore phase mineralisation was first suggested to be between 320 and 265 Ma based on K-Ar dating of fault gouge clays (Ineson and Mitchell, 1974). Ore fluid composition was then used to imply a Carboniferous (Dinantian) timing of ore mineralisation (Samson and Banks, 1988).

5.5.2 Samples

The hematite samples selected for dating were collected from three mine dumps: NG 10, NGEM, NGLC, and NGLF from New Glencrieff (55° 24' 3" North, 3° 47' 40" West); WH1 from Glengonnar (55° 24' 19" North, 3° 45' 60" West); and WCL1 from Whyte's Cleuch (55° 24' 14" North, 3° 47' 16" West). Samples with substantial paragenetically well-constrained

hematite mineralisation were rare and were largely confined to the southwest of the LWO, the majority found at the New Glencrieff mine dump.

Hematite primarily occurs as vein fill with botryoidal habit or colloform banding alongside Fe-carbonate/calcite (Fig. 5.17). Small rock chips were imaged using a FEI Quanta 200F environmental scanning electron microscopy (SEM) operated at 20 kV at the ISAAC facility at University of Glasgow (Lee et al., 2014). SEM revealed crystal morphology to be fibrous to micaceous-platy with plates typically < 1 µm wide and < 30 µm along c-axis (Figs. 5.18-23). Crystals tend to flake away from massive hematite when the chip is fractured. Fe-carbonate bands within the hematite bands is common.

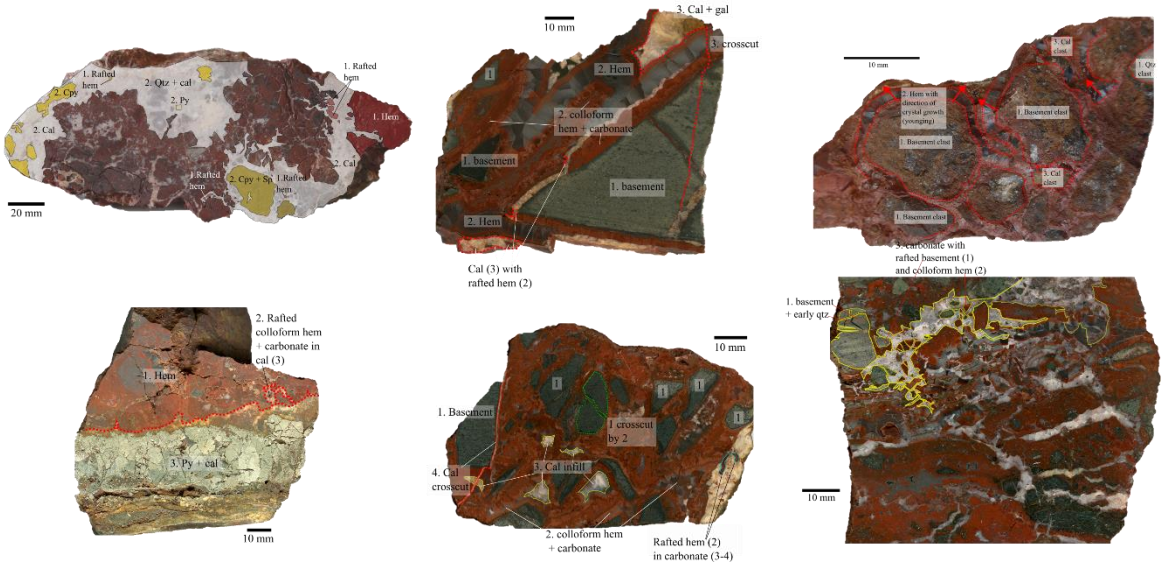

Figure 5.17: Photographs of the six hand samples used for (U-Th)/Ne dating. Top left to bottom right: NG10, NGEM, WH1, WCL1, NGLC, and NGLF. Descriptions of these samples are provided in the paragenesis section.

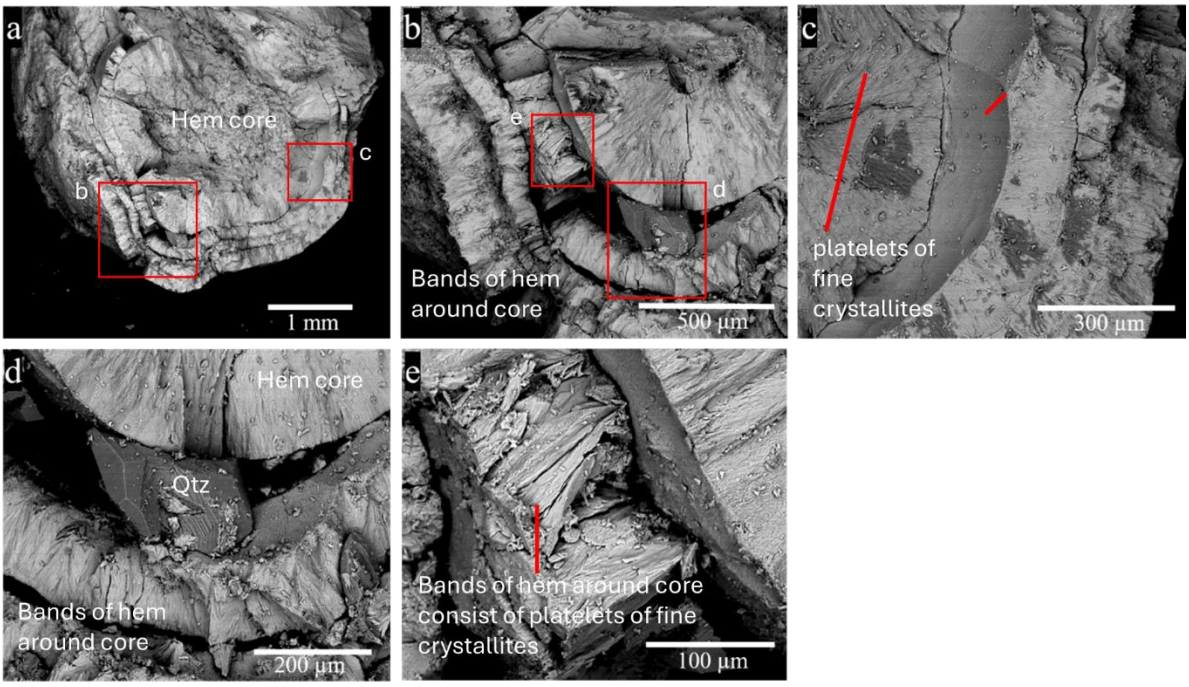

Figure 5.18: Back-scattered electron scanning electron microscopy (BSE-SEM) images of sample chip of NG10 showing hematite crystal morphology. a) Chip showing solid hematite core with multiple bands of hematite surrounding it. b) successive hematite bands of < 200 µm radiating from central portion of chip. c) botryoidal morphology of hematite bands with one face appearing smooth and perpendicular faces showing rougher smaller platelets which form the bands. d) conchoidally fractured quartz grain wedged between bands of hematite. Rough, outward facing surface of hematite bands shows < 1 µm x 100 µm crystals. e) fine platelet morphology of hematite crystals typically < 1 µm x 100 µm.

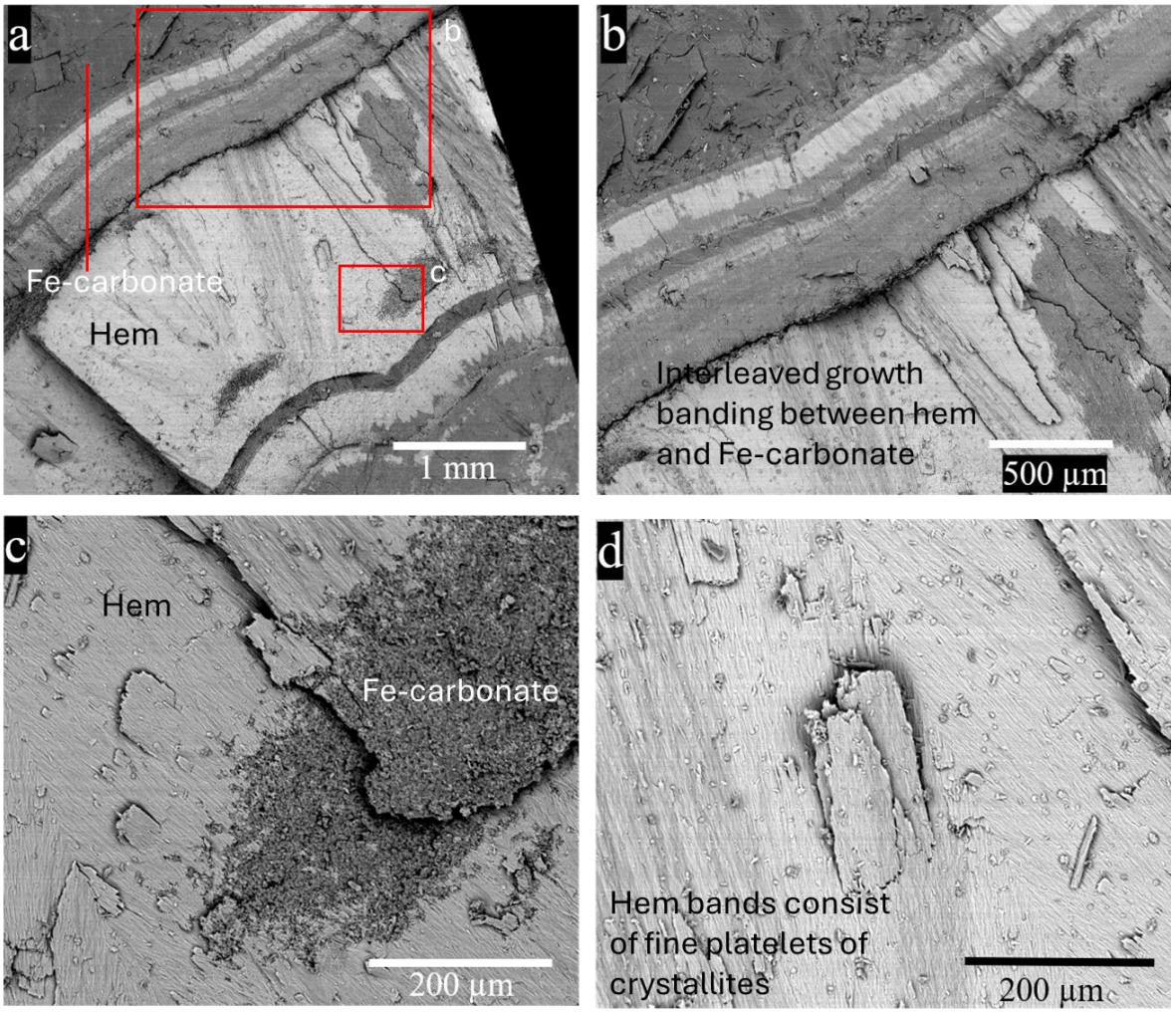

Figure 5.19: BSE-SEM images of sample chip of NGEM showing hematite crystal morphology and relationship with Fe-carbonates a) hematite bands interleaved with Fe-carbonate. b) successive hematite and Fe-carbonate bands radiating from central band of the chip. c) crystal morphology of hematite bands and Fe-carbonate. d) hematite bands shows < 1 µm x 100 µm crystals composed of many finer crystallites.

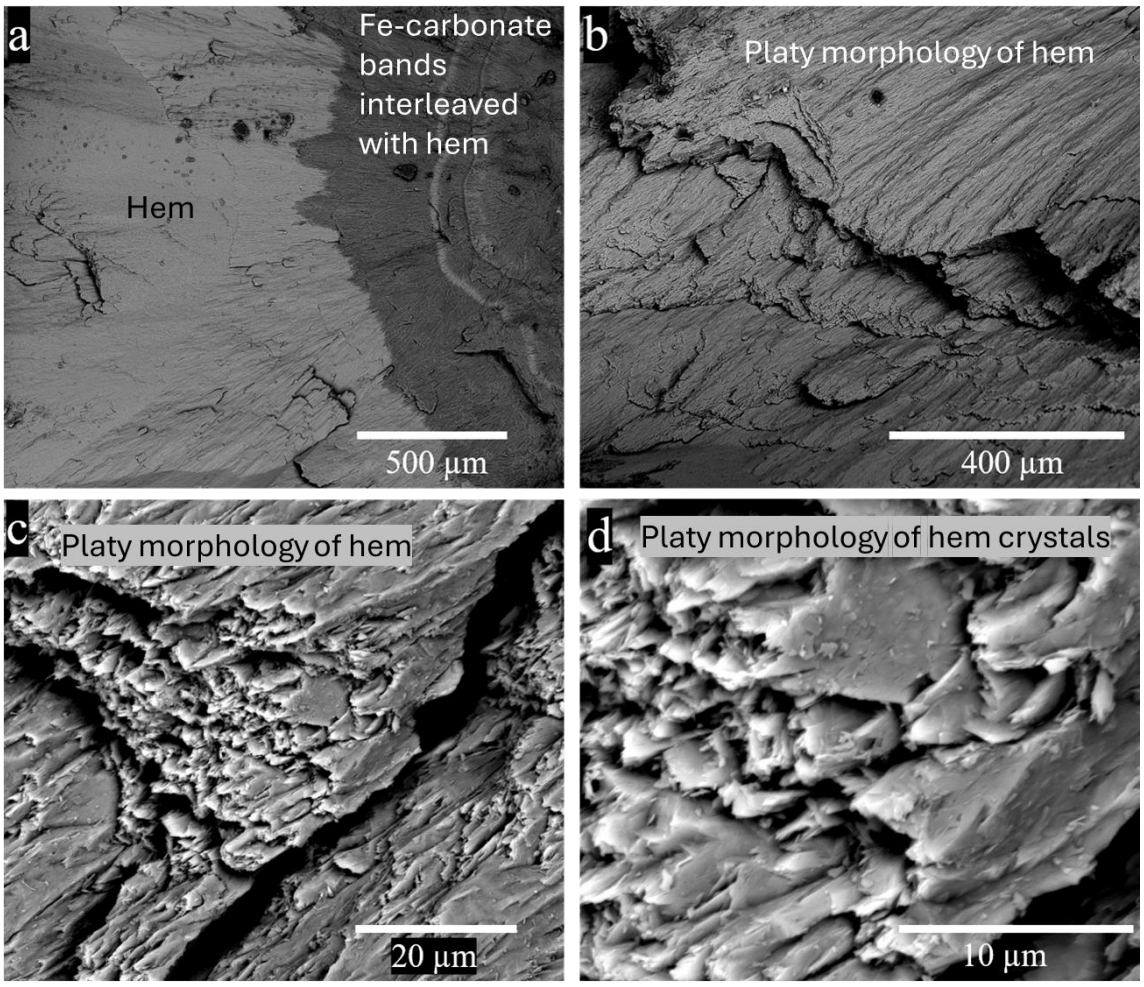

Figure 5.20: BSE-SEM images of sample chip of WH1 showing hematite crystal morphology and relationship with Fe-carbonates, similar to NGEM. a) Chip showing hematite bands interleaved with Fe-carbonate. b) zoom of (a) showing micaceous/platy morphology radiating from central band of the chip. c) Zoom of (a) showing individual crystals of hematite which make up the bands. d) Zoom of (a) showing individual < 1 µm x 10 µm crystals which tend to flake away like in NGEM.

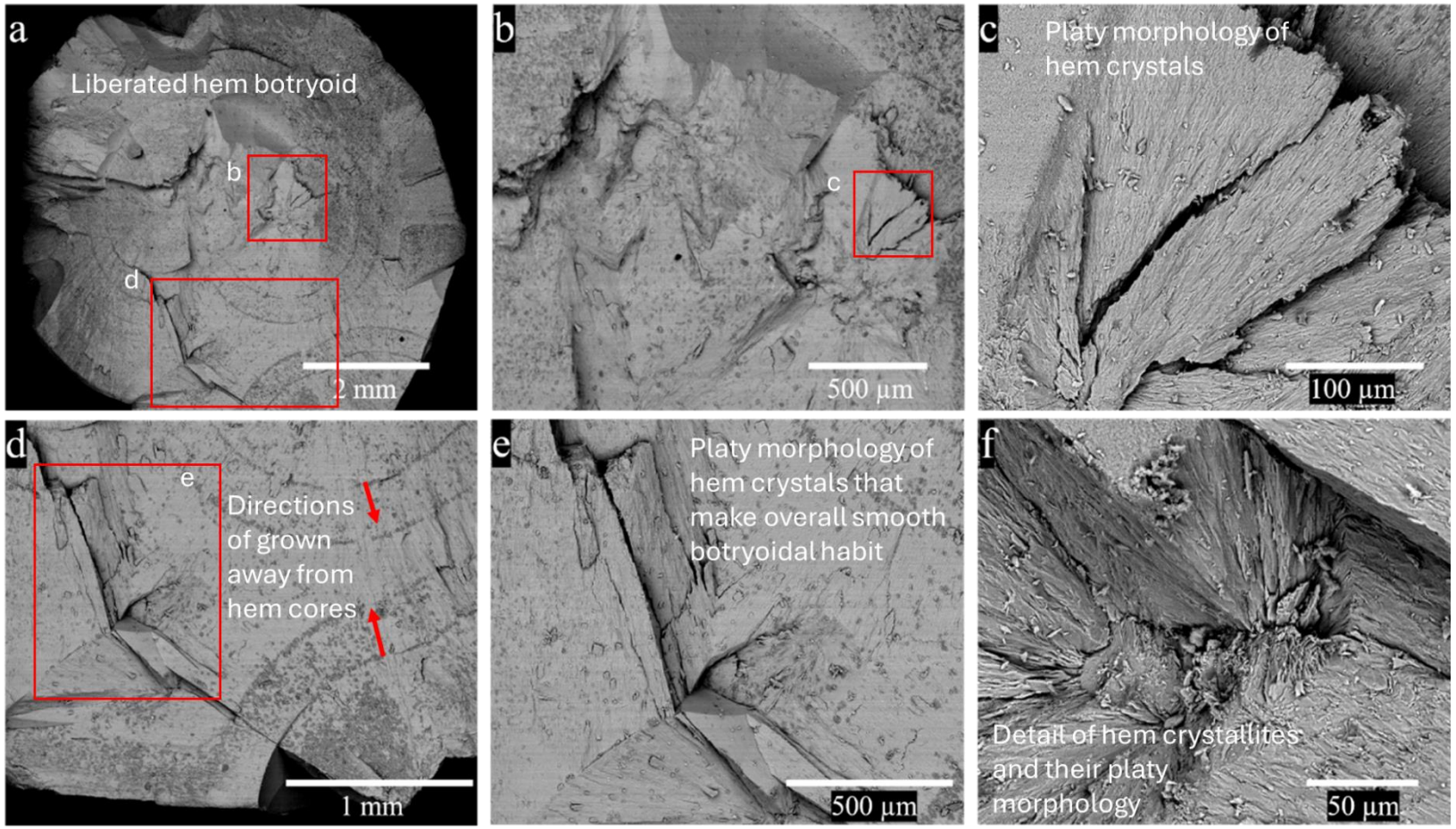

Figure 5.21: BSE-SEM images of sample chip of WCL2, related to WCL1 which is dated in this study, showing botryoidal habit of hematite and crystal morphology. a) botryoidal habit radiating from a central cores and merging. b) Zoom of (a) platy crystal morphology of hematite core and flaky fracturing similar to NGEM and WH1. c) fractured section of hematite which seems to flake away from the main body in < 1 µm x 10 µm crystals. d) two bands of hematite growing towards each other from the centres of their respective cores. e) platy crystal morphology of hematite crystals typically < 1 µm x 100 µm and part of a larger hematite mass. f) individual crystals < 1 µm x 10 µm radiating from a central point and flaking away like in NGEM and WH1.

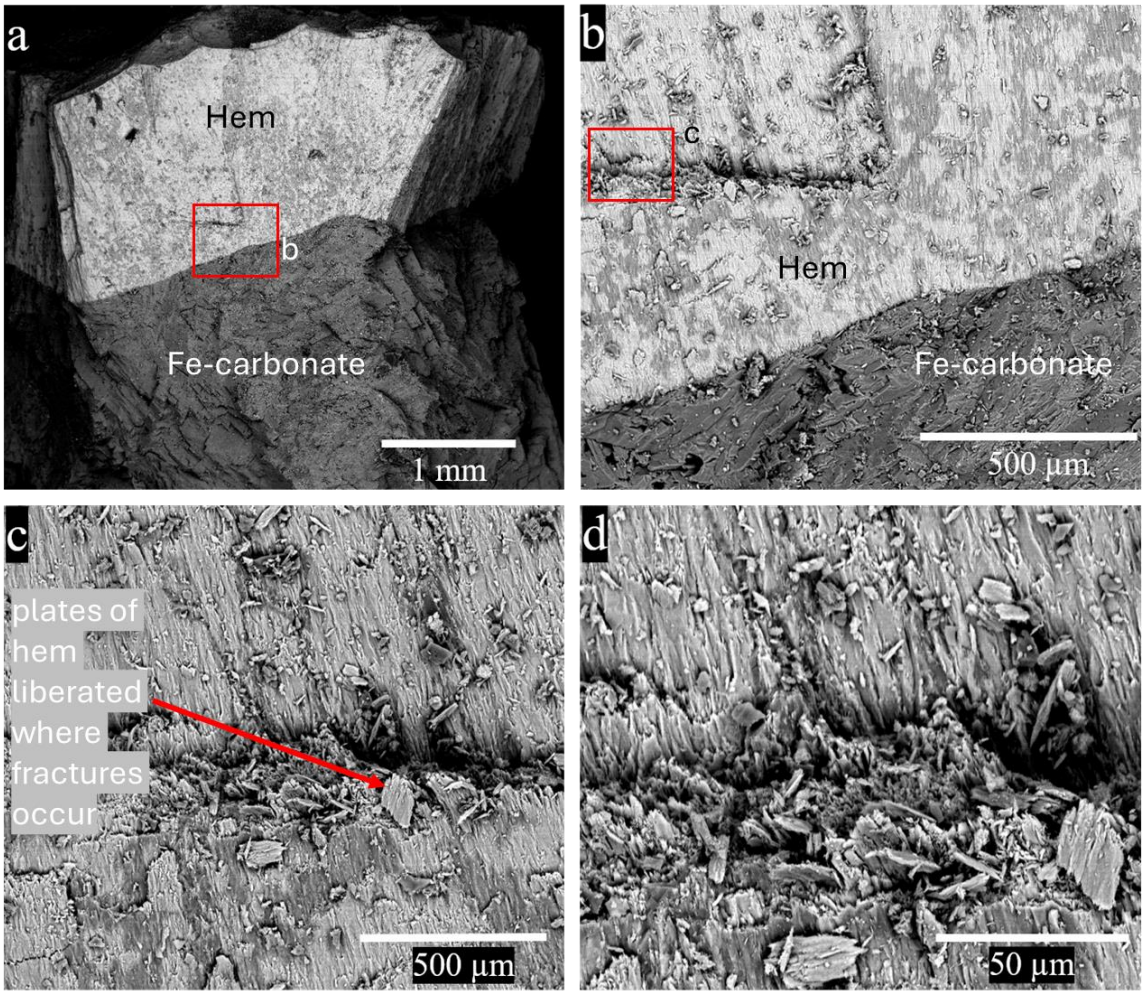

Figure 5.22: BSE-SEM images of sample chip of NGLC. a) Chip showing sharp contact between hematite and carbonate. Hematite band roughly 1 mm diameter. b) platy crystal morphology of hematite with flaky fracturing similar to NGEM, WH1, and WCL2. Hematite appears to be peppered with darker Fe-carbonate. c) fractured section of hematite which seems to flake away from the main body in < 1 µm x 50 µm crystals. d) Zoom of (c) platelets of hematite liberated in fractured areas of the mineral phase. D) zoom of image c to highlight crystal morphology of hematite.

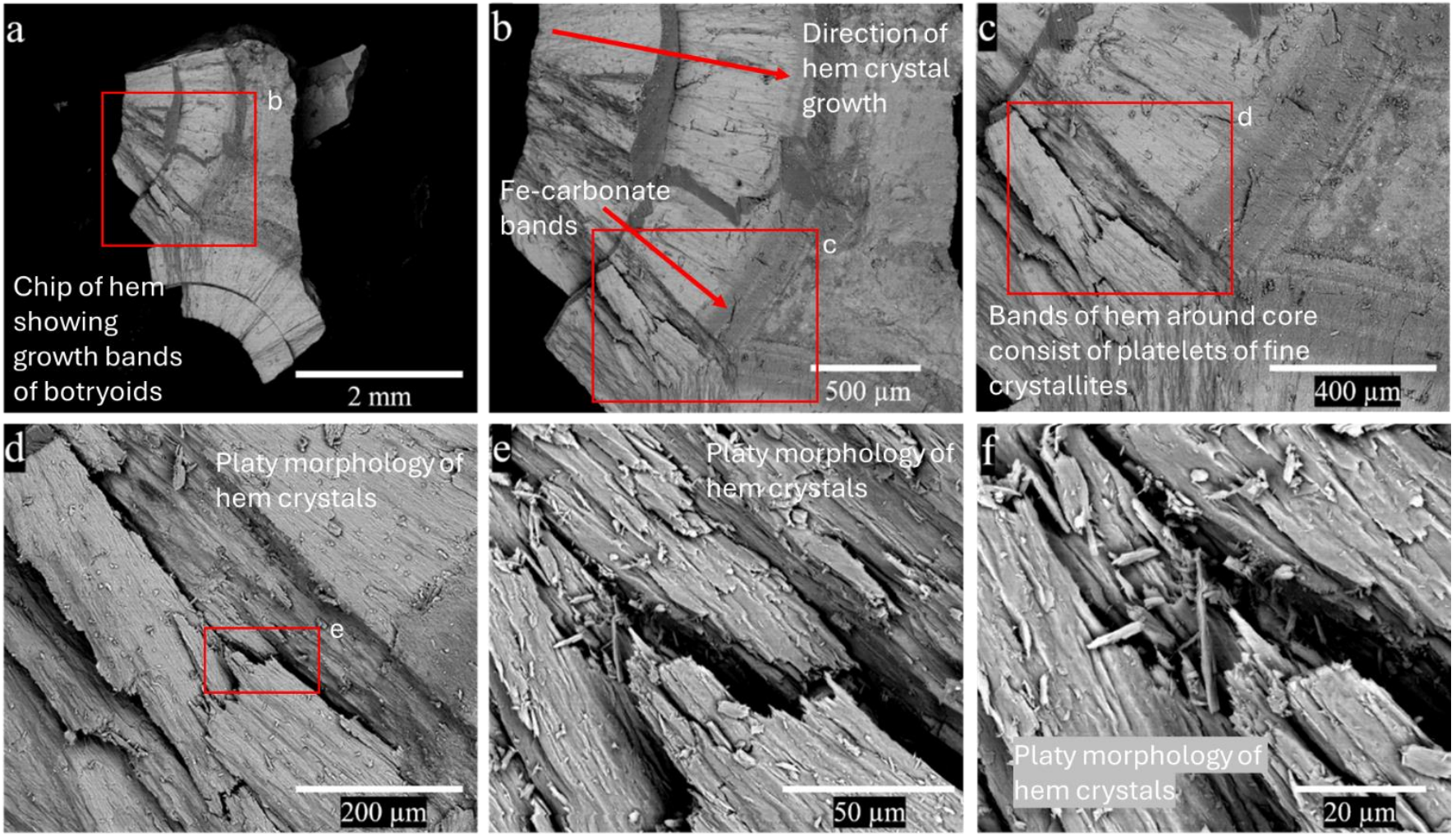

Figure 5.23: BSE-SEM images of sample chip of NGLF. a) chip showing two sets of hematite bands b) platy crystal morphology of botryoidal hematite bands growing left to right away from central hematite core. with flaky fracturing similar to most other sample chips. c) fractured section of hematite highlighting flaky/plate-like morphology d), e), and f) are gradual zoomed images Zoom of (c) showing fractured platy hematite in < 1 µm x 30 µm crystals.

5.5.3 Methods

Complete descriptions of the methods used for Ne, U and Th concentration determinations are provided in Chapter 3.

5.5.4 Results

Helium concentrations were not measured in these samples. We believed that the samples may have been too old with too high of a closure temperature to provide any meaningful (U-Th)/He geochronological data. Therefore, in the interest of time efficiency, only Ne concentrations were obtained in the thermochronology lab. ^{21}Ne concentrations range from 2.26 to 6.04 pccSTP/g (Table 5.3). Aliquot mass ranged from 15.7 to 20.5 mg. Weighing error, blank corrections and mass spectrometer sensitivity variation means that individual Ne concentration determinations have an uncertainty of between 1.5 and 17.2 %. This is more than the range of Ne concentrations measured of multiple aliquots of each sample (±2.4 to 8.5 %). Reheats of NG10D and NG10F, undertaken at 1100 °C following exact protocols of initial sample analysis, yielded 3 % and 4 % additional ^{21}Ne release prior to blank correction, thus made no significant contribution to Ne abundance and was excluded from final age calculation.

WH1 hematite from the Glengonnar mine location was measured using the MAP-215-50 mass spectrometer. Aliquot mass of 268 and 67.6 mg were analysed and contained 158 and 159 ± 0.79 Mat/g ^{21}Ne (5.89 ± 0.03 pcc/g). Reheats of each aliquot at ~1600°C were carried out to check complete degassing. Each aliquot reheat ^{21}Ne counts per second value was <0.5 % of first heat value, thus each aliquot was degassed effectively by first heat. All samples, analysed on ARGUS VI and MAP 215-50, give excess ^{21}Ne and plot to the right of the air-cosmogenic Ne mixing line (Niedermann et al., 1994; Shafer et al., 1999; Gyore et al., 2019), indicative of nucleogenic ^{21}Ne as the primary source of ^{21}Ne (Fig. 5.24).

For all samples, ^{238}U concentrations range from 4.03 to 8.22 ppm and ^{232}Th concentrations range from 0.21 to 0.55. Th/U ratios range from 0.034 to 0.113. Single U and Th concentration determinations typically have an uncertainty of less than ± 2 %. The within-sample effective uranium content (eU = [U] + 0.235 x [Th]) is typically ± 4 %.

Hematite (U-Th)/Ne ages for each sample was calculated using the mean Ne, U and Th concentrations using MATLAB software developed by Cox et al. (2015) using the latest version found at www.stephencoxgeology.com/neon_age_calc/index.html. Mean Ne ages ares: NG10 = 200.1 ± 6.9 Ma; NGEM = 173.4 ± 15.2 Ma; WH1 = 210.6 ± 12.2 Ma; WCL1 = 229 ± 13.7 Ma; NGLF = 153.3 ± 11.5 Ma; NGLC = 229.6 ± 13.4 Ma. No alpha-ejection correction was applied since the dimensions of the initial sample (10s of millimetres) are larger than the a-stopping distance; consistent with other Ne dating studies of hematite (Farley and Flowers, 2012; Farley and McKeon, 2015).

Table 5.3: Summary of Ne, U, and Th concentrations and ages of LWO hematite, Ne concentrations in CREU-1 quartz standard, and (U-Th)/He data of Elba hematite used here as a standard for U and Th measurements.

		Neon					Uranium - Thorium						
Sample	Aliquot	Mass (mg)	$^{21}Ne/^{20}Ne$	$^{22}Ne/^{20}Ne$	^{21}Ne (pcc/g)	±	Aliquot	Mass (mg)	^{238}U (ppm)	^{232}Th (ppm)	Th/U	eU	Age (Ma)	±
NG10	D	15.7	0.00746	0.09662	6.04	0.61	A	2.0	8.03	0.27	0.034	8.09	200.07	6.91
	F	15.8	0.00715	0.09871	5.87	0.39	B	2.5	8.21	0.30	0.036	8.27		
	G	16.8	0.00717	0.09857	5.64	0.46	C	2.2	*	0.29				
	H	16.3	0.00687	0.09737	5.71	0.85	D	2.0	8.22	*				
	I	17.1	0.00646	0.09804	5.57	0.79								
				mean	5.76				8.15	0.29	0.035	8.18		
				±	0.19				0.11	0.01	0.002	0.13		
NGEM	A	16.8	0.00466	0.10206	3.65	0.20	1	2.7	6.46	0.55	0.085	6.58	173.36	15.16
	B	18.8	0.00491	0.10309	4.12	0.20	2	4.7	6.22	0.51	0.082	6.34		
							3	2.9	6.08	0.52	0.085	6.20		
				mean	3.89				6.25	0.53	0.084	6.38		
				±	0.33				0.19	0.02	0.001	0.19		
WH1	4	268.0	0.02115	0.10302	5.90	0.03								
	6	67.6	0.01879	0.10246	5.88	0.03								
				mean	5.89				7.89	0.34	0.043	7.97	210.57	12.18
				±	0.03				0.47	0.15				
WCL1	A	20.5	0.00946	0.08925	4.12	0.71	2	2.0	4.83	0.26	0.054	4.89	229.04	13.70
	B	17.2	0.01016	0.08572	4.26	0.72	3	4.1	5.12	0.30	0.058	5.19		
							4	2.0	5.43	0.29	0.054	5.49		
				mean	4.19				5.13	0.28	0.055	5.19		
				±	0.10				0.30	0.02	0.002	0.30		
NGLF	A	18.0	0.00517	0.09927	2.46	0.10	1	2.9	4.44	0.45	0.102	4.54	153.31	11.47
	B	19.4	0.00489	0.09775	2.26	0.13	2	2.2	4.49	0.51	0.113	4.61		
							3	3.3	4.03	0.42	0.104	4.13		
							4	5.8	4.15	0.39	0.095	4.25		
				mean	2.36				4.28	0.44	0.103	4.38		
				±	0.14				0.22	0.05	0.007	0.23		
NGLC	A	16.5	0.00614	0.09418	3.79	0.42	1	2.3	4.97	0.27	0.055	5.03	229.56	13.35
	B	18.2	0.00635	0.09648	3.96	0.44	2	3.3	4.56	0.21	0.046	4.61		
							3	2.5	4.92	0.26	0.053	4.98		
							5	2.8	4.48	0.27	0.060	4.55		
				mean	3.87				4.73	0.25	0.053	4.79		
				±	0.12				0.25	0.03	0.006	0.25		
					^{21}Ne (Mat/g)									
CREU1	A	19.67	0.00836	0.10924	334	10.3								
	B	19.45	0.01019	0.11133	339	7.7								
	C	19.36	0.01316	0.11345	386	10.8								
	D	20.08	0.01215	0.11286	366	10.6								
	E	20.88	0.01174	0.11185	338	8.6								
	F	20.29	0.01380	0.11446	342	15.7								
	H	19.44	0.01329	0.11220	322	11.6								
	J	19.98	0.01265	0.11395	332	11.2								
				mean	345									
				±	21									
						Mean ^{4}He (ccSTP/mg)(10^{-10})								
Elba-Hematite	Italy-4A					2.76 ± 0.02 ^		7.90	0.30	0.43	1.44	0.40	5.60	0.23
	Italy-4B							8.10	0.31	0.42	1.35	0.41	5.58	0.20

* Aliquot > 25 % outside of the mean

^ Data from Wu et al. (2019)

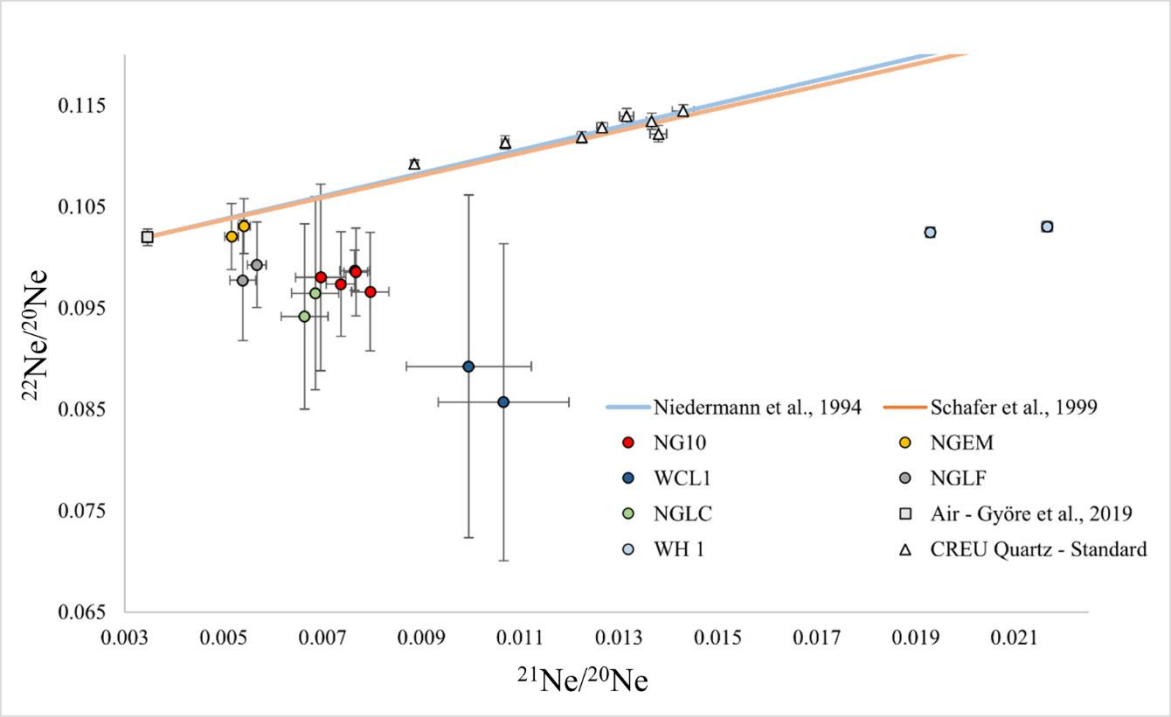

Figure 5.24: Neon isotope ratios of the LWO hematite samples and CREU-1 quartz standard. The air-cosmogenic Ne mixing lines of Niedermann et al. (1994) and Schafer et al. (1999) are shown, with Ne isotope ratio of air from Gyore et al. (2019).

5.5.5 Discussion

5.5.5.1 Hematite (U-Th)/Ne ages

Average hematite (U-Th)/Ne ages for each sample calculated using mean Ne and U and Th concentrations range from 153.3 to 229.6 Ma (Table 5.3). The total uncertainty of the average Ne ages is ± 3 to 9% (1σ). NG10 has the highest number of Ne abundance measurements and lies closest to the mean age of all samples at 200.1 ± 6.9 Ma, thus may be considered the most robust Ne age of the sample set.

Neon diffusion in hematite is linked to crystallite size distribution (Farley and Flowers, 2012). Farley and Flowers (2012) note that Ne was strongly retained at temperatures >150°C and that the age recorded for hydrothermal hematite corresponded to a hydrothermal event with temperatures proposed to reach >350°C. Cox et al. (2015) were able to further constrain the closure temperature (T_c) of Ne in the most retentive hematite crystallites to approximately

500°C with 94% of Ne being retained at temperatures over 290°C. At a cooling rate of 10°C/Myr, the theoretical T_c for Ne in hematite has been calculated to be 297, 250, and 210°C for spherical domains (crystallites) of 1 µm, 0.1 µm, and 0.01 µm (or 10 nm) respectively (Balout et al., 2017). Balout et al. (2017) suggest that Ne is almost completely retained in crystallites of 10 µm at temperatures <40 °C which is significantly higher than most of Earth's average surface temperature. Hematite samples used in this study have crystallite size > 50 nm and form part of mm scale mineralisation, thus likely have a T_c in excess of 210°C. Since fluid inclusions in hematite-bearing samples from LWO yielded temperatures < 150°C (Samson and Banks, 1988) and ore fluid temperatures based on sulfur isotope equilibrium calculations are <210°C, the Ne age data here represent hematite precipitation ages and not cooling ages. I am more comfortable viewing hematite precipitation ages here as three discrete events at ~230, 200, and 155 Ma rather than a single event at 190 Ma ± 40 Ma, for example. This interpretation is more in keeping with the geotectonic history of the area as discussed later in this chapter.

5.5.5.2 Contextualising the Ne age data

Based on fluid inclusion studies (Samson and Banks, 1988), faulting may have been restricted to the upper crust allowing for precipitation of minerals from a proximal fluid source. The Fe-phase mineralisation appears limited to the western portion of the LWO orefield which is in closest proximity to the Thornhill Basin. Alluvial gold with a red-bed affiliation has been recorded in stream sediments surrounding the LWO with links to the Thornhill Basin (Leake et al., 1998). Therefore, the Fe-phase cross-cutting Caledonian quartz but earlier than base metal mineralisation may be a product of Mesozoic red-bed/evaporitic brine fluid flow leading to mineral precipitation when conditions permitted.

There does not appear to be a single phase of hematite precipitation. Each age likely represents a period of basin to basement fluid flow and mineral precipitation with a causative tectonic event. The initiation of the breakup of Pangea (Vaughan and Storey, 2007) and subsequent phases of breakup related events (Vaughan and Livermore, 2005; Bartolini and Larson, 2001; Ruiz-Martinez et al., 2012) coincide with each phase of hematite mineralisation (~230 Ma, ~200 Ma, and ~155 Ma).

Along the continental crust of eastern North America, the first signs of Pangea breakup are recorded between 227 and 221 Ma (Manspeizer, 1988). Triassic to Jurassic sedimentary basins

are recorded around southern Scotland, Ireland, and northern England, likely the products of this same initial phase of Pangean rifting (Tyrrell et al., 2007; Tyrrell et al., 2012). Perhaps this phase of initial rifting resulted in the first phase of hematite precipitation at LWO, with iron sourced from meteoric water in the Thornhill Basin.

Approximately 120 km south of LWO, the West Cumbrian iron ore field is located on the eastern margin of the Permo-Cretaceous East Irish Sea extensional sedimentary basin (Banks et al., 2019). Field relationships between country rock and hematite mineralisation have been used to imply that it is typically younger than St. Bees Evaporite and Sandstone Fm., making the deposit younger than Early Triassic (Dunham, 1984). Palaeomagnetic dating of hematite from several locations across the Cumbrian ore field and Isle of Man suggests a Middle Triassic age for ore formation and that the deposit formed in a single event lasting <10 Ma (Crowley et al., 2014). Mineralising fluid compositions across the Cumbrian ore field and LWO are similar: fluid inclusion temperatures ranging between 80 and 120 °C; salinity between 10 and 24 equiv. wt% NaCl; and Na-Ca-Cl brine composition (Shepherd and Goldring, 1993). The style of hematite mineralisation across the Cumbrian ore field varies from stratiform to metasomatic replacement to fault-related fracture-hosted to karst-like (Crowley et al., 2014). Perhaps the middle Triassic (~230 Ma) event recorded by palaeomagnetic data is also recorded in the LWO.

A second phase of deformation related to the breakup of Pangea spans the Triassic-Jurassic boundary at 202 to 197 Ma (Vaughan and Storey, 2007). This phase is coeval with the eruption of the Central Atlantic Magmatic Province (CAMP), extended normal magnetic polarity, and mass extinction (Vaughan and Storey, 2007). Supercontinent separation is though likely to have commenced from 190-180 Ma with a pulse in subduction increasing the rate of spreading and fragmentation of Pangea at this time (Bartolini and Larson, 2001). Again, this pulse of rifting likely resulted in fluid flow from basin to basement in the LWO area and allowed for the precipitation of the iron phase.

A peak age range of 180-210 Ma (n=84) has been determined for NW trending U-bearing polymetallic veins near Needle's Eye around 50 km south of LWO (Parnell, 1995). NW trending fractures hosting U-bearing vein mineralisation are thought to have been generated by dextral movement on the North Solway Fault, a major basin controlling feature across the Solway and Carlisle area (Parnell, 1995). Parnell (1995) suggests that this Triassic-Jurassic age is an indication of hydrocarbon migration through the North Solway Fault system with hydrocarbons sourced from Carboniferous strata at depth. Parnell (1997) goes on to link these

veins, and their ore genesis, with the LWO veins, the Blackcraig group of PbS-rich veins near Newton Stewart, and Pb-Zn veins at Conlig, County Down, Northern Ireland. Each of these deposits lie a few km to the north of late Palaeozoic-Mesozoic sedimentary basins (Parnell, 1997). The event leading to U-mineralisation at Needles Eye is broadly synchronous with the LWO hematite ages (210-170 Ma).

The youngest hematite Ne age of 153.3 ± 11.5 Ma coincides with peak spreading rates during the breakup of Pangea. Initial separation of Laurentia and Gondwana (then parts of Pangea), recorded by palaeomagnetic data in SE Iberia, was slow between 200 Ma and 175 Ma (<1.9 cm/yr) but increased to peak velocity by 155 Ma (3.4 cm/yr) (Ruiz-Martinez et al., 2012). Deformation at this time is suggested to be global (Vaughan and Livermore, 2005) and may have allowed for further extensional fault-related fracturing, fluid flow, and iron mineral precipitation at LWO. Figure 5.25 is provided to assist with relating my results to the literature in this section of the discussion.

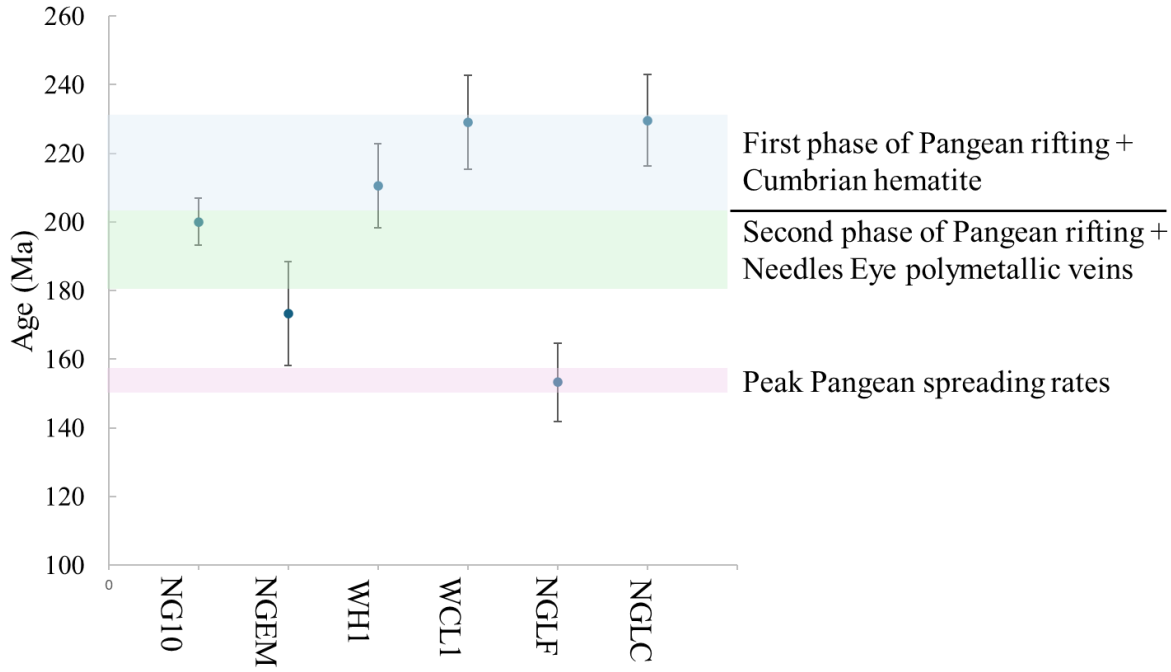

Figure 5.25: Hematite (U-Th)/Ne ages of samples from Leadhills-Wanlockhead orefield. Blue rectangle provides age range for first phase of Pangean rifting and the likely precipitation age of Cumbrian hematite deposits. Green box provides age range for second phase of Pangean rifting and the likely precipitation age of Needles Eye polymetallic veins. Violet box provides age range for peak crustal spreading rates related to the rifting of Pangea.

5.6 Background of work undertaken to achieve results in this chapter

Field work. Three days searching spoil heaps for samples containing both hematite and sulfide mineralisation.

Sample preparation. Initially, multiple weeks (perhaps months) spent separating hematite from quartz, carbonate phases, and other gangue and sulfide phases to create as pure a hematite separate as possible. This included many days of hand picking and magnetic separation. Many more days were then spent creating hematite powders used for X-ray diffraction geochronological purposes.

Gas extraction and purification (Chapter 3: Section 3.3). Initially, many months were spent experimenting to find the most effective/efficient process to purify and separate gases for Ne isotope analysis. This was done using air bottles attached to ARGUS VI and my assistance with this is in part published in Györe et al (2021). The final process for gas extraction and purification for hematite samples is documented in Chapter 3 Section 3.3, though, unfortunately, all the failures are not documented as they were so many and frequent that detailed records were not retained. Key aspects of experimentation were the time and temperatures that gas is exposed to alloy getters, charcoal coldfingers, and to the cryopump. Cleaning of this hardware by baking and pumping were just as critical. Once these were optimised, analysis became more consistent.

Laser combustion procedure (Chapter 3: Section 3.3): The process of attaching the laser system to the ARGUS VI had never been done before in the Thermochronology Laboratory at SUERC prior to this phase of experimentation; only furnace heating attached to the gas line on the MAP 50 had been attempted. This change in procedure had to be carefully planned and was carried out over the course of several days. Fortunately, I had refined the laser heating schedule for goethite and hematite by this point (see Chapter 3 Section 3.2), so only minor adjustments were made in the gas extraction procedure for Ne analysis, including amount of sample material in each Pt tube (around 3 times more than for He) and the amount of heating time to release all Ne into the gas extraction line (twice as long than for He). To analyse the material recorded in the results, including CRUE standards, took around three weeks in late 2020 during a window in the COVID restrictions.

Chemistry procedure: see Chapter 4.

All raw data should be stored in instrument software and associated spreadsheets in the Thermochronology Laboratory, SUERC, East Kilbride. If anyone would like this data, please contact Prof. Fin Stuart.

6.0 Helium and sulfur isotope geochemistry of the Leadhills-Wanlockhead Orefield

6.1 Introduction

Understanding He and S isotope geochemistry of ore deposits continues to be a valuable tool in ore-genesis studies (Seal, 2006 for review; Stuart et al, 1994, 1995; Davidheiser-Kroll et al., 2014). The stable isotope composition of common crustal elements and ore sulfides can be applied to determine mineralising fluid temperatures, fluid sources, water-rock interaction histories, heat sources, and precipitation mechanisms in hydrothermal systems (Myint et al., 2018; Kouhestani et al., 2019; Spence-Jones et al., 2018; Zeng et al., 2017; Davidheiser-Kroll et al., 2014); unravel multi-generational ore precipitation events and their palaeoclimate signatures (Yapp, 2020); and as a discriminator for distinguishing ore-bearing strata from barren strata in ore exploration (Large et al., 2001).

The helium isotope composition of ore fluids provides constraints on the heat sources, driving mechanisms and ultimately the tectonic setting of ore deposits. Volatiles trapped in oceanic basalts are enriched in ^{3}He implying that Earth's interior has not lost all its primordial volatiles (Lupton and Craig, 1975). Mid-ocean-ridge-basalt (MORB) have $^{3}He/^{4}He$ of 8 ± 1 R_a indicative of the upper mantle (Hilton and Craig, 1989; Ballentine and Burnard, 2002, for example). Helium in the continental crust is radiogenic and primarily produced by the decay of U and Th, producing gases with $^{3}He/^{4}He$ typically less than 0.05 R_a (O'Nions and Oxburgh, 1983). The three orders of magnitude difference between crustal and mantle helium reservoirs provides a powerful tracer of fluid origins in modern (Oxburgh et al., 1986; Ballentine et al., 1991; Griesshaber et al., 1992) and ancient fluids, particularly those responsible for ore deposition (Stuart et al., 1995; Davidheiser-Kroll, 2014; Wu et al., 2018).

The sulfur isotope systematics of sulfide minerals like galena, sphalerite, and chalcopyrite, can be used to determine temperature they precipitated and whether they precipitated in a state of geochemical equilibrium (Ohmoto and Rye, 1979). The temperature dependence of sulfur isotope fractionation between two phases has resulted in its use as a geothermometer (Ohmoto and Rye, 1979). Meaningful use of sulfur isotopes for geothermometry depends on the following: 1) the two phases (typically solid minerals) formed contemporaneously and in equilibrium at a single temperature; 2) no subsequent re-equilibrium or alteration of either

phase may have taken place; 3) phases must be separated prior to analysis; 4) temperature dependence of the fractionation factors must be known (Seal, 2006). The following equation can be used to calculate the temperature recorded by coexisting sphalerite (Sl) and galena (Gn) with explanation of derivation in Seal (2006):

(Equation 4)

$$T\ (°C) = \sqrt{\frac{0.73\ \times\ 10^6}{\Delta_{Sl-Gn}}} - 273.15$$

Here I report the first thorough He and S isotope study of the Leadhills-Wanlockhead Orefield (LWO) to determine the He isotope values of ore sulfides and $\delta^{34}S$ values of ore sulfides and sulfate. This data provides constraints on the source of He and consequently heat sources for mineralisation across the orefield and sulfur source, isotope fractionation temperatures of sulfides, precipitation mechanisms, whether differences in vein orientation across the orefield reflects multiple ore precipitation events. This chapter concludes by taking data from Chapters 5 and 6 and applying them to a wider discussion on ore forming processes and where the LWO fits in a big-picture holistic view of geologically/tectonically/geochronologically similar ore forming events. This is done to aid in any future mineral systems approach work that may want to consider data from the LWO.

6.2 Previous He and S studies at Leadhills-Wanlockhead

Although once Scotland's foremost Pb-Zn producer, there is no consensus on the heat source(s), driving mechanisms or tectonic setting for ore mineralisation at LWO. Early studies from Temple (1954, 1956), conducted as tectonic theory was coming to light (Holmes, 1944; Wilson 1966), suggest that the ore deposit is probably derived from the top of the tholeiitic layer/base of the granitic crustal layer and was genetically associated with the Hercynian orogeny. Through stable isotope (H, O) analysis of fluid inclusions related to ore phase mineralisation, Samson and Banks (1988) related heat flow/heat source to crustal fluid convection with no magmatic influence during a period of extensional tectonic in the Lower Carboniferous (Dinantian). Pattrick and Russell (1989) and Anderson et al. (1989) suggest, from S isotope analysis of sulfide and sulfate ore minerals, that deep-seated convection of hydrothermal fluid

within the Lower Palaeozoic basement was likely responsible for the scavenging of sulfides whilst sulfate was sourced from down going surface fluids. They note that mixing of these fluids in the upper reaches of the veins resulted in ore precipitation coeval with Carboniferous age Irish Zn-Pb mineralisation. The convection system may have reached depths of between 2 and 5 km at lowest estimate (Samson and Banks, 1988) and 10 km at deepest estimates (Pattrick and Russel, 1989). Helium isotopes have previously been used to suggest that Irish-type Pb-Zn mineralisation is unequivocally linked to a mantle-derived heat source (Davidheiser-Kroll et al., 2014).

Sulfur isotope data from LWO was first generated by Anderson et al. (1989) and provides a galena $\delta^{34}S$ range of -10.3 to -8.1 ‰ (n=9) and -5.9 ‰ to -5.1 ‰ (n=10) for sphalerite with equilibrium temperature suggested to be between of 170°C and 240°C. These values overlap with pyrite in the underlying Moffat Shales which exhibits a $\delta^{34}S$ range of -17.1 ‰ to -0.6 ‰ with a mean of -8.4 ‰ (n=9). A subsequent sulfur isotope study by Pattrick and Russell (1989) gives a mean galena $\delta^{34}S$ value of -9.76 ‰, -5.98 ‰ for sphalerite, and 3.9 ‰ for barite with an equilibrium temperature of 166°C. Since sulfur isotopic composition of vein sulfides at LWO is almost identical to the mean value of pyrite in Moffat Shales, Anderson et al. (1989) believe that vein sulfides represent a leached and homogenised Lower Palaeozoic diagenetic sulfide. This is echoed by Pattrick and Russell (1989) who go on to claim that vein mineralisation at the LWO may have formed from a large hydrothermal convection system reaching depths of around 10 km. The $\delta^{34}S$ value of barite is explained as either a result of H_2S oxidation in solution if barite formed in late fluids with high fO_2 where $SO_4^2 > H_2S$ or sourced from groundwater with sulfur derived from isotopically light Moffat Shales (Pattrick and Russell, 1989).

6.3 Samples and methods

6.3.1 Helium isotopes

Helium isotopes were analysed in fifteen samples of sulfide (galena, chalcopyrite, sphalerite, and pyrite) from eight mines across the LWO; New Glencrieff, Whyte's Cleuch, Straightstep, West Groove, Bay Vein, Hopeful Vein, Susanna, and Glengonnar (Table 6.1). Three samples (WC3, NG10, and NG12) were taken from mine dumps whilst all others were from the National Museum of Scotland's Leadhills-Wanlockhead collection.

Samples were gently crushed to ~2 mm grains with sulfides handpicked under binocular microscope prior to rinsing in acetone and drying under normal room conditions. The helium isotope composition of trapped fluids in ore sulfides were determined at SUERC using a ThermoFisher Scientific Helix-SFT mass spectrometer. Grains were loaded into a multi-sample hydraulic crusher and baked at around 150°C under ultrahigh vacuum for > 24 hours to remove adhered atmospheric gases. Prior to He isotope determinations, volatiles released from crushing were expanded into an all-metal gas line for purification by two SAES® GP50 getters (one at 250°C, one at room temperature) and a liquid N_2-cooled charcoal finger. Ultra-high vacuum was held by an ion pump and pumping of unwanted gas species by a Pfeiffer HiCube turbomolecular pump. After correcting for instrument blank levels, radiogenic ^{4}He is on average > 2000 times blank level, with lowest ^{4}He in sample >30 times and most abundant ^{4}He in samples >5800 times blank level. After correcting for instrument blank levels, ^{3}He is on average >16 times blank level, with lowest ^{4}He sample within error of blank, and most abundant >50 times blank level. Calibrations over the duration of analyses varied by 0.97 % (n = 23).

6.3.2 Sulfur isotopes

Sulfide samples (galena – PbS; sphalerite – ZnS; chalcopyrite - $CuFeS_2$; and pyrite - FeS_2) used for sulfur isotope analysis are primarily from a collection of old mine workings supplied by the Nation Museum of Scotland, Edinburgh, supplemented by several samples collected from LWO mine dumps to provide regional spread. Samples of sulfate, barite ($BaSO_4$), were collected from seven mines across the LWO (Table 6.1).

Sulfides and sulfates were liberated from samples by micro-drilling or by hand picking after gentle crushing. Isotopic analyses of sulfur in galena, sphalerite, chalcopyrite, and pyrite were carried out at SUERC using conventional methods of Robinson and Kusakabe (1975) in which SO_2 gas was liberated by combusting the sulfides with excess Cu_2O under vacuum at ~1075 °C. Barite isotopic analysis was carried out at SUERC using conventional methods of Coleman and Moore (1978) in which SO_2 gas is liberated by combustion with excess Cu_2O and silica at ~1125 °C. Liberated gases were analysed using a VG SIRA II gas mass spectrometer with standard corrections made to $\delta^{66}SO_2$ values to produce true $\delta^{34}S$ values. Reproducibility of internal and international laboratory standards (CPI, BIS, NBS 123, and IAEA-S-3) was better than ± 0.3 ‰, thus a ± 0.3 ‰ uncertainty is applied to all sample measurements. Data are

reported in $\delta^{34}S$ notation as per mil (‰) variations from the Vienna Canyon Diablo Troilite (VCDT) standard.

6.4 Results

6.4.1 He-isotopes

The $^{3}He/^{4}He$ ratios range from 0.021 to 0.33 R_a (Table 6.1). Only two samples yielded $^{3}He/^{4}He$ > 0.05 R_a, the value typically assumed to indicate a purely crustal radiogenic He source. These two samples (WC3 and O4C) have extremely low He content with ^{3}He close to blank levels imparting large uncertainties. Consequently, they are not included in the following discussion.

The $^{3}He/^{4}He$ range from 0.021 to 0.067 R_a with an average value of 0.039 ± 0.012 R_a (n=13). There is no systematic control of $^{3}He/^{4}He$ or He content governed by mineral composition.

6.4.2 S-isotopes

$\delta^{34}S$ results are as follows: galena; -11.6 to -7.9 ‰ with an average of -9.7 ± 0.8 ‰ (n=48): sphalerite; -7.0 to -5.0 ‰ with an average of -6.4 ± 0.5 ‰ (n=16): chalcopyrite; -8.4 to -6.5 ‰ with an average of -7.0 ± 0.6 ‰ (n=8): barite; 2.1 to 5.1 ‰ with an average of 3.7 ± 1.3 ‰ (n=7) (Table 6.1). Two barite-bearing samples had cogenetic galena in hand sample which was analysed and shows $\delta^{34}S$ values of -11.3 ‰ and -10 ‰, consistent with all other galena samples analysed. One pyrite-bearing mudstone from the New Glencrieff mine dump gave a $\delta^{34}S$ value of -5.2 ‰. One pyrite-bearing felsite from New Glencrieff mine dump gave a $\delta^{34}S$ value of -0.7 ‰. Data agree with previous work by Anderson et al. (1989) and Pattrick and Russell (1989) (Fig. 6.2)

In this study, $\delta^{34}S$ values of galena, chalcopyrite, and sphalerite trend from lighter to heavier, respectively. This is common for sulfide ore deposits and suggests that minerals precipitated in a state of chemical equilibrium (Rye and Ohmoto, 1974). In their example of a hydrothermal solution at T = 200°C, Rye and Ohmoto (1974) expect the variation of $\delta^{34}S$ between galena and sphalerite to be around 3.3 ‰ and a difference of around 36.5 ‰ between sulphate minerals and galena. Thus, for barite to be considered to have precipitated in equilibrium with sulfide minerals a $\delta^{34}S$ value of +26 ‰ would be expected. Here barite $\delta^{34}S$ is on average +3.7 ‰

average which is similar to that recorded in Pattrick and Russell (1989) (Fig. 6.2). Therefore, barite is not considered to have precipitated in equilibrium with sulfide minerals.

Vein orientation varies by around 35° across the LWO and in general trend between N-S and NW-SE (Table 1). One vein set trends NNW-SSE (from 330 to 350°) and a second trends NW-SE (315 to 330°). Vein orientation has no bearing on the $\delta^{34}S$ value of sulfide minerals across the LWO.

Table 6.1: Results for helium and sulfur isotope geochemistry for sulfides and sulfates from the Leadhills-Wanlockhead Orefield

Sample ID	Associated Ore Vein	Vein Strike (°)	Vein Dip (°)	Vein Length (km)	$\delta^{34}S$					^4He (cm^3STP)	$^3He/^4He$	error
					Gn	Ccp	Sp	Py	Brt	($x10^{-7}$)	(R/Ra)	
NMS001	New Glencrieff	320-350	70-80	2.7	-9.3					1.15	0.031	0.004
NMS002	New Glencrieff	320-350	70-80	2.7	-8.9					2.59	0.038	0.005
NMS003	New Glencrieff	320-350	70-80	2.7	-9.6					1.12	0.033	0.006
NMS14a	Straightstep				-10.1					0.44	0.021	0.007
NMS028	New Glencrieff	320-350	70-80	2.7	-9.8					1.57	0.038	0.005
WC3	Whyte's Cleuch				-9.7					0.06	0.099	0.054
NMS016	West Groove				-9.2					4.7	0.042	0.003
NMS017	Bay Vein				-8.4					4.42	0.045	0.002
04C	Hopeful Vein	315	90	1.1	-8.6					0.03	0.33	0.089
NMS029	Susanna	315	40-50	0.55	-11.6					3.54	0.035	0.003
NMS018	Bay Vein	320-330		2.7			-6.8			1.31	0.051	0.003
NMS021	West Groove						-6.4			0.44	0.048	0.008
NG10	New Glencrieff	320-350	70-80	2.7		-7.1				0.76	0.041	0.007
NG12	New Glencrieff	320-350	70-80	2.7		-7.1				0.26	0.024	0.013
100848	Glengonnar									1.63	0.067	0.004
DS03A	New Glencrieff	320-350	70-80	2.7	-8.9	-6.5						
DS03A	New Glencrieff	320-350	70-80	2.7	-9	-6.5						
DS03A	New Glencrieff	320-350	70-80	2.7	-8.9							
NMS014	New Glencrieff	320-350	70-80	2.7	-9.7							
FIN-NG1	New Glencrieff	320-350	70-80	2.7	-9.6	-7.1						
FIN-NG2	New Glencrieff	320-350	70-80	2.7			-5					
FIN-NG-3	New Glencrieff	320-350	70-80	2.7	-9.2	-6.6						
HM748DM	New Glencrieff	320-350	70-80	2.7	-9.6		-6.1					
HM748DM	New Glencrieff	320-350	70-80	2.7	-9.6		-6.3					
HM748DM	New Glencrieff	320-350	70-80	2.7	-9.8		-6					
HM748DM	New Glencrieff	320-350	70-80	2.7	-9.6		-6.5					
HM748DM	New Glencrieff	320-350	70-80	2.7	-10							

HM748DM	New Glencrieff	320-350	70-80	2.7	-9.5				
HM276	New Glencrieff	320-350	70-80	2.7		-6			
HM276	New Glencrieff	320-350	70-80	2.7		-6.7			
HM276	New Glencrieff	320-350	70-80	2.7		-7			
HM277	New Glencrieff	320-350	70-80	2.7		-6.2			
NMS001C	New Glencrieff	320-350	70-80	2.7	-10.2				
NMS004	New Glencrieff	320-350	70-80	2.7	-10.2				
NMS007	New Glencrieff	320-350	70-80	2.7		-8.4			
NMS008	New Glencrieff	320-350	70-80	2.7	-9				
NMS023	New Glencrieff	320-350	70-80	2.7	-7.5				
NMS027	New Glencrieff	320-350	70-80	2.7	-9.8				
NMS037	New Glencrieff	320-350	70-80	2.7	-9.9				
NMS038	New Glencrieff	320-350	70-80	2.7	-11.6				
NMS012	New Glencrieff	320-350	70-80	2.7		-6.6			
NMS034	New Glencrieff	320-350	70-80	2.7	-9.7				
NMS011	New Glencrieff	320-350	70-80	2.7	-10.8				
NGB1A	New Glencrieff	320-350	70-80	2.7					5.1
NGP1A	New Glencrieff	320-350	70-80	2.7				-5.2	
NGFP1A	New Glencrieff	320-350	70-80	2.7				-0.7	
NMS029	Susanna	315	40-50	0.55	-9				
DS057	Susanna	315	40-50	0.55	-7.9				
DS05D	Susanna	315	40-50	0.55		-6.8			
NMS024	Brown's Vein	350	70	2.2	-9.6				
WCB1A	Whyte's Cleuch								2.1
HM740	Whyte's Cleuch				-9.2				
HM741	Whyte's Cleuch					-6.9			
HM739	Broad Law	350	90	1.5	-9.2				
BLB1A	Broad Law	350	90	1.5					4.8
DS04B	Hopeful Vein	315	90	1.1	-8.6		-6.4		
DS04B	Hopeful Vein	315	90	1.1	-8.6				
DS03B	Hopeful Vein	315	90	1.1			-6.2		

HM737	Hopeful Vein	315	90	1.1	-10.5		
HM738	Hopeful Vein	315	90	1.1	-11.2		
LAHB1A	Lady Anne/Hopeful						2.6
LMS4B1A	Lady Anne/Hopeful						5.1
NMS015	Straightstep	350	60-70	2	-9.1		
NMS018	Bay Vein	320-330	70	2.7		-6.8	
NMS032	Lochnell	350	70	0.82	-11.6		
03A-1	unknown				-9.8		
03A-2	unknown				-10		
03A-2	unknown				-9.9		
03A-3	unknown				-10		
BWGB1A	Big Wool Gill						3.6
BWGG1A	Big Wool Gill				-11.3		
GGB1A	Glengonnar						2.7
GGG1A	Glengonnar				-10		

6.5 Discussion

6.5.1 He-isotopes

The $^{3}He/^{4}He$ data across the LWO is diagnostic of radiogenic crustal ^{4}He, with no need for any contribution of magmatic He. It is widely held that *in vacuo* crushing extraction of He from sulfides reflects the gas from fluid inclusions with only trivial contribution of He from post-mineralisation processes. The contribution of ^{3}He by neutron capture via the reaction $^{6}Li(n, \alpha)^{3}H$ from Li in the minerals is never significant as Li contents and the α flux are trivial (Kendrick and Burnard, 2013). Cosmogenic ^{3}He is produced in minerals when samples spend an extended period in the upper 1.5 m of Earth's surface (Goehring et al., 2010). This effect is negligible since all samples are from underground mine workings and have spent less than 100 years at the Earth's surface. *In situ* production of radiogenic ^{4}He in minerals can lower $^{3}He/^{4}He$ signatures in old minerals, albeit strongly dependant on the starting He concentration of fluid inclusions (Burnard and Polya, 2004). In situ production of radiogenic ^{4}He in fluid inclusions is likely to be insignificant since U and Th concentrations in hydrothermal fluids is negligible (e.g. Hu et al., 2009). Kendrick and Burnard (2013) note that only under exceptional circumstances, like in Precambrian U deposits, would in situ production of ^{4}He in fluid inclusion alter the $^{3}He/^{4}He$ of a sample. Further, in situ production of ^{4}He in fluid inclusions can be disregarded since α-particle ejection recoils ^{4}He from fluid inclusions < 20 μm in diameter (Stuart et al., 1995). During in vacuo crushing of sulfides, $^{3}He/^{4}He$ decreases as crushing continues due to ^{4}He release from fluid inclusions and or crystal lattice defects (Stuart et al., 1995). Thus, the $^{3}He/^{4}He$ determined from the initial crush is likely a minimum value of $^{3}He/^{4}He$ from initial fluid trapping within the host mineral (Stuart et al., 1995).

A clear crustal $^{3}He/^{4}He$ signature, as defined by O'Nions and Oxburgh (1988) is present in the LWO ore fluids and is not similar to data from Irish-Type Pb-Zn (Davidheiser-Kroll et al., 2014), active rift basins including the Rhine Basin (Oxburgh et al., 1986; Hooker et al., 1985), sub continental lithospheric mantle (Gautheron and Moreira, 2002) and mid ocean ridge basalts (Ballentine and Burnard, 2002) (Fig. 1). These data rule out Temple's (1956) original hypothesis that the deposit is ultimately of magmatic origin. This also rules out a link between Irish-type Pb-Zn mineralisation and the LWO, since Irish-type has a clear mantle He

component (Davidheiser-Kroll et al., 2014) (Fig. 6.1). A crustal signature does gives credence to the models that propose convection of hydrothermal fluids to depths of up to 10 km in the continental crust (Samson and Banks, 1988; Anderson et al., 1989; Pattrick and Russell, 1989). This will be discussed further later in this chapter.

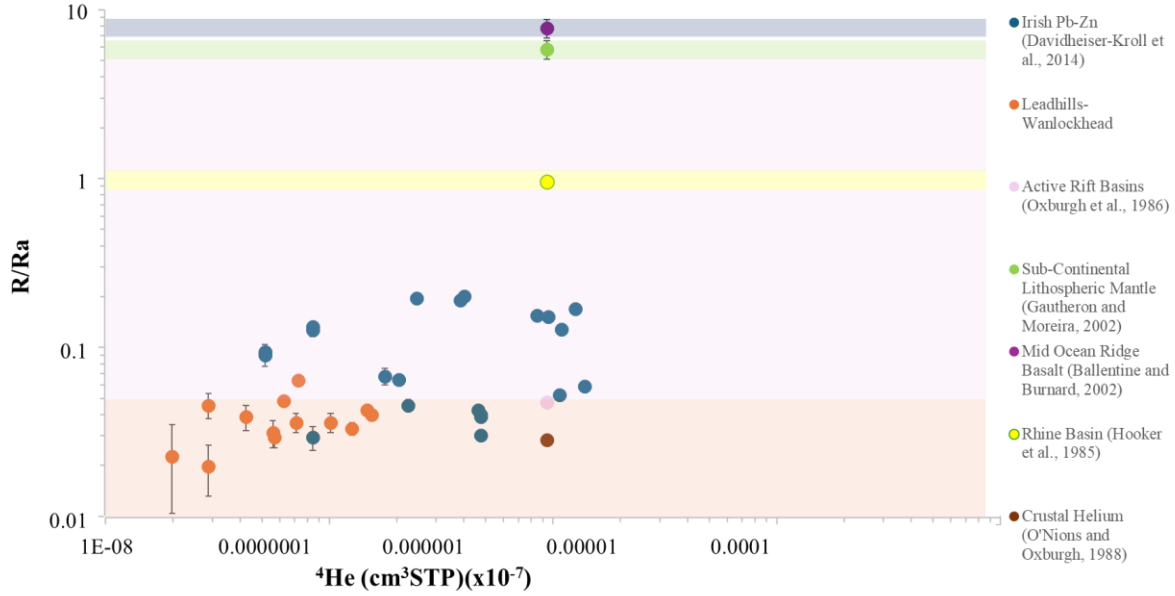

Figure 6.1: ^{4}He vs R/Ra data from many studies highlighting differences between Leadhills-Wanlockhead Orefield (LWO), Irish-Type Pb-Zn, active rift basons, Rhine Basin, sub continental lithospheric mantle, and mid ocean ridge basalts. Note that all bar one sample from LWO sit within the crustal helium zone.

6.5.2 S-isotopes

The LWO veins are hosted in lower Palaeozoic shales and greywacke, with diagenetic pyrite $\delta^{34}S$ values ranging from -0.6 to -17.1 ‰ with average of -8.4 ‰ (n=9; Anderson et al., 1989). Sulfide sulfur $\delta^{34}S$ values recorded in this study overlap with Anderson et al. (1989) and Pattrick and Russell (1989) (Fig. 6.2). I agree that sulfide sulfur was likely sourced from the underlying basement lithologies by hydrothermal convection, as previously outlined (Anderson et al., 1989; Pattrick and Russell., 1989).

Minimal variation in $\delta^{34}S$ values for each mineral phase regardless of vein orientation, suggests that sulfur source, ore fluid temperature, and oxidation state remained stable during the mineralisation process. Thus, ore fluids may have exploited a dense fracture system across the Leadhills-Wanlockhead area since the end-Caledonian orogeny allowing for fluids to equilibrate with the lower Palaeozoic basement prior to base metal precipitation in one short-lived event. The variation in vein orientation across the LWO may be the result of several

phases of crustal fracturing following reactivation of Caledonian structures, or a response to a conjugate-like stress field as suggested in the North Pennine Orefield (Coward, 1993; Anderson et al., 1995; Dempsey et al., 2021).

LWO does not show S-isotope bacteriogenic and/or remobilisation signatures observed across Irish-type Zn-Pb deposits at Lisheen and Tara Deep (Doren et al., 2022; Yesares et al., 2019) (Fig. 6.2), a further reason to consider the LWO as separate to any Irish-type style of ore mineralisation. LWO galena, sphalerite, chalcopyrite, and pyrite does not show any overlapping relationship with magmatic sulfur sources (Hutchinson et al., 2020). Considering the discussion in Section 6.4.1 and many studies that highlights magmatic sulfur to have a $\delta^{34}S$ value closer to 0 to +5 ‰ (Hutchinson et al., 2020 and references therein), it is evident that this is not a magmatic sulfur signature as He and S isotope data strongly suggest an absence of magmatism in the ore forming process.

Barite shows no overlap with Mesozoic or modern seawater sulfate sources (Botterell et al., 2006; Seal, 2006) (Fig. 2). The source of barite at LWO has previously been explained as either a result of H_2S oxidation in solution if barite formed in late fluids with high fO_2 where $SO_4^2 > H_2S$ or sourced from groundwater with sulfur derived from isotopically light Moffat Shales (Pattrick and Russell, 1989). Given how widespread barite mineralisation is across LWO, further stable isotopic investigation may provide insight into multiple conditions during sulphate deposition, palaeoenvironmental reconstruction of the area, and increased knowledge regarding relative timing of the LWO ore phase may be possible.

No work was undertaken on the potential for the Thornhill Basin to be a source of fluids or metals. No study on the source of base metals has been carried out at L-W, but it can be suggested that they are sourced from the Lower Palaeozoic basement since Irish Zn-Pb metals are sourced from strata within the same terrane (O'Keefe, 1986; LeHuray et al., 1987; Fallick et al., 2001; Everett et al., 2003; Wilkinson et al., 2005).

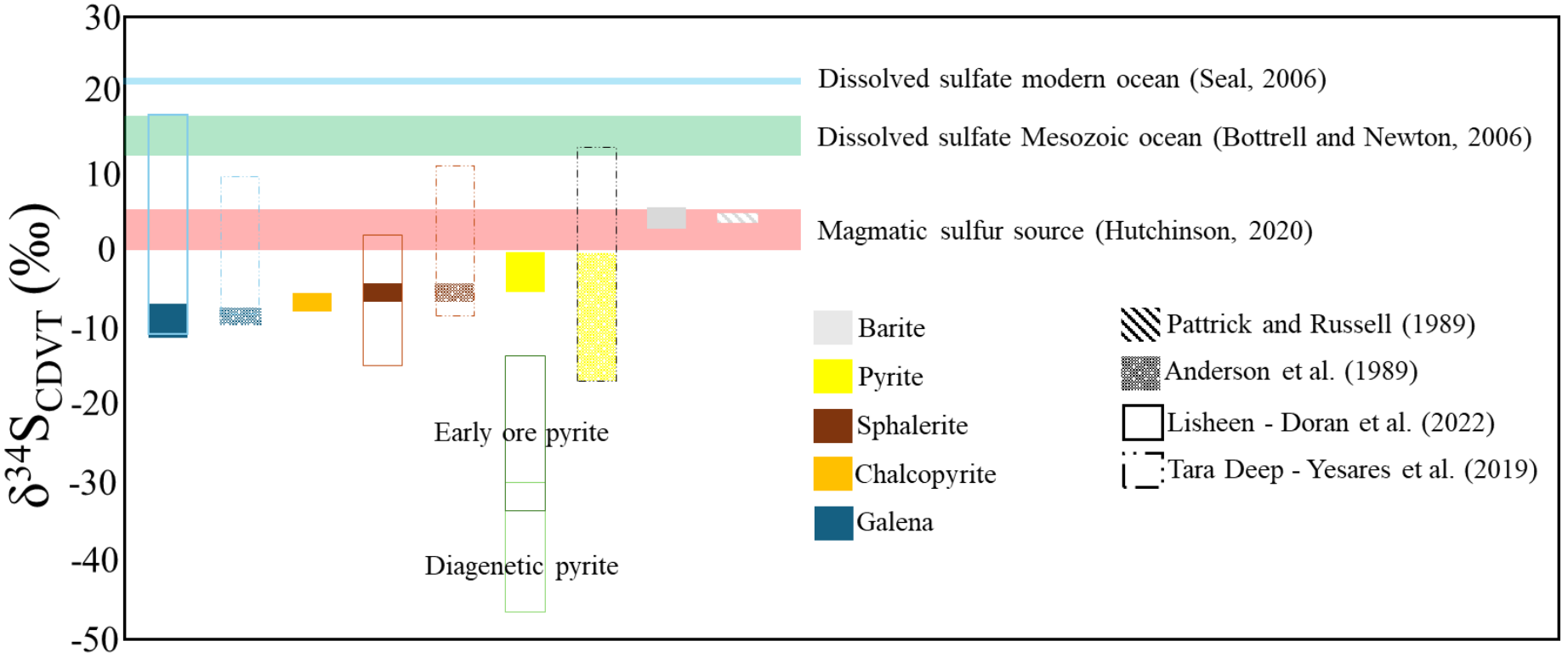

Figure 6.2: Sulfur isotope results for the Leadhills-Wanlockhead Orefield (LWO) compared against previous work by Anderson et al. (1989) and Pattrick and Russell (1989) as well as Irish-type Zn-Pb deposits at Lisheen (Doran et al., 2022) and Tara Deep (Yesares et al., 2019), magmatic sulfur sources (Hutchinson et al., 2020), dissolved sulfate in Mesozoic oceans (Bottrell and Newton, 2006) and dissolved sulfate in modern oceans (Seal, 2006).

The narrow range in sulfide sulfur values for each phase allows for an average value to be used for fluid temperature calculation. Using the equation 4 and the average $\delta^{34}S$ of galena (-9.7 ‰) and sphalerite (-6.2 ‰) from this study, a temperature for isotopic fractionation of 184 ± 20°C can be determined. In sample HM748DM galena and sphalerite are cogenetic and can be used for geothermometry. Multiple galena (n=6) and sphalerite (n=4) $\delta^{34}S$ determinations were undertaken allowing for a range of fractionation temperatures to be calculated as follows: maximum = 220°C ($\delta^{34}S$ galena = -9.5 ‰; $\delta^{34}S$ sphalerite = -6.5 ‰); minimum = 154°C ($\delta^{34}S$ galena = -10 ‰; $\delta^{34}S$ sphalerite = -6 ‰); and average = 186°C ($\delta^{34}S$ galena = -9.67 ‰; $\delta^{34}S$ sphalerite = -6.23 ‰).

In this study, the galena-sphalerite pair is considered the most robust geothermometer, especially where the two phases are found to be cogenetic in the same sample (Rye and Ohmoto, 1974). Sulfides were likely to have precipitated in a single short-lived event at temperatures between 170°C and 210°C with sulfur isotope signature representing a leached and homogenized basement sulfide.

6.6 An ore genesis model for the Leadhills-Wanlockhead Orefield

6.6.1 A holistic approach to ore genesis

Traditional deposit-centric models for ore genesis can fail to consider ore mineral formation and preservation in response to larger scale geological processes (Hagemann et al., 2016; Groves et al., 2022). Thus, it may be necessary to take a step back and consider the processes which may have led to the formation of the LWO given the data now available from Chapters 5 and 6 as well as any previous studies carried out on the LWO. In doing so, this work may be useful in future discussions regarding the formation of vein-type base metal deposits and their potential mineral components necessary in future economies.

In the mineral system approach to orogenic gold deposits Groves et al. (2022) suggest four key parameters are required to form a coherent mineral system model as follows: Fertility; Geodynamics; Architecture (fluid plumbing system); and Preservation. In this section, I will assign critical aspects of these parameters to processes at the LWO to provide a more holistic genetic model.

Fertility describes the metals and ligands necessary to form the ore mineralisation. In the case of LWO, these are the fluids associated with the Lower Palaeozoic basement previously

described by Samson and Banks (1988) and Anderson et al (1989) and potentially from the Mesozoic Thornhill Basin to the south.

The geodynamic parameter describes the dynamic settings of ore mineralization. At LWO, ore mineralization is hosted within a low-grade metamorphic volcano-sedimentary accretionary complex near a Mesozoic basin containing mixed carbonate, clastic, and volcanic lithologies. Plate/terrane motion is known to have switched from compressional/transpressional orogenic to transtensional basin-forming over the course of several hundred million years (Stone, 2014 and references therein). This complex plate/terrane motion is the likely cause of the fluid plumbing system at LWO. Importantly, plate/terrane motion and switch to extension can be suggested as the controlling factor in basin architecture and the concentration and channelling of ore forming fluids along faults across the LWO. At LWO, extension is suggested to be the result of the progressive breakup of Pangaea.

The architecture parameter, or the fluid plumbing system, describes the connectivity in relation to the transport of fluids along conduits and the eventual precipitation of economic grades of metals. The LWO is a fault-hosted vein-type deposit, thus we can attribute architecture to deep crustal scale faulting. Connectivity between the Thornhill Basin and Lower Palaeozoic greywacke through fault-related fracture-systems likely resulted in fluid mixing and the generation of metal-rich hydrothermal fluids. It is not uncommon for interaction between extensional fault-controlled basins and a fractured basement to result in mineralisation of economic interest (Gleeson and Yardley, 2002; Wilkinson et al., 2005). Basinal brines have higher densities and are known to pond at the base of aquifers (Gleeson and Yardley, 2003) and may lie dormant in basins until renewed tectonic activity acts as a trigger for fluids to permeate into the basement along crustal fractures (Gleeson and Yardley, 2002; 2003) with saline fluids known to reach depths of ~ 10 km (Bons et al., 2014). If fluids reach depths of up to 10 km, their temperature and salinity are likely to increase significantly enough to equilibrate with the basement and allow for effective scavenging of sulfur and metals (Bons et al., 2014). The focussing of large volumes of hot, metal carrying fluids from depth into a restricted part of the crust can then occur (Gleeson and Yardley, 2003) with mineral precipitation likely when physical parameters like pressure and temperature decrease sufficiently (Robb, 2005).

Russell (1978) was first to suggest that ore deposits may form from the downward propagation of hydrothermal cells in an extensional tectonic environment. They went on to state that water-rock interaction and the extraction of heat from the basement can increase

basement permeability and, if aided by further extension, the convection cell may deepen. In this study, a crustal source of helium is recognised from $^{3}He/^{4}He$ ratios of ore sulfide fluids which gives credence to the non-magmatic hydrothermal convection cell hypothesis for ore-forming processes first suggested by Russell (1978). The system can be considered largely independent of mantle derived heat. Based on a geothermal gradient of 30°C/km, sulfur equilibrium temperatures of between 170 and 210°C, and a conservative ore fluid temperature of <150°C previously suggested by Samson and Banks (1988) hydrothermal convection to depths of between 4 and 7 km is most likely.

Trapping of ore mineralization is evident as LWO along the Leadhills Fault Zone, where cherts, mudstones, and volcanics in a shear zone inhibit the mass transfer of fluids across the fault any further to the north of the area. Minor breaches of this structural trap are recognised but are not common.

The preservation parameter describes the distribution of deposits through time. Preservation is more likely in areas of tectonic stability like on or adjacent to thickened or buoyant continental crust. Denudation may reveal, destroy, or enhance the preservation potential of ore minerals. Denudation in response to rock uplift, due to tectonism or upwelling mantle, and glacial processes appears to have brought the LWO vein system close to the surface. The presence of detrital gold but no obvious gold-bearing quartz veins or basin-related gold may reflect the removal of other deposit in the recent geological past. The preservation of the rich secondary mineralization at LWO suggests that much of the upper portion of the ore system is still intact. The LWO is currently at high elevation – Wanlockhead is known as the highest village in Scotland. Perhaps this increased elevation prevented fatal erosion of the orefield from its inception despite uplift events related to distal plume uplift events and several ice ages throughout the Cenozoic (Łuszczak et al., 2017).

6.6.2 Wider correlation with European base metal mineralisation

Few of the clear ore deposits in southern Scotland have been radiometrically dated thus there is no ability to correlate continental breakup and ore mineralisation, as proposed by Russell (1972). Russell (1972) attributes the N-S ‘geofractures’ of the Thornhill Basin and LWO as pathways for stress in the crust, and which they correlate to those which resulted in the opening of the Atlantic. More broadly this is an active hypothesis to explain the epigenetic hydrothermal base metal mineralisation preserved across western Europe (Burisch et al., 2022). In these deposits, ore fluids are typically saline (10-30 wt% NaCl + CaCl), low

temperature (<200°C), and are commonly related to post-orogenic extensional tectonism with ore mineralisation concentrated in normal fault related fracture systems (Gleeson et al., 2001; Gleeson and Yardley, 2002; Munoz et al., 1994; Muchez et al., 2005; Cathelineau et al., 2012). The importance of magmatism as a source of metals, fluid, and heat for these deposits is widely debated and basin-to-basement fluid transfer during crustal extension, where metal and sulfur are scavenged from the basement during deep fluid convection without magmatic heat input, is thought possible (Cardellach et al., 1990; Munoz et al., 1994; Muchez et al., 2005; Cathelineau et al., 2012; Kirnbauer et al., 2012).

Hydrothermal vein-type deposits across southwest England were dated between 180 to 220 Ma and correlated with the initiation of North Atlantic rifting/Pangaean break-up (Mitchell and Halliday, 1976). They used K-Ar dating of adularia in veins found in the Lizard peninsula to establish this hypothesis and then suggested a much wider hydrothermal event may have occurred across western Europe. Halliday and Mitchell (1984) found that K-Ar dating of clay concentrates within ore, gangue, and wall rock has a common age range of 210-230 Ma in structurally controlled vein-type ore deposits in and around the Pedroches Batholith, Spain, indicating a hydrothermal event synchronous with rapid fracturing of the crust and increased geothermal gradient associated with the break-up of Pangaea. Surface waters were suggested to have penetrated deep into the crust prior to expulsion along rejuvenated fracture systems where ore predominantly precipitated (Halliday and Mitchell, 1984). Reactivation of crustal fractures was deemed most likely close to then actively rifting Mesozoic sedimentary basins, with hydrothermal activity linked directly to fracturing and basin formation (Halliday and Mitchell, 1984). Notably, Halliday and Mitchell (1984) question the need for mantle-derived magmatism to generate fluid convection within the shallow crust and suggest that Ireland may have acted as a stable block during the Mesozoic, thus remaining largely unaffected by these hydrothermal events.

Across the Aquitaine region of France and into the Pyrenees, epigenetic Zn (± Pb, Cu, Ag, U, F, Ba, Ge) vein-type deposits record a Triassic to late Jurassic age for main phase mineralisation (Munoz et al., 1994; Munoz et al., 2016; Le Guen et al., 1991; Sinclair et al., 1993; Johnson et al., 1996; Velasco et al., 1996). In the Pyrenees, Munoz et al. (2016) use Pb isotope modelling to decipher two phases of Pb-Zn mineralisation: first Les Argentieres deposit at 231-241 Ma and second the Lacore deposit at 155-164 Ma. These deposits share common characteristics: low temperature (80 – 200°C) high salinity (up to 25 wt% NaCl-$CaCl_2$) basinal brine derived ore fluids; common structural trends with proximal extensional Mesozoic basins; and non-magmatic. In the Saint-Salvy Zn-Ge deposit, southwest France

main phase mineralisation is characterised by low temperature (80-140°C) high salinity (~25 wt.% NaCl eq.) ore fluids inferred to have leached from evaporitic salts and hydrocarbon bearing sedimentary sequences from the nearby Aquitain basin with (Munoz et al., 1994). They go on to state that there is no influence from the nearby Sidobre granite on any part of the ore system and imply a Lias-Dogger (early Jurassic) age of main phase mineralisation since most hydrothermal alteration around the area occurs at that time and post-dates evaporite formation.

In Central France, Cathelineau et al. (2012) carried out K-Ar and Ar-Ar dating of clays and adularia from vein mineralisation at Charroux, Mauze, Melle-Thorigne, and Challac Pb-Zn-F-Ba deposits and determined ages of between 140 and 200 Ma. They go on to suggest similarities between the timing and fluids characteristics of these deposits and an extensive array of Pb-Zn-F-Ba across western Europe, primarily in Spain, Germany, and Poland (Cathelineau et al., 2012 Table 7 and Figure 13). Many of these deposits have been dated by K-Ar of clays in alteration zones associated with ore mineralisation, but several have been dated by Sm-Nd of fluorite in the ore phase with a distinct cluster around 146-156 Ma. Like in the UK and southern France, ore fluids in deposits highlighted by Cathelineau et al. (2012) range between 60 and 200°C with salinity commonly > 15 wt.% equivalent NaCl. They suggest these deposits may not be directly related to Pangaean break-up or North Atlantic opening, but rather by fluid mobilisation caused by the presence of brines in the lowermost portion of adjacent basins, deepening of these basins, reactivation of ancient basement faults, and local thermal anomalies either due to clay cap and granitic heating or by elevated geothermal gradient. This makes it possible for fluid movement and vein-type Pb-Zn-F-Ba deposits formation in basinal areas of restricted tectonic activity in central portions of continental crust (Cathelineau et al., 2012). However, they do call for a reassessment of fringe effects of major geodynamic events on mass/heat transfer in sedimentary basins.

In Northern Spain, particularly along the Catalonian coastal ranges, multiple Pb-Zn (± Cu, Ni, Co, Ag) sulphide and arsenide deposits can be found (Canals and Cardellach, 1990; 1993; 1997). These deposits vary along the coast as follows: Pb-rich with dolomitic and ankeritic gangue and hosted entirely in basement lithology; F-rich basement hosted veins; barite-rich veins with minor galena or arsenides related to normal faults and primarily basement hosted but occasionally cross-cutting lower Triassic sediments; and Pb-Zn (Cu) veins cross-cutting Triassic cover (Canals and Cardellach, 1990; 1997). Like veins across the UK, Southern France and the Pyrenees, ore fluids across the Catalonian coastal ranges are low temperature (75 to 200 °C) and highly saline likely the result of deep penetration of basinal brines into

fractured basement prior to mineral precipitation from late Triassic into the Jurassic period (Canals and Cardellach (1990; 1993; 1997). Sánchez et al. (2006) propose an early Jurassic timing (185 ± 28 Ma) of F based on Sr-Nd dating across the Asurias district of northern Spain and imply coincidence with opening of the North Atlantic opening (Sánchez et al., 2010). These veins are typically hosted in limestones within Palaeozoic basement or in highly silicified Permo-Triassic red-beds, record no magmatic heat input, and share ore fluid conditions of many other deposits across western Europe already discussed (Sánchez et al., 2010).

Across Europe and North Africa, Burisch et al (2022) have linked ore geochronology with rifting events related to the breakup of Pangaea. In doing so, they have uncovered three phases of extensional tectonism related to ore mineralisation at stepped intervals from the centre of rifting with oldest ore phase closest to earliest rifting, then progressively younger ore phases farther from the centre of rifting. Though this is a wide-ranging geographic area with several styles of ore deposit, they have defined these phases of rift-related ore mineralisation at roughly 230 – 200 Ma, 180 – 140 Ma, and 140 – 90 Ma; not dissimilar to that of hematite and proposed younger Pb-Zn mineralisation at LWO. No UK mineral deposits are discussed in their work.

6.7 Conclusions

It is evident from this study that the use of new methods can provide new perspectives on ore forming processes and perhaps provide evidence in support of larger holistic models. By adopting the mineral systems approach of Groves et al. (2022), key parameters controlling the formation of the LWO were identified based on the data gathered in this study. The revised paragenesis suggests hematite was found to post-date early quartz veining of Caledonian age and pre-dates main phase base metal mineralisation previously thought to be Carboniferous in age. Hematite (U-Th)/Ne geochronology was developed and applied and resulted in the discovery of three hematite precipitation phases from around 230 Ma to 150 Ma. Sulfur isotope composition of ore sulfides revealed a homogenous signal across the LWO regardless of vein orientation and suggest an equilibrium precipitation temperature of 170 to 210°C. Helium isotope composition of ore sulfides reveals a crustal source of heat in the ore-forming process at LWO.

This new data suggests the following: source of metals and ligands is the underlying basement; initial Caledonian compression and transpression followed by extensional tectonism related to the breakup of Pangaea acted as the geodynamic parameters responsible for the creation of a deep (possible ~7 km) non-magmatic hydrothermal convection system capable of driving ligand and metal scavenging from the basement; connectivity between basin and basement allowed for the mixing of fluids and eventual precipitation of metals as temperature and pressure of the system dropped; structural controls along the Leadhills Shear Zone led to the trapping of ore fluids; orefield preservation may have been the result of minor denudation due to the high elevation of the area throughout the Cenozoic/ice ages.

7.0 Conclusions and future work

7.1 Summary

Work presented here shows that Fe-oxide-oxyhydroxide (U-Th)/He and Ne chronometry can provide otherwise unobtainable ages to aid in the interpretation of events in the geological past. Here, Fe-oxide-oxyhydroxide (U-Th)/He and Ne chronometers have been used to date the timing of hydrothermal and supergene ore mineralisation in the Mesozoic and the post-Miocene, respectively. These are common styles of ore deposit which span much of Earth history and when dated can be used to better understand crustal scale processes and palaeoenvironmental evolution. Stable isotope geochemistry has then been utilised as a tool to investigate specific aspects of the ore-forming system to build a more holistic ore genesis model.

In a first attempt to constrain the timing of supergene ore mineralisation in southern Turkey, multi-aliquot Fe-oxide-oxyhydroxide (U-Th)/He was developed and applied to a suite of samples from the Attepe iron deposits. The Attepe iron deposits are located on the southern margin of the Central Anatolian Plateau where an orographic barrier separates the cold semi-arid interior to the north from the mild Mediterranean coast to the south, thus making them ideally suited to studying interactions between climate and tectonics.

An optimal degassing schedule was developed for He analysis from Wu et al. (2019) and resulted in <0.2 % additional He release following aliquot reheats. The addition of extra cleaning steps during column chemistry allowed for stable blank measurements and the analysis of lower U and Th levels by ICP-MS. The method applied here to date Fe-oxide-oxyhydroxide was successful in that it provided predominantly reproducible within-sample results and avoided U-Th volatilisation issues experienced in other Fe-oxide-oxyhydroxide (U-Th)/He studies (Vasconcelos et al., 2013; Hofmann et al., 2020). Results for U and Th work carried out on Italy-4 hematite (Elba, Italy) are in keeping with those reposted in Wu et al. (2019), thus validating the method.

Ages from four mine sites ranged between 5 Ma and 1 Ma and, in mines with two samples from varying elevation, water table lowering/rock uplift rates were constrained to between 6 and 12 m/Myr. Goethite provided insight into palaeoclimatic conditions, implying hot-humid condition persisted throughout the Pliocene into the Pleistocene with a switch to cold semi-arid condition thereafter. Since rock uplift rates do not correspond to those of rapidly

uplifting basins to the south, the elevation of the Attepe iron deposits is suggested to have been at or close to current elevation since late Miocene times. Therefore, regional climate cooling, rather than surface uplift, is considered the main driver of aridification and cessation of supergene mineralisation.

The genesis of the Leadhills-Wanlockhead Pb-Zn deposit in southern Scotland, despite its status as Scotland's foremost Pb-Zn producers prior to closure, lacked modern study. It was chosen as a testing ground for hematite (U-Th)/Ne dating since a revised paragenesis recognised hematite later than early quartz but earlier than main phase base metal mineralisation. This provided the opportunity to use hematite, a ubiquitous mineral across a plethora of ore deposit types, to constrain the earliest timing of an otherwise undatable epigenetic hydrothermal vein-type base metal deposit of which there are countless globally. Sulfur and helium isotope geochemistry was used to constrain the sources of sulfur and heat in ore fluids, respectively with the former also allowing for ore fluid equilibrium temperature to be calculated. Combining data from this study with previous work and wider geological data provided a means to test past ore genesis models and propose a revised model.

Analysing CREU-1 quartz standard, accuracy and precision of Ne isotope measurements are roughly equivalent using the ARGUS VI + laser system and MAP 215-50 + furnace system and fall within interlaboratory abundances reported in Vermeesch et al. (2015) and Cronus-A of Farley et al. (2020). However, around 10 times less sample material was needed to achieve results by ARGUS VI + laser system method. Using a laser system and less sample mass will reduce the amount of sample needed and reduce the chance of damage to the extraction system and occurrence of failed analyses making the ARGUS VI + laser system more sustainable for future work.

Hematite (U-Th)/Ne ages at LWO range from 230 to 150 Ma, around 100 Ma younger than previously thought. Closure temperature for Ne in hematite is likely > 210°C, thus the ages represent the timing of hematite precipitation. Sulfur isotope geochemistry suggests that base metal sulfide sulfur was sourced from the underlying Lower Palaeozoic shales and greywackes in line with previous work whilst sulfate may have been sourced from an overlying Mesozoic intracontinental basin or basins. Helium isotope geochemistry suggests that the ore fluids had no interaction with magmatic bodies nor was heated in extensional basins tapping into mantle. Reactivation of Caledonian ages structures during a period or several periods of transtension throughout the Mesozoic likely resulted in conditions necessary for the precipitation of vein minerals at LWO. The similarity of LWO fluids, sulfur and heat source, structural controls, proximity to Mesozoic basins, and timing of ore

mineralisation to several deposits across western Europe, imply that the LWO is the result of a major ore-forming event prevalent from Late Triassic times and linked to the initial break up of Pangaea.

7.2 Future work

The vertical extent of the oxidation zone is poorly mapped across the Attepe iron deposits. Further fieldwork to collect samples would allow insight into the Miocene climate and uplift history and a potentially more precise determination of the cessation of supergene conditions across the region. Mine workings and exploration are still active so this opportunity may exist in the future.

The $^{4}He/^{3}He$ technique is an elegant method for determining the diffusive loss of He from Fe-oxide-oxyhydroxide samples (Shuster et al., 2005; Heim et al., 2006; Vasconcelos et al., 2013; Monteiro et al., 2014; Deng et al. 2017). For the Attepe iron deposits study, I developed a method to determine the He loss based on the petrographic study of samples like in that of Allard et al (2018). However, this is rarely done in even the latest studies (eg dos Santos Albuquerque et al. 2020). Helium loss was rather insignificant in the Attepe iron deposit study (< 5%) but clearly applying the $^{4}He/^{3}He$ technique would provide an assessment of the veracity of the corrections.

The multi-aliquot technique used here avoids U-volatilisation but assumes complete homogenization of the sample. Subtle within-sample variations due to multiple Fe-oxide-oxyhydroxide generations, like in pisolites or nodules (Wells et al. 2019), may not be recognised. Mineral banding may indicate periods of dissolution and reprecipitation into open space are fairly common in goethite (Shuster et al., 2005). Here, care was taken to avoid sample areas with visible banding. However, new developments by Hoffman et al (2020) that allow the single aliquot method to be applied without U-volatilisation would be worth applying to most Fe-oxide-oxyhydroxide (U-Th)/He dating projects. If it could be coupled with the ARGUS VI + laser system presented in this study, an exciting method for single-aliquot hematite (U-Th)/Ne dating could be established and applied.

The Fe-oxide-oxyhydroxide (U-Th)/He and Ne chronometers have an exciting and rich future ahead of them. Dating of ore deposits may yield a more detailed understanding of the genesis of economic concentrations of resources needed for a more sustainable future. Recent work by Miller et al. (2020) shows that goethite may act as a single mineral

palaeothermometer, one which can be dated absolutely and hold further data on past climate conditions (Yapp, 2020 and references therein). Therefore, once creases in method development and data processing have been ironed out, goethite may act as a new and widely applicable tool in terrestrial palaeoclimatology.

8.0 References

Alçiçek, H. & Alçiçek, M.C. 2014. Palustrine carbonates and pedogenic calcretes in the Çal basin of SW Anatolia: Implications for the Plio-Pleistocene regional climatic pattern in the eastern Mediterranean. Catena, 112, 48-55.

Allard, T., Gautheron, C., Bressan Riffel, S., Balan, E., Soares, B.F., Pinna-Jamme, R., Derycke, A., Morin, G., Bueno, G.T. and do Nascimento, N. 2018. Combined dating of goethites and kaolinites from ferruginous duricrusts. Deciphering the Late Neogene erosion history of Central Amazonia. Chemical Geology. 479, 136–150.

Allen, P.M., Cooper, D.C., Parker, M.E., Easterbrook, G.D., Haslam, H.W. 1982. Mineral exploration in the area of the Fore Burn igneous complex, southwestern Scotland Mineral reconnaissance programme. Rep Institute of Geological Sciences. No. 55.

Allmendinger, R. W., Jordan, T. E., Kay, S. M. & Isacks, B. L. 1997. The evolution of the Altiplano-Puna plateau of the Central Andes, Annual Review of Earth and Planetary Sciences, 25(1), 139–174.

Andersen, J.C., Stickland, R.J., Rollinson, G.K. and Shail, R.K., 2016. Indium mineralisation in SW England: host parageneses and mineralogical relations. Ore Geology Reviews, 78, pp.213-238.

Anderson, I.K., Andrew, C.J., Ashton, J.H., Boyce, A.J., Caulfield, J.B.D., Fallick, A.E. and Russell, M.J. 1989. Preliminary sulphur isotope data of diagenetic and vein sulphides in the lower Palaeozoic strata of Ireland and southern Scotland: Implications for Zn + Pb + Ba mineralization. Journal of the Geological Society. 146 (4), 715–720.

Anderson, T.B. Parnell, J., Ruffell, A.H. 1995. Influence of basement on the geometry of Permo-Triassic basins in the northwest British Isles. In: Boldly, S.A.R., Permian and Triassic rifting in northwest Europe. Journal of the Geological Society. Special. 91, 103-122.

Aquilina, L. Boulvais, P. and Mossmann, J.R. 2011. Fluid migration at the basement/sediment interface along the margin of the Southeast basin (France): implications for Pb–Zn ore formation. Mineralium Deposita, 46(8), pp.959-979.

Ault, A.K. 2020. Hematite fault rock thermochronometry and textures inform fault zone processes. Journal of Structural Geology, 133, 104002

Bahr, R., Lippolt H. J., Wernicke, R. S. 1994. Temperature-induced 4He degassing of specularite and botryoidal hematite: A 4He retentivity study. Journal of Geophysical Research. 99, 17695-17707

Bai, X.J., Qiu, H.N., Liu, W.G. and Mei, L.F. 2018. Automatic 40 Ar/39 Ar dating techniques using multicollector ARGUS VI noble gas mass spectrometer with self-made peripheral apparatus. Journal of Earth Science, 29(2), pp.408-415.

Ballentine, C.J., O'Nions, R.K., Oxburgh, E.R., Horvath, F. and Deak, J. 1991. Rare gas constraints on hydrocarbon accumulation, crustal degassing and groundwater flow in the Pannonian Basin. Earth and Planetary Science Letters, 105(1-3), pp.229-246.

Balout, H., Roques, J., Gautheron, C., Tassan-Got, L. and Mbongo-Djimbi, D., 2017a. Helium diffusion in pure hematite (α-Fe2O3) for thermochronometric applications: A theoretical multi-scale study. Computational and Theoretical Chemistry, 1099, pp.21-28.

Balout, H., Roques, J., Gautheron, C. and Tassan-Got, L. 2017b. Computational investigation of interstitial neon diffusion in pure hematite. Computational Materials Science. 128, 67-74.

Banks, D., Steven, J.K., Berry, J., Burnside, N., Boyce, A.J. 2019. A combined pumping test and heat extraction/recirculation trial in an abandoned haematite ore mine shaft, Egremont, Cumbria, UK. Sustainable Water Resource Management. 5, 51-69.

Bartolini, A. and Larson, R.L., 2001. Pacific microplate and the Pangea supercontinent in the Early to Middle Jurassic. Geology, 29(8), pp.735-738.

Beauvais, A., Bonnet, N.J., Chardon, D., Arnaud, N. and Jayananda, A. 2016. Very long term stability of passive margin escarpment constrained by $^{40}Ar/^{39}Ar$ dating of K-Mn oxides. Geology, 44, 299-302.

Bode, M., Hauptmann, A., Mezger, K. 2009. Tracing Roman lead sources using lead isotope analyses in conjunction with archaeological and epigraphic evidence - a case study from Augustan/Tiberian Germania. Archaeological and Anthropological Sciences. 1, 177-194

Bons, P.D., Fusswinkel, T., Gomez-Rivas, E., Markl, G., Wagner, T. and Walter, B. 2014. Fluid mixing from below in unconformity-related hydrothermal ore deposits. Geology, 42(12), pp.1035-1038.

Bottrell. S. H., and Newton, R. J. 2006. Reconstruction of changes in global sulfur cycling from marine sulfate isotopes. Earth-Science Reviews, 75, 59-83.

Bozkurt, E. 2001. Neotectonics of Turkey–a synthesis, Geodinamica acta, 14(1-3), 3–30.

Bozkurt, E. 2000. Timing of extension on the Büyük Menderes Graben, western Turkey, and its tectonic implications. Geological Society, London, Special Publications, 173(1), 385-403.

British Geological Survey. 2005. Leadhills, Scotland Sheet 15E; Solid Geology 1:50000. Keyworth, Nottingham, UK: British Geological Survey.

Brown, M.J. Leake, R.C., Parker, M.E., Fortey, N.J., 1979. Porphyry style copper mineralisation at Black Stockarton Moor south-west Scotland. Mineral reconnaissance programme. Rep Institute of Geological Sciences. No. 30

Brown, R. 1919. The mines and minerals of Wanlockhead and Leadhills. Transactions of the Dumfriesshire & Galloway Natural History & Antiquarian Society. 6, 124-137.

Brown, R. 1925. More about the mines and minerals of Wanlockhead and Leadhills. Transactions of the Dumfriesshire & Galloway Natural History & Antiquarian Society. 13, 58-79.

Browne, M.A.E., Smith, R.A., Aitken, A.M. 2002. Stratigraphical framework for the Devonian (Old Red Sandstone) rocks of Scotland south of a line from Fort William to Aberdeen. BGS Survey Research Report, RR/01/04, 67.

Burisch, M., Markl, G. and Gutzmer, J., 2022. Breakup with benefits-hydrothermal mineral systems related to the disintegration of a supercontinent. Earth and Planetary Science Letters, 580, p.117373.

Burnard, P.G. and Polya, D.A. 2004. Importance of mantle derived fluids during granite associated hydrothermal circulation: He and Ar isotopes of ore minerals from Panasqueira. Geochimica et Cosmochimica Acta, 68(7), pp.1607-1615.

Canals, A. and Cardellach, E., 1993. Strontium and sulphur isotope geochemistry of low-temperature barite-fluorite veins of the Catalonian Coastal Ranges (NE Spain): a fluid mixing model and age constraints. Chemical Geology, 104(1-4), pp.269-280.

Canals, A. and Cardellach, E., 1997. Ore lead and sulphur isotope pattern from the low-temperature veins of the Catalonian Coastal Ranges (NE Spain). Mineralium Deposita, 32(3), p.243.

Canals, A., Cardellach, E., Rye, D.M., Ayora, C. 1992. Origin of the Atrevida Vein (Catalonian Coastal Ranges, Spain): Mineralogic, fluid inclusion and stable isotope study. Economic Geology. 87, 142-153.

Cann, J.R., Banks, D.A. 2001. Constraints on the genesis of the mineralization of the Alston Block, Northern Pennine Orefield, northern England. Proceedings of the Yorkshire Geological Society. 53 (3) 187-195

Cardellach, E., Canals, A., Tritlla, J. 1990. Late and post-Hercynian low temperature veins in the Catalonian Coastal Ranges. Acta Geologica Hispanica. 25, 75-81.

Cathelineau, M., Boiron, M.C., Fourcade, S., Ruffet, G., Clauer, N., Belcourt, O., Coulibaly, Y., Banks, D.A. and Guillocheau, F. 2012. A major Late Jurassic fluid event at the basin/basement unconformity in western France: 40Ar/39Ar and K–Ar dating, fluid chemistry, and related geodynamic context. Chemical Geology, 322, pp.99-120.

Cherniak, D.J., Watson, E.B., Grove, M. and Harrison, T.M., 2004. Pb diffusion in monazite: a combined RBS/SIMS study. Geochimica et Cosmochimica Acta, 68(4), pp.829-840.

Chew, D., and Spikings, R. 2015. Geochronology and Thermochronology Using Apatite: Time and Temperature, Lower Crust to Surface. Elements, 11 (3), 189-194.

Chew, D.M., Sylvester, P.J. and Tubrett, M.N., 2011. U–Pb and Th–Pb dating of apatite by LA-ICPMS. Chemical Geology, 280(1-2), pp.200-216.

Çiner, A., Doğan, U., Yıldırım, C., Akçar, N., Ivy-Ochs, S., Alfimov, V., Kubik, P. W. & Schlüchter, C. 2015. Quaternary uplift rates of the Central Anatolian Plateau, Turkey: insights from cosmogenic isochron-burial nuclide dating of the Kızılırmak river terraces, Quaternary Science Reviews, 107, 81–97.

Coleman, M.L. and Moore, M.P. 1978. Direct reduction of sulfates to sulfate dioxide for isotopic analysis. Analytical Chemistry, 50(11), pp.1594-1595.

Cooper, F., Adams, B., Blundy, J., Farley, K., McKeon, R. & Ruggiero, A. 2016. Aridity induced Miocene canyon incision in the Central Andes, Geology, 44(8), 675–678.

Courtney-Davies, L., Tapster, S.R., Ciobanu, C.L., Cook, N.J., Verdugo-Ihl, M.R., Ehrig, K.J., Kennedy, A.K., Gilbert, S.E., Condon, D.J. and Wade, B.P., 2019. A multi-technique evaluation of hydrothermal hematite UPb isotope systematics: Implications for ore deposit geochronology. Chemical Geology, 513, pp.54-72.

Cosentino, D., Schildgen, T. F., Cipollari, P., Faranda, C., Gliozzi, E., Hudáčková, N., Lucifora, S. & Strecker, M. R. 2012. Late Miocene surface uplift of the southern margin of the Central Anatolian Plateau, central Taurides, Turkey, GSA Bulletin 124(1-2), 133–145.

Coward, M.P. 1993. The effect of Late Caledonian and Variscan continental escape tectonics on basement structure, Paleozoic basin kinematics and subsequent Mesozoic basin development in NW Europe. In Geological Society, London, Petroleum Geology Conference Series, 4 (1), 1095-1108.

Cox, S., Farley, K. and Cherniak, D. 2015. Direct measurement of neon production rates by (α,n) reactions in minerals. Geochimica et Cosmochimica Acta. 148, 130-144.

Cox, S.E., Farley, K.A., and Cherniak, D.J. 2015. Direct measurement of neon production rates by (an) reactions in minerals: Geochimica et Cosmochimica Acta. 148, 130–144.

Crowley, J., Schoene, B. and Bowring, S. 2007. U-Pb dating of zircon in the Bishop Tuff at the millennial scale. Geology. 35 (12), 1123-1126

Crowley, S.F., Piper, J.D.A., Bamarouf, T. and Roberts, A.P. 2014. Palaeomagnetic evidence for the age of the Cumbrian and Manx hematite ore deposits: Implications for the origin of hematite mineralization at the margins of the east Irish Sea basin, UK. Journal of the Geological Society. 171 (1), 49–64.

Danišík, M., Evans, N.J., Ramanaidou, E.R., McDonald, B.J., Mayers, C. and McInnes, B.I. 2013. (U–Th)/He chronology of the Robe River channel iron deposits, Hamersley Province, Western Australia. Chemical Geology, 354, pp.150-162.

Davidheiser-Kroll, B., Stuart, F.M. and Boyce, A.J. 2014. Mantle heat drives hydrothermal fluids responsible for carbonate-hosted base metal deposits: evidence from 3 He/4 He of ore fluids in the Irish Pb-Zn ore district. Mineralium Deposita, 49(5), pp.547-553.

Dawson, J., Floyd, J.D., Phillips, P.R., Burley, A.J., Allsop, J.M., Bennet, J.R.P., Marsden, G.R., Leake, R.C., Brown, M.J. 1977. A mineral reconnaissance survey of the Doon-Glenkens area, southwest Scotland. Mineral reconnaissance programme. Rep Inst. Geol. Sci. No. 18

Dean, M.T., Browne, M.A.E., Waters, C.N., Powell, J.H. 2011. A lithostratigraphical framework for the Carboniferous successions of northern Great Britain (Onshore). BGS Research Report, RR/10/07. 174

Deng, X.-D., Li, J.-W. & Shuster, D. L. 2017. Late Mio-Pliocene chemical weathering of the Yulong porphyry Cu deposit in the eastern Tibetan Plateau constrained by goethite (U–Th)/He dating: Implication for Asian summer monsoon, Earth and Planetary Science Letters 472, 289–298.

Dietz, R.S. and Holden, J.C. 1970. Reconstruction of Pangaea: breakup and dispersion of continents, Permian to present. Journal of Geophysical Research, 75(26), pp.4939-4956.

Dilek, Y. & Sandvol, E. 2009. Seismic structure, crustal architecture and tectonic evolution of the Anatolian-African plate boundary and the Cenozoic orogenic belts in the Eastern Mediterranean region. Geological Society, London, Special Publications, 327(1), pp.127-160

Dixon, J.E. and Robertson, A.H., 1984. The geological evolution of the eastern Mediterranean. Univ. of Edinburgh.

Dobson, K.J., 2006. The zircon (U-Th)/He thermochronometer: development and application of thermochronometers in igneous provinces (Doctoral dissertation, University of Glasgow).

Dodson, M. H. 1973. Closure temperatures in cooling geochronological and petrological systems. Contributions to Mineralogy and Petrology. 40, 259-274.

Doğan, U. 2011. Climate-controlled river terrace formation in the Kızılırmak Valley, Cappadocia section, Turkey: inferred from Ar–Ar dating of Quaternary basalts and terraces stratigraphy. Geomorphology, 126(1-2), 66-81.

Doran, A. L., Hollis, S. P., Mengue, J. F., Piercey, S. J., Boyce, A. J., Johnson, S., Güven, J., Turner, O. 2022. A Distal, High-Grade Irish-Type Orebody: Petrographic, Sulfur Isotope, and Sulfide Chemistry of the Island Pod Zn-Pb Orebody, Lisheen, Ireland. Economic Geology, 117, no. 2, 306-325

dos Santos Albuquerque, M.F., Horbe, A.M.C. & Danišík, M. 2020. Episodic weathering in Southwestern Amazonia based on (U-Th)/He dating of Fe and Mn lateritic duricrust. Chemical Geology, 553, 119792.

Dunham, K.C. 1984. Classification, age and origin of the Cumbrian hematite. Proc. Cumberland Geol. Soc. 4, 259–268.

Dunham, K.C. 1968. Earth science and ore science, Presidential Address. Trans. Instn Min. Metall, 72, pp.697-714.

Dunham, K.C. 1990. Geology of the Northern Pennine orefield (Vol. 19). HM Stationery Office.

Edmondson, J.C. 1989. Mining in the Later Roman Empire and beyond: Continuity or Disruption? J. Roman Studies. 79, 84-102.

Ehlers, T. A. & Poulsen, C. J. 2009. Influence of Andean uplift on climate and paleoaltimetry estimates, Earth and Planetary Science Letters, 281(3-4), 238–248.

Eren, M., Kadir, S., Hatipoglu, Z. and Gül, M. 2008. Quaternary calcrete development in the Mersin area, southern Turkey. Turkish Journal of Earth Sciences, 17(4), pp.763-784.

Everett C, Rye D, Ellam R. 2003. Source or sink? An assessment of the role of the Old Red Sandstone in the genesis of the Irish Zn-Pb deposits. Econ Geol. 98 (1), 31–50.

Fallick, A.E., Ashton, J.H., Boyce, A.J., Ellam, R.M. and Russell, M.J., 2001. Bacteria were responsible for the magnitude of the world-class hydrothermal base metal sulfide orebody at Navan, Ireland. Economic Geology, 96(4), pp.885-890.

Farley, K. A. 2018. Helium diffusion parameters of hematite from a single-diffusion-domain crystal, Geochimica et Cosmochimica Acta, 231, 117–129.

Farley, K. A. 2000. Helium diffusion from apatite: General behavior as illustrated by Durango fluorapatite. Journal of Geophysical Research. 105 (B2), 2903-2914.

Farley, K. A. 2002. (U-Th)/He dating: techniques, calibrations, and applications. in Porcelli, D., Ballentine, C. K., & Wieler, R. (eds) Noble gases in geochemistry and cosmochemistry. Reviews in Mineralogy and Geochmeistry. Mineralogical Society of America. 47, 819-843.

Farley, K. A., Flowers, R., M. 2012. (U–Th)/Ne and multidomain (U–Th)/He systematics of a hydrothermal hematite from eastern Grand Canyon. Earth and Planetary Science Letters. 359–360, 131–140.

Farley, K.A. and McKeon, R. 2015. Radiometric dating and temperature history of banded iron formation–associated hematite, Gogebic iron range, Michigan, USA. Geology, 43(12), pp.1083-1086.

Farley, K.A., Treffkorn, J. and Hamilton, D. 2020. Isobar-free neon isotope measurements of flux-fused potential reference minerals on a Helix-MC-Plus10K mass spectrometer. Chemical Geology, 537, p.119487.

Farley, K. A., Wolf, R. A., Silver, L. T. 1996. The effects of long alpha-stopping distances on (U-Th)/He ages. Geochimica et Cosmochimica Acta. 60 (21), 4223-4229.

Foeken, J. P., Stuart, F. M., Dobson, K. J., Persano, C. & Vilbert, D. 2006. A diode laser system for heating minerals for (U-Th)/He chronometry, Geochemistry, Geophysics, Geosystems, 7(4).

Gallagher, M.J., Stone, P., Kemp, A.E.S., Hills, M.G., Jones, R.C., Smith, R.T., Peachey, D., Vickers, B.P., Parker, M.E., Rollin, K.E. and Skilton, B.R.H., 1983. Stratabound arsenic and vein antimony mineralisation in Silurian greywackes at Glendinning, south Scotland.

Gautheron, C., Tassan-Got, L., Farley, K. 2006. (U–Th)/Ne chronometry. Earth and Planetary Science Letters. 243, 520–535.

Gilfillan, S.M.V., Györe, D., Flude, S., Johnson, G., Bond, C.E., Hicks, N., Lister, R., Jones, D.G., Kremer, Y., Haszeldine, R.S. and Stuart, F.M., 2019. Noble gases confirm plume-related mantle degassing beneath Southern Africa. Nature communications, 10(1), p.5028.

Gillanders, R.J. 1981. The Leadhills-Wanlockhead district, Scotland. The Mineralogical Record. 235-250.

Gleeson, S.A., Wilkinson, J.J., Stuart, F.M., Banks, D.A. 2001. The origin and evolution of base metal mineralising brines and hydrothermal fluids, South Cornwall, UK. Geochim et Cosmochim Acta. 65 (13), 2067–2079.

Gleeson, S.A., and Yardley, B.W.D. 2002. Extensional veins and Pb-Zn mineralisation in basement rocks: the role of penetration of formational brines. In Stober, I., and Butcher, K. 2002. Water-rock interactions. Kluwer Academic Publishers. Netherlands.

Gleeson, S.A., and Yardley, B.W.D., 2003. Surface-derived fluids in basement rocks: inferences from palaeo-hydrothermal systems. Journal of Geochemical Exploration, 78, pp.61-65.

Goehring, B.M., Kurz, M.D., Balco, G., Schaefer, J.M., Licciardi, J. and Lifton, N., 2010. A reevaluation of in situ cosmogenic 3He production rates. Quaternary Geochronology, 5(4), pp.410-418.

Gökce, A., Bozkaya, G. 2007. Lead and sulfur isotopic studies of the barite–galena deposits in the Karalar area (Gazipaoa–Antalya), Southern Turkey. J. Asian Earth Sci. 30, 53-62.

Griesshaber, E., O'nions, R.K. and Oxburgh, E.R. 1992. Helium and carbon isotope systematics in crustal fluids from the Eifel, the Rhine Graben and Black Forest, FRG. Chemical Geology, 99(4), pp.213-235.

Groves, D.I., Santosh, M., Müller, D., Zhang, L., Deng, J., Yang, L.Q. and Wang, Q.F., 2022. Mineral systems: Their advantages in terms of developing holistic genetic models and for target generation in global mineral exploration. Geosystems and Geoenvironment, 1(1), p.100001.

Györe, D., Tait, A., Hamilton, D. and Stuart, F.M. 2019. The formation of NeH+ in static vacuum mass spectrometers and re-determination of 21Ne/20Ne of air. Geochimica et Cosmochimica Acta, 263, pp.1-12.

Györe, D., Di Nicola, L., Currie, D., and Stuart, F.M., 2021. New System for Measuring Cosmogenic Ne in Terrestrial and Extra-Terrestrial Rocks. Geosciences 11, no. 8: 353.

Hagemann, S.G., Lisitsin, V.A. and Huston, D.L., 2016. Mineral system analysis: Quo vadis. Ore Geology Reviews, 76, pp.504-522.

Halliday, A.N., Mitchell, J.G. 1984. K-Ar ages of clay-size concentrates from the mineralisation of the Pedroches Batholith, Spain, and evidence for Mesozoic hydrothermal activity associated with the break up of Pangaea. Earth and Planetary Science Letters. 68, 229-239.

Halliday, A.N., Shepherd, T.J., Dickin, A.P. and Chesley, J.T. 1990. Sm–Nd evidence for the age and origin of a Mississippi Valley Type ore deposit. Nature, 344(6261), pp.54-56.

Hatzfeld, D. & Molnar, P. 2010. Comparisons of the kinematics and deep structures of the Zagros and Himalaya and of the Iranian and Tibetan plateaus and geodynamic implications, Reviews of Geophysics 48(2).

Heim, J. A., Vasconcelos, P. M., Shuster, D. L., Farley, K. A. & Broadbent, G. 2006. Dating paleochannel iron ore by (U-Th)/He analysis of supergene goethite, Hamersley province, Australia, Geology, 34(3), 173–176.

Hilton, D.R. and Craig, H. 1989. A helium isotope transect along the Indonesian archipelago. Nature, 342(6252), pp.906-908.

Hofmann, F., Treffkorn, J. & Farley, K. A. 2020. U-loss associated with laser-heating of hematite and goethite in vacuum during (U–Th)/He dating and prevention using high O_2 partial pressure, Chemical Geology, 532, 119350

Holliday, D.W., Holloway, S., McMillan, A.A., Jones, N.S., Warrington, G. and Akhurst, M.C. 2004. The evolution of the Carlisle Basin, NW England and SW Scotland. Proceedings of the Yorkshire geological Society, 55(1), pp.1-19.

Holmes, A. 1944. Principles of Physical Geology: London, Thomas Nelson & Sons.

Hu, R.Z., Burnard, P.G., Bi, X.W., Zhou, M.F., Peng, J.T., Su, W.C. and Zhao, J.H. 2009. Mantle-derived gaseous components in ore-forming fluids of the Xiangshan uranium deposit,

Jiangxi province, China: evidence from He, Ar and C isotopes. Chemical Geology, 266(1-2), pp.86-95.

Hutchinson, W., Finch, A. A., Boyce, A. J. 2020. The sulfur isotope evolution of magmatic-hydrothermal fluids: insight into ore-forming processes. Geochemica et Cosmochimica Acta, 288, 176-198.

Ineson, P.R. and Mitchell, J.G. 1974. K-At isotopic age determinations from some Scottish mineral localities. Transactions of the Institution of Mining and Metallurgy. 83, 3-18.

Jaffey, N. & Robertson, A.H. 2001. New sedimentological and structural data from the Ecemiş Fault Zone, southern Turkey: implications for its timing and offset and the Cenozoic tectonic escape of Anatolia. Journal of the Geological Society, 158(2), 367-378.

Jaffey, N. & Robertson, A. H. 2005. Non-marine sedimentation associated with Oligocene-recent exhumation and uplift of the central Taurus mountains, S Turkey, Sedimentary Geology. 173(1-4), 53–89.

Jenkin, G.R., Al-Bassam, A.Z., Harris, R.C., Abbott, A.P., Smith, D.J., Holwell, D.A., Chapman, R.J. and Stanley, C.J., 2016. The application of deep eutectic solvent ionic liquids for environmentally-friendly dissolution and recovery of precious metals. Minerals Engineering, 87, pp.18-24.

Jenkin, G.R.T, Lusty, P.A., McDonald, I., Smith, M.P., Boyce, A.J., and Wilkinson, J.J. 2015. Ore deposits in an evolving Earth: an introduction. Geological Society, London, Special Publications, 393(1), pp.1-8.

Jenkin, G.R.T., Fallick, A.E., Feely, M. 1997. The geometry of mixing of surface and basinal fluids in the Galway Granite, Connemara, Western Ireland. Geofluids II extended abstracts. 374-377.

Jensen, J.L., Siddoway, C.S., Reiners, P.W., Ault, A.K., Thomson, S.N. and Steele-MacInnis, M. 2018. Single-crystal hematite (U–Th)/He dates and fluid inclusions document widespread Cryogenian sand injection in crystalline basement. Earth and Planetary Science Letters, 500, pp.145-155.

Johnson, C.A., Cardellach, E., Tritlla, J. and Hanan, B.B. 1996. Cierco Pb-Zn-Ag vein deposits; isotopic and fluid inclusion evidence for formation during the Mesozoic extension in the Pyrenees of Spain. Economic Geology, 91(3), pp.497-506.

Kaplan, M.Y., Eren, M., Kadir, S. & Kapur, S. 2013. Mineralogical, geochemical and isotopic characteristics of Quaternary calcretes in the Adana region, southern Turkey: Implications on their origin. Catena, 101, pp.164-177.

Kapur, S., Yaman, S., Go, S.L. & Yetis, C. 1993. Soil stratigraphy and Quaternary caliche in the Misis area of the Adana Basin, southern Turkey. Catena, 20(5), 431-445.

Kayseri-Özer, M. S. 2017. Cenozoic vegetation and climate change in Anatolia—a study based on the IPR-vegetation analysis, Palaeogeography, Palaeoclimatology, Palaeoecology 467, 37–68.

Kemp, S.J. and Merriman, R.J., 2001. Metamorphism of the Lower Palaeozoic rocks of the Leadhills district, southern Scotland, 1: 50K sheets 15E & 23E.

Kendrick, M.A. and Burnard, P. 2013. Noble gases and halogens in fluid inclusions: a journey through the Earth's crust. In The noble gases as geochemical tracers (pp. 319-369). Springer, Berlin, Heidelberg.

Keskin, S. 2016. Attepe Demir Yatağı (Mansurlu Havzası, Adana) ve Çevresi Demir Yatakları ve Zuhurlarının Jeolojisi, Yapısal Özellikleri ve Tektoniği, PhD Thesis, Ankara Üniversitesi Fen Bilimleri Enstitüsü Doktora Tezi, 218 s., Ankara (yayınlanmamış).

Keskin, S**.,** & Ünlü, T. 2016. Attepe Bölgesindeki Siderit Oluşumlarının Mineralojik Özellikleri ve Jeotektonik Ortamı (Kayseri-Adana Havzası, Türkiye). Hacettepe Üniversitesi, Yerbilimleri Dergisi,. 37 (2), 93-120.

Ketcham, R. 2005. Forward and inverse modelling of low-temperature thermochronometry data. Reviews in Mineralogy and Geochemistry, 58 (1), 275-314.

Ketcham, R., Gautheron, C. and Tassan-Got, L. 2011. Accounting for long alpha-particle stopping distances in (U–Th–Sm)/He geochronology: Refinement of the baseline case. Geochimica et Cosmochimica Acta, 75 (24), 7779-7791.

Kim, J., and Jeon, S.I. 2015. 40 Ar/39 Ar age determination using ARGUS VI multiple-collector noble gas mass spectrometer: performance and its application to geosciences. Journal of Analytical Science and Technology, 6(1), pp.1-7.

Kirnbauer, T., Wagner, T., Taubald, H. and Bode, M., 2012. Post-Variscan hydrothermal vein mineralization, Taunus, Rhenish Massif (Germany): Constraints from stable and radiogenic isotope data. Ore geology reviews, 48, pp.239-257.

Kouhestani, H., Mokhtari, M.A.A., Qin, K. and Zhao, J. 2019. Fluid inclusion and stable isotope constraints on ore genesis of the Zajkan epithermal base metal deposit, Tarom–Hashtjin metallogenic belt, NW Iran. Ore Geology Reviews, 109, pp.564-584.

Kullerud, G. 1953. The FeS-ZnS system, a geological thermometer. Doctoral dissertation, Mineral and Geological Museum, Oslo, Norway.

Küpeli, Ş. 2010. Trace and rare-earth element behaviors during alteration and mineralization in the Attepe iron deposits (Feke-Adana, southern Turkey), Journal of Geochemical Exploration, 105(3), 51–74.

Küpeli, Ş., Karadag, M. M., Ayhan, A., Döyen, A. & Arık, F. 2007. C, O, S and Sr isotope studies on the genesis of Fe-carbonate and barite mineralizations in the Attepe iron district (Adana, southern Turkey), Geochemistry, 67(4), 313–322.

Lagios, E. and Hipkin, R.G. 1979. The Tweeddale Granite—a newly discovered batholith in the Southern Uplands. Nature, 280(5724), pp.672-675.

Large, R.R., Gemmell, J.B., Paulick, H. and Huston, D.L. 2001. The alteration box plot: A simple approach to understanding the relationship between alteration mineralogy and lithogeochemistry associated with volcanic-hosted massive sulfide deposits. Economic geology, 96(5), pp.957-971.

Le Guen, M., Orgeval, J.J. and Lancelot, J. 1991. Lead isotope behaviour in a polyphased Pb-Zn ore deposit: Les Malines (Cévennes, France). Mineralium Deposita, 26(3), pp.180-188.

Le Huray, A.P., Caulfield, J.B.D., Rye, D.M., Dixon, P.R. 1987. Basement controls on sediment-hosted P-Zn deposits: a lead isotope study of Carboniferous mineralisation in Central Ireland. Economic Geology. 1695-1709.

Leake, R.C., Auld, H.A., Stone, P., Johnson, C.E. 1981. Gold mineralisation at the southern margin of the Loch Doon granitoid complex, south-west Scotland. Mineral reconnaissance programme. Rep Institute of Geological Science. No. 46.

Leake, R.C., Chapman, R.J., Bland, D.J., Stone, P., Cameron, D.G. and Styles, M.T. 1998. The origin of alluvial gold in the Leadhills area of Scotland: Evidence from interpretation of internal chemical characteristics, Journal of Geochemical Exploration. 63 (1), 7–36.

Leake, R.C., Cooper, C. 1983. The Black Stockarton Moor subvolcanic complex, Galloway. Journal of the Geological Society of London. 140, 665-676.

Lee, M.R., Lindgren, P. and Sofe, M.R. 2014. Aragonite, breunnerite, calcite and dolomite in the CM carbonaceous chondrites: High fidelity recorders of progressive parent body aqueous alteration. Geochimica et Cosmochimica Acta, 144, pp.126-156.

Leeder, M.R. 1988. Recent developments in Carboniferous geology: a critical review with implications for the British Isles and N.W. Europe. Proceedings of the Geologists' Association. 99 (2), 73-100.

Leggett, J.K., McKerrow, W.S. and Eales, M.H. 1979. The southern uplands of Scotland: A lower Palaeozoic accretionary prism. Journal of the Geological Society. 136 (6) 755–770.

Leya, I., Wieler, R. 1999. Nucleogenic production of Ne isotopes in Earth's crust and upper mantle induced by alpha particles from the decay of U and Th. Journal of Geophysical Research. 104, 15439–15450.

Lippolt, H.J., Wernicke, R.F., Bahr, R. 1995. Paragenetic specularite and adularia (Elba, Italy): Concordant (U + Th) -He and K-Ar ages. Earth and Planetary Science Letters. 132, 43-51

Lisiecki, L.E. & Raymo, M.E. 2005. A Pliocene-Pleistocene stack of 57 globally distributed benthic δ18O records. Paleoceanography, 20(1).

Litt, T., Pickarski, N., Heumann, G., Stockhecke, M. & Tzedakis, P.C. 2014. A 600,000 year long continental pollen record from Lake Van, eastern Anatolia (Turkey). Quaternary Science Reviews, 104, 30-41.

Lowry, D., Boyce, A.J., Fallick, A.E., Stephens, W.E., Grassineau, N.V. 2005. Terrane and basement discrimination in northern Britain using sulphur isotopes and mineralogy of ore deposits. From: McDonald, I., Boyce, A.J., Butler, I.B., Herrington, R.J. & Polya, D.A. (eds). 2005. Mineral Deposits and Earth Evolution. Geological Society of London, Special. 248, 133-151.

Lüdecke, T., Mikes, T., Rojay, F. B., Cosca, M. A. & Mulch, A. 2013. Stable isotope-based reconstruction of Oligo-Miocene paleoenvironment and paleohydrology of central Anatolian lake basins (Turkey), Turkish Journal of Earth Sciences, 22(5), 793–819.

Lupton, J.E. and Craig, H. 1975. Excess 3He in oceanic basalts: evidence for terrestrial primordial helium. Earth and Planetary Science Letters, 26(2), pp.133-139.

Łuszczak, K., Persano, C., Braun, J. and Stuart, F.M., 2017. How local crustal thermal properties influence the amount of denudation derived from low-temperature thermochronometry. Geology, 45(9), pp.779-782.

Łuszczak, K., Persano, C., Stuart, F.M. 2018. Early Cenozoic denudation of central west Britain in response to transient and permanent uplift above a mantle plume. Tectonics, 37, 914–934.

Mackay, R.A. 1959. The Leadhills-Wanlockhead mining district. In: symposium on the future of non-ferrous mining in Great Britain and Ireland, Transactions of the Institution of Mining and Metallurgy. London.

Manspeizer, W., 1988. Triassic–Jurassic rifting and opening of the Atlantic: an overview. Developments in Geotectonics, 22, pp.41-79.

Marques de Sá, C., Noronha, F., Cardellach, E., Bobos, I. 2019. Fluid inclusion and (S, C, O, Pb) isotope study of Pb-Zn-(Cu-Ag) hydrothermal veins from Central and Northern Portugal – Metallogenic implications. Ore Geology Reviews. 112, 103043.

McMillan, A.A. and Brand, P.J. 1995. Depositional setting of Permian and upper Carboniferous strata of the Thornhill basin, Dumfriesshire. Scottish Journal of Geology 31 (1), 43–52.

Meesters, A. & Dunai, T. 2005. A noniterative solution of the (U-Th)/He age equation, Geochemistry, Geophysics, Geosystems 6(4).

Meijers, M.J., Brocard, G.Y., Cosca, M.A., Lüdecke, T., Teyssier, C., Whitney, D.L. and Mulch, A., 2018. Rapid late Miocene surface uplift of the Central Anatolian Plateau margin. Earth and Planetary Science Letters, 497, pp.29-41.

Meijers, M. J., Brocard, G. Y., Whitney, D. L. & Mulch, A. 2020. Paleoenvironmental conditions and drainage evolution of the Central Anatolian lake system (Turkey) during late Miocene to Pliocene surface uplift, Geosphere, 16(2), 490–509.

Meijers, M. J., Strauss, B. E., Özkaptan, M., Feinberg, J. M., Mulch, A., Whitney, D. L. & Kaymakçı, N. 2016. Age and paleoenvironmental reconstruction of partially remagnetized lacustrine sedimentary rocks (Oligocene Aktoprak basin, central Anatolia, Turkey), Geochemistry, Geophysics, Geosystems, 17(3), 914–939.

Mitchell, J.G., Halliday, A.N. 1976. Extent of Triassic/Jurassic hydrothermal ore deposits on the North Atlantic margins, Transactions of the Institution of Mining and Metallurgy. 85, 159-161.

Molnar, P. 2005. Mio-Pliocene growth of the Tibetan plateau and evolution of east Asian climate, Palaeontologia Electronica, 8(1), 1–23.

Molnar, P., England, P. & Martinod, J. 1993. Mantle dynamics, uplift of the Tibetan plateau, and the Indian monsoon, Reviews of Geophysics, 31(4), 357–396.

Monshi, A., Foroughi, M.R. and Monshi, M.R., 2012. Modified Scherrer equation to estimate more accurately nano-crystallite size using XRD. World journal of nano science and engineering, 2(3), pp.154-160.

Monteiro, H., Vasconcelos, P., Farley, K., Spier, C. and Mello, C. 2014. (U–Th)/He geochronology of goethite and the origin and evolution of Cangas. Geochimica et Cosmochimica Acta, 131, 267-289.

Moscati, R.J. and Neymark, L.A., 2020. U–Pb geochronology of tin deposits associated with the Cornubian Batholith of southwest England: Direct dating of cassiterite by in situ LA-ICPMS. Mineralium Deposita, 55(1), pp.1-20.

Muchez, P., Heijlen, W., Banks, D., Blundell, D., Boni, M., Grandia, F. 2005. Extensional tectonics and the timing and formation of basin-hosted deposits in Europe. Ore Geol Rev. 241-267.

Munoz, M., Baron, S., Boucher, A., Béziat, D. and Salvi, S. 2016. Mesozoic vein-type Pb–Zn mineralization in the Pyrenees: Lead isotopic and fluid inclusion evidence from the Les Argentières and Lacore deposits. Comptes Rendus Geoscience, 348(3-4), pp.322-332.

Munoz, M., Boyce. A.J., Courjault-Rade, P., Fallick, A. E., Tollon, F. 1994. Multi-stage fluid incursion in the Palaeozoic basement-hosted Saint-Salvy ore deposit (NW Montagne Noir France). Applied Geochemistry. 9, 609-626.

Myint, A.Z., Yonezu, K., Boyce, A.J., Selby, D., Scherstén, A., Tindell, T., Watanabe, K. and Swe, Y.M. 2018. Stable isotope and geochronological study of the Mawchi Sn-W deposit, Myanmar: Implications for timing of mineralization and ore genesis. Ore Geology Reviews, 95, pp.663-679.

Neymark, L.A., Holm-Denoma, C.S., Pietruszka, A.J., Aleinikoff, J.N., Fanning, C.M., Pillers, R.M. and Moscati, R.J., 2016. High spatial resolution U-Pb geochronology and Pb

isotope geochemistry of magnetite-apatite ore from the Pea Ridge iron oxide-apatite deposit, St. Francois Mountains, southeast Missouri, USA. Economic Geology, 111(8), pp.1915-1933.

Niedermann, S., Graf, T., Kim, J.S., Kohl, C.P., Marti, K. and Nishiizumi, K. 1994. Cosmic-ray-produced ^{21}Ne in terrestrial quartz: the neon inventory of Sierra Nevada quartz separates. Earth and Planetary Science Letters, 125(1-4), pp.341-355.

O'Keefe, W.G. 1986. Age and postulated source rocks for mineralisation in Central Ireland, as indicated by lead isotopes. In: Andrew, C.J., Crowe, R.W.A., Finlay, S., Pennel, W.M., Payne., J. Geology and genesis of mineral deposits in Ireland. Irish Association of Economic Geology, 617-624.

Ocakoğlu, F. 2002. Palaeoenvironmental analysis of a Miocene basin in the high Taurus mountains (southern Turkey) and its palaeogeographical and structural significance, Geological Magazine, 139(4), 473–487.

Öğretmen, N., Cipollari, P., Frezza, V., Faranda, C., Karanika, K., Gliozzi, E., Radeff, G. & Cosentino, D. 2018. Evidence for 1.5 km of uplift of the Central Anatolian plateau's southern margin in the last 450 kyr and implications for its multiphased uplift history, Tectonics 37(1), 359–390.

Ohmoto, H., and Rye, R.O. 1979. Isotope of sulfur and carbon in H.L. Barnes (Ed.), Geochemistry of Hydrothermal ore deposits, John Wiley and Sons, New York (1979), pp. 509-567

O'Nions, R.K. and Oxburgh, E.R. 1983. Heat and helium in the Earth. Nature, 306(5942), pp.429-431.

Oxburgh, R.E., O'Nions, R.K., Hill, R.I. 1986. Helium isotopes in sedimentary basins. Nature. 324, 632-635.

Parnell, J. 1995. Hydrocarbon migration in the Solway Basin. Geol. J. 30, 25-38.

Parnell, J. 1997. Fluid migration in the north Irish Seas-North Channel region. From Meadows, N. S., Trueblood, S. P., Hardman, M. & Cowan, G. (eds), 1997, Petroleum Geology of the Irish Sea and Adjacent Areas, Geological Society. Special. 124, 213-228.

Patterson, C., Tilton, G. and Inghram, M. 1955. Age of the Earth. Science, 121(3134), pp.69-75.

Pattrick, R.A.D. and Bowell, R.J. 1991. The genesis of the West Shropshire Orefield: evidence from fluid inclusions, sphalerite chemistry, and sulphur isotopic ratios. Geological Journal, 26(2), pp.101-115.

Pattrick, R.A.D., Russel, M.J. 1989. Sulphur isotopic investigation of Lower Carboniferous vein deposits of the British Isles. Mineralium Deposita. 24, 148-153.

Peace, W.M. and Wallace, M.W. 2000. Timing of mineralization at the Navan Zn-Pb deposit: A post-Arundian age for Irish mineralization. Geology, 28(8), pp.711-714.

Pearson, D.G., Emeleus, C.H. and Kelley, S.P., 1996. Precise 40Ar/39Ar age for the initiation of Palaeogene volcanism in the Inner Hebrides and its regional significance. Journal of the Geological Society, 153(6), pp.815-818.

Persano, C., Bishop, P., Barfod, D. N. 2002. Apatite (U-Th)/He age constraints on the development of the Great Escarpment on the southeastern Australian passive margin. Earth and Planetary Science Letters. **200.** (1-2), 79-90.

Porteous, J.M. 1876. "God's Treasure-house in Scotland", a History of Times, Mines, and Lands in the Southern Highlands. Simpkin, Marshall, & Company.

Racano, S., Jara-Muñoz, J., Cosentino, D. & Melnick, D. 2020. Variable quaternary uplift along the southern margin of the Central Anatolian plateau inferred from modelling marine terrace sequences, Tectonics

Radeff, G. 2014. Geohistory of the Central Anatolian plateau southern margin (southern Turkey). PhD thesis, Potsdam University.

Rasmussen, B., Sheppard, S. and Fletcher, I.R., 2006. Testing ore deposit models using in situ U-Pb geochronology of hydrothermal monazite: Paleoproterozoic gold mineralization in northern Australia. Geology, 34(2), pp.77-80.

Reed, M.H. 1997. Hydrothermal Alteration and its Relationship to Ore Fluid Composition. In Barnes, H.L., 1997. Geochemistry of Hydrothermal Ore Deposits, 3rd edn., New York: Wiley – Blackwell

Reiners, P. W. 2005. Zircon (U-Th)/He thermochronometry. in Reiners, P. W., Ehlers, T.A. (eds) Thermochronology. Reviews in Mineralogy and Geochemistry. Mineralogical Society of America 58 151-179.

Reiners, P., and Farley, K. 1999. Helium diffusion and (U–Th)/He thermochronometry of titanite. Geochimica et Cosmochimica Acta, 63 (22), 3845-3859.

Riffel, S.B., Vasconcelos, P.M., Carmo, I.O. and Farley, K.A., 2016. Goethite (U–Th)/He geochronology and precipitation mechanisms during weathering of basalts. Chemical Geology, 446, pp.18-32.

Robb, J., 2005. Hydrothermal ore forming processes. Introduction to ore forming processes. Johannesburg, Black well Publishing Company, pp.129-214.

Robertson, A. & Grasso, M. 1995. Overview of the late Tertiary–recent tectonic and palaeo environmental development of the Mediterranean region, Terra Nova, 7(2), 114–127.

Robertson, A.H.F., Parlak, O., Rizaoğlu, T., Ünlügenç, Ü., İnan, N., Tasli, K. and Ustaömer, T., 2007. Tectonic evolution of the South Tethyan ocean: evidence from the Eastern Taurus Mountains (Elazığ region, SE Turkey). Geological Society, London, Special Publications, 272(1), pp.231-270.

Robinson, B.W., Kusakabe, M. 1975. Quantitative preparation of SO_2 for $^{34}S/^{32}S$ analysis from sulphides by combustion with cuprous oxides. Analytical Chemistry. 47, 1179-1181.

Ruiz-Martínez, V.C., Torsvik, T.H., van Hinsbergen, D.J. and Gaina, C., 2012. Earth at 200 Ma: Global palaeogeography refined from CAMP palaeomagnetic data. Earth and Planetary Science Letters, 331, pp.67-79.

Russell, M.J., 1968. Structural controls of base metal mineralization in Ireland in relation to continental drift. Transactions of the Institution of Mining and Metallurgy, 77, pp.B117-B128.

Russell, M.J., 1972. The geological environment of post-Caledonian base-metal mineralization in Ireland (Doctoral dissertation, Durham University).

Russell, M.J., 1978. Downward-excavating hydrothermal cells and Irish type ore deposits: Importance of an underlying thick Caledonian prism: Institution of Mining and Metallurgy Transactions, v. 87, p. B168 B, 171.

Rutherford, E. 1905. Present problem in radioactivity. Popular Science Monthly. May. 1-34.

Ryan, W.B., Carbotte, S.M., Coplan, J.O., O'Hara, S., Melkonian, A., Arko, R., Weissel, R.A., Ferrini, V., Goodwillie, A., Nitsche, F. and Bonczkowski, J. 2009. Global multi-resolution topography synthesis. Geochemistry, Geophysics, Geosystems, 10(3).

Rye, R.O. and Ohmoto, H., 1974. Sulfur and carbon isotopes and ore genesis: A review. Economic Geology, 69(6), pp.826-842.

Samson, I. M., Banks, D. A. 1988. Epithermal base-metal vein mineralization in the southern uplands of Scotland: Nature and origin of the fluids. Mineralium Deposita. 23 (1) 1-8.

Sánchez, V., Cardellach, E., Corbella, M., Vindel, E., Martín-Crespo, T. and Boyce, A.J. 2010. Variability in fluid sources in the fluorite deposits from Asturias (N Spain): Further evidences from REE, radiogenic (Sr, Sm, Nd) and stable (S, C, O) isotope data. Ore Geology Reviews, 37 (2), pp. 87-100.

Sánchez, V., Corbella, M., Fuenlabrada, JM, Vindel, E. and Martín-Crespo, T. 2006. Sr and Nd isotope data from the fluorspar district of Asturias, northern Spain. Journal of Geochemical Exploration, 89 (1-3), pp. 348-350.

Sarıkaya, M.A., Yıldırım, C. & Çiner, A. 2015. Late Quaternary alluvial fans of Emli Valley in the Ecemiş Fault Zone, south central Turkey: Insights from cosmogenic nuclides. Geomorphology, 228, pp.512-525.

Schäfer, J.M., Ivy-Ochs, S., Wieler, R., Leya, I., Baur, H., Denton, G.H. and Schlüchter, C. 1999. Cosmogenic noble gas studies in the oldest landscape on earth: surface exposure ages of the Dry Valleys, Antarctica. Earth and Planetary Science Letters, 167(3-4), pp.215-226.

Schemmel, F., Mikes, T., Rojay, B. & Mulch, A. 2013. The impact of topography on isotopes in precipitation across the Central Anatolian plateau (Turkey), American Journal of Science, 313(2), 61–80.

Schildgen, T.F., Cosentino, D., Bookhagen, B., Niedermann, S., Yıldırım, C., Echtler, H., Wittmann, H. & Strecker, M. R. 2012. Multi-phased uplift of the southern margin of the Central Anatolian plateau, Turkey: A record of tectonic and upper mantle processes, Earth and Planetary Science Letters, 317, 85–95.

Schildgen, T.F., Yıldırım, C., Cosentino, D. & Strecker, M. R. 2014. Linking slab break-off, Hellenic trench retreat, and uplift of the Central and Eastern Anatolian plateaus, Earth Science Reviews, 128, 147–168.

Schneider, J., Quadt, A.V., Wilkinson, J.J., Boyce, A.J. and Andrew, C.J. 2007. August. Age of Silvermines Irish-type Zn-Pb deposit from direct Rb-Sr dating of sphalerite. In Digging deeper: Proceedings of the Ninth Biennial SGA meeting: Dublin, Ireland, Irish Association for Economic Geology (pp. 373-376).

Seal, R.R. 2006. Sulfur Isotope geochemistry of sulfide minerals. Reviews in Mineralogy and Geochemistry. 61, 633–677

Şengör, A., Görür, N. & Şaroğlu, F. 1985. Strike-slip faulting and related basin formation in zones of tectonic escape: Turkey as a case study. in Strike-Slip Faulting and Basin Formation, edited by Biddle, K.T., & Christie-Blick, N. Special publication - Society of Economic Paleontologists and Mineralogists, 37, 227-264.

Şengör, A.C. and Yilmaz, Y., 1981. Tethyan evolution of Turkey: a plate tectonic approach. Tectonophysics, 75(3-4), pp.181-241.

Sensoy, S. 2004. The mountains influence on Turkey climate, in Balwois Conference on Water Observation and Information System for Decision Support.

Shaw, M.H., Fortey, N.J., Gibberd, A.J., Rollin, K.E. 1995. Gold exploration in the Duns area, Southern Uplands, Scotland. Mineral Reconnaissance Programme Report, BGS. No. 138.

Shepherd, T.J. and Goldring, D.C. 1993. Cumbrian hematite deposits, Northwest England. In: Pattrick, R.A.D. & Polya, D. Mineralisation in the British Isles. Chapman & Hall, London, 419–445.

Shuster, D.L. and Farley, K.A., 2004. 4He/3He thermochronometry. Earth and Planetary Science Letters, 217(1-2), pp.1-17.

Shuster, D. L., Farley, K. A., Vasconcelos, P. M., Balco G., Monteiro, H. S., Waltenberg, K., Stone, J. O. 2012. Cosmogenic He-3 in hematite and goethite from Brazilian ‘‘canga” duricrust demonstrates the extreme stability of these surfaces. Earth and Planetary Science Letters. 329, 41–50.

Shuster, D. L., Vasconcelos, P. M., Heim, J. A. & Farley, K. A. 2005. Weathering geochronology by (U-Th)/He dating of goethite, Geochimica et Cosmochimica Acta, 69(3), 659–673.

Simon, J. and Reid, M. 2005. The pace of rhyolite differentiation and storage in an ‘archetypical’ silicic magma system, Long Valley, California. Earth and Planetary Science Letters. 235 (1-2), 123-140.

Simpson, J.B., Richey, M.C., MacGregor, A.G., Pringle, J. 1936. The geology of the Sanquhar coalfield and adjacent basin of Thornhill. Memoirs of the Geological Survey of Scotland.

Sinclair, A.J., Macquar, J.C. and Rouvier, H. 1993. Re-evaluation of lead isotopic data, southern Massif Central, France. Mineralium Deposita, 28(2), pp.122-128.

Speakman, S.A., 2014. Estimating crystallite size using XRD. MIT Center for Materials Science and Engineering, 2, p.14.

Spence-Jones, C.P., Jenkin, G.R., Boyce, A.J., Hill, N.J. and Sangster, C.J. 2018. Tellurium, magmatic fluids and orogenic gold: An early magmatic fluid pulse at Cononish gold deposit, Scotland. Ore Geology Reviews, 102, pp.894-905.

Stensgaard, B.M., Stendal, H., Kalvig, P. and Hanghøj, K., 2017. Review of potential resources for critical minerals in Greenland. Videncenter for Mineralske Råstoffer og Materialer, De Nationale Geologiske Undersøgelser for Danmark og Grønland.

Stone, P, McMillan, A A, Floyd, J D, Barnes, R P, and Phillips, E R. 2012. British regional geology: South of Scotland. Fourth edition. Keyworth, Nottingham: British Geological Survey.

Stone, P. 2014. The Southern Uplands Terrane in Scotland – a notional controversy revisited. Scottish Journal of Geology. 50, 97-123

Stone, P., Rushton, W.A. 2018. On the age of the Ballantrae Complex, SW Scotland. Scottish Journal of Geology. 54, 77-86.

Strutt, R. J. 1905. On the radioactive minerals. Proceedings of the Royal Society of London. A76, 88-101.

Strutt, R.J. 1908. On the accumulation of helium in geological time. Proceedings of the Royal Society of London. Series A, Containing Papers of a Mathematical and Physical Character, 81(547), pp.272-277.

Stuart, F.M., Burnard, P.G., Taylor, R.E.A. and Turner, G. 1995. Resolving mantle and crustal contributions to ancient hydrothermal fluids: He-Ar isotopes in fluid inclusions from Dae Hwa W-Mo mineralisation, South Korea. Geochimica et Cosmochimica Acta, 59(22), pp.4663-4673.

Stuart, F.M., Ellam, R.M., Harrop, P.J., Fitton, J.G. and Bell, B.R., 2000. Constraints on mantle plumes from the helium isotopic composition of basalts from the British Tertiary Igneous Province. Earth and Planetary Science Letters, 177(3-4), pp.273-285.

Svenning, J.C., (2003), Deterministic Plio-Pleistocene extinctions in the European cool-temperate tree flora. Ecology Letters, 6(7), 646-653.

Tapster, S. and Bright, J.W., 2020. High-precision ID-TIMS cassiterite U–Pb systematics using a low-contamination hydrothermal decomposition: implications for LA-ICP-MS and ore deposit geochronology. Geochronology, 2(2), pp.425-441.

Tardy, Y. and Nahon, D. 1985. Geochemistry of laterites, stability of Al-goethite, Al-hematite, and Fe^{3+}-kaolinite in bauxites and ferricretes: an approach to the mechanism of concretion formation. American Journal of Science, 285(10), 865-903.

Temple, A.K. 1954. The paragenetical mineralogy of the Leadhills and Wanlockhead lead and zinc deposits, PhD thesis, University of Leeds.

Temple, A.K. 1956. The Leadhills-Wanlockhead lead and zinc deposit. Transactions of the Royal Society of Edinburgh. 63, 85-113.

Thompson, R.N. and Gibson, S.A., 1991. Subcontinental mantle plumes, hotspots and pre-existing thinspots. Journal of the Geological Society, 148(6), pp.973-977.

Tremblay, M., Fox, M., Schmidt, J., Tripathy-Lang, A., Wielicki, M., Harrison, T., Zeitler, P. and Shuster, D. 2015. Erosion in southern Tibet shut down at ∼10 Ma due to enhanced rock uplift within the Himalaya. Proceedings of the National Academy of Sciences. 112 (39), 12030-12035.

Turner, G. and Stuart, F. 1992. Helium/heat ratios and deposition temperatures of sulphides from the ocean floor. Nature, 357(6379), pp.581-583.

Tylecote, R. F., 1964. Roman lead working in Britain. The British Journal for the History of Science. 2 (1), 25-43.

Tyrrell, S., Haughton, P.D. and Daly, J.S., 2007. Drainage reorganization during breakup of Pangea revealed by in-situ Pb isotopic analysis of detrital K-feldspar. Geology, 35(11), pp.971-974.

Tyrrell, S., Haughton, P.D., Souders, A.K., Daly, J.S. and Shannon, P.M., 2012. Large-scale, linked drainage systems in the NW European Triassic: insights from the Pb isotopic composition of detrital K-feldspar. Journal of the Geological Society, 169(3), pp.279-295.

Tzedakis, P.C., Hooghiemstra, H. & Pälike, H. 2006. The last 1.35 million years at Tenaghi Philippon: revised chronostratigraphy and long-term vegetation trends. Quaternary Science Reviews, 25(23-24), 3416-3430.

Valley, P.M., Hanchar, J.M. and Whitehouse, M.J., 2009. Direct dating of Fe oxide-(Cu-Au) mineralization by U/Pb zircon geochronology. Geology, 37(3), pp.223-226.

Vasconcelos, P. M., Heim, J. A., Farley, K. A., Monteiro, H. S., Waltenberg, K. 2013. 40Ar/39Ar and (U–Th)/He - 4He/3He geochronology of landscape evolution and channel iron deposit genesis at Lynn Peak, Western, Australia. Geochimica et Cosmochimica Acta. 117, 283–312.

Vasconcelos, P.M. 1999. K-Ar and $^{40}Ar/^{39}Ar$ geochronology of weathering processes, Annual Review of Earth and Planetary Sciences, 27(1), 183–229.

Vasconcelos, P.M., Reich, M. & Shuster, D. L. 2015. The paleoclimatic signatures of supergene metal deposits, Elements, 11(5), 317–322.

Vaughan, A.P.M. and Livermore, R.A., 2005. Episodicity of Mesozoic terrane accretion along the Pacific margin of Gondwana: implications for superplume-plate interactions. Geological Society, London, Special Publications, 246(1), pp.143-178.

Vaughan, A.P. and Storey, B.C., 2007. A new supercontinent self-destruct mechanism: evidence from the Late Triassic–Early Jurassic. Journal of the Geological Society, 164(2), pp.383-392.

Velasco, F., Pesquera, A. and Herrero, J.M., 1996. Lead isotope study of Zn-Pb ore deposits associated with the Basque-Cantabrian basin and Paleozoic basement, northern Spain. Mineralium Deposita, 31(1), pp.84-92.

Vermeesch, P., Balco, G., Blard, P-H., Dunai, T.J., Kober, F., Niedermann, S., Shuster, D.L., Strasky, S., Stuart, F.M., Wieler, R., Zimmermann, L. 2015. Interlaboratory comparison of cosmogenic ^{21}Ne in quartz. Quaternary Geochronology. 26, 20-28.

Wells, M., Danišík, M., McInnes, B. and Morris, P. 2019. (U-Th)/He-dating of ferruginous duricrust: Insight into laterite formation at Boddington, WA. Chemical Geology, 522, 148-161.

Wernicke, R.S., Lippolt, H.J. 1994. Dating of vein Specularite using internal $(U+Th)/^{4}He$ isochrons. Geophysical Research Letters. 21, 345–347.

Wetherill, G. W. 1954. Variations in the isotopic abundances of neon and argon extracted from radioactive minerals. Physical Reviews. 96, 679–683.

Wilkinson, J.J., Eyre, S.L., Boyce., A.J. 2005. Ore-forming processes in Irish-type carbonate-hosted Zn-Pb deposits: Evidence from mineralogy, chemistry, and isotopic composition of sulfides at the Lisheen mine. Economic Geology. 100 (1), 63-86.

Wilson, G.V., and Flett, J.S. 1921. The lead, zinc, copper, and nickel ores of Scotland. Mem. Geol. Sur. Scot. Special Reports on the Mineral Resources of Great Britain. 17, 1-42.

Wilson, J.T. 1966. Did the Atlantic Close and then Re-Open? Nature, 211(5050), pp.676-681.

Wu, L.Y., Hu, R.Z., Li, X.F., Stuart, F.M., Jiang, G.H., Qi, Y.Q. and Zhu, J.J. 2018. Mantle volatiles and heat contributions in high sulfidation epithermal deposit from the Zijinshan Cu-Au-Mo-Ag orefield, Fujian Province, China: Evidence from He and Ar isotopes. Chemical Geology, 480, pp.58-65.

Wu, L.Y., Stuart, F.M., Di Nicola, L., Heizler, M., Benvenuti, M. and Hu, R.Z., 2019. Multi-aliquot method for determining (U+ Th)/He ages of hydrothermal hematite: Returning to Elba. Chemical Geology, 504, pp.151-157.

Yakubovich, O., Vikentyev, I., Zarubina, O., Bryanskiy, N., Gorokhovskii, B., Kotov, A., Dril, S. and Bortnikov, N. 2019. U–Th–He dating of pyrite from the Uzelga copper-zinc massive sulfide deposit (South Urals, Russia): first application of a new geochronometer. Doklady Earth Sciences. 485(2), 368-371.

Yapp, C.J. 2020. Recovery and interpretation of the $^{18}O/^{16}O$ of Miocene oolitic goethites in multi-generational mixtures of Fe (III) oxides from a channel iron deposit of Western Australia. Geochimica et Cosmochimica Acta, 279, pp.143-164.

Yatsevich, I. and Honda, M. 1997. Production of nucleogenic neon in the Earth from natural radioactive decay. Journal of Geophysical Research. 102, 10291.

Yesares, L. Drummond, D. Hollis, S. P., Doran, A. L., Mengue, J. F., Boyce, A. J., Blakeman, R.J., Ashton, J. H. 2019. 'Coupling mineralogy, textures, stable and radiogenic isotopes in identifying ore-forming processes in Irish-type carbonate-hosted Zn–Pb deposits', Minerals, 9(6), p. 335.

Yıldırım, C., Sarıkaya, M. A. & Çiner, A. 2016. Late Pleistocene intraplate extension of the central Anatolian plateau, Turkey: Inferences from cosmogenic exposure dating of alluvial fan, landslide, and moraine surfaces along the Ecemiş fault zone, Tectonics 35(6), 1446–1464.

Young, K., van Soest, M., Hodges, K., Watson, E., Adams, B. and Lee, P. 2013. Impact thermochronology and the age of Haughton impact structure, Canada. Geophysical Research Letters. 40 (15), 3836-3840.

Zachos, J., Pagani, M., Sloan, L., Thomas, E. & Billups, K. (2001), Trends, rhythms, and aberrations in global climate 65 Ma to present, Science, 292(5517), 686–693.

Ziegler, J. F. 1977. Helium: Stopping powers and ranges in all elemental matter. Pergamon, New York

Zeitler, P. K., Herczig, A. L., McDougall, I., Honda, M. 1987. U-Th-He dating of apatite: A potential thermochronometer. Geochimica et Cosmochimica Acta. 51:2865-2868

Zeng, Z., Ma, Y., Chen, S., Selby, D., Wang, X. and Yin, X., 2017. Sulfur and lead isotopic compositions of massive sulfides from deep-sea hydrothermal systems: implications for ore genesis and fluid circulation. Ore Geology Reviews, 87, pp.155-171.